

Core helium burning and low-metallicity AGB stars: structure and evolution

Thomas Constantino

B.Sc. (Hons.) B.Eng. (Hons.)

A thesis submitted for the degree of Doctor of Philosophy

Monash Centre for Astrophysics
School of Physics and Astronomy
Monash University, Australia

December 2015

Copyright notice

© Thomas Constantino 2015. Except as provided in the Copyright Act 1968, this thesis may not be reproduced in any form without the written permission of the author.

I certify that I have made all reasonable efforts to secure copyright permissions for third-party content included in this thesis and have not knowingly added copyright content to my work without the owner's permission.

Contents

Abstract	v
Publications	vii
Acknowledgements	viii
1. Introduction	1
1.1 The importance of stars	1
1.2 The lives of low-mass stars	2
1.3 Stellar structure code	6
1.3.1 Updates to the equations of state	8
1.3.2 Improved low-temperature opacity	9
1.4 Stellar pulsations	9
1.4.1 Pulsation calculations	11
1.5 Some shortcomings in stellar models	12
1.6 Thesis outline	14
2. The treatment of mixing in core helium burning models –	
I. Implications for asteroseismology	17
2.1 Abstract	18
2.2 Introduction	19
2.2.1 Brief overview	19
2.2.2 The problem of convective boundaries	19
2.2.3 Classical constraints from globular clusters	21
2.2.4 Asteroseismology of CHeB stars	22
2.2.5 The core mass at the flash	24
2.2.6 Clues from subdwarf B stars	24
2.2.7 The challenges and potential of CHeB asteroseismology	25
2.3 Methods	26
2.3.1 Evolution code	26
2.3.2 Pulsation analysis	26
2.3.3 Core mixing schemes	29
2.3.4 Composition smoothing	33
2.4 Results	34
2.4.1 Overview of the CHeB structure	34
2.4.2 $\Delta\Pi_1$ dependence on bulk core properties	37
2.4.3 Pulsations in early post core-flash CHeB models	40
2.4.4 Pulsation properties for models with different mixing schemes	49

2.4.5	Matching ensemble $\Delta\Pi_1$ observations	55
2.4.6	The effect of the boundary of the convective core on pulsations . . .	62
2.4.7	Subdwarf B models	64
2.4.8	Dependence on input physics	69
2.4.9	Late-CHeB and early-AGB models	70
2.5	Summary and conclusions	74
3.	The treatment of mixing in core helium burning models –	
	II. Cluster star counts	79
3.1	Abstract	80
3.2	Introduction	80
3.2.1	CHeB models: Key properties and uncertainties	81
3.2.2	Insights from asteroseismology	82
3.2.3	Globular cluster star counts and the AGB clump	82
3.2.4	Other uncertainties	84
3.2.5	Revisiting the R-method	84
3.3	Observational data	85
3.3.1	Photometry	85
3.3.2	Sample selection	86
3.3.3	Comparison of R_2 between different data sets	86
3.3.4	Colour transformations and bolometric corrections	88
3.3.5	Luminosity probability density functions	89
3.3.6	Statistical errors	91
3.3.7	Cluster metallicity and HB morphology	92
3.3.8	General observed properties of red-HB clusters	94
3.4	Stellar models	95
3.4.1	Description of models	95
3.4.2	Mixing schemes	102
3.4.3	Diagnostics for models	103
3.4.4	Overall comparison between models and observations	103
3.4.5	Effect of the mixing prescription	104
3.4.6	Effects of composition and other input physics	106
3.4.7	Numerical effects	119
3.4.8	Core breathing pulses and their suppression	123
3.4.9	Post-CHeB maximal overshoot evolution	125
3.4.10	The AGB luminosity limit	127
3.5	Summary and conclusions	130
4.	On the necessity of composition-dependent	
	low-temperature opacity in metal-poor AGB models	135
4.1	Abstract	136
4.2	Introduction	137
4.3	Methods	140
4.3.1	Stellar structure code	140
4.3.2	Updated low-T opacity treatment	140

4.3.3	Stellar models	141
4.4	Stellar model results	142
4.4.1	Importance for HBB models	142
4.4.2	Borderline HBB models	147
4.4.3	Low-mass models	147
4.4.4	Lessons from zero-metallicity models	157
4.5	Discussion	158
4.5.1	Key findings	158
4.5.2	Implications for CEMP and NEMP stars	158
4.5.3	AGB stars as globular cluster polluters	162
4.5.4	Uncertainties	165
4.6	Conclusions	166
4.6.1	Low-mass models	167
4.6.2	Borderline HBB models	167
4.6.3	HBB models	168
4.6.4	Implications for chemical evolution	168
5.	Conclusions	169
5.1	Future work	171
	References	175

Abstract

In this thesis we scrutinize and improve theoretical models of the two helium burning stages of low-mass ($M \lesssim 8 M_{\odot}$) stellar evolution – the core helium burning (CHeB) and asymptotic giant branch (AGB) phases. Accurate stellar models of these phases are essential for the understanding of the physics of stars, the chemical evolution of galaxies, and astrophysics more generally, where the observation of starlight is paramount.

In this study we use new models and observational data to investigate two particular important uncertainties during the CHeB and AGB stages that have compounding effects on the evolution. In CHeB models, feedback from convective overshoot can lead to the development of a ‘semiconvection’ zone outside the convective core that can extend the lifetime of the phase by up to a factor of two. In the later thermally pulsing-AGB phase, accounting for the opacity increase due to in situ composition changes can increase the stellar radius, and therefore mass loss rate, truncating the evolution.

We compute a grid of CHeB stellar models with four different treatments of convective boundaries using the Monash University stellar evolution code MONSTAR. Theoretical non-radial adiabatic pulsations for these models are then compared with recent asteroseismic observations from the *Kepler* telescope. Next, we infer the horizontal branch and AGB lifetimes of globular cluster stars from star counts in HST photometry and compare these with predictions from evolution sequences with the different mixing schemes. Finally, for models of the thermally-pulsing AGB phase we incorporate into MONSTAR new low-temperature molecular opacity data that accounts for changes in the surface abundance of carbon, nitrogen, and oxygen. The effect of this update is tested by computing a grid of low-metallicity AGB models that experience the third dredge-up.

We identify two distinct CHeB structures that can simultaneously match the globular cluster and asteroseismic observations: those with (i) a slowly mixing region outside the convective core that traps oscillation modes, or (ii) the largest possible convective core, requiring a novel scheme for convective overshoot. We may be able to discriminate between these two possibilities with further work, including the analysis of biases in the observed sample and multi-dimensional simulations.

The inclusion of composition-dependent low-T opacity in low-metallicity models shortens the AGB lifetime, increases the mass threshold for hot bottom burning, and radically affects chemical yields. By computing initially metal-free models, we demonstrate that if the third dredge-up occurs, there is no metallicity below which composition-dependent low-T opacity may be neglected. The reduced nitrogen yield from models with the new opacity may help explain the observed numbers of carbon- and nitrogen-enhanced metal-poor stars: this should be confirmed with binary population synthesis calculations.

Monash University

Declaration for thesis based or partially based on conjointly published or unpublished work

General Declaration

In accordance with Monash University Doctorate Regulation 17.2 Doctor of Philosophy and Research Master's regulations the following declarations are made:

I hereby declare that this thesis contains no material which has been accepted for the award of any other degree or diploma at any university or equivalent institution and that, to the best of my knowledge and belief, this thesis contains no material previously published or written by another person, except where due reference is made in the text of the thesis.


This thesis includes two original papers published in peer reviewed journals and one original paper submitted for publication. The core theme of the thesis is the structure and evolution of core helium burning and AGB stars. The ideas, development and writing up of all the papers in the thesis were the principal responsibility of myself, the candidate, working within the School of Physics and Astronomy under the supervision of John Lattanzio.

The inclusion of co-authors reflects the fact that the work came from active collaboration between researchers and acknowledges input into team-based research.

In the case of Chapter 2, 3, and 4, my contribution to the work involved the following:

Thesis chapter	Publication title	Publication status	Nature and extent of candidate's contribution
2	The treatment of mixing in core helium burning models - I. Implications for asteroseismology	Published	First author; code development, calculations, analysis of results, manuscript preparation.
3	The treatment of mixing in core helium burning models -- II. Cluster star counts	Submitted	First author; code development, calculations, analysis of results, manuscript preparation.
4	On the Necessity of Composition-dependent Low-temperature Opacity in Models of Metal-poor Asymptotic Giant Branch Stars	Published	First author; code development, calculations, analysis of results, manuscript preparation.

I have renumbered sections of submitted and published papers in order to generate a consistent presentation within the thesis.

Signed: 

Date: 2 - 9 - 15

Publications

Refereed

1. Constantino, T., Campbell, S.W., Christensen-Dalsgaard, J., Lattanzio, J., Stello, D. (2015). “The treatment of mixing in core helium burning models – I. Implications for asteroseismology”, *Monthly Notices of the Royal Astronomical Society*, 452, 123.
2. Angelou, G., D’Orazi, V., Constantino, T., Church, R., Stancliffe, R., Lattanzio, J. (2015). “Diagnostics of Stellar Modelling from Spectroscopy and Photometry of Globular Clusters”, *Monthly Notices of the Royal Astronomical Society*, 450, 2423.
3. Constantino, T., Campbell, S.W., Gil-Pons, P., Lattanzio, J. (2014). “On the Necessity of Composition-dependent Low-temperature Opacity in Models of Metal-poor Asymptotic Giant Branch Stars”, *The Astrophysical Journal*, 784, 56.
4. Campbell, S.W., D’Orazi, V., Yong, D., Constantino, T., Lattanzio, J., Stancliffe, R., Angelou, G., Wylie-de Boer, E., Grundahl, F. (2013). “Sodium content as a predictor of the advanced evolution of globular cluster stars”, *Nature*, 498, 198.

In preparation

1. Constantino, T., Campbell, S.W., Lattanzio, J., van Duijneveldt, A. (2015). “The treatment of mixing in core helium burning models – II. Cluster star counts”, *Monthly Notices of the Royal Astronomical Society*, submitted July 2015.

Non-refereed

1. Constantino, T., Campbell, S.W., Lattanzio, J. (2014). “What asteroseismology can teach us about low-mass core helium burning models” in *IAU Symposium, Vol. 301, IAU Symposium*, Guzik J. A., Chaplin W. J., Handler G., Pigulski A., eds., p. 399.
2. Campbell, S.W.; D’Orazi, V.; Constantino, T., Yong, D., Lattanzio, J., Angelou, G., Wylie-de Boer, E., Stancliffe, R., Martell, S., Grundahl, F. (2013). “The asymptotic giant branches of GCs: selective entry only”, *Memorie della Societa Astronomica Italiana*, 84, 101.

Acknowledgements

I consider myself immensely fortunate to have been supervised by Simon Campbell and John Lattanzio. Together, they have provided much needed insight, guidance, suggestions, feedback, and encouragement. Additionally, it would be remiss of me to omit my appreciation of John's generous hospitality throughout my honours and PhD studies. In the following acknowledgements I shall be sparing with names – I could not possibly thank every individual who has helped me along the way. First, I recognise my scientific collaborators, especially those with whom I am now a co-author. A special thanks goes to Jørgen Christensen-Dalsgaard who generously provided his vital expertise, and equally importantly enthusiasm, for the asteroseismology work in this thesis. I must also thank the academics, researchers, students, and visitors to the Monash Centre for Astrophysics who have made it an intellectually stimulating environment. Another special acknowledgement goes to Carolyn Doherty, with whom I shared an office for the majority of my PhD studies, and who, despite my regular interruptions, was always willing to offer valuable assistance. In addition, I am grateful to the administrative staff, particularly those in the School of Mathematical Sciences, where I spent the first three years of my studies. Finally, I thank my family for always supporting me along this journey.

Introduction

1.1 The importance of stars

The evolution of stars plays a pivotal role in shaping everything around us. All of the heavy elements (i.e. those other than hydrogen and helium), from which the Earth and its life are made, were created within stars. The energy that sustains almost all life on Earth comes from nuclear fusion in the Sun, which is, apart from our proximity to it, an otherwise unremarkable star in the Galaxy.

In order to comprehend and describe the lives and deaths of stars we require stellar models. The construction of these models demands knowledge about the nature of matter and its interactions over an extreme range of environments and scales. In density, for example, this range includes the interior of neutron stars, where matter is nearly a million billion times more dense than liquid water, and molecules at the surface of red giants where the density is only one millionth that of air. The range in temperature is no less astonishing: In five billion years, after it has engulfed the orbit of Mercury (and possibly that of Venus and Earth; Sackmann et al. 1993), the Sun's surface will have cooled to a tepid 3000 K (comparable to the tungsten filament in an incandescent light bulb) while simultaneously, deep in the interior, runaway helium burning will be occurring at 200 million K.

If tracing the origin of the elements and predicting the fate of the solar system are not motivating enough, then we can add that understanding the interior structure and evolution of stars is essential for other branches of astrophysics too. These include fields as diverse as planet detection, galaxy evolution, and cosmology, because in one way or another they rely on the observation of star light. Stars are also laboratories for advancing knowledge about fundamental physics. This is because stars contain within them environments too extreme to be replicated on Earth. The vast lifespan of stars also permits the detection of processes that occur too slowly to be practically reproduced and observed

on Earth.

1.2 The lives of low-mass stars

Stars are formed by the gravitational collapse of giant molecular clouds that are composed primarily of hydrogen and helium, along with traces of heavier elements, or ‘metals’. The subsequent evolution is fundamentally a competition between gravity, which continuously works to pull the matter towards the centre, and pressure that resists it. In the stars we discuss here, this pressure results from a combination of quantum degeneracy and the energy released by either nuclear fusion reactions or by the contraction itself.

Observed stars are often defined by their position in the colour-magnitude diagram (CMD), which describes their magnitude (brightness) and their colour. The CMD is closely related to the theoretical Hertzsprung-Russell diagram (HRD) where stellar luminosity is plotted against effective temperature. In Figure 1.1 we show the evolution in the HRD of $1 M_{\odot}$ and $3 M_{\odot}$ stellar models computed with MONSTAR.

The main sequence lifetime of a star begins when the core becomes hot enough for hydrogen fusion to release enough energy to resist further gravitational contraction. The main sequence is so named because core hydrogen burning is the longest phase of nuclear burning in the life of a star and these stars form a highly populated sequence in the CMD and HRD (where their position on it depends chiefly on their mass). Compared with later phases, the evolution of the surface temperature and luminosity is very gradual during the main sequence.

When hydrogen is finally exhausted in the core, the nuclear burning moves to a shell above the helium ashes. Hydrogen burning continues to grow the mass of the helium core, leading it to contract enough to be increasingly supported by electron degeneracy pressure. At the same time, the core temperature and hydrogen burning energy production rate continue to rise. These factors lead to the expansion and cooling of the surface layers. This increase in luminosity and surface cooling is the beginning of the ascent of the red giant branch (RGB) in the HRD. At the same time, the outer convective ‘envelope’ penetrates deeper into the star (by mass). This is shown at around 12 Gyr in the example $1 M_{\odot}$ model in Figure 1.2.

The growth in the mass of the helium core from shell hydrogen burning is sustained until the core is hot enough for helium to ignite (around 100 million K). If the stellar mass is less than about $2 M_{\odot}$, this occurs under degenerate conditions and proceeds explosively in the process known as the ‘core flash’. After the energy from burning lifts the degeneracy, quiescent ‘core helium burning’ begins. During the core helium burning (CHeB) phase,

helium burns to carbon and oxygen in a convective core while hydrogen burning proceeds in a radiative shell above it (see the structure after 12.8 Gyr in the model in Figure 1.2). In stars of low enough mass ($M \lesssim 3 M_{\odot}$), the ignition of helium in the core reduces the temperature and pressure at the hydrogen burning shell, and consequently the energy generation rate and total luminosity. These stars then settle on the horizontal branch in the HRD.

Analogous to the end of core hydrogen burning, core helium burning ceases when the core becomes exhausted of helium. The burning front then moves to a shell. The star thus begins its second ascent of the giant branch in the HRD, i.e. the asymptotic giant branch (AGB). This is the final stage of nuclear burning in low-mass stars ($M \lesssim 8 M_{\odot}$). The concentric shells of hydrogen burning and helium burning constitute an unstable configuration that eventually gives rise to ‘thermal pulses’, the periodic oscillation between helium-shell dormancy and brief, but intense, runaway helium burning. The mixing process known as the ‘third dredge-up’ can occur during these cycles. In that process, the changing depth of surface convection (in mass) during the thermal-pulse cycle allows elements newly synthesized from helium burning and the *s*-process to be mixed into the convective envelope.

In the AGB phase the outer layers of the star are shed in a stellar wind. This wind enriches the interstellar medium in the material mixed to the surface by the third dredge-up. It can also contain the products of hydrogen burning if the envelope was hot enough for ‘hot bottom burning’ to occur there. When none of the envelope remains, and there is no more fuel available, the hot remnant core begins slowly cooling as a carbon-oxygen white dwarf, often via a planetary nebular phase.

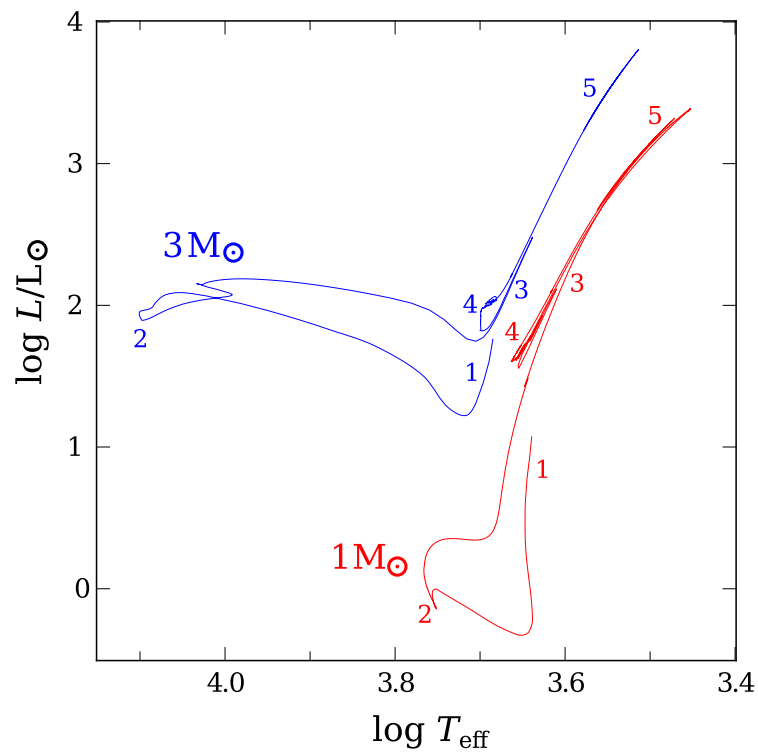


Figure 1.1: Hertzsprung-Russell diagram showing the evolution, from the pre-main sequence to the thermally pulsing-AGB phase, for $1 M_{\odot}$ and $3 M_{\odot}$ solar-metallicity models computed with MONSTAR. The stages of evolution indicated are the pre-main sequence (1), main sequence (2), red giant branch (3), horizontal branch (4), and asymptotic giant branch (5).

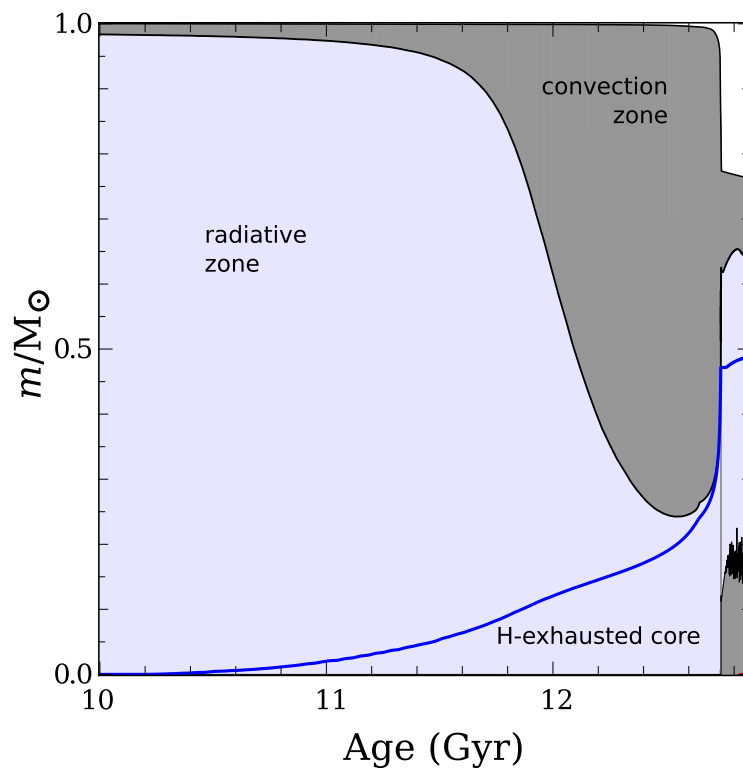


Figure 1.2: Kippenhahn diagram of the internal evolution, from the late-main sequence to the thermally pulsing-AGB phase, of a solar-calibrated model computed with MONSTAR. The blue and red lines show the respective mass coordinates of hydrogen- and helium-exhaustion, respectively. Convective regions are shaded in grey and radiative regions are shaded in light blue.

1.3 Stellar structure code

Throughout this thesis, the stellar structure models are calculated with the one-dimensional Monash University stellar evolution code MONSTAR, which is derived from the Mount Stromlo Stellar Structure Program (Faulkner, 1968; Robertson, 1971; Faulkner and Wood, 1972; Gingold, 1974; Wood and Zarro, 1981). The code has since undergone significant development relevant to this work. Because of these improvements, it can now model processes such as semiconvection and convective overshooting (Lattanzio, 1986), the third dredge-up (Lattanzio, 1989; Frost and Lattanzio, 1996), hot bottom burning (Lattanzio, 1992; Frost et al., 1998), and time-dependent mixing of chemical species (Campbell and Lattanzio, 2008). There are also new updates and additions made specifically for this work:

- new equations of state;
- updated low-temperature radiative opacity (Chapter 4; Constantino et al., 2014a);
- updated electron conduction opacity;
- a method for automatically generating initial models for evolution calculations (main sequence or pre-main sequence);
- stellar structure outputs compatible with pulsation codes; and
- two new schemes for chemical mixing during the CHeB phase (Chapter 2; Constantino et al., 2015).

We briefly summarise the equation of state and low-T opacity updates in Section 1.3.1 and Section 1.3.2, respectively. These modifications are also described in detail where necessary in subsequent chapters.

The one-dimensional stellar structure is determined by solving, with appropriate boundary conditions, the system of differential equations that describe mass conservation, hydrostatic equilibrium, energy conservation, and energy transport (Equations 1.1-1.4). Additionally, composition, density, temperature, pressure, and internal energy must be related by equations of state, and the opacity and nuclear reaction rates must be determined.

In this section we include a very brief description of the method used in MONSTAR. Here we show the differential equations for the gradients of variables radius r , pressure p , luminosity l , and temperature T with enclosed mass m . These can be derived from considering how each variable must change over an infinitesimally thin spherical shell. Mass conservation dictates that

$$\frac{dr}{dm} = \frac{1}{4\pi r^2 \rho}, \quad (1.1)$$

where ρ is the density. In hydrostatic equilibrium the pressure force on a shell must be balanced by gravity and therefore

$$\frac{dp}{dm} = -\frac{Gm}{4\pi r^2}, \quad (1.2)$$

where G is the gravitational constant. From energy conservation we have

$$\frac{dl}{dm} = \epsilon, \quad (1.3)$$

where ϵ accounts for nuclear energy generation, losses from neutrinos, PdV work, and changes in internal energy. The temperature gradient is that required to transport the energy, which we express as

$$\frac{dT}{dm} = -\frac{GmT}{4\pi r^4 p} \nabla, \quad (1.4)$$

where

$$\nabla = \frac{d \ln T}{d \ln p}. \quad (1.5)$$

In the case where photons carry the energy flux, radiation is modelled as a diffusive process:

$$\nabla = \nabla_{\text{rad}} = \frac{3\kappa lp}{16\pi acGmT^4}, \quad (1.6)$$

where κ is the Rosseland mean opacity, a is radiation density constant, and c is the speed of light. The mixing length theory is used to determine ∇ where there is convection. Where this is efficient, such as in the deep interior, the temperature gradient is essentially the adiabatic one, i.e. $\nabla = \nabla_{\text{ad}}$.

The differential equations (1.1–1.4) are solved by adopting certain boundary conditions. In the centre, m , r , l , and $\frac{dp}{dr}$ must vanish. The temperature close to the centre is then determined by assuming that the density, pressure, and energy generation rate are constant (with respect to r). The pressure at the surface can be determined from the Eddington approximation result that the optical depth of the photosphere is $\tau = 2/3$, that the pressure there comes mostly from the weight of atmosphere immediately above, and by assuming that near there the opacity and gravity are approximately constant locally. From the assumption that stars radiate as a black body, luminosity and the temperature at the photosphere T_{eff} are related by

$$L = 4\pi R^2 \sigma T_{\text{eff}}^4, \quad (1.7)$$

where σ is the Stefan-Boltzmann constant. The system of four first-order differential equations (1.1–1.4) for variables r , p , l , and T can be rewritten as difference equations for very thin, concentric spherical shells. The structure is then solved iteratively using the Newton-Raphson or ‘Henyei’ method (Henyei et al., 1964), until the difference equations for each zone are satisfied to within a specified tolerance. The time step by which the model evolves is reduced if these conditions cannot be met or if the change over the time step in any of r , p , l , T , or composition, is more than permitted.

1.3.1 Updates to the equations of state

Before calculating the models for this thesis we implemented new equations of state in MONSTAR. All of the models were then calculated using the OPAL EOS (Rogers et al., 1996; Rogers and Nayfonov, 2002) at low temperature ($T \lesssim 2$ MK) and the Helmholtz EOS (Timmes and Swesty, 2000) at high temperature.

The OPAL EOS is incorporated into MONSTAR via precomputed thermodynamic quantities tabulated according to density, temperature, and composition. The thermodynamic variables at the particular temperatures and densities in the stellar structure are determined from a new bicubic interpolation routine that ensures smooth derivatives. The OPAL EOS tables extend only up to 200 MK and do not include the contribution from pair production which becomes important at higher temperatures. In that regime we therefore use either the Helmholtz EOS or Nadyozhin EOS (Timmes and Swesty, 2000). We have also implemented the Timmes EOS, which was used to calculate the data for the Helmholtz EOS tables. The Timmes EOS routines can also calculate and account for the equilibrium ionization of the elements but they are too slow for general use in evolution calculations.

The new equations of state have a number of advantages for MONSTAR. The OPAL EOS accounts for the ionization state of elements heavier than helium which may be important when the envelope becomes enriched in metals from the third dredge-up. The OPAL EOS can be used to accurately calculate the evolution of stars less massive than was previously possible with MONSTAR, down to $M \approx 0.3 M_{\odot}$, where pressure ionization becomes significant. The stellar models generated from MONSTAR using either the Helmholtz EOS or Nadyozhin EOS are compatible with hydrodynamics codes that have those equations of state, such as FLASH (Fryxell et al., 2000). This is important because many of the unresolved problems in stellar evolution involve multi-dimensional processes. We introduce some of these in Section 1.5 and also discuss them throughout this thesis. Finally, the implementation of the new equations of state enables comparisons with other evolution codes without the equation of state being a variable.

1.3.2 Improved low-temperature opacity

In stellar evolution calculations, the Rosseland mean opacity, which governs the transport of energy via radiation (in e.g. Equation 1.6), is typically interpolated from precomputed tables to avoid repeating costly calculations. We have implemented new low-temperature ($T \leq 10,000$ K) opacity data from AESOPUS (Marigo and Aringer, 2009) that crucially accounts for the sensitivity of the molecular composition, and therefore the opacity, to the precise abundance of each element. Figure 1.3 shows the opacity, computed with AESOPUS, for several mixtures with varying levels of carbon enhancement. The extreme sensitivity of the opacity to the carbon to oxygen ratio has been largely ignored in stellar models until recently (e.g., Marigo 2002; Ventura and Marigo 2009; see also Chapter 4).

We chose a temperature resolution for the opacity tables of $\Delta \log T = 0.02$ for $\log T < 3.50$, where the opacity is strongly dependent on the temperature (Figure 1.3), and $\Delta \log T = 0.05$ elsewhere. The range in temperature, density, and composition required were determined from tests with evolution models. The different chemical mixtures in the grid of opacity tables were selected by testing the sensitivity of the opacity to composition changes under a range of conditions. This ultimately amounted to the construction of a grid that includes more than 10^5 unique chemical mixtures. The implementation of the updated opacity in MONSTAR is described in more detail in Section 4.

1.4 Stellar pulsations

In the previous section we presented equations that describe the structure of stars in hydrostatic equilibrium. This is not always strictly the case in reality though. The structure may be subjected to ongoing disturbances, such as those from the turbulent flow of convective elements. Although the resulting perturbations are often small, they can give rise to oscillations about the hydrostatic equilibrium structure. In the red giant stars studied in Chapter 2, the oscillations are continuously damped (i.e. the waves lose energy) but are also simultaneously excited stochastically by turbulent convection.

The waves generated by the perturbations to the equilibrium structure are defined by their restoring force. The two types of waves of interest to us, because they propagate in red giants, are well known in more familiar contexts. The first type are pressure waves, where pressure provides the restoring force. These are ordinary sound waves. The second type are gravity waves, where buoyancy provides the restoring force. This is exactly the same mechanism by which ocean waves propagate. When many of these waves are excited, they can combine to form standing waves, or normal modes, that have the resonant frequencies of the star. The frequency of each mode depends on its radial

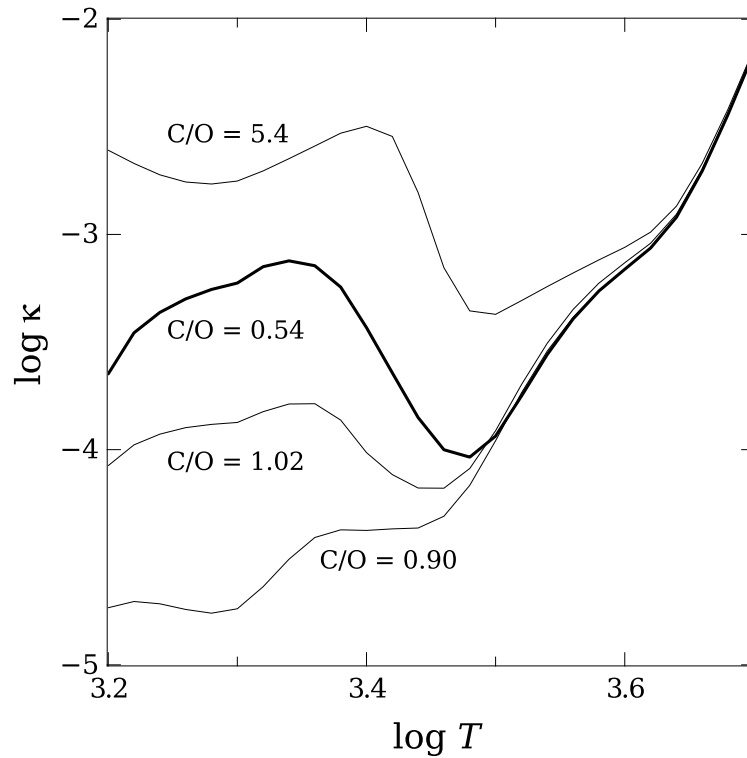


Figure 1.3: Rosseland mean opacity κ calculated with AESOPUS (Marigo and Aringer, 2009) for four different chemical mixtures. The mixtures differ only in the abundance of carbon (which is increased at the expense of helium). The composition is otherwise the scaled solar abundance according to Grevesse et al. (2007) with total metallicity $Z = 0.001$. The opacity for the mixture with the solar C/O ratio (C/O = 0.54 by number) is shown by the thick line. The density is set so that $\log \rho/T^3 = -19$, which is typical for the surface layers of cool red giants.

order n (the number of nodes in the radial direction), the spherical harmonic angular degree ℓ , and azimuthal order m . The modes formed from pressure waves are referred to as pressure- or p-modes, and those from gravity waves are gravity- or g-modes.

The global oscillations evident from observations of the surface of the Sun are p-modes. These p-modes have a higher frequency than the g-modes thought to propagate in the radiative interior. The two types of modes therefore do not interact in the Sun. Compared with the Sun however, red giants have a sparser envelope and more compact core. This reduces the frequency of the p-modes and increases the frequency of g-modes that propagate in those respective regions. The two types of modes can therefore couple as mixed modes, meaning surface oscillations convey information about the deep interior. The observation of mixed modes in CHeB stars by the *Kepler* (e.g. Bedding et al., 2011) and CoRoT (e.g. Mosser et al., 2011) telescopes adds an invaluable new constraint for models of their interior structure. Particularly interesting to us are inferences of the period spacing between ‘pure’ g-modes of successive radial order in CHeB stars (Mosser et al., 2012, 2014), because that period spacing depends only on the buoyancy frequency of the plasma in the core and can be calculated from stellar structure models.

1.4.1 Pulsation calculations

Theoretical pulsation frequencies can be computed from stellar structure models, specifically from ρ , p , the thermodynamic quantity Γ_1 , and the gravitational acceleration g , as functions of radius r . We use the Aarhus adiabatic oscillations package ADIPLS (Christensen-Dalsgaard, 2008) to calculate the radial and non-radial adiabatic pulsation frequencies for the stellar models from MONSTAR. In the adiabatic approximation, the heating term in the energy equation is neglected. This is generally justified because the characteristic time scale for radiation is usually much longer than the oscillation period. These calculations do not account for the stability of modes, which depends on their excitation and damping rates.

The oscillation frequencies are calculated by first replacing the variables in the hydrodynamic equations for mass, momentum, and energy conservation by an unperturbed plus perturbed variable. The equations can then be simplified because the unperturbed quantities satisfy the equations of stellar structure and do not have any time dependence. The equations are then only functions of the perturbed quantities. To solve the system of equations, the radial, angular, and time components of the solution are separated. The angular components of the solutions are just multiples of the spherical harmonics and the time dependence is sinusoidal. This can then be used to produce a fourth-order system of ordinary differential equations with four variables that are functions of r : the radial

displacement ξ_r , the Eulerian perturbations to the pressure p' and gravitational potential Φ' , and $\frac{d\Phi'}{dr}$. The system is an eigenvalue problem because only certain eigenfrequencies have solutions that satisfy the boundary conditions. These eigenfrequencies are the oscillation frequencies of each mode. In our study, we focus on dipole $\ell = 1$ mixed-modes which propagate as g-modes in the core and as acoustic waves (p-modes) in the envelope.

1.5 Some shortcomings in stellar models

Low-mass stars dominate the stellar initial mass function (Scalo, 1986). Among low-mass stars that are massive enough to evolve in a time comparable to the age of the universe, the CHeB and AGB phases are the final stages of nuclear burning. In the evolution of models of these stars, the internal structure is subject to increasing uncertainty after the ignition of helium in the core. Theoretical predictions for the following CHeB (e.g. Langer et al., 1985; Paxton et al., 2013) and shell helium burning AGB (e.g. Stancliffe et al., 2005; Doherty et al., 2014) phases of evolution are thus notoriously model dependent. In this thesis we critically examine the physics upon which models of these stars are built, and how well they can match the latest observations, including photometry, spectroscopy, and asteroseismology.

There are several reasons why the uncertain models of the CHeB and AGB phases need to be improved. Models of these stars are vital to understanding the evolution of single and binary star systems. Stars in these phases are important contributors to the integrated light through which the evolution of distant star clusters and galaxies are studied, particularly in the near-infrared (Melbourne et al., 2012). Extreme blue horizontal branch stars (which are also CHeB) are also thought to be responsible for UV upturn in elliptical galaxies (Ferguson et al., 1991; Dorman et al., 1995; Brown et al., 1995, 1997, 2000). Observations of CHeB stars have been used as constraints for elementary particle physics (e.g. Raffelt and Dearborn, 1987). Core helium burning RR-Lyrae variables and even red clump stars (Paczynski and Stanek, 1998) can be used as standard candles. Thermally pulsing-AGB stars are one of the sites of slow neutron capture (*s*-process) nucleosynthesis (see e.g. Smith and Lambert, 1990) and their stellar winds contribute to Galactic chemical evolution. Finally, AGB stars are candidates for the polluters in the still unexplained globular cluster self-enrichment scenario (e.g. Ventura et al., 2002; Gratton et al., 2012a).

Stellar models require several simplifying assumptions so that they can follow evolutionary time scales. An obvious assumption is that of spherical symmetry, i.e. the models are one-dimensional. Phenomena that are inherently three-dimensional can therefore at

best be approximated. Ordinary turbulent convection in stellar interiors is usually modelled with the mixing length theory. Various prescriptions exist for quantifying the mixing across convective boundaries (which we shall refer to as ‘overshoot’), or the mixing that occurs when the fluid is stably stratified according to the Ledoux criterion but unstable according to the Schwarzschild criterion (semiconvection), or vice versa (‘thermohaline’ or ‘fingering’ convection). Rotation distorts the stellar structure away from spherical symmetry (e.g. Kippenhahn et al., 1970; Endal and Sofia, 1976) and can also induce mixing from meridional circulation and shear from differential rotation (e.g. Zahn, 1992). Magnetic fields in stellar evolution are often neglected, but their effects on angular momentum transport and mixing can be similarly approximated with one-dimensional prescriptions (e.g. Spruit, 2002). The manifold difficulties in modelling the complexity of real stars with one-dimensional calculations underlines the importance of confronting our simplified theoretical models with observational evidence.

A fundamental problem in stellar evolution calculations is the modelling of three-dimensional flows near convective boundaries. The convective boundary is usually defined as the point in the one-dimensional structure where turbulent convective elements begin to decelerate because of buoyancy forces. How far into the adjacent stable region these elements penetrate, and the extent of chemical mixing, requires a parametrization in one-dimensional calculations. The sensitivity of models to this treatment depends on the phase of evolution in question. During CHeB, calculations with different treatments of convective boundaries diverge because of a compounding effect from mixing beyond the boundary on the internal structure. This is problematic for constructing accurate stellar models, but it also presents the opportunity to better understand the mechanism at play if the structure can be determined empirically. To this end, we compare state of the art CHeB models with recent novel observations in Chapters 2 and 3.

The accuracy of models can also be compromised by neglecting physics that is known, but thought to be either unimportant to the evolution, too computationally expensive, too difficult to implement, or some combination of each of these factors. An example of this is the effect on the molecular opacity from changes to the abundance of light elements such as carbon, nitrogen, and oxygen. The assumption that any such effect can be neglected is generally, but not always, valid: stellar interiors are usually either too hot, or the composition changes too small, for it to be important. In Chapter 4 we systematically investigate the validity and importance of this assumption for low-metallicity AGB models, where the third dredge-up can mix newly synthesized chemical elements all the way to the cool surface.

1.6 Thesis outline

Apart from the introduction and conclusion chapters, this thesis comprises two published works and another submitted for publication, each of which is reproduced as a chapter. Here we give an overview of each these three Chapters. A detailed summary of the relevant background is contained within each Chapter.

Chapter 2: The treatment of mixing in core helium burning models – I. Implications for asteroseismology

The internal structure of core helium burning stars is uncertain because theoretical predictions are sensitive to the treatment of mixing near convective boundaries. The revolutionary CoRoT and *Kepler* missions have provided unprecedented data – in both quality and quantity – for asteroseismic analysis of CHeB stars. The resulting detection of mixed modes in red clump stars and g-modes in subdwarf B stars, which convey information about the stellar structure deep in the core, provides an opportunity to constrain the uncertain stellar models of this phase of evolution. In this Chapter we are particularly interested in why the predictions from standard models for the asymptotic limit of the g-mode period spacing between $\ell = 1$ modes of consecutive radial order, $\Delta\Pi_1$, are lower than is inferred from observations. We address this by comparing the observations with calculations of non-radial adiabatic pulsation frequencies for a grid of stellar models with four different mixing schemes, and consequently different internal structures. We also investigate the effects from other uncertainties in the models and from the steep composition gradients remaining from the earlier RGB and core helium flash phases.

Chapter 3: The treatment of mixing in core helium burning models – II. Cluster star counts

In this Chapter we extend the study in Chapter 2 by using star counts in globular clusters for an additional constraint on the mixing in CHeB models. This is possible because the number of horizontal branch and AGB stars in globular clusters is thought to correspond to the relative lifetime of the two phases of evolution, which in models is strongly dependent on the mixing scheme. We use Hubble Space Telescope photometry of 48 globular clusters with well-populated and separated AGBs from two recent surveys. This provides a large sample and significantly reduces the statistical uncertainty compared with previous studies. We also derive luminosity probability density functions from the observations and compare the luminosity difference between the horizontal branch and the AGB clump with

predictions from models computed with the four different mixing schemes introduced in Chapter 2. Finally, we quantify the effect that other physical uncertainties in the models could have on our findings.

Chapter 4: On the necessity of composition-dependent low-temperature opacity in metal-poor AGB models

In this study we investigate the importance of newly available composition-dependent low-temperature opacity data for the evolution of low-metallicity AGB models. This follows the work of Marigo (2002) that demonstrated that if the third dredge-up mixes enough carbon to the surface for carbon to become more abundant than oxygen, there is a sudden transition from oxygen-rich to carbon-rich chemistry, radically increasing the opacity. That study, and some subsequent studies, highlighted the need to account for composition-dependent low-T opacity in metal-rich AGB models. The consequences of the higher opacity include the expansion and cooling of the convective envelope, increased mass loss rate, and shorter AGB lifetime. It has been speculated that these effects may not be as important when the metallicity is lower. Firstly, there is a reduced absolute abundance of molecule forming species. Secondly, lower-metallicity stars have hotter surface layers, hindering molecule formation. We generate low-T opacity tables from the AESOPUS tool (Marigo and Aringer, 2009) and implement them in MONSTAR to test their effect. It is vital that the stellar evolution community know whether it is necessary to include this new data in stellar models. Because it affects stellar radius, the low-T opacity treatment also has implications for the evolution of binary star systems. We therefore also discuss how the new models affect predictions for the formation of carbon-enhanced metal-poor (CEMP) and nitrogen-enhanced metal-poor (NEMP) stars.

Monash University

Declaration for Thesis Chapter 2

Declaration by candidate

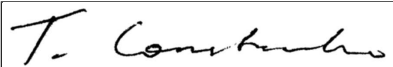
In the case of Chapter 2, the nature and extent of my contribution to the work was the following:

Nature of contribution	Extent of contribution (%)
First author; code development, calculations, analysis of results, figure preparation, writing, manuscript preparation.	80

The following co-authors contributed to the work. If co-authors are students at Monash University, the extent of their contribution in percentage terms must be stated:

Name	Nature of contribution	Extent of contribution (%) for student co-authors only
Simon Campbell	Project development, analysis of results, manuscript editing.	
Jørgen Christensen-Dalsgaard	Integration of pulsation code, pulsation calculation analysis.	
John Lattanzio	Project development, analysis of results.	
Dennis Stello	Integration of pulsation code, pulsation calculation analysis.	

The undersigned hereby certify that the above declaration correctly reflects the nature and extent of the candidate's and co-authors' contributions to this work*.

Candidate's Signature		Date 2-9-15
------------------------------	---	-----------------------

Main Supervisor's Signature		Date 2-9-15
------------------------------------	---	-----------------------

*Note: Where the responsible author is not the candidate's main supervisor, the main supervisor should consult with the responsible author to agree on the respective contributions of the authors.

The treatment of mixing in core helium burning models – I. Implications for asteroseismology

Thomas Constantino¹, Simon W. Campbell^{1,2}, Jørgen Christensen-Dalsgaard³, John C. Lattanzio¹ and Dennis Stello^{4,3}

¹Monash Centre for Astrophysics (MoCA), School of Physics and Astronomy, Monash University, Victoria, 3800, Australia

²Max-Planck-Institut für Astrophysik, Karl-Schwarzschild-Straße 1, 85748 Garching bei München, Germany

³Stellar Astrophysics Centre, Department of Physics and Astronomy, Aarhus University, Ny Munkegade 120, DK-8000 Aarhus C, Denmark

⁴Institute for Astronomy (SifA), School of Physics, University of Sydney, NSW 2006, Australia

Published in *MNRAS* 452, 123, September 2015.

2.1 Abstract

The detection of mixed oscillation modes offers a unique insight into the internal structure of core helium burning (CHeB) stars. The stellar structure during CHeB is very uncertain because the growth of the convective core, and/or the development of a semiconvection zone, is critically dependent on the treatment of convective boundaries. In this study we calculate a suite of stellar structure models and their non-radial pulsations to investigate why the predicted asymptotic g-mode $\ell = 1$ period spacing $\Delta\Pi_1$ is systematically lower than is inferred from *Kepler* field stars. We find that only models with large convective cores, such as those calculated with our newly proposed ‘maximal-overshoot’ scheme, can match the average $\Delta\Pi_1$ reported. However, we also find another possible solution that is related to the method used to determine $\Delta\Pi_1$: mode trapping can raise the observationally inferred $\Delta\Pi_1$ well above its true value. Even after accounting for these two proposed resolutions to the discrepancy in average $\Delta\Pi_1$, models still predict more CHeB stars with low $\Delta\Pi_1$ ($\lesssim 270$ s) than are observed. We establish two possible remedies for this: (i) there may be a difficulty in determining $\Delta\Pi_1$ for early CHeB stars (when $\Delta\Pi_1$ is lowest) because of the effect that the sharp composition profile at the hydrogen burning shell has on the pulsations, or (ii) the mass of the helium core at the flash is higher than predicted. Our conclusions highlight the need for the reporting of selection effects in asteroseismic population studies in order to safely use this information to constrain stellar evolution theory.

2.2 Introduction

In low-mass stellar evolution the core helium burning (CHeB) phase is the third stage of nuclear burning – after core and shell hydrogen burning. In evolution calculations the core structure during this phase is highly uncertain, but it has been postulated for more than four decades that CHeB stars develop a zone of slow mixing, or ‘semiconvection’, beyond the fully convective core (e.g. Schwarzschild and Härm, 1969). How this develops in models, if at all, depends on the treatment of convective boundaries – a major source of uncertainty generally in stellar models (see Section 3.4.2). Later evolution depends on the structure at the end of this phase, and this is typically where the results of different stellar evolution codes begin to diverge (see e.g. Castellani et al. 1971a; Figure 15 in Paxton et al. 2013).

2.2.1 Brief overview

In this paper we make use of potent new constraints on the structure of CHeB models – mixed modes of oscillation detected from asteroseismology. We present calculations of non-radial pulsations for CHeB models evolved with a variety of mixing prescriptions: models with and without convective overshoot as well as those with a semiconvection region. We also introduce a new algorithm for core mixing during the CHeB phase that can better match the asymptotic g-mode period spacing inferred from asteroseismology with the use of otherwise standard physics. Finally, we compute pulsation spectra at different stages of the CHeB phase. In order to make this paper more accessible to non-experts, we provide an extensive summary in Section 2.5, which includes clear references to previous sections that contain more technical detail.

2.2.2 The problem of convective boundaries

CHeB stars, in their various (observational) flavours, may be known as subdwarf B (sdB), horizontal branch (HB), RR-Lyrae, red clump (RC), or secondary clump (Girardi, 1999) stars. Most of the variation between these types of CHeB stars is due to differences in the mass of the convective envelope and the hydrogen-exhausted core beneath it (where all of the hydrogen has been burned to helium). The common thread between them is that they are all thought to contain a central helium-burning convection zone that is surrounded by a helium-rich region that is not convective.

In their convective cores, CHeB stars produce carbon via the triple- α reaction, and oxygen via $^{12}\text{C}(\alpha, \gamma)^{16}\text{O}$. This burning produces a growing abundance discontinuity at the formal boundary of the convection zone if there is no convective overshoot to induce

mixing beyond it. This boundary is usually defined as the point of convective neutrality (i.e. where a displaced fluid element experiences no acceleration). If the Schwarzschild (1906) criterion is applied then this is where the radiative temperature gradient ∇_{rad} is equal to the adiabatic temperature gradient ∇_{ad} . Therefore the criterion for convective stability is

$$\nabla_{\text{rad}} < \nabla_{\text{ad}}, \quad (2.1)$$

where

$$\nabla_{\text{ad}} = \left(\frac{\partial \ln T}{\partial \ln p} \right)_{\text{ad}}, \quad \nabla_{\text{rad}} = \left(\frac{d \ln T}{d \ln p} \right)_{\text{rad}}, \quad (2.2)$$

and ∇_{rad} is the temperature gradient required for radiation to carry the total energy flux. In low-mass CHeB models the location of this boundary is unstable. The increasingly C- and O-rich mixture in the convection zone is more opaque than the He-rich material just beyond the boundary. Because of this, any mixing from convective overshoot (which has a sound physical basis because the boundary is defined only as the point of zero acceleration but where convective elements still carry momentum; see Castellani et al. 1971b for a quantitative analysis) will increase the opacity and therefore ∇_{rad} , and cause the convection zone to grow. Schwarzschild and Härm (1969) first found that in CHeB models a partially mixed or ‘semiconvection’ region can then develop (see also Schwarzschild, 1970; Paczyński, 1970b). While only marginally stable according to the Schwarzschild criterion ($\nabla_{\text{rad}} \approx \nabla_{\text{ad}}$), the semiconvective region is stable when the effect of the molecular weight gradient is considered. This is accounted for in the Ledoux (1947) criterion for convective stability

$$\nabla_{\text{rad}} < \nabla_{\text{ad}} + \frac{\varphi}{\delta} \nabla_{\mu}, \quad (2.3)$$

where

$$\nabla_{\mu} = \frac{d \ln \mu}{d \ln p}, \quad \varphi = \left(\frac{\partial \ln \rho}{\partial \ln \mu} \right)_{T,p}, \quad \delta = - \left(\frac{\partial \ln \rho}{\partial \ln T} \right)_{p,\mu}. \quad (2.4)$$

Semiconvection regions are usually defined as stable (not convective) according to the Ledoux criterion but convective (or neutral) according to Schwarzschild.

In early studies, algorithms were developed that produce what we shall refer to as ‘classical semiconvection’, where the composition is adjusted to produce $\nabla_{\text{rad}}/\nabla_{\text{ad}} = 1$, which results in a smooth abundance profile (e.g., Simpson, 1971; Robertson and Faulkner, 1972; Faulkner and Cannon, 1973). Even if there is no explicit process for allowing semiconvection, a similar chemical profile and temperature gradient is produced from localized mixing episodes in evolution sequences that have instantaneous mixing in convection zones and an overshooting prescription that allows mixing beyond the Schwarzschild boundary (Lattanzio, 1986; Caloi and Mazzitelli, 1990). The most obvious difference is that the

local mixing events leave behind numerous small composition discontinuities. By the end of CHeB, both of these schemes permit the partially mixed region to grow to such an extent that its enclosed mass is around double that of the convective core (Figure 2.2b). Typically, models initially experience a period of rapid growth of the convective core. The expansion rate of the convective core then slows as a result of the emergence and subsequent growth of a partially mixed region. The semiconvection region in the $1.5 M_{\odot}$ model from Faulkner and Cannon (1973), for example, appears when the central helium mass fraction has reduced to 0.75 (from 0.978 initially), at which time the convective core growth rate is halved.

The total mass of helium that burns during the CHeB phase differs from code to code. The principal reason is mixing: specifically whether the criterion for convection is Schwarzschild or Ledoux, and whether convective overshoot or a scheme for semiconvection is applied. Recently, Gabriel et al. (2014) also highlighted the significance of whether the location of a convective boundary is determined from inside or outside the convection zone. The greater opacity of the products of helium burning means that in this phase, numerical subtleties such as these have a compounding effect on the evolution.

2.2.3 Classical constraints from globular clusters

Despite making a vast difference to the evolution of the interior, the core mixing has little immediate effect on the conditions at the surface. By controlling the amount of helium that is burnt, the mixing scheme does, however, affect the CHeB and early-asymptotic giant branch (AGB) lifetimes. Empirically, the lifetime of various phases of evolution can be inferred from star counts in globular clusters. This is because they have large and (relatively) homogeneous stellar populations. By using the so-called R-method on a sample of 15 globular clusters (i.e. determining R_1 , the ratio of AGB to red giant branch stars), Buzzoni et al. (1983) found indications for the existence of a fully developed semiconvective zone.

Late in the CHeB phase, models can also show the phenomenon of ‘core breathing pulses’, the rapid growth in the mass of the convective core when the central helium abundance is very low (Sweigart and Demarque, 1973; Castellani et al., 1985). Despite their emergence in stellar evolution calculations, Caputo et al. (1989) and Cassisi et al. (2001) contend that evidence from star counts in globular clusters discredits the existence of core breathing pulses, because they further prolong the HB lifetime and shorten the early-AGB. This conflict between theoretical predictions and observations exposes the uncertainty of stellar models during the CHeB phase.

2.2.4 Asteroseismology of CHeB stars

The study of asteroseismology promises a unique chance to constrain CHeB models. The long time series observations from the CoRoT and *Kepler* missions have yielded unprecedented potential for red-giant asteroseismology. Solar-like oscillations have now been detected in more than 13,000 giants in the *Kepler* field (Stello et al., 2013).

Bedding et al. (2010) first detected mixed modes in the surface oscillations of red giants in the *Kepler* field. These propagate as acoustic modes in the convective envelope and as gravity modes in the radiative core (Aizenman et al., 1977). Crucially, the observed period spacing ΔP of the dipole ($\ell = 1$) modes is thought to provide a lower bound on the asymptotic ‘pure g-mode’ spacing $\Delta\Pi_1$ (Beck et al., 2011). Bedding et al. (2011) showed that this period spacing can reliably distinguish CHeB stars from photometrically similar, but shell hydrogen burning, red giant branch (RGB) stars. This is possible because the mixed-mode period spacing is sensitive to the conditions in the core, which change substantially between the RGB and CHeB phases. More recently, Mosser et al. (2012) have developed a method to infer $\Delta\Pi_1$ from the relatively small fraction of mixed modes that are detectable. The CHeB stars for which they reported $\Delta\Pi_1$ mostly have asteroseismic scaling-relation-determined masses of $0.8 < M/M_\odot < 2.6$, while a handful have masses up to $M = 3.4 M_\odot$. The metallicity ($[M/H]$) distribution of the stars in the latest (and larger) CHeB sample with $\Delta\Pi_1$ determinations from Mosser et al. (2014) is strongly peaked around the solar value (determined from the stars also in the APOKASC catalogue; Pinsonneault et al. 2014).

Measurement of $\Delta\Pi_1$ is a particularly useful diagnostic because it depends only on the Brunt–Väisälä frequency N , which is easily computed from a given stellar structure. Specifically, N is the frequency of oscillation that an adiabatically displaced mass element will undergo due to buoyancy forces. In a convective region, displaced elements are buoyantly unstable, therefore such oscillations cannot occur, and gravity waves are damped. In the asymptotic limit, the gravity mode period spacing is

$$\Delta\Pi_\ell = \frac{2\pi^2}{\sqrt{\ell(\ell+1)}} \left[\int \frac{N}{r} dr \right]^{-1}, \quad (2.5)$$

where the integral is over the region with $N^2 > 0$, ℓ is the spherical harmonic degree,

$$N^2 = g \left(\frac{1}{\Gamma_1} \frac{d \ln p}{dr} - \frac{d \ln \rho}{dr} \right), \quad (2.6)$$

and g is the local gravitational acceleration (Dziembowski, 1977). If $N^2 > 0$ then N is

real, which is equivalent to the Ledoux criterion for convective stability

$$\frac{d \ln \rho}{d \ln p} > \frac{1}{\Gamma_1}, \quad (2.7)$$

where

$$\Gamma_1 = \left(\frac{\partial \ln p}{\partial \ln \rho} \right)_{ad}, \quad (2.8)$$

and the subscript *ad* signifies an adiabatic change. Another key observable from asteroseismology is the large frequency separation, whose asymptotic value $\Delta\nu$ can be computed as

$$\Delta\nu = \left[2 \int_0^R \frac{dr}{c} \right]^{-1}, \quad (2.9)$$

where c is the adiabatic sound speed (Vandakurov, 1967; Tassoul, 1980). Under a homologous transformation this scales with the square root of the mean stellar density, which is a finding that is supported by models (Ulrich, 1986).

If $\Delta\nu$ and ΔP (or $\Delta\Pi_1$) are both determined for a star, it can be placed on the $\Delta\nu - \Delta P$ (or $\Delta\nu - \Delta\Pi_1$) diagram. When this procedure is performed for the *Kepler* field stars, two distinct groups are found, comprising the CHeB and RGB stars respectively (e.g., Figure 3 in Mosser et al. 2012 and Figure 1 in Mosser et al. 2014). The most striking feature of the $\Delta\nu - \Delta\Pi_1$ diagram is how tightly most of the low-mass ($M/M_\odot \lesssim 1.75$) CHeB stars are grouped, with $250 \lesssim \Delta\Pi_1(\text{s}) \lesssim 340$ and $\Delta\nu \sim 4$ MHz. To date, however, CHeB models have been unable to properly match the $\Delta\Pi_1$ inferred from the observations (e.g. Figure 2.1).

Montalbán et al. (2013) identified a linear dependence of $\Delta\Pi_1$ on the radius of the convective core for CHeB models. They also noticed how the $\Delta\Pi_1$ dependence on stellar mass is similar to that for M_{He} , and emphasized a linear dependence of ΔP between ‘observable’ modes on M_{He} for models massive enough to avoid the degenerate ignition of helium ($M \gtrsim 2.2 M_\odot$). Additionally, they suggested that a model with a semiconvection zone will have a lower $\Delta\Pi_1$ than a model with an identically sized convective core but without semiconvection. Their comparison between $\Delta\Pi_1$ from models (of around solar composition and $0.7 - 3.0 M_\odot$ computed with the ATON evolution code; Ventura et al. 2008) and the observations reported by Mosser et al. (2012) reveals a general offset, with the theoretical $\Delta\Pi_1$ lower than observed (their Figure 7). This offset is also evident from models computed with MESA (Bildsten et al., 2012; Stello et al., 2013) and the Monash University code MONSTAR (Constantino et al., 2014b), making it apparent in at least three independent evolution codes. It is not as obvious that this offset exists for more massive, higher- $\Delta\nu$ models. However, the higher-mass models without overshoot by Montalbán

et al. (2013) do not match the whole observed spread of $\Delta\Pi_1$. Those models have roughly $160 \lesssim \Delta\Pi_1 \text{ (s)} \lesssim 230$ compared to $145 \lesssim \Delta\Pi_1 \text{ (s)} \lesssim 300$ observed. Interestingly, for the $1.5 M_\odot$ model at least, it appears that convective overshoot during CHeB considerably increases $\Delta\Pi_1$ (by around 50 s).

Recently it has been shown that additional diagnostic information about mixing events may be obtained from the effect that resulting sharp features in the buoyancy frequency have on the observed mode frequencies (Cunha et al., 2015). Such features can arise from composition discontinuities left by first dredge-up during the RGB evolution or, as we discuss in this paper, from those that may arise in the CHeB phase.

2.2.5 The core mass at the flash

Sweigart and Gross (1976) showed that the zero-age horizontal branch (ZAHB) convective core mass depends predominantly on the H-exhausted core mass M_{He} (and is insensitive to composition and total mass). Since there is a close relationship between radius of the convective core (and therefore its mass) and $\Delta\Pi_1$ (Montalbán et al., 2013), there must also be one between M_{He} and $\Delta\Pi_1$. The mass of the H-exhausted core is therefore a crucial quantity for the seismology of CHeB stars.

In low-mass CHeB models ($M \lesssim 2.2 M_\odot$), helium ignition occurs under degenerate conditions, triggering a thermal runaway known as the core flash. The minimum M_{He} required for this ignition is fairly constant over a wide range of stellar masses and only decreases slightly with increasing metallicity or helium. Salaris and Cassisi (2005) show, for instance, that there is a $0.03 M_\odot$ difference in M_{He} between $Z = 0.02$, $Y = 0.273$ and $Z = 10^{-4}$, $Y = 0.245$ solar-mass models. Catelan et al. (1996) explored the uncertainties in the physics in stellar models that could influence M_{He} , including neutrino losses, rotation, conductive opacity, coulomb effects on the equation of state, reaction rates and screening factors, and element diffusion. They constrained the possible core mass increase compared with standard models to $\Delta M_{\text{He}} = 0.01 \pm 0.015 M_\odot$. The best observational constraint on M_{He} comes from comparisons with globular clusters, but additional factors must be considered there as well, such as the composition, MLT mixing length, bolometric corrections, and distance determination (Viaux et al., 2013b).

2.2.6 Clues from subdwarf B stars

In contrast to the more massive red clump stars, the core mass of sdB stars is less uncertain because of the very thin hydrogen envelope. The mass distribution of sdB stars, determined from asteroseismology and eclipsing binaries, is peaked at $\sim 0.47 M_\odot$ (Van

Grootel et al., 2013b). This corresponds closely to the canonical core mass at the core flash. What we may be able to learn from this mass distribution though is dependent on understanding the conditions under which helium ignition occurs. When a sample of sdB stars is plotted in the $\log g - T_{\text{eff}}$ plane there is evidence for two distinct groups (Green et al., 2008), perhaps suggesting different formation channels (Van Grootel et al., 2013b). Proposed binary mechanisms include common-envelope ejection, stable Roche lobe overflow and double helium white dwarf mergers (Han et al., 2002). If an sdB star is formed via the stable Roche lobe overflow channel then it is likely that its mass is close to the minimum H-exhausted core mass required for helium ignition. Even if we cannot reliably deduce the H-exhausted core mass of other CHeB stars from the empirical mass of sdB stars, their observed pulsation properties can still serve as a useful constraint on the physics *during* the CHeB phase.

Space based observations of g-mode sdB pulsators have proven to be superior to earlier efforts from the ground (Charpinet et al., 2010). Structural properties, such as core and envelope mass and central helium abundance, of a handful of such stars have now been estimated (Van Grootel et al., 2010a,b,c; Charpinet et al., 2011). In their method they determine these quantities by finding a least-squares fit between the observed and the theoretical periods from models with different structural parameters (Brassard and Fontaine, 2008). It has been reported, for example, that the sdB star KPD 1943+4058 has a larger mixed core (defined as the mass interior to the unmixed He-rich radiative zone) than models by Dorman et al. (1993) which do not include convective overshooting. It is unclear, however, whether the determined structure includes a semiconvection region.

Reed et al. (2011) found a period spacing range of $231 \leq \Delta\Pi_1 \text{ (s)} \leq 271$ with an average of 254s for 13 g-mode pulsating sdB stars observed by *Kepler* and another by CoRoT. This period spacing is clearly lower than the more massive CHeB stars in the Mosser et al. (2012) sample, which have reported $\Delta\Pi_1$ typically around 300s.

2.2.7 The challenges and potential of CHeB asteroseismology

The pulsations in CHeB models can be far more complex than they are in RGB models. Importantly for the propagation of g-modes, there is only a single radiative zone in RGB stars, whose structure is well understood, and apart from the discontinuity left by first dredge-up, it contains only smooth variations in chemical composition. In contrast, the structure of CHeB models is sensitive to the treatment of convective boundaries in the core as well as to prior evolution, especially the core flash. They may contain multiple convection zones and composition discontinuities. The deficit in our understanding of the mixing during CHeB spans a broad mass range, from $M \gtrsim 0.47 M_{\odot}$ to at least $M \sim 20 M_{\odot}$.

(Langer, 1991). Part of the reason for this uncertainty is that until now the core mixing has been hidden from view.

The detailed study of pulsations in models of CHeB stars is imperative if we are to properly interpret asteroseismic observations and gain understanding about the behaviour of convection near the boundary of the convective core. In this paper we address this need by analysing the non-radial pulsations in a range of CHeB models with disparate internal structures stemming from different treatments of convective boundaries. Any insights about this mixing will also have implications for the treatment of convective boundaries in stellar models more generally.

2.3 Methods

2.3.1 Evolution code

In this study our evolution models are computed with MONSTAR, the Monash University stellar structure code, which has been described in detail previously (e.g., Lattanzio, 1986; Campbell and Lattanzio, 2008; Constantino et al., 2014a). Unless stated otherwise, our models are $1 M_{\odot}$, solar metallicity (Asplund et al., 2009), with initial helium mass fraction $Y = 0.278$.

2.3.2 Pulsation analysis

The models we use for pulsation calculations are usually mid-way through CHeB and have central helium abundance $Y = 0.4$ or $Y = 0.5$. The pulsations are computed with the Aarhus adiabatic oscillation package ADIPLS (Christensen-Dalsgaard, 2008). In this study we restrict our analysis of non-radial modes to the $\ell = 1$ case. Each structure model we present is converged and in hydrostatic equilibrium, and the Brunt–Väisälä frequency is calculated directly from P , ρ , r , and Γ_1 according to Equation 2.6.

The estimates of the frequency of maximum power ν_{\max} for the models in this paper use the assumption that it scales with the acoustic cut-off frequency (Brown et al., 1991), and therefore that

$$\nu_{\max} = \frac{g}{g_{\odot}} \sqrt{\frac{T_{\text{eff},\odot}}{T_{\text{eff}}}} \nu_{\max,\odot}, \quad (2.10)$$

where g is the surface gravity, $g_{\odot} = 2.74 \times 10^4 \text{ cm s}^{-2}$, $\nu_{\max,\odot} = 3.1 \text{ mHz}$, and $T_{\text{eff},\odot} = 5778 \text{ K}$.

We obtain frequencies of individual modes from the pulsation calculations and hence the actual period spacing ΔP between modes of adjacent order. We present these results

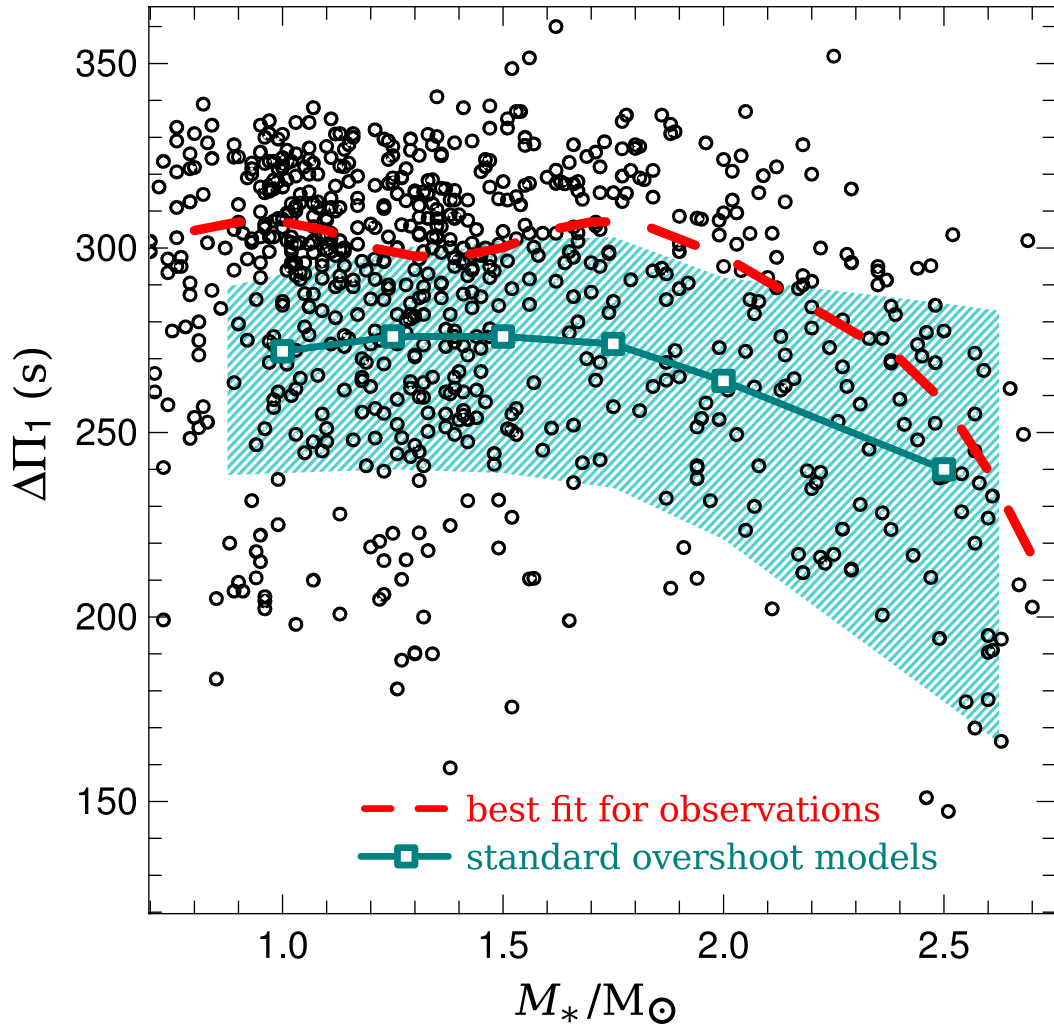


Figure 2.1: Comparison between $\Delta\Pi_1$ inferred from observations of likely CHEB stars with seismic mass determinations (black circles; Mosser et al., 2014) and the average computed from CHEB models with standard overshoot (cyan line; with markers showing each calculation). The line of best fit for observations (red dashes) follows the mode of the $\Delta\Pi_1$ distribution. The shaded area gives the range of $\Delta\Pi_1$ in which the models spend 95 per cent of their CHEB lifetime.

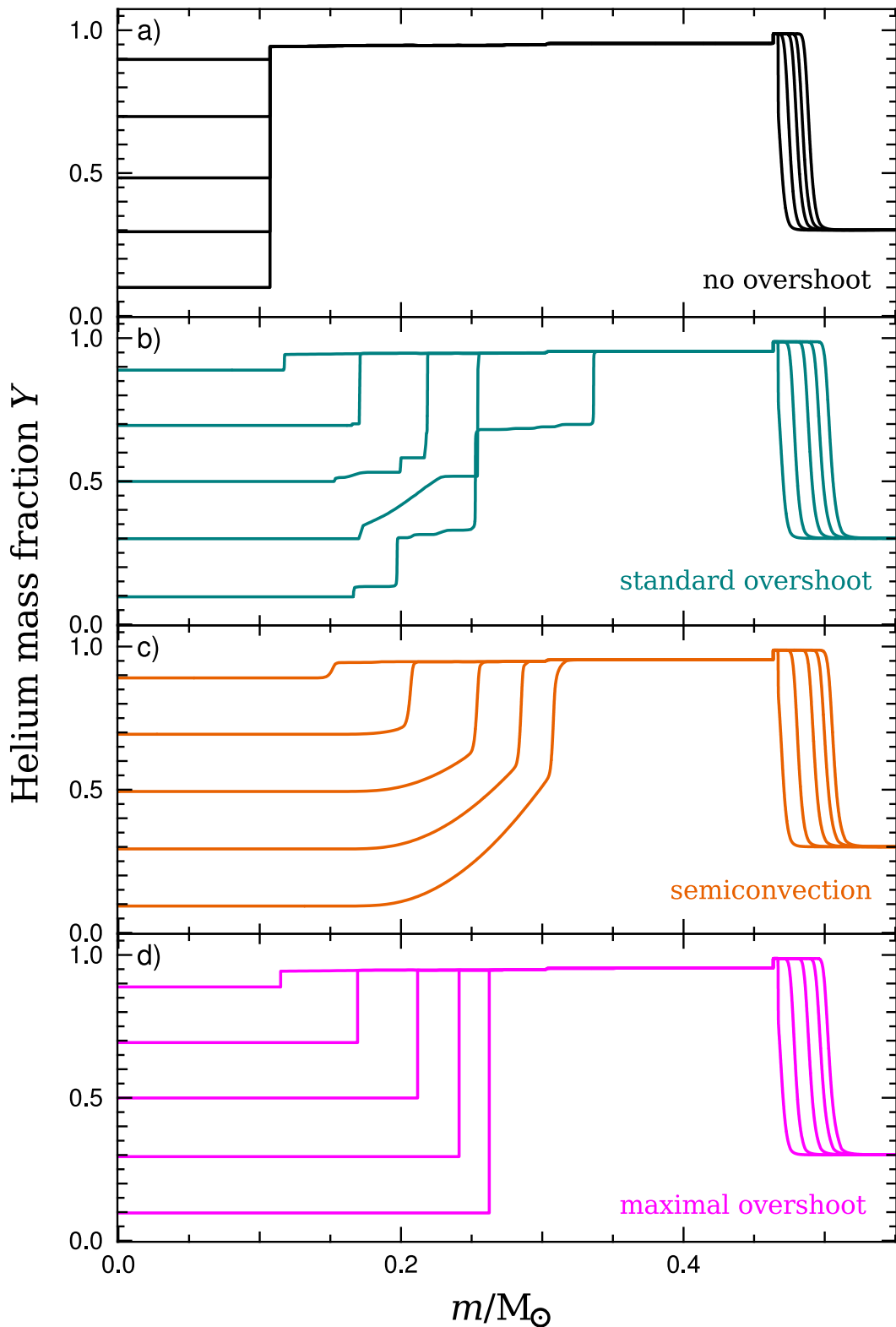


Figure 2.2: Evolution of internal helium abundance during CHeB with four different mixing prescriptions. Each panel shows the profile at five different times. The mixing prescriptions are, from top to bottom, no overshoot (Section 2.3.3; black), standard (pure Schwarzschild) overshoot (Section 2.3.3; cyan), semiconvection (Section 2.3.3; orange), and maximal overshoot (Section 2.3.3; magenta).

by showing ΔP as a function of frequency. In several examples we use the period échelle diagram, where the mode frequency is plotted against the mode period, modulo some period spacing $\Delta P_{\text{éch}}$. This is used because g-modes tend to be approximately equally spaced in period (the asymptotic limit is given in Equation 2.5). This is important because in the method developed by Mosser et al. (2012), $\Delta\Pi_1$ corresponds to the $\Delta P_{\text{éch}}$ which produces a regular pattern in the échelle diagram. Thus it allows us to predict the value of $\Delta\Pi_1$ that would be inferred from observations of our theoretical models.

We report the mode inertia E from the pulsation calculations which is defined as

$$E = \frac{\int_{r_1}^{R_s} [\xi_r^2 + \ell(\ell + 1)\xi_h^2] \rho r^2 dr}{M\xi_r(R_s)^2}, \quad (2.11)$$

where R_s is the radius at the outermost point, r_1 is the location of the innermost mesh point, and ξ_r and ξ_h are the radial and horizontal displacement eigenfunctions, respectively, which are both functions of r . This is a measure of kinetic energy of a mode relative to the radial displacement at the surface. In the plots of eigenfunctions we show the scaled horizontal displacement

$$y_2 = \frac{\ell(\ell + 1)}{R}\xi_h, \quad (2.12)$$

where R is the photospheric radius and ξ_h is scaled so that $\xi_r/R = 1$ at the surface.

2.3.3 Core mixing schemes

Models without convective overshoot

In the stellar models without convective overshoot the Schwarzschild criterion for convection is strictly applied. The resulting internal structure is shown in Figure 2.2(a) and Figure 2.3. In this case a convection zone may only grow (in mass) if the conditions change in a radiative zone so that $\nabla_{\text{rad}} > \nabla_{\text{ad}}$. In the CHeB phase this will give the smallest possible convective core (at least for models with the Schwarzschild criterion) because the region outside the core is close to convective neutrality (see Figure 2.3). In this study we do not compute any models using the Ledoux criterion for convection, but we note that we do not expect it to make any difference to our models either with or without convective overshoot, if properly implemented. This is because in our models without overshoot the convective boundary hardly moves (by less than $0.001 M_\odot$ in the $1 M_\odot$ solar-metallicity run; Figure 2.2), so any restriction in growth due to the composition gradient would be insignificant. In the overshooting models, the mixing beyond the boundary tends to erase

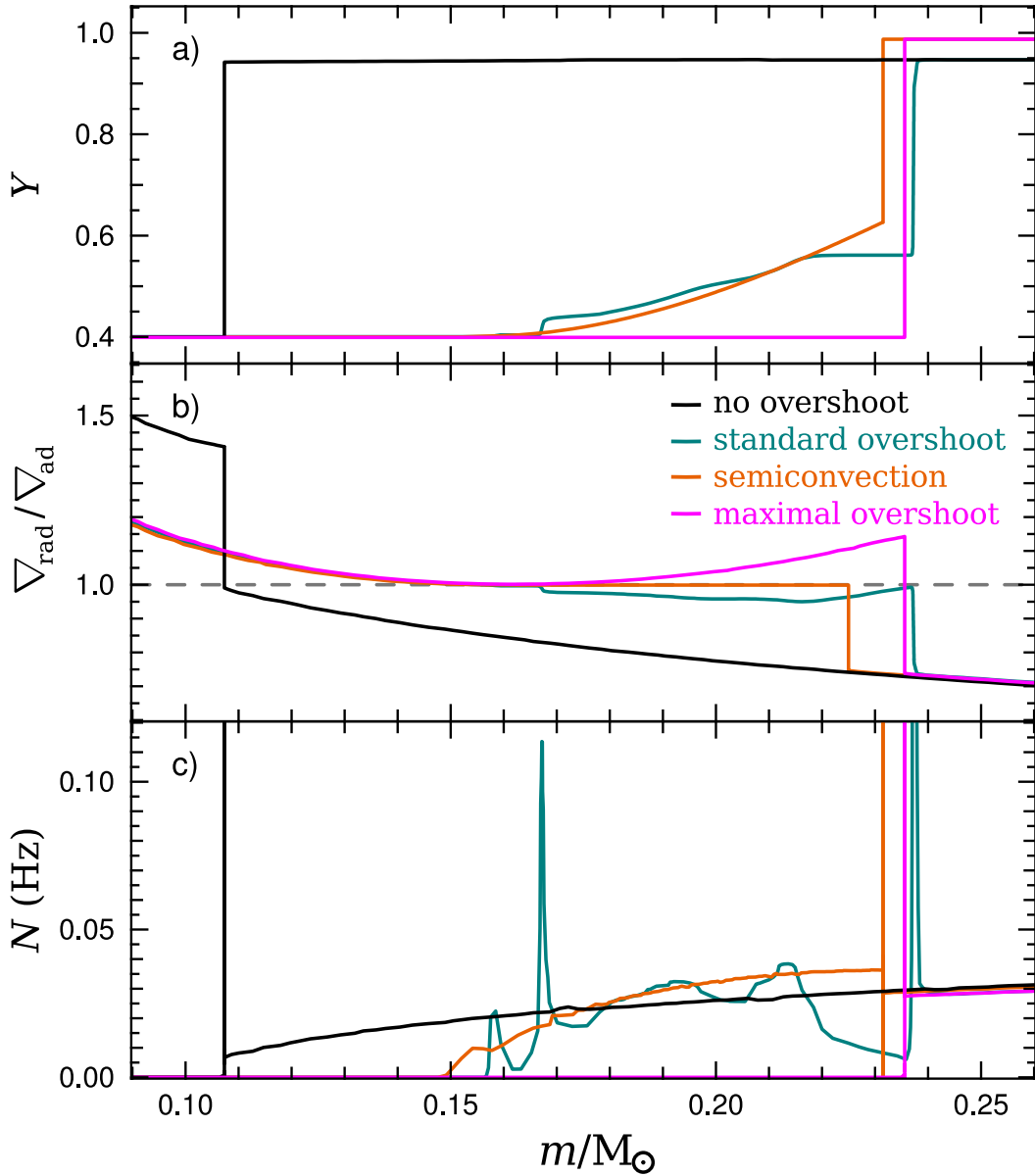


Figure 2.3: Internal properties of the $1 M_{\odot}$ models with four different mixing prescriptions when $Y = 0.4$ in the centre. The helium mass fraction Y , ratio of temperature gradients $\nabla_{\text{rad}}/\nabla_{\text{ad}}$, and Brunt-Väisälä frequency are shown. The four mixing prescriptions are no overshoot (Section 2.3.3; black), standard overshoot (Section 2.3.3; cyan), classical semiconvection (Section 2.3.3; orange), and maximal overshoot (Section 2.3.3; magenta). This colour scheme is used for mixing comparisons throughout this paper.

any stabilizing composition gradients and therefore reduces the Ledoux criterion to the Schwarzschild one.

Models with convective overshoot

We have implemented overshooting (Campbell and Lattanzio, 2008) with an exponential decay in the diffusion coefficient according to the scheme proposed by Herwig et al. (1997). This is expressed as

$$D_{\text{OS}}(z) = D_0 e^{\frac{-2z}{H_v}}, \quad (2.13)$$

where $D_{\text{OS}}(z)$ is the diffusion coefficient at distance z from the convective boundary and D_0 is the diffusion coefficient just inside the boundary. H_v is the ‘velocity scale height’ defined as

$$H_v = f_{\text{OS}} H_p, \quad (2.14)$$

where H_p is the pressure scale height, and we have chosen $f_{\text{OS}} = 0.001$. We refer to this as ‘standard overshoot’, but the exact value of f_{OS} is not important because our models are insensitive to the formulation of convective overshoot. The resulting internal structure is shown in Figure 2.2(b) and Figure 2.3.

Our models with convective overshoot and time-dependent mixing of chemical species (Campbell and Lattanzio, 2008) evolve similarly to those with instant mixing and the search for convective neutrality (Lattanzio, 1986). In the latter method, the convective boundary is found by testing whether mixing at the Schwarzschild boundary would cause the next radiative zone to become convective, while the former always mixes beyond the Schwarzschild boundary (i.e. without a test). The outcome is similar because at these conditions C and O are so much more opaque than He, so this mixing usually results in the radiative zone adjacent to the Schwarzschild boundary at the outer edge of the convective core becoming unstable to convection. This feedback contrasts with other phases in evolution when the extent of mixing is dependent on the overshooting distance because the resulting mixing does not alter the location of the Schwarzschild boundary.

In CHeB models, any overshoot tends to grow the core enough so that a minimum in $\nabla_{\text{rad}}/\nabla_{\text{ad}}$ appears in the convection zone; see the magenta line in Figure 2.3(b) for an example. Eventually this minimum falls below unity and the convection zone splits. This process continuously repeats, leaving behind the characteristic stepped abundance profile seen in Figure 2.2(b). If properly resolved, the partially mixed region created beyond the convective core by overshooting will have temperature gradient $\nabla_{\text{rad}}/\nabla_{\text{ad}} \approx 1$, resembling semiconvection (see Section 2.3.3).

Models with semiconvection

We have developed a simple method to mimic the structure that is found using semi-convection routines. We do this by allowing slow mixing in sub-adiabatic conditions. Specifically, we set a mixing rate that depends only on how close a zone is to being convective according to the Schwarzschild criterion (which neglects the stabilizing effect of any composition gradients). If $\nabla_{\text{rad}} < \nabla_{\text{ad}}$ then we set the diffusion coefficient D according to

$$\log D = \log D' - c_1(1 - \nabla_{\text{rad}}/\nabla_{\text{ad}}), \quad (2.15)$$

but also specify a maximum gradient so that

$$\left| \frac{d \ln D}{d \ln p} \right| \leq c_2, \quad (2.16)$$

where D' , c_1 , and c_2 are constants that are chosen at discretion and varied with experience (cf. Iben, 1967). In this study we use $\log D' = 10$, $c_1 = 100$, and $c_2 = 90$ to give D in units of cm^2s^{-1} . The structure that is produced by this scheme is shown in Figure 2.2(c). This differs slightly from previous routines that have a zone with exactly $\nabla_{\text{rad}} = \nabla_{\text{ad}}$ and a smooth composition profile which ends with a discontinuity (herein the ‘classical’ semiconvection structure). An example of the classical structure is shown in Figure 2.3. The most obvious difference produced by our routine is that the composition is everywhere smoothly varying, i.e. there is no discontinuity at the outer boundary of the partially mixed region.

We also use a different method to construct classical semiconvection models. For a given central composition we artificially increase the mass fraction of the convective core until there is a minimum in $\nabla_{\text{rad}}/\nabla_{\text{ad}}$ inside the convection zone with $\nabla_{\text{rad}}/\nabla_{\text{ad}} = 1$ (the structure during this intermediate step is identical to that of the maximal-overshoot models shown in Figure 2.3 and discussed below). The location of this minimum is the first guess for the boundary between the convection and semiconvection zones, while the edge of the convective region becomes the outer boundary of the semiconvection zone. We then adjust the composition between these two points until this region has $\nabla_{\text{rad}}/\nabla_{\text{ad}} = 1$ everywhere (and also make small adjustments to the location of the boundaries if needed). This contrasts with the method of Robertson and Faulkner (1972) where, during each time step, the composition changes due to nuclear burning and then mixing proceeds outwards from the centre, point by point, to give exactly $\nabla_{\text{rad}} = \nabla_{\text{ad}}$.

Models with maximal overshoot

If the helium-burning convective core is large enough, it will contain within it a minimum $\nabla_{\text{rad}}/\nabla_{\text{ad}}$, such as that shown by the magenta line in Figure 2.3(b). Further core growth will continue to reduce the value of this minimum until it reaches $\nabla_{\text{rad}}/\nabla_{\text{ad}} < 1$, which splits the convection zone into two. This is avoided in our newly developed ‘maximal-overshoot’ scheme by making convective overshoot dependent on the value of this minimum, so that the core growth slows (and then can stop) if the convective core is close to splitting. In its present ad hoc implementation the amount of mass beyond the convective boundary that is mixed each time step is proportional to the minimum of $\nabla_{\text{rad}}/\nabla_{\text{ad}} - 1$ in the convection zone, and overshoot is stopped if that minimum falls below 0.002. This ensures that the model attains the largest possible convective core throughout the evolution. This structure is shown in Figure 2.2(d) and Figure 2.3. We do not propose a physical justification for achieving this exact structure. Instead we use it as a comparison to standard models which is interesting because of its extreme core size and the effect on $\Delta\Pi_1$. Finally, we note that although our maximal-overshoot models are generated by a different mechanism, their structure is similar to some earlier models with large fully mixed cores (e.g., Bressan et al., 1986; Straniero et al., 2003).

2.3.4 Composition smoothing

The period spacing pattern in CHeB models taken directly from the evolution code tends to be inconsistent with observations (e.g. Figure 2 in Mosser et al., 2012). In Section 2.4.3 we analyse this in detail and show that it is primarily a relic of the burning during the core-flash phase. Therefore, in a number of our ZAHB models we remove the composition discontinuities between the H-burning shell and the convective core that this burning produces. We have good reason to do this: the chemical profile that the core flash leaves behind is dependent on unknown factors such as the extent of convective overshoot and mixing at boundaries, the extent of burning during each episode of convection (or ‘subflash’) as burning progresses inward, and the number of these subflashes. We remove this feature either by artificially resetting the composition to the mixture that existed immediately prior to the core flash or by smoothing the composition over a larger interval in mass. In the latter method we set the mass fraction X_i of species i according to

$$X_i = \frac{X_{i,1} + X_{i,2}}{2} + \frac{X_{i,2} - X_{i,1}}{2} \sin \left[\frac{m - m_0}{\Delta m} \pi \right], \quad (2.17)$$

where Δm is the mass over which the composition is smoothed, centred at m_0 , and $X_{i,1}$ and $X_{i,2}$ denote the interior and exterior compositions. After modifying the composition using either method we then evolve the model in the evolution code to allow it to return to hydrostatic equilibrium before computing the pulsations.

2.4 Results

2.4.1 Overview of the CHeB structure

We show a schematic of the evolution of the internal structure of a CHeB model in Figure 2.4. The profile of the Brunt–Väisälä frequency that develops is crucially dependent on the mixing scheme used at the boundary of the convective core, which is evident from the difference between the models in Figure 2.3(c). The significant features affecting the Brunt–Väisälä frequency (proceeding outward from the centre) are as follows.

- (i) A fully mixed convective core that is Ledoux and Schwarzschild unstable ($N \simeq 0$).
- (ii) A region that may surround the convective core in which material is slowly mixed (see e.g. the grey stripes in Figure 2.4). Depending on the mixing scheme there can emerge zones with a stabilizing chemical gradient (Schwarzschild marginally stable, Ledoux stable, and $N \gg 0$) or regions which are convective and well-mixed ($N \simeq 0$). The erratic nature of overshoot can create an irregular N profile in this region that constantly evolves. In this study, such a region only emerges in the standard-overshoot (Section 2.3.3) and semiconvection (Section 2.3.3) models.
- (iii) A helium-rich radiative region with $N > 0$. In models in which helium ignition begins with the core flash there will be composition gradients between the (fully or partially mixed) core and the H-burning shell (blue line in Figure 2.4). Only a small fraction of the helium burns in the core-flash phase (around 3 per cent in our $1 M_{\odot}$ models) but this is enough to cause detectable spikes in N from the molecular weight gradients formed at the boundaries of flash and subflash convection zones, e.g. near $r = 4.2 \times 10^9$ cm in Figure 2.9. In our models the largest spike is caused by the burning in the initial core flash (closest to the H-burning shell).
- (iv) The H-burning shell, which is strongly stable due to the molecular weight gradient ($N \gg 0$; blue line in Figure 2.4).
- (v) A radiative zone below the convective envelope (or the surface if the star is not massive enough to have a convective envelope). N decreases monotonically until the

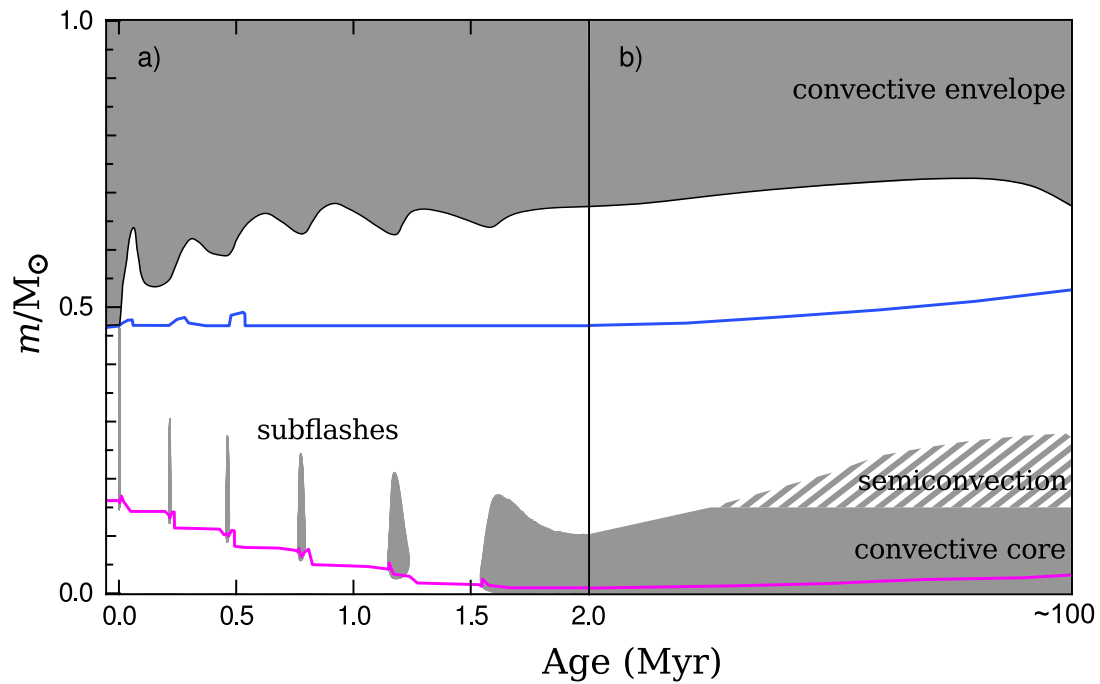


Figure 2.4: Left panel: Kippenhahn plot of the core-flash phase of a $1 M_{\odot}$ solar-metallicity model. Right panel: schematic Kippenhahn plot of subsequent quiescent CHeB evolution. Shaded areas (grey) denote convection zones. The upper curve (blue) and lower curve (magenta) denote the respective positions of maximum H- and He-burning luminosity. In the right panel the grey stripes show the region where partial mixing or semiconvection may occur.

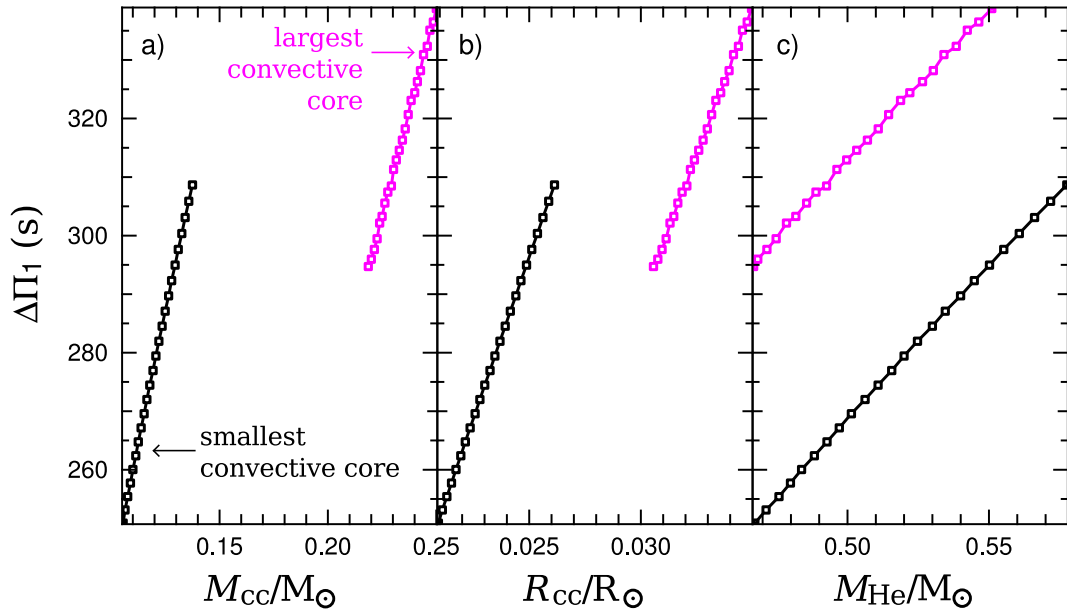


Figure 2.5: Dependence of the asymptotic g-mode period spacing $\Delta\Pi_1$ on core properties (mass of the convective core M_{cc} , radius of the convective core R_{cc} , and mass of the H-exhausted core M_{He}) for models with the smallest (black) and largest (magenta) possible convective core, artificially constructed by varying M_{He} . The models are $1 M_{\odot}$, solar-composition, and consist of a chemically homogeneous convection zone beneath the H-burning shell. Each model has central helium $Y = 0.5$.

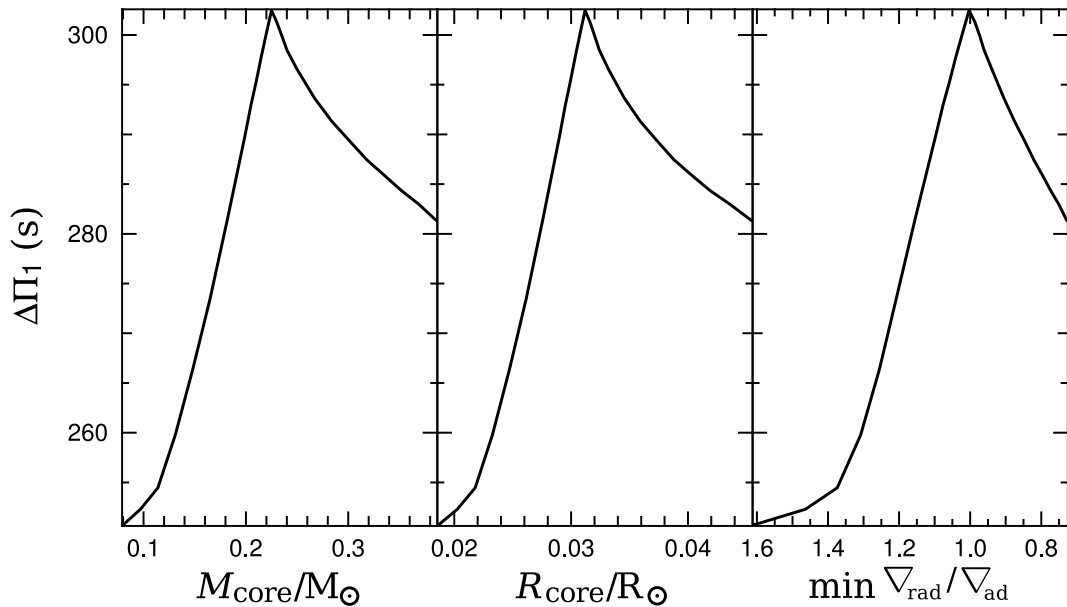


Figure 2.6: $\Delta\Pi_1$ dependence on the mass, radius and minimum of ∇_{rad}/∇_{ad} of the fully mixed core M_{core} . These models are constructed by varying M_{core} while keeping $M_{He} = 0.488 M_{\odot}$ and the core convection zone composition constant with $Y = 0.5$. Each model is $1 M_{\odot}$ and solar metallicity.

convective envelope, where $N \simeq 0$. The convective envelope extends all the way to the surface (or close enough for the pulsation calculations we perform in this study).

The radiative region between the convective envelope and the convective core is where g-modes propagate. Importantly, this includes any partially mixed or semiconvection region surrounding the convective core (e.g., the grey stripes in Figure 2.4).

2.4.2 $\Delta\Pi_1$ dependence on bulk core properties

We have tested the dependence of $\Delta\Pi_1$ on the fundamental properties of the core – the mass of the H-exhausted core M_{He} (Figure 2.5) and the mass of the fully mixed core M_{core} (Figure 2.6).

In Figure 2.5 we increase M_{He} through H-burning then construct models with the smallest (black markers) and largest (magenta markers) possible convective cores for a fixed central composition of $Y = 0.5$. In this test the mass of the convective core M_{cc} (Figure 2.5a) and radius of the convective core R_{cc} (Figure 2.5b) are dependent variables. The smallest convective core is found by extending it only until the region adjacent to the convection zone (i.e. the radiative side) is marginally stable to convection, which gives the same structure as the ‘no overshoot’ models in this study. In contrast, the models with the largest core are constructed by extending the convective core as far as possible so that the entire region within it remains convectively unstable, which is the same as for the maximal-overshoot models (Figure 2.3, Section 2.4.4). We find that in both the smallest and largest convective core cases M_{cc} , R_{cc} , and $\Delta\Pi_1$ are linearly dependent on M_{He} . Montalbán et al. (2013) have already highlighted the linear dependence of $\Delta\Pi_1$ on R_{cc} in low-mass CHeB models, as well as the importance of M_{He} , including a linear relationship between $\Delta\Pi_1$ and M_{He} for more massive models. The difference in $\Delta\Pi_1$ between the smallest and largest core cases is 45 s. It is evident from the fact that two values of R_{cc} can correspond to the same value of $\Delta\Pi_1$ that there is not a single linear dependence of $\Delta\Pi_1$ on R_{cc} (Figure 2.5b). In this case the relationship also depends on how the convective boundary is defined.

In Figure 2.6 we show the effect of artificially changing the mass of the homogeneous (fully mixed) region in the core, M_{core} , while keeping the central composition and the H-exhausted core mass constant. Note that M_{core} differs from M_{cc} in that there is no requirement that the entire region enclosed by M_{core} is convective according to the Schwarzschild criterion. The peak in $\Delta\Pi_1$ occurs exactly when the convective zone is as large as possible ($M_{\text{core}} = 0.22 M_{\odot}$). This clearly demonstrates that further extending the fully mixed core (e.g. as a result of overshoot; such as the ‘high overshoot’ model from Straniero et al. 2003) does *not* continue to increase $\Delta\Pi_1$ when part of it becomes

stable to convection according to Schwarzschild, allowing g-modes to propagate. This is of interest because it is not unreasonable to imagine that convective overshoot could allow the composition of two nearby convection zones to remain homogeneous. In this example, models with $0.22 < M_{\text{core}}/M_{\odot} < 0.33$ have two separate convection zones.

In Figure 2.7 we compare the $\ell = 1$ period spacing for models with fully mixed cores of different sizes: one with a fully mixed core mass of $0.215 M_{\odot}$ (black dashes) and another otherwise identical model, with a fully mixed core mass of $0.255 M_{\odot}$ (orange dashes), which is too large to be convective throughout and therefore gives rise to an additional radiative region ($1.7 \times 10^9 \text{ cm} \lesssim r \lesssim 2.3 \times 10^9 \text{ cm}$ in Figure 2.7). The asymptotic period spacing (from integrating over the entire structure according to Equation 2.5) is slightly lower for the model with the larger core (by 3 s). Some modes in this model are very closely spaced in period because they are trapped in the additional radiative region (see also Sections 2.4.4 and 2.4.4), whereas most pairs of modes have $\Delta P > \Delta \Pi_1$. If the mode periods are plotted in the échelle diagram (see Section 2.3.2), the period spacing required for a regular pattern, $\Delta P_{\text{éch}}$, is 19 s higher than the asymptotic value. The reason for this can be understood by considering the local buoyancy radius $\Pi^{-1}(r)$ described by Miglio et al. (2008). At a given point r , this is defined by

$$\Pi^{-1}(r) = \int_{r_0}^r \frac{N}{r'} dr', \quad (2.18)$$

where r_0 is the radius at the edge of the convective core ($r \simeq 1.7 \times 10^9 \text{ cm}$ in Figure 2.7). This gives the contribution to the integral in Equation 2.5 from the region enclosed by the point at radius r . The total buoyancy radius is the same integral evaluated over the entire g-mode propagation zone.

In the model with the larger fully mixed core (orange dashes in Figure 2.7) the interior buoyancy cavity accounts for 7.8 per cent of the total buoyancy radius, which corresponds to the difference between $\Delta \Pi_1$ and $\Delta P_{\text{éch}}$ (which are 284 s compared to 307 s respectively). If we exclude this interior cavity from the calculation of $\Delta \Pi_1$ we get almost exactly $\Delta \Pi_1 = \Delta P_{\text{éch}}$ (308 s compared to 307 s). This divergence between $\Delta \Pi_1$ and $\Delta P_{\text{éch}}$ is also apparent for the model with a sharp composition profile in Figure 2.7 (in blue), demonstrating that it does not depend on the composition profile at the edge of the fully mixed core. We therefore expect that the existence of a second radiative zone would generally cause the observationally inferred value of $\Delta \Pi_1$ (using the method of Mosser et al. 2012) to increase above its theoretical value (computed by integrating over the entire structure). This example highlights the possibility that a difficulty in accurately determining $\Delta \Pi_1$ from observations may contribute to its apparent discrepancy with

predictions from models. This phenomenon is discussed in more detail for a related example in Section 2.4.4.

Figure 2.8 shows the evolution of the internal structure of models with the four different mixing schemes. The size (in mass and radius) of the convective core in the semiconvection and standard-overshoot sequences is similar throughout the evolution, except when overshooting permits core breathing pulses near core helium exhaustion. This explains the similarity in $\Delta\Pi_1$ evolution. In both the semiconvection and standard-overshoot sequences almost all of the growth in the mass of the convective core occurs during the first 20 Myr (Figure 2.8c). Subsequently, helium is transported into the core by the expansion of the partially mixed region. Interestingly, the rate of depletion of helium in the core is exactly the same for the maximal-overshoot and standard-overshoot runs until the final (and largest) core breathing pulse extends the standard-overshoot model CHeB lifetime.

At the beginning of CHeB, each of the four standard sequences (solid lines) shows a decrease in $\Delta\Pi_1$ (Figure 2.8a). This can be attributed to the softening of the steep composition gradient at the H-burning shell. This is further discussed in Section 2.4.3 and its effect on $\Delta\Pi_1$ is also explained for an analogous case in Section 2.4.5. After hydrogen burning resumes over the entire shell, the evolution of $\Delta\Pi_1$ closely tracks the radius of the convective core, which has been shown by Montalbán et al. (2013).

In dashed lines in Figure 2.8(a) we also show additional sequences with standard and maximal overshoot that result from enlarging M_{He} by $\Delta M_{\text{He}} = 0.025 M_{\odot}$ at the beginning of CHeB. This was achieved by delaying helium ignition through an ad hoc increase to the neutrino emission rate during the RGB phase. This increases the average $\Delta\Pi_1$ during CHeB by 18 s for the standard-overshoot sequence and 11 s for the maximal-overshoot case. Most significantly, it increases $\Delta\Pi_1$ by around 20 s early in the CHeB phase for both sequences. The faster rate of helium burning resulting from the larger M_{He} exhausts the fuel earlier, shortening the CHeB lifetime by around 25 per cent for both mixing schemes.

As CHeB progresses, the convective core becomes increasingly C- and O-rich (Figure 2.8d) and consequently more dense. This causes the convective core radius to decrease (Figure 2.8b), even when its mass does not and irrespective of the mixing scheme (Figure 2.8c). It is evident from the decrease in $\Delta\Pi_1$ towards the end of CHeB for every sequence shown in Figure 2.8(a) that $\Delta\Pi_1$ is more closely dependent on convective core radius than mass. The final composition of the degenerate C-O core is another potential diagnostic for mixing, but the range covered by these four different schemes is small (oxygen varies by around 15 per cent) and the situation is further complicated by reaction rate uncertainties (Straniero et al., 2003).

In this section we have explored how differences in the stellar structure affect $\Delta\Pi_1$. Even among the models without a semiconvection or partially mixed zone, $\Delta\Pi_1$ depends on a number of factors: R_{cc} , M_{He} , and core composition. Additionally, if the chemically homogeneous region in the core is large enough for part of it to become radiative, mode trapping can cause the period spacing to increase above the asymptotic value. Such an effect would increase the $\Delta\Pi_1$ inferred from observations, and therefore help to explain why standard CHeB models do not match the average $\Delta\Pi_1$ for the *Kepler* field stars.

2.4.3 Pulsations in early post core-flash CHeB models

Neutrino emission from plasmon decay during the RGB phase is strongest at the centre, where the density is highest. This energy loss is enough to move the position of maximum temperature, and therefore He-ignition, off-centre. After helium ignition a sequence of several subflashes move inward until the burning reaches the core and quiescent CHeB begins (Figure 2.4). In one of the first studies making use of the mixed mode detection in red giants, Bildsten et al. (2012) found that it may be possible to identify stars in the core-flash phase by using the fact that (between the subflashes) the g-mode period spacing is expected to be much lower than for quiescent CHeB stars, but still higher than for RGB stars. Their approach of studying the population in the *Kepler* field, if successful, could reveal the lifetime of the core-flash phase and the nature of the mixing, and therefore also shed light on the structure before the core flash (which is dependent on neutrino losses for example). Here we examine the computed pulsation spectra of a model in the early post core-flash phase, and test the effect of the remaining abundance profile.

The inward progression of convection and burning during the core-flash phase has a lasting effect on the Brunt–Väisälä frequency. Two of these features in our early-CHeB model are visible in Figure 2.9: the peak in N at $r = 1.5 \times 10^9$ cm, due to the initial recession of the convective core at the beginning of CHeB; and another at $r = 4.2 \times 10^9$ cm, which is caused by the first episode of core-flash burning. However, from a seismic perspective, the dominant feature of early-CHeB models is the thinness of the H-burning shell, which is due to the relatively steep temperature gradient in the prior luminous RGB phase. In Figure 2.9 we confirm that the composition profile at the H-burning shell causes the irregular period spacing pattern by showing that it still exists for a model with the sharp N feature from the first episode of core-flash burning removed (blue model).

In our solar-mass runs it takes more than 14 Myr for hydrogen burning to smooth out the composition gradient at the inside of the shell at $r = 4.5 \times 10^9$ cm, as shown in Figure 2.10, and thus for a regular pattern in the period spacing to emerge. In Figure 2.11

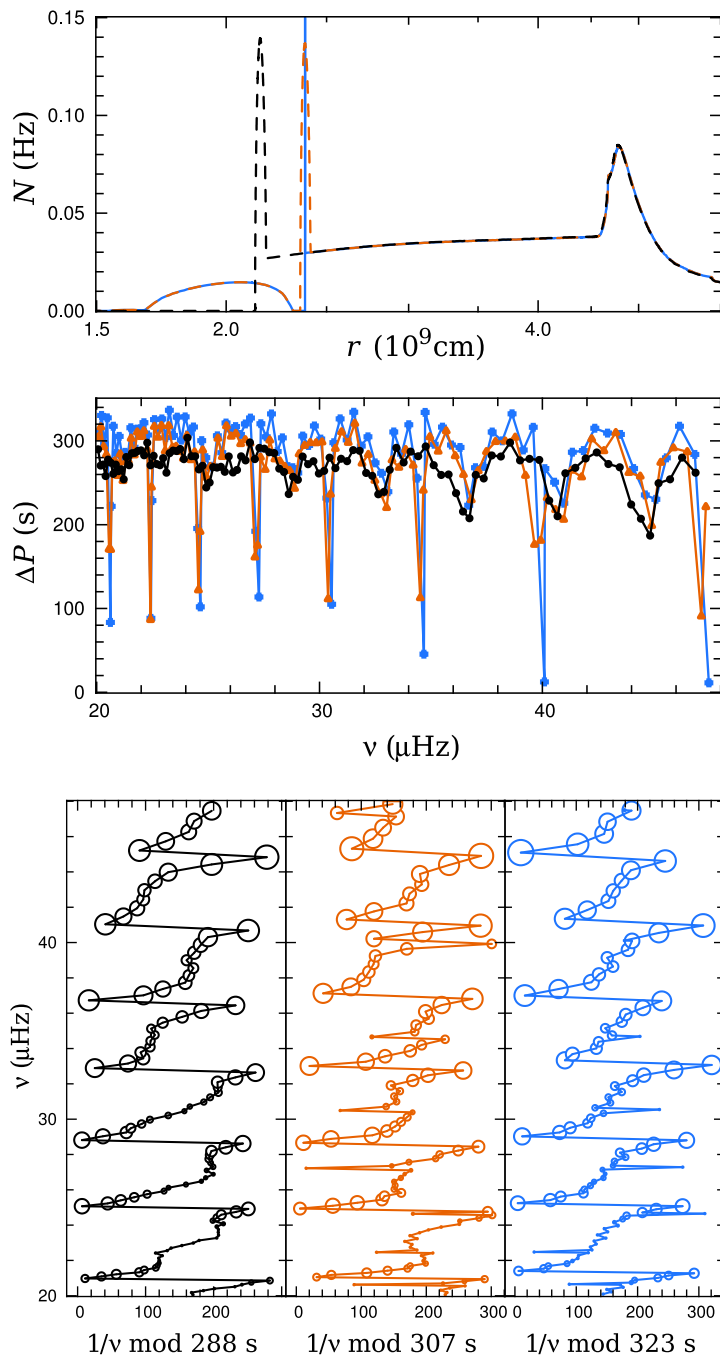


Figure 2.7: Upper panels: Brunt–Väisälä frequency and $\ell = 1$ period spacing for three models with different sized fully mixed cores and different chemical profiles near the boundary. Here we have (i) a smooth boundary with a fully mixed core that is convective (black), and (ii) a fully mixed core too large to be convective with a smooth (orange) and (iii) sharp (blue) composition profile at the boundary. The composition profiles are set according to Equation 2.17 with $\Delta m = 0.01 M_{\odot}$ (smooth profile) and $\Delta m = 10^{-5} M_{\odot}$ (sharp profile). Lower panels: period échelle diagrams for the three models. Larger symbols correspond to lower mode inertia. The best fits for ΔP_{ech} are achieved for period modulo 288 s, 307 s, and 323 s. This compares to the asymptotic g-mode period spacing ($\Delta \Pi_1$) of 287 s, 284 s, and 295 s, respectively. Each model has approximately $R = 10.7 R_{\odot}$, $T_{\text{eff}} = 4760$ K, and $\nu_{\text{max}} = 27 \mu\text{Hz}$.

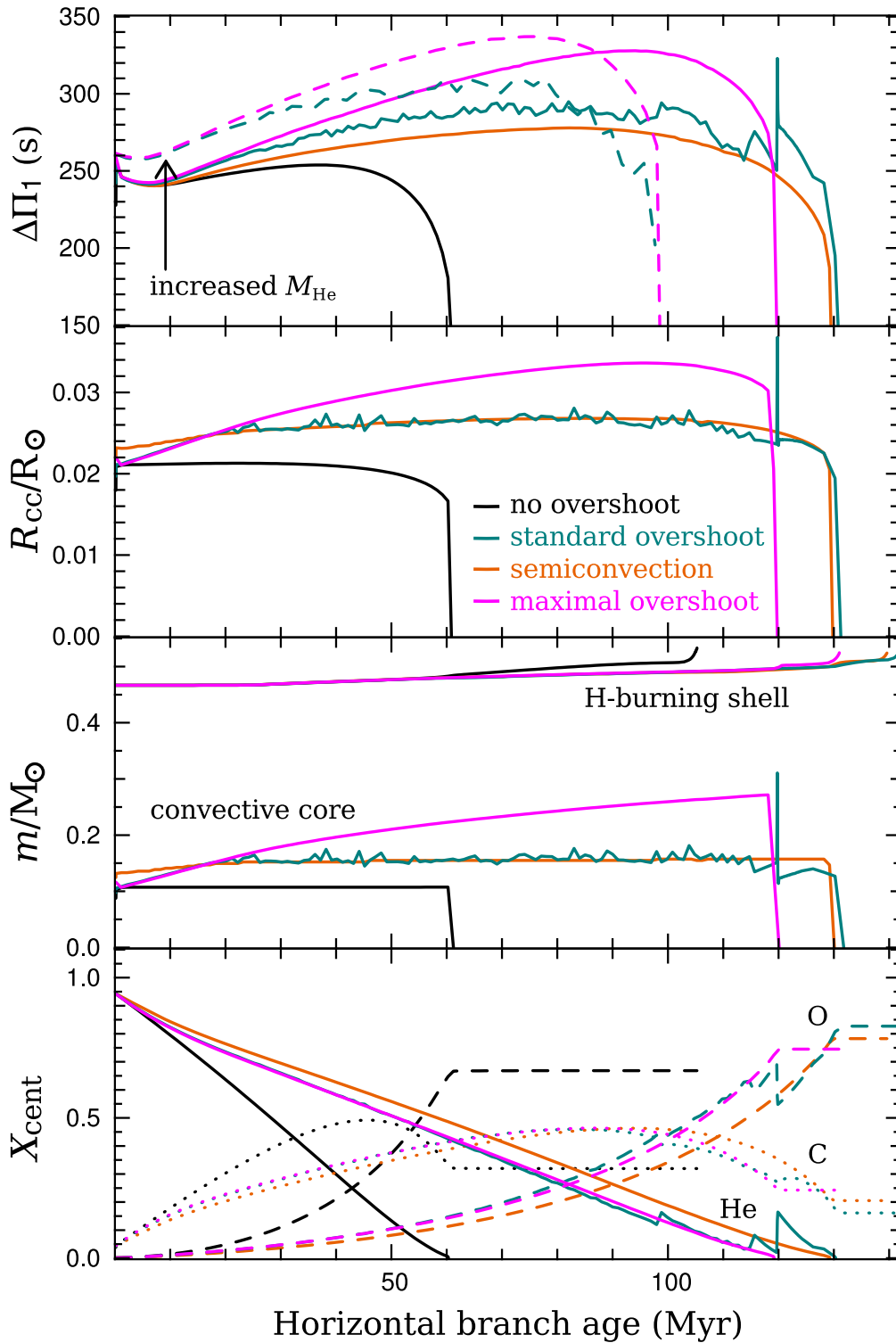


Figure 2.8: Evolution of the various $1 M_{\odot}$ models with four different treatments of convective boundaries during the CHeB phase. Models have the same colours as Figures 2.2 and 2.3. Properties shown, from top to bottom, are the asymptotic g-mode period spacing $\Delta\Pi_1$, the radius of the convective core R_{cc} , the mass of the H-exhausted and the convective core, and the central helium (solid line), carbon (dots) and oxygen (dashes) mass fractions. In the top panel dashed lines indicate models with an increased core mass $\Delta M_{\text{He}} = 0.025 M_{\odot}$ at the beginning of the CHeB phase.

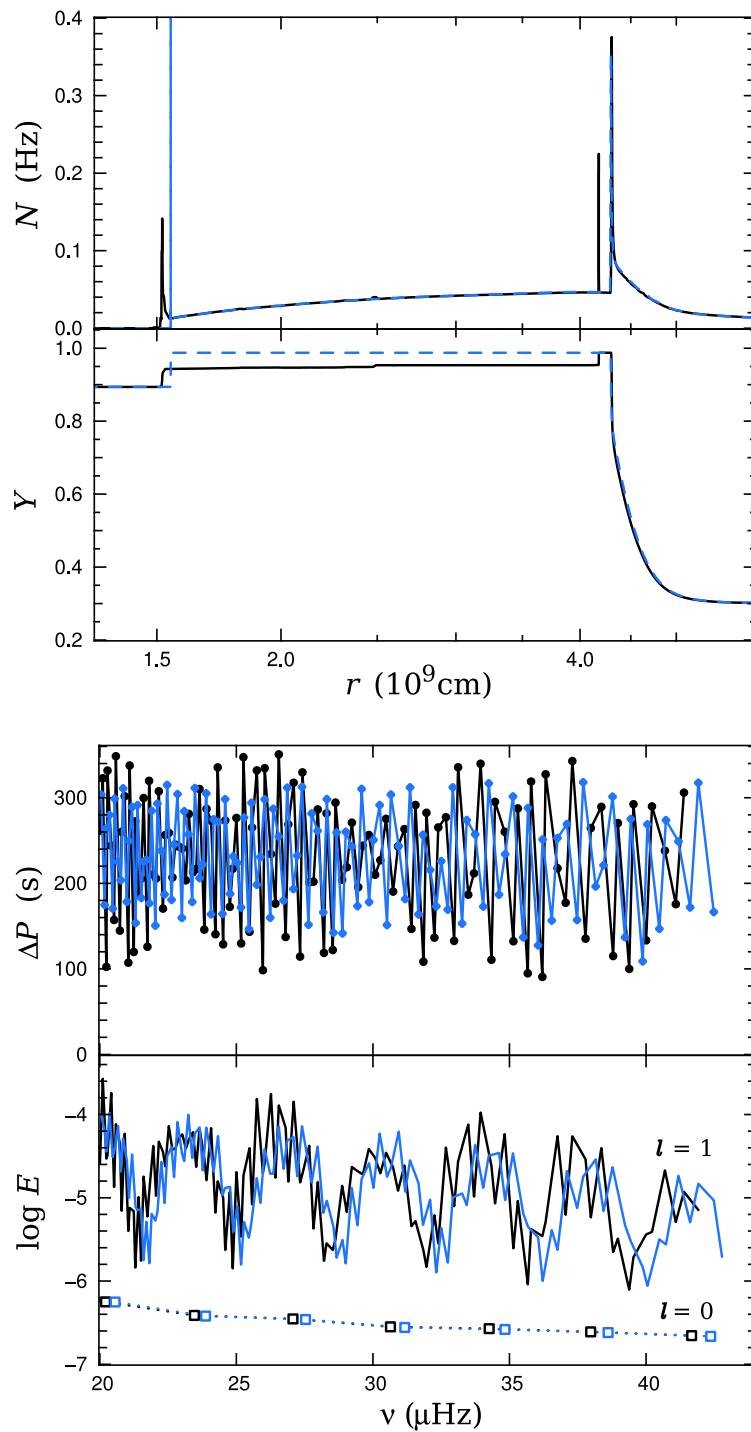


Figure 2.9: Pulsation properties of $1 M_{\odot}$ models with standard overshoot 2.7 Myr after the onset of convective CHeB taken directly from the evolution code (black) and with the region outside the convective core homogenized (blue). First panel: Brunt–Väisälä frequency N . Second panel: helium mass fraction Y . Third panel: $\ell = 1$ period spacing. Fourth panel: $\ell = 0$ and $\ell = 1$ mode inertia normalized to the surface radial displacement. The model from the evolution code has $\Delta\Pi_1 = 240$ s, $R = 11.6 R_{\odot}$, $T_{\text{eff}} = 4580$ K, and $\nu_{\text{max}} = 23 \mu\text{Hz}$ whereas the model with the homogenized composition has $\Delta\Pi_1 = 238$ s, $R = 11.5 R_{\odot}$, $T_{\text{eff}} = 4570$ K, and $\nu_{\text{max}} = 24 \mu\text{Hz}$.

we show the effect of this sharp composition gradient on the eigenfunctions. After the core flash there is a sharp peak in the buoyancy frequency (at $r = 4.3 \times 10^9$ cm in Figure 2.11a) which traps modes of consecutive radial order to very different extents (Figure 2.11c). This buoyancy peak is then slowly eroded by hydrogen burning (Figure 2.11b), and once the hydrogen burning shell completely reactivates the buoyancy peak is broad compared to the characteristic eigenfunction wavelength (Figure 2.11d), leaving the period spacing more regular. If this picture is true for real stars we anticipate difficulty in determining $\Delta\Pi_1$ for up to 15 per cent of red clump stars (based on a 100 Myr CHeB lifetime) and also every star in the core-flash phase.

Only after hydrogen burning resumes throughout the shell does the effect of any composition profile left by the core flash become dominant (it is responsible for the difference between the two models in Figure 2.10). In Figure 2.12 we show that the nature of this chemical profile strongly affects the pulsations. We compare two chemical profiles that vary smoothly according to Equation 2.17 and one that has the composition profile from the evolution code. It is clear in the case with the composition gradient spread over $\Delta m = 0.002 M_\odot$ (central panels in Figure 2.12) that the high-frequency (low radial order) modes are most sensitive to this feature (blue model in Figure 2.12). This is because adjacent modes are affected differently when the characteristic eigenfunction wavelength is large enough to be comparable to the size of the peak in N . This causes the variation in ΔP between consecutive pairs of modes. If the composition profile is smoother, the effect of this feature diminishes (e.g., in the orange model with $\Delta m = 0.01 M_\odot$; left panel in Figure 2.12), and the period spacing resembles models where it is absent (e.g. the blue model in Figure 2.10). Conversely, the sharper composition profile produced by the evolution code (and dependent on the treatment of the convective boundary during the core flash) produces a very obvious effect on the period spacing. Specifically, it introduces a large mode-to-mode variation in ΔP throughout the frequency range examined (black model in Figure 2.10). This behaviour can be explained by analysing the eigenfunctions. The spike in N is located at about half the buoyancy radius (it is at 57 per cent of the total buoyancy radius in this particular case) where neighbouring eigenfunctions are separated in phase by about $\pi/2$, so it affects consecutive modes differently. In this case $\Delta m \approx 10^{-4} M_\odot$ which is small compared to the eigenfunction wavelength.

These examples serve as a note of caution when computing pulsations for models with steep composition gradients. The steepness of those resulting from the core-flash phase is particularly dependent on convective overshoot, which is uncertain. This is the reason we have smoothed the composition profile after the core-flash phase for many models shown in this paper.

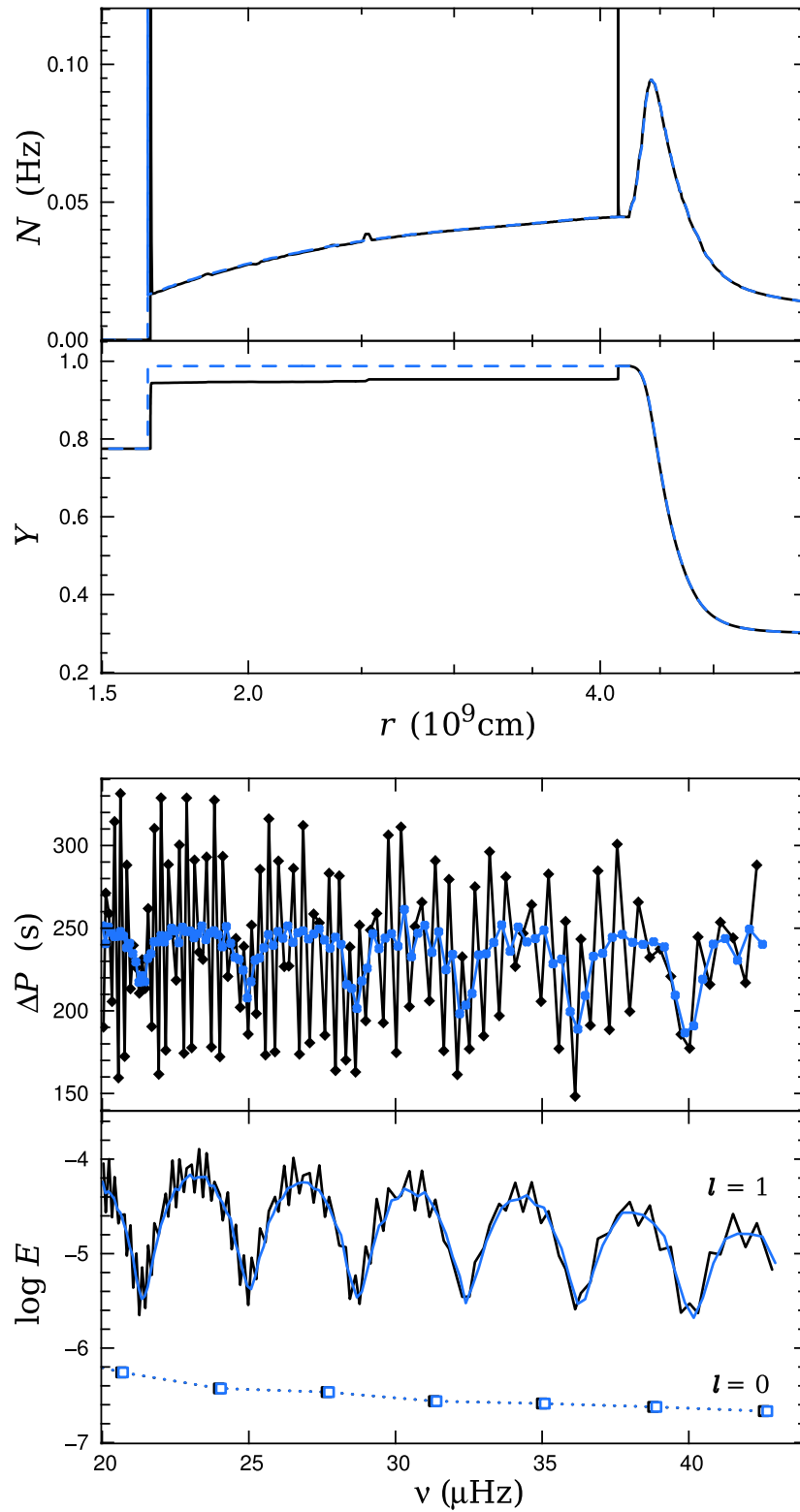


Figure 2.10: Pulsation properties of $1 M_{\odot}$ models with standard overshoot 14.8 Myr after the end of the core-flash phase from the evolution code (black) and with the region outside the convective core homogenized (blue). Both models have $\Delta\Pi_1 = 247$ s. These models have $R = 11.4 R_{\odot}$, $T_{\text{eff}} = 4590$ K, and $\nu_{\text{max}} = 24 \mu\text{Hz}$.

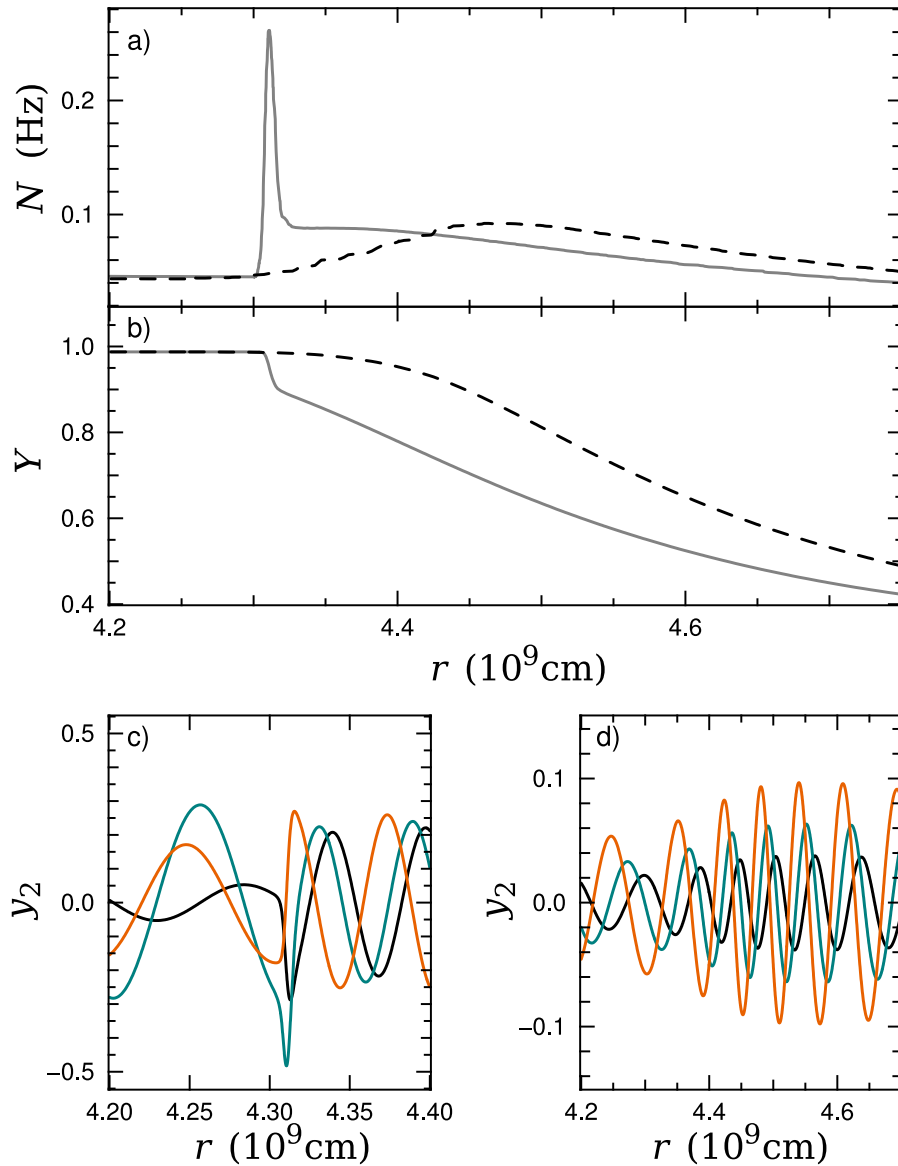


Figure 2.11: Upper panels: comparison of the Brunt–Väisälä frequency N and helium mass fraction Y near the edge of the H-exhausted core for two early-CHeB models. The model represented by the solid lines is 6.8 Myr after the beginning of the CHeB phase and the dashed model has evolved for another 10 Myr. Lower panels: scaled horizontal displacement eigenfunctions y_2 (defined in Equation 2.12) for $\ell = 1$ modes in (c) the earlier, and (d) the later model. The modes are of consecutive radial order $n = -91, -92, -93$ (in orange, cyan, and black, respectively), and have frequency of roughly $42 \mu\text{Hz}$. These models have approximately $R = 11.3 R_\odot$, $T_{\text{eff}} = 4570 \text{ K}$, and $\nu_{\text{max}} = 24 \mu\text{Hz}$.

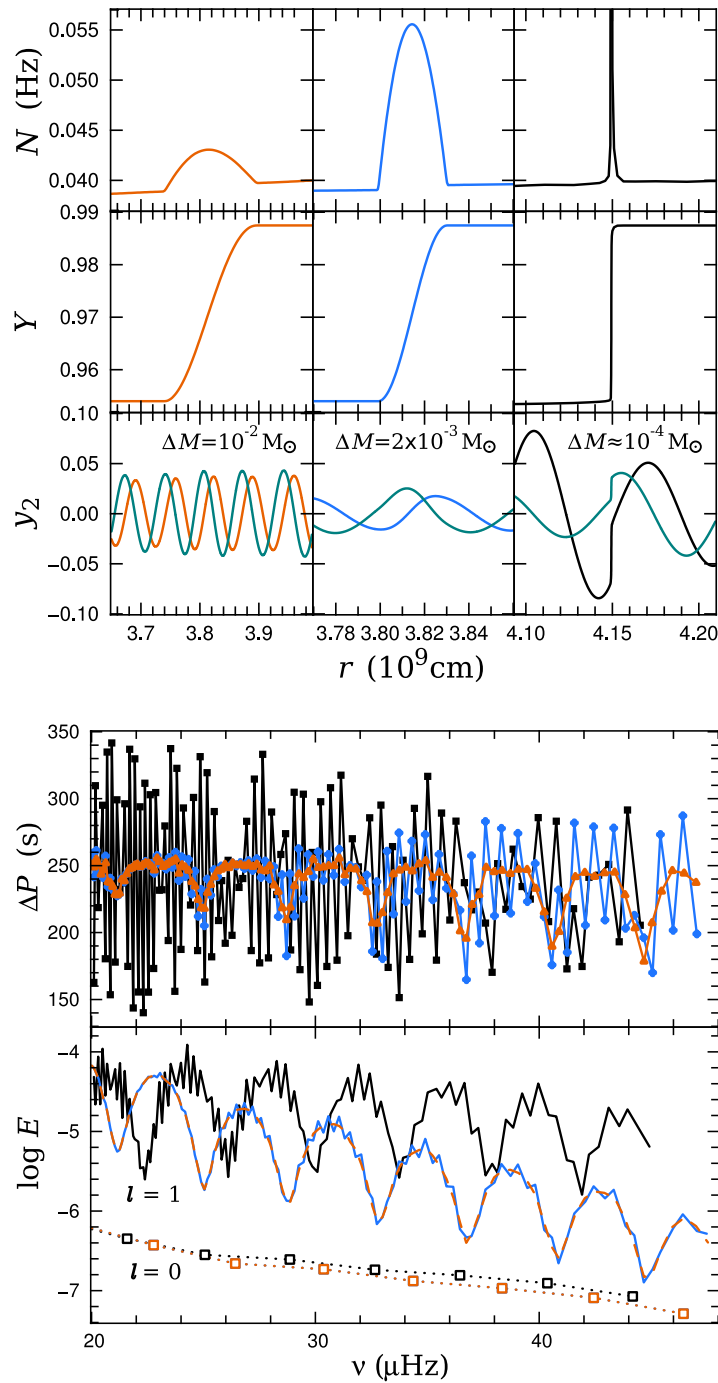


Figure 2.12: Comparison of pulsation properties of the $1 M_{\odot}$ models with different composition profiles from the initial core flash. Upper panels: Brunt–Väisälä frequency N , helium mass fraction Y , and scaled horizontal displacement eigenfunctions y_2 (defined in Equation 2.12) for two consecutive $\ell = 1$ modes with $\nu \approx 26 \mu\text{Hz}$. From left to right the models have chemical profiles artificially smoothed over $0.01 M_{\odot}$ (orange), $0.002 M_{\odot}$ (blue), and approximately $10^{-4} M_{\odot}$ (from the evolution code; black). The former two are of the form described by Equation 2.17 and have approximately $R = 11.1 R_{\odot}$, $T_{\text{eff}} = 4750 \text{ K}$, and $\nu_{\text{max}} = 27 \mu\text{Hz}$ while the latter model has $R = 11.1 R_{\odot}$, $T_{\text{eff}} = 4610 \text{ K}$, and $\nu_{\text{max}} = 25 \mu\text{Hz}$. Lower panels: $\ell = 1$ mode period spacing and normalized inertia for the above models (same colours).

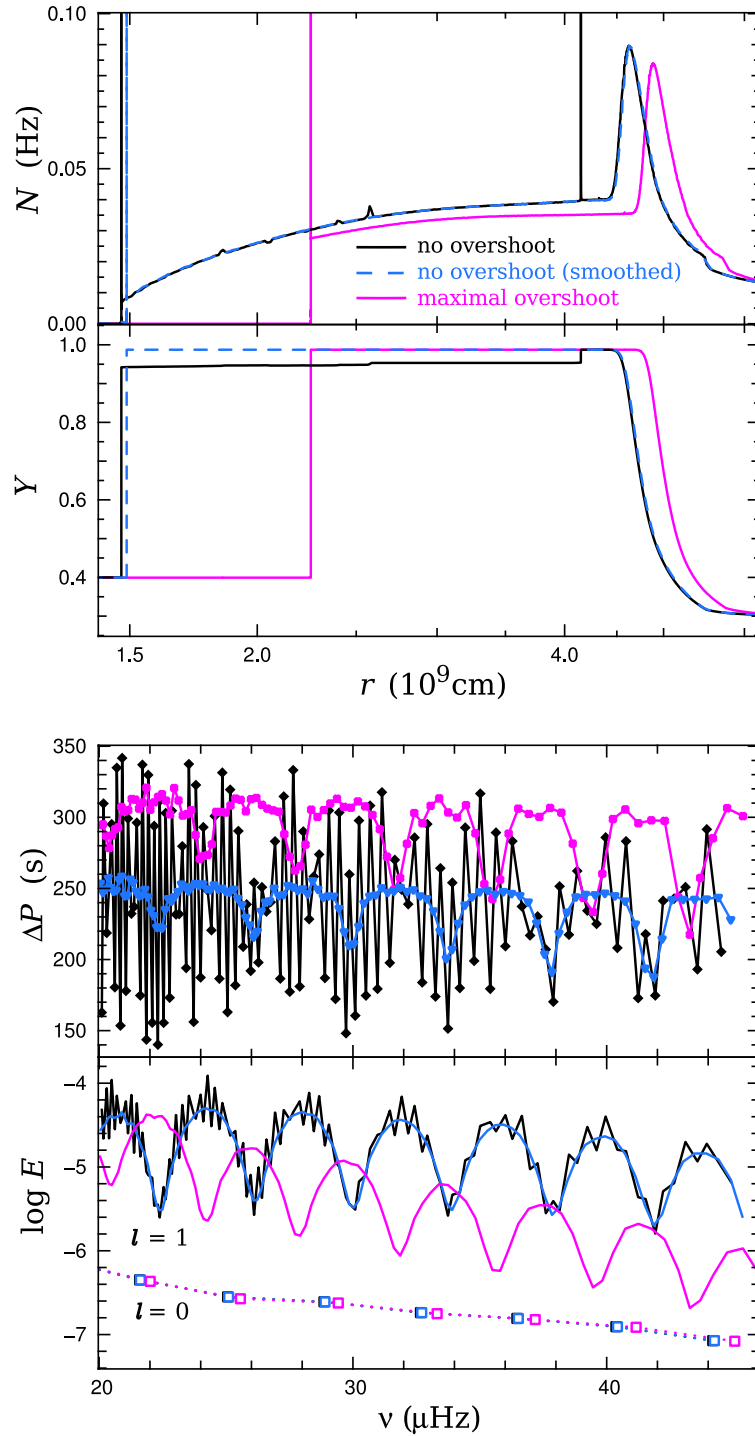


Figure 2.13: Pulsation properties of $1M_{\odot}$ models without convective overshoot from the evolution code (black) and with the region outside the convective core homogenized (blue), and a model with maximal overshoot (magenta). Both models without overshoot have $\Delta\Pi_1 = 252$ s while the model with maximal overshoot has $\Delta\Pi_1 = 314$ s. The models have approximately $R = 11.1 R_{\odot}$, $T_{\text{eff}} = 4610$ K, and $\nu_{\text{max}} = 25 \mu\text{Hz}$.

2.4.4 Pulsation properties for models with different mixing schemes

Models without convective overshoot

Our models without convective overshoot do not develop a partially mixed region, and experience negligible growth in the mass of the convective core. When the effects of core flash mixing are excluded, and after H-burning broadens the shell, these models have a simple buoyancy profile, and consequently a simple period spacing pattern (Figure 2.13). This period spacing pattern closely resembles RGB models (e.g. Figure 1b in Bedding et al. 2011) and observations (e.g. KIC 9882316 in Figure 1 in Mosser et al. 2012) except that the period spacing is higher.

Models with standard overshoot

The dominant factor in the computed pulsations of our standard-overshoot model shown in black in Figure 2.14 is the main composition discontinuity left by the core flash (see Section 2.4.3 for the analysis of the effect of this discontinuity). In order to isolate the effect of the partially mixed region resulting from CHEB ($r < 2.3 \times 10^9$ cm) we have smoothed the composition profile created during the core-flash phase.

In addition, we have also smoothed the chemical profile at the edge of the partially mixed zone ($r \simeq 2.3 \times 10^9$ cm) in order to make the period spacing slightly more regular. The resulting period spacing pattern shown in cyan in Figure 2.14 differs from the earlier models without a partially mixed region by the appearance of consecutive modes that are very closely spaced in period. These have a regular dependence on radial order n and are separated by $\Delta n \approx 11$. These modes are also of very high inertia, and their effect on ΔP in Figure 2.14 appears superimposed on the pattern produced by a structure without a partially mixed region (e.g. the blue model in Figure 2.13). The reason for this is clear from Figure 2.15(b), where it can be seen that these modes are ‘trapped’ in the partially mixed region by the discontinuity at its boundary. The period spacing between other modes is affected too: the position of nodes in the eigenfunctions of neighbouring modes in the trapping region is nearly identical, so the period spacing between most of them is as if the interior cavity does not exist, i.e. their ΔP is more consistent with the asymptotic calculation excluding this cavity and is therefore higher. This is demonstrated in the period échelle diagram in Figure 2.15 (see also the analogous case in Figure 2.7). In this example, the $\Delta P_{\text{éch}}$ that produces the best fit for the échelle diagram is 315 s, which is well above the asymptotic value of 281 s. This suggests that inferences from asteroseismology about the theoretical $\Delta \Pi_1$ as specified in Equation 2.5 may be dubious if the stars have a structure comparable to our standard-overshoot models. Moreover, the trapped modes

that are responsible for this behaviour have a relatively small amplitude at the surface and may therefore be impossible to detect.

Models with semiconvection

We have computed the pulsation spectra for four models with semiconvection-like structures. In Figure 2.16 we compare the classical semiconvection structure to those where the abundance discontinuity at the outer boundary of the semiconvection zone has been softened. In Figure 2.17 we analyse the structure that is produced by our routine that mimics semiconvection.

In classical semiconvection models the sharp composition gradient between the semiconvection zone (which is relatively C- and O-rich and has stabilizing composition gradient) and the He-rich zone produces a step in the Brunt–Väisälä frequency (at $r = 2.2 \times 10^9$ cm in Figure 2.16). This causes variation in ΔP between consecutive pairs of low-frequency modes and also in the inertia of every second mode (Figure 2.16). The replacement of this discontinuity by a linear composition profile spread over $0.01 M_{\odot}$ introduces a second periodicity in ΔP of $\Delta n \simeq 7$, where n is the radial order. This is consistent with the expression derived by Miglio et al. (2008):

$$\Delta n \simeq \frac{\Pi_{\mu}}{\Pi_0}, \quad (2.19)$$

where Π_{μ}^{-1} is the buoyancy radius at the location of the composition gradient and Π_0^{-1} is the total buoyancy radius (defined in Equation 2.18). This relatively smooth composition profile has only a small effect on period spacing and mode inertia compared with the case where the composition varies over just $2 \times 10^{-4} M_{\odot}$ (cyan dashes in Figure 2.16). In the latter case, modes are very strongly trapped in the semiconvection zone (with about the same periodicity), which increases the period spacing between the non-trapped modes to around 300 s, well above the asymptotic value of 271 s. This model has a regular period spacing pattern when plotted in the échelle diagram with $\Delta P_{\text{éch}} = 306$ s, which is consistent with the $\Delta \Pi_1$ calculation excluding the region interior to the composition discontinuity. This is analogous to the model with strong mode trapping in Figures 2.14 and 2.15. In both cases, the low ΔP between certain pairs of modes provides the only hint that the typical ΔP is actually above the asymptotic value. One of the modes in each of these pairs, however, is unlikely to be detected because it has high inertia and is trapped in the semiconvection/partially mixed zone.

In contrast with the classical semiconvection models, the buoyancy spike produced by the ad hoc semiconvection scheme in the evolution code only weakly traps modes. This is

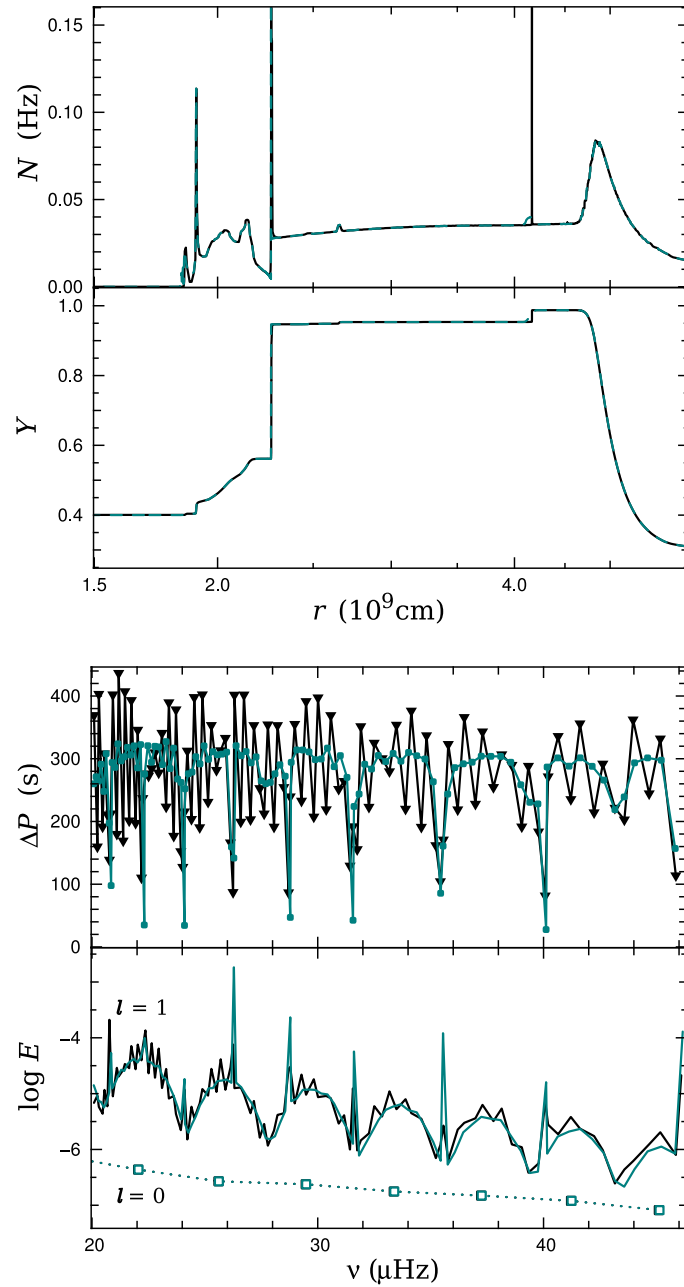


Figure 2.14: Pulsation properties of $1 M_{\odot}$ models with standard overshoot from the evolution code (black) and with some composition smoothing (cyan). The composition profile in the latter model has been smoothed near $r = 4.2 \times 10^9$ cm by using Equation 2.17 with $\Delta m = 0.008 \times M_{\odot}$, which is sufficient for it to not affect the computed frequencies. The discontinuity at the edge of the partially mixed zone (2.3×10^9 cm) has been smoothed with $\Delta m = 2 \times 10^{-4} M_{\odot}$. The model from the evolution code has $\Delta \Pi_1 = 278$ s while the model with smoothing has $\Delta \Pi_1 = 281$ s. Both models have $R = 11.0 R_{\odot}$, $T_{\text{eff}} = 4600$ K, and $\nu_{\text{max}} = 26 \mu\text{Hz}$.

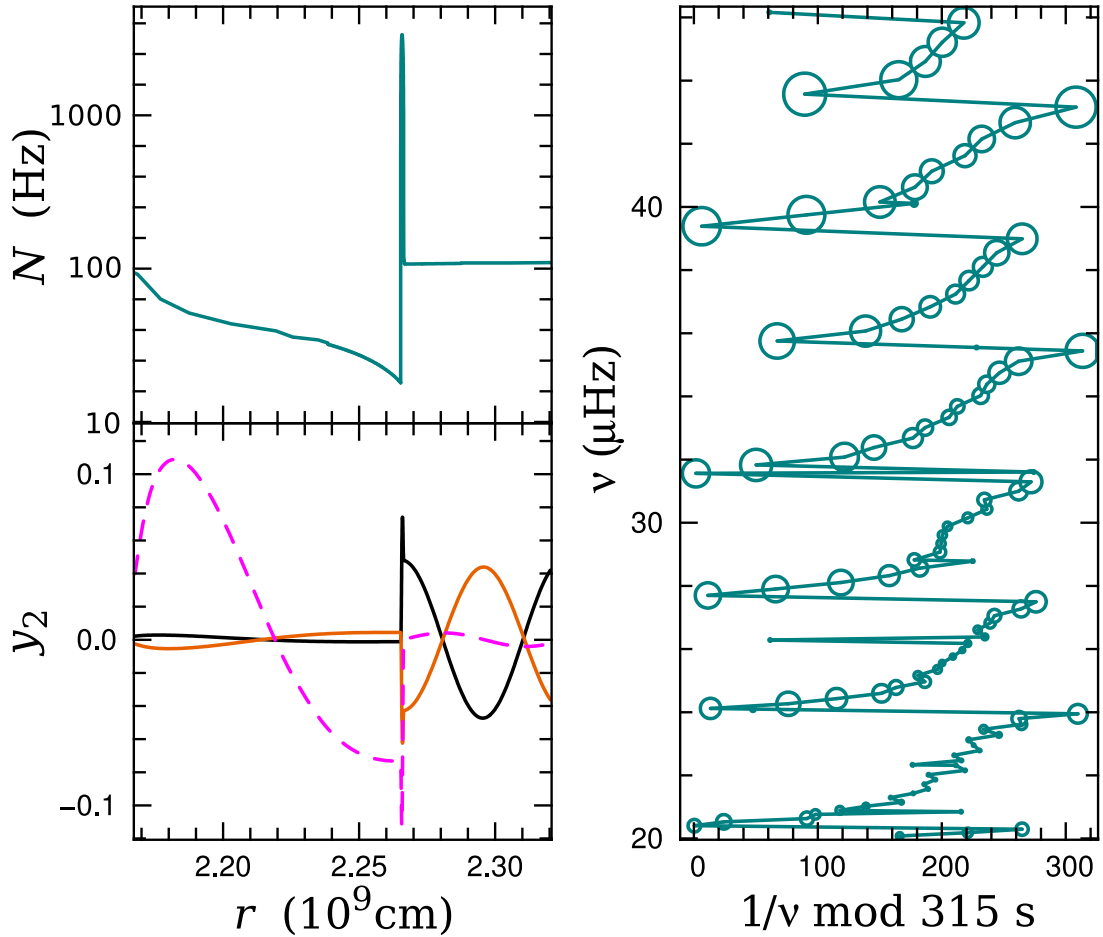


Figure 2.15: Seismic properties of the standard-overshoot model in Figure 2.14 with composition smoothing. Left panel: Brunt-väisälä frequency and scaled horizontal displacement eigenfunctions (where y_2 is defined in Equation 2.12) with radial order $n = -130, -129, -128$ (black line, orange line, and magenta dashes, respectively) and $\nu \approx 26 \mu\text{Hz}$ near the abundance discontinuity at the edge of the partially mixed zone ($r = 2.3 \times 10^9$ cm in Figure 2.14). The eigenfunctions of the ‘trapped’ mode ($n = -128$; magenta) has been rescaled by a factor of 0.1 for clarity. Right panel: Échelle diagram with $\Delta P_{\text{éch}} = 315$ s. This model has $\Delta\Pi_1 = 281$ s, but if the calculation includes only the region exterior to the discontinuity then $\Delta\Pi_1 = 315$ s.

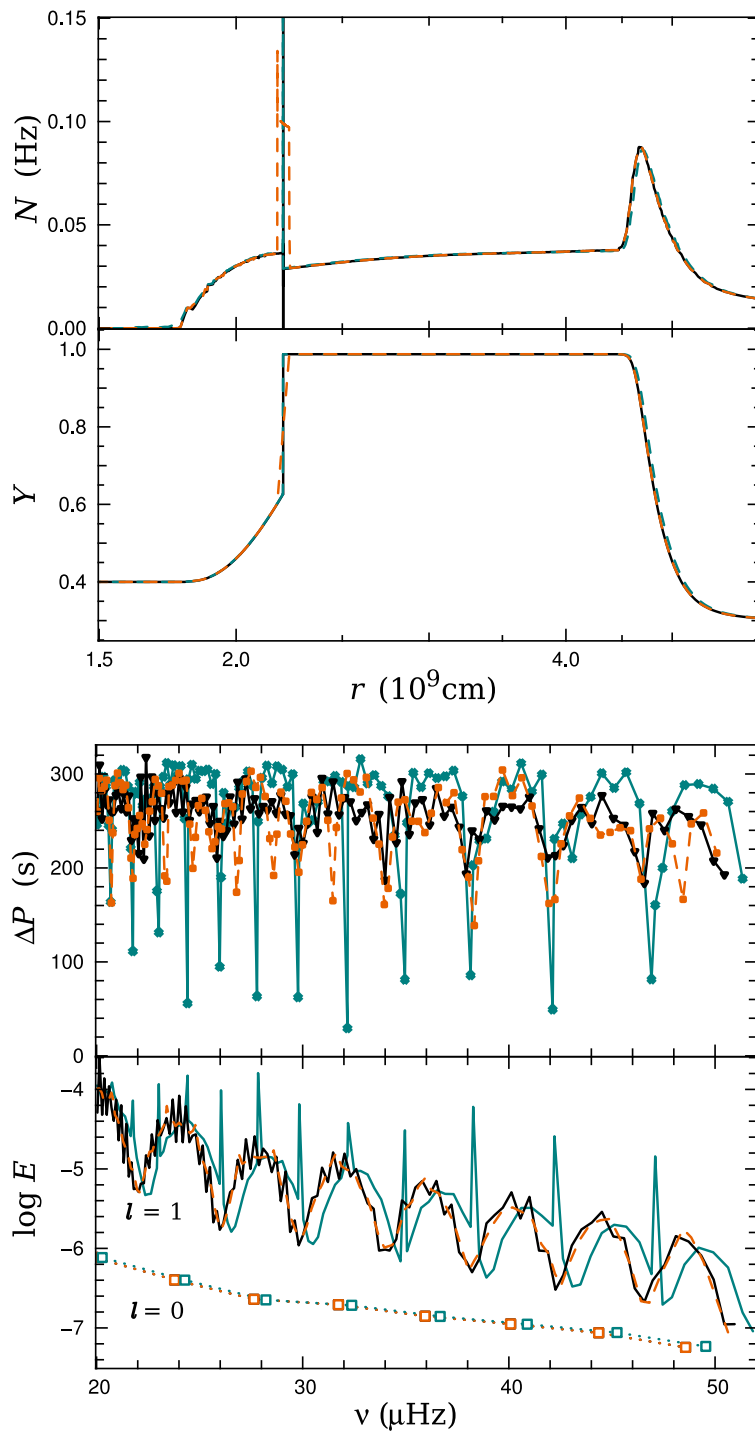


Figure 2.16: Pulsation properties of a $1 M_{\odot}$ classical semiconvection model with exactly $\nabla_{\text{rad}} = \nabla_{\text{ad}}$ outside the convective core (black) and otherwise identical models where the composition discontinuity at the outer edge of the semiconvection region has been smoothed over $0.01 M_{\odot}$ (orange dashes) and $2 \times 10^{-4} M_{\odot}$ (cyan). The region beyond the semiconvection zone has been homogenized in each model (see Section 2.3.2). The model without smoothing has $\Delta\Pi_1 = 273$ s, the model with fine smoothing has $\Delta\Pi_1 = 271$ s, and the model with broad smoothing has $\Delta\Pi_1 = 264$ s. These models have approximately $R = 10.4 R_{\odot}$, $T_{\text{eff}} = 4640$ K, and $\nu_{\text{max}} = 28 \mu\text{Hz}$.

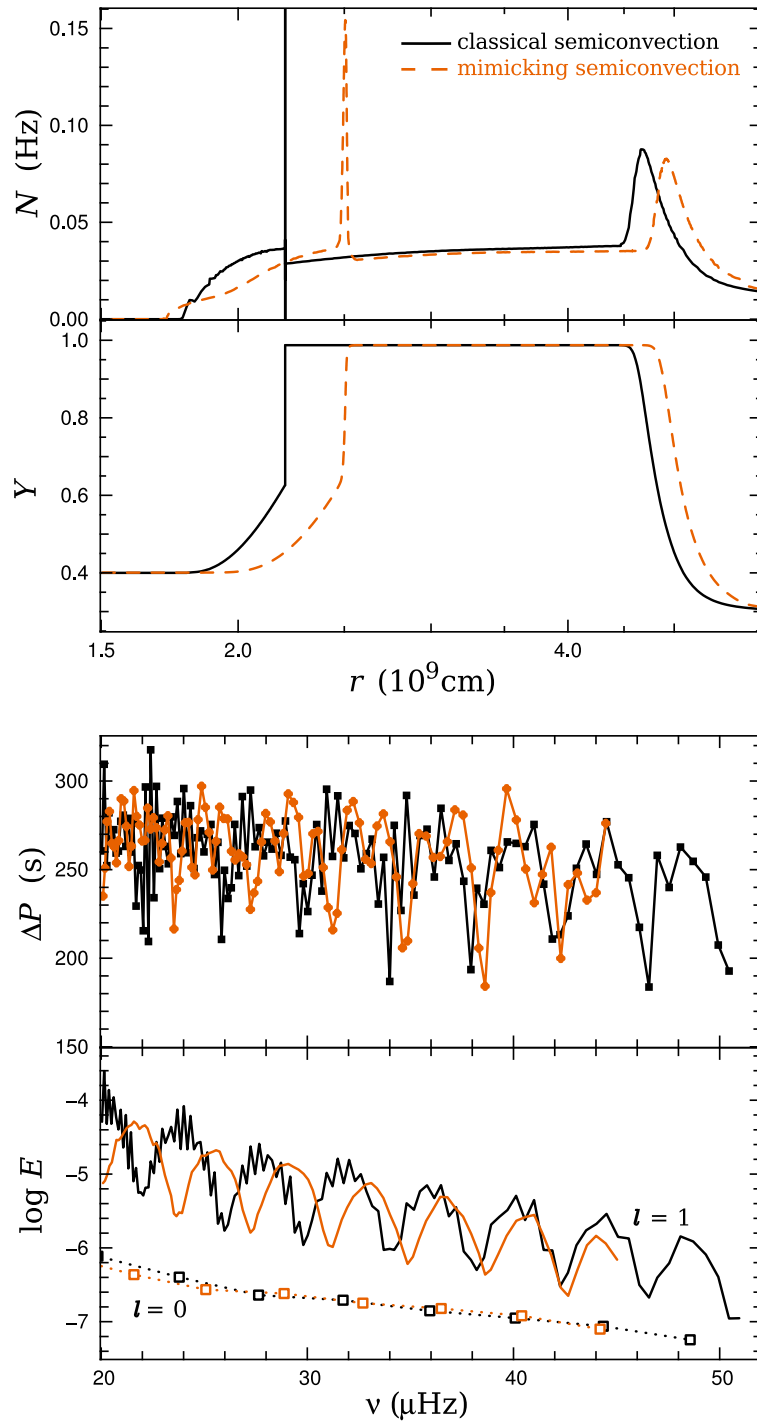


Figure 2.17: Comparison between the pulsation properties of a $1 M_{\odot}$ model with the classical semiconvection with exactly $\nabla_{\text{rad}} = \nabla_{\text{ad}}$ outside the convective core (black) and a model produced by the evolution code using our new mixing scheme (orange; described in Section 2.3.3). The region beyond the semiconvection zone has been homogenized in both models. The classical semiconvection model has $\Delta\Pi_1 = 273$ s while the model from the evolution code has $\Delta\Pi_1 = 268$ s. The model from the evolution code has $R = 11.1 R_{\odot}$, $T_{\text{eff}} = 4600$ K, and $\nu_{\text{max}} = 31 \mu\text{Hz}$ (see Figure 2.16 for the properties of the other model).

still enough to clearly add a periodicity to the period spacing (with $\Delta n \simeq 5$; Figure 2.17). This is consistent with Equation 2.19 because exactly 20 per cent of the total buoyancy radius is contained within the partially mixed zone.

Models with maximal overshoot

The structure of the maximal-overshoot models is very similar to the no-overshoot models except that the convective core is larger (Figure 2.2). There is no mixing beyond the convection zone by design. One difference is that the growth of the core can eradicate some of the remnants of the previous core-flash burning. Overall, the period spacing pattern is similar to the no-overshoot models (Figure 2.13). Importantly for the $\Delta\Pi_1$ discrepancy, however, the larger convective core also increases the mean ΔP , while modes of the same radial order have a lower frequency.

2.4.5 Matching ensemble $\Delta\Pi_1$ observations

In this section we compare the inferred $\Delta\Pi_1$ from the population of *Kepler* field stars with predictions from evolution models. We have chosen two representative masses: $1 M_\odot$ which experiences typical evolution for a red clump star (due to the uniformity of H-exhausted core mass at the flash), and $2.5 M_\odot$ which is massive enough to undergo core He-ignition in non-degenerate conditions (i.e. avoid the core flash) and then move to the so-called secondary clump in the HR diagram. We compare the models and observations with probability density functions $P(\Delta\Pi_1)$ constructed by the addition of Gaussian functions according to

$$P(\Delta\Pi_1) = \frac{1}{N} \sum_{i=1}^N \frac{1}{\sigma\sqrt{2\pi}} \exp\left[-\frac{(\Delta\Pi_1 - \Delta\Pi_{1,i})^2}{2\sigma^2}\right], \quad (2.20)$$

where $\Delta\Pi_{1,i}$ represent each value from observations, or in the case of models, calculations at 1 Myr intervals, and N is the total of number of observations or calculated values. We use a standard deviation of $\sigma = 4$ s and $\sigma = 8$ s for the $1 M_\odot$ and $2.5 M_\odot$ cases, respectively (Figures 2.18 and 2.19).

In the $1 M_\odot$ case the maximal-overshoot models have the highest $\Delta\Pi_1$, followed by the standard-overshoot, semiconvection, and no-overshoot models. The spreads of the $\Delta\Pi_1$ probability density functions for the semiconvection and overshoot cases are smaller than is observed, and offset to lower values, as shown in Figure 2.18. In contrast, the spread for the maximal-overshoot $1 M_\odot$ model appears too broad, especially considering that we have computed single evolution sequences rather than a population which would widen the distribution.

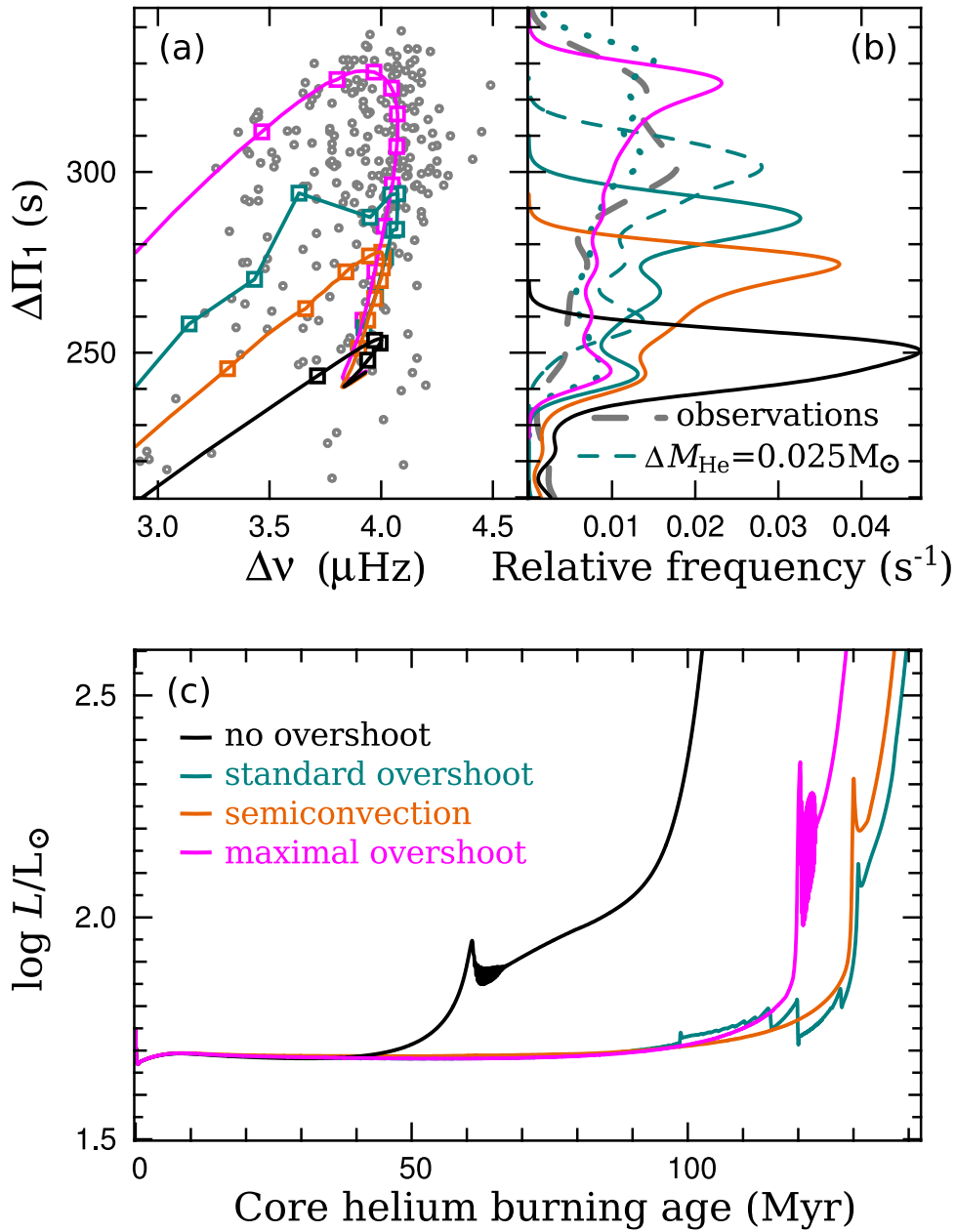


Figure 2.18: Upper left panel: evolution of $1 M_\odot$ CHeB models with different mixing schemes (no overshoot, standard overshoot, semiconvection, and maximal overshoot; in black, cyan, orange, and magenta respectively) in the $\Delta\nu - \Delta\Pi_1$ plane. Markers are at 10 Myr intervals. Determinations for *Kepler* field stars (grey dots) are from Mosser et al. (2014), and are limited to those with reported mass $0.8 < M/M_\odot < 1.25$. Upper right panel: probability density functions (Equation 2.20) for models in the upper left panel (same colours), standard overshoot with $\Delta\Pi_1$ computed using only the region outside the partially mixed zone (cyan dots), standard overshoot with increased M_{He} (cyan dashes), and observations (grey dashes). Lower panel: surface luminosity evolution for the models in the upper left panel.

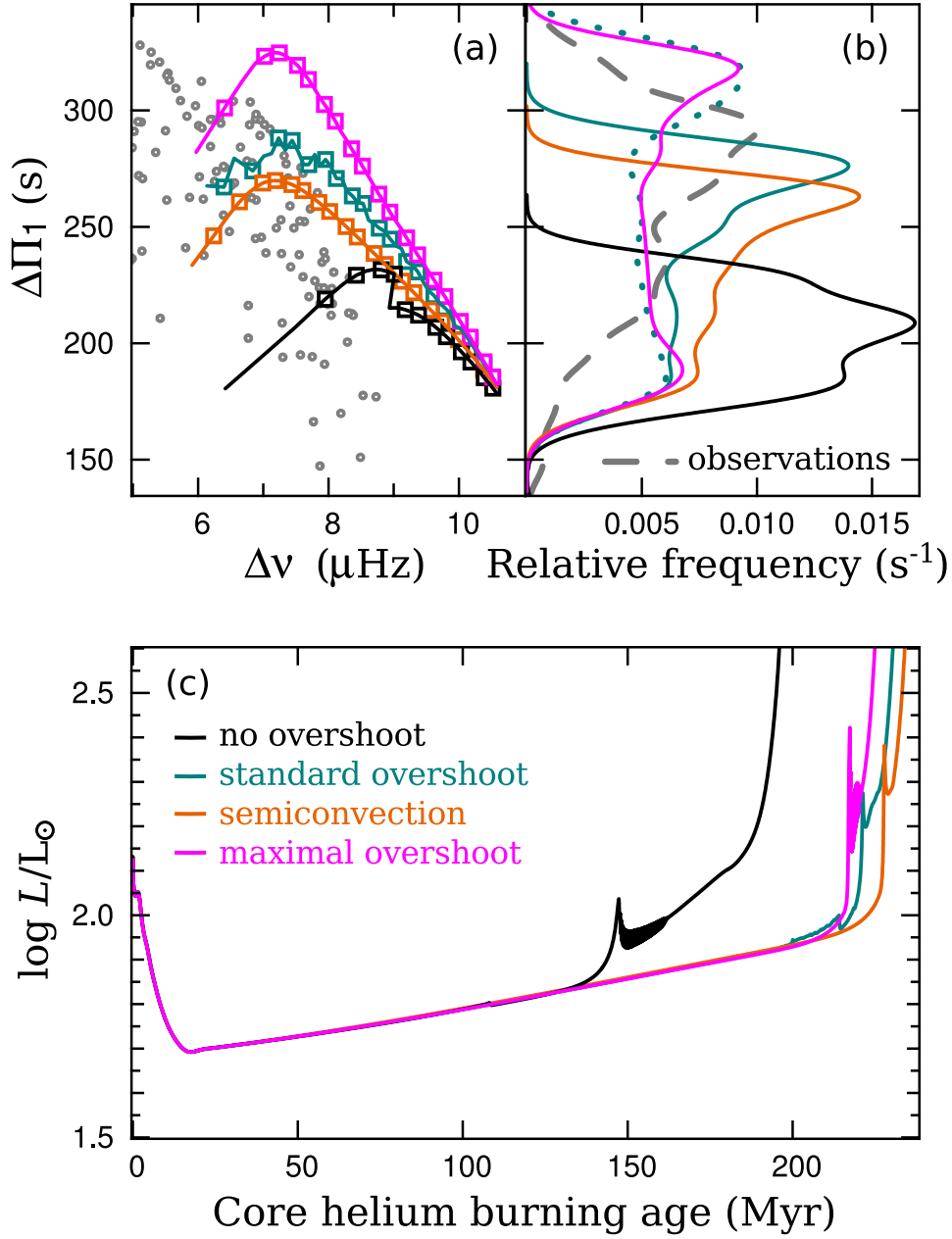


Figure 2.19: Upper left panel: evolution of $2.5 M_\odot$ CHeB models with different mixing schemes (no overshoot, standard overshoot, semiconvection, and maximal overshoot; in black, cyan, orange, and magenta respectively) in the $\Delta\nu - \Delta\Pi_1$ plane. Markers are at 10 Myr intervals. Determinations for *Kepler* field stars (grey dots) are from Mosser et al. (2014), and are limited to those with reported mass $2 < M/M_\odot < 3$. Upper right panel: probability density functions (Equation 2.20) for models in the upper left panel (same colours), observations (grey dashes), and standard-overshoot model with $\Delta\Pi_1$ computed using only the region outside the partially mixed zone (cyan dots). Lower panel: surface luminosity evolution for the models in the upper left panel.

Every one of the four low-mass models appears to spend too much time with a low $\Delta\Pi_1$. Two possible resolutions are (i) an increased H-exhausted core mass at the flash, which increases $\Delta\Pi_1$ (dashed lines in Figures 2.8 and 2.18), or (ii) that there is a difficulty in observationally determining $\Delta\Pi_1$ for stars that have recently begun CHeB (discussed in Section 2.4.3). Both of these affect the beginning of the CHeB, when $\Delta\Pi_1$ is lowest. The fact that this discrepancy exists even for the maximal-overshoot run, when the convective core is the largest possible, suggests that the treatment of convective boundaries cannot be the sole reason for it. In addition, Figure 2.19 shows that there is no evidence that this problem exists for any of the higher-mass models. These more massive models do not experience the core flash, do not ascend the RGB to as high luminosity, and have more luminous hydrogen burning at the beginning of the CHeB phase, and thus would be unaffected by the proposed resolutions. In Figure 2.18 the appearance of the discrepancy at low $\Delta\Pi_1$ is worsened for the semiconvection and standard-overshoot runs by the slow decrease in $\Delta\Pi_1$ towards the end of CHeB. This alone cannot explain the discrepancy, however, because it is still present for sequences that do not undergo this slow drop in $\Delta\Pi_1$ late in CHeB (e.g. the dotted curve in Figure 2.18; discussed later in this section).

The maximal-overshoot model is the only one of the four with different mixing prescriptions that can reach $\Delta\Pi_1$ values consistent with the bulk of the low-mass observations. Among the remaining cases, the standard-overshoot model is closest to the observations. The shape of its $\Delta\Pi_1$ probability density function also looks reasonable, except that it is offset by at least 25 s. Even a substantial increase in the H-exhausted core mass $\Delta M_{\text{He}} = 0.025 M_{\odot}$ (the most permitted by Catelan et al. 1996) at the start of CHeB is not enough to match the entire observed $\Delta\Pi_1$ range. In that case it shifts the $\Delta\Pi_1$ probability density function higher by around 20 s.

The $1 M_{\odot}$ semiconvection sequence has a lower $\Delta\Pi_1$ than our standard-overshoot case, by around 10 s. This is despite the similar evolution of R_{cc} and M_{He} which strongly influence $\Delta\Pi_1$ (see Section 2.4.2). It is also evident from Figure 2.2 that the evolution of the size of the partially mixed region is similar for both sequences. We therefore attribute the difference in $\Delta\Pi_1$ to the way the composition always varies smoothly in the semiconvection case, increasing N over a large interval in radius instead of over sharp spikes.

We have performed an explicit test of the effect of the steepness of composition profiles on $\Delta\Pi_1$. The three models in Figure 2.16 are identical except for the composition near the edge of the semiconvection zone at $r \simeq 2.2 \times 10^9$ cm. The buoyancy frequency is nearly identical elsewhere in the structure (Figure 2.16b) so any difference in $\Delta\Pi_1$ must be due to the composition smoothing. In this case, smoothing the discontinuity over

$\Delta m = 0.01 M_{\odot}$ decreases $\Delta\Pi_1$ by 9 s.

This effect is also apparent in Figure 2.20, where smoothing the edge of the fully mixed core increases $\Delta\Pi_1$. It can be seen in panel (a) that this smoothing increases the width of the peak in N (in the log scale) by more than it reduces its height. This increases the area under the curve, which reduces $\Delta\Pi_1$. This is evident when we rewrite the integral in the asymptotic solution for $\Delta\Pi_{\ell}$ in terms of $\log r$ to get

$$\Delta\Pi_{\ell} = \frac{2\pi^2}{\sqrt{\ell(\ell+1)}} \left[\int \frac{N}{r} dr \right]^{-1} = \frac{2\pi^2}{\sqrt{\ell(\ell+1)}} \left[\int N d \ln r \right]^{-1}. \quad (2.21)$$

The $1 M_{\odot}$ sequence without overshoot has the lowest $\Delta\Pi_1$. $\Delta\Pi_1$ stays around 250 s, around 50 s below the bulk of the observations, for the entire CHeB phase. This can be attributed to the lack of growth of the convective core (Figure 2.8c). The evolution of $\Delta\Pi_1$ in our $1 M_{\odot}$ and $2.5 M_{\odot}$ sequences without overshoot is almost identical to the corresponding models (also without overshoot) from MESA (Stello et al., 2013).

We have emulated the effect of mode trapping on the more easily observable (non-trapped) modes in the standard-overshoot models (discussed in Section 2.4.4) by excluding the partially mixed region from the calculation of $\Delta\Pi_1$ (dotted curve in Figure 2.18b). The impact of this is increasingly significant as CHeB progresses and the partially mixed region grows. This makes the $\Delta\Pi_1$ evolution very similar to that resulting from the maximal-overshoot scheme, except that it slightly exceeds the observed values (by less than 10 s) near the end of CHeB. However, this is late in CHeB when this crude approximation of the effects of mode trapping is least valid, because the mode trapping cavity, and consequently the fraction of modes that become trapped, is large (making a neat fit in the period échelle diagram difficult; see Section 2.4.9). At the other extreme, $\Delta\Pi_1$ is still too low in the early stages of CHeB compared to the observations.

The CHeB lifetime of the $1 M_{\odot}$ no-overshoot model is by far the shortest, followed by the maximal-overshoot case (Figure 2.18c). The semiconvection and overshoot sequences have nearly identical lifetimes. The surface luminosity of the models is independent of the mixing scheme when they are still burning helium in the core (the variation in $\log L/L_{\odot}$ is less than 0.01). The relative energy generation rates from hydrogen and helium burning differ by a little more. The semiconvection model has more luminous H burning than the other sequences, while the no-overshoot model has the most luminous He burning, and the standard-overshoot and maximal-overshoot sequences are almost identical until the occurrence of a core breathing pulse after 98 Myr.

Star counts in globular clusters can be used as a constraint on the mixing scheme. This

is because the CHeB lifetime is dependent on the amount of helium that is transported into the core. Models that consume less helium during CHeB have more helium that must be burnt during subsequent shell helium burning, and consequently have a longer early-AGB lifetime (compare the swift exit from the red clump of the no-overshoot sequence with its sluggish ascent of the early-AGB in Figure 2.18c). The parameter $R_2 = n_{\text{AGB}}/n_{\text{CHeB}}$ (the number ratio of observed AGB to CHeB stars) for globular clusters is thought to correspond to the ratio of the respective phase lifetimes. Caputo et al. (1989) argued that models with semiconvection, but without breathing pulses, give the best fit to observations of the globular cluster M5. In their models, the suppression of breathing pulses (by not allowing the growth in the convection zone if it would increase the central helium abundance) increased R_2 from 0.10 to 0.14 or 0.15 (depending on the extent of core-flash burning), matching observations.

We have computed R_2 for our models by considering luminosity bins comparable to the observed range in metal-rich globular clusters. We have defined the CHeB lifetime to be when $\log L/L_\odot$ is within 0.1 of its mean value before core helium depletion, and the AGB to be when $\log L/L_\odot$ is no more than 1.0 higher than the CHeB range. We find values of $R_2 = t_{\text{AGB}}/t_{\text{CHeB}}$ of 0.110, 0.113, and 0.117 for the standard-overshoot, semiconvection, and maximal-overshoot schemes respectively. This would make them practically indistinguishable from one another by observations of star clusters. In contrast, the no-overshoot model has $R_2 = 0.743$, which is a difference that could easily be detected. We will address constraints from star counts in the next paper in this series (by computing less massive and more metal-poor models relevant to Galactic globular clusters; Harris 1996).

There are a number of common trends between the $1 M_\odot$ (Figure 2.18) and $2.5 M_\odot$ (Figure 2.19) models. In the $2.5 M_\odot$ runs the mixing scheme has a very similar effect on mean $\Delta\Pi_1$, CHeB lifetime, and the H- and He-burning luminosity. We also find a very similar effect from our emulation of mode trapping in the standard-overshoot model (dotted curve Figure 2.19). The probability density functions for the $2.5 M_\odot$ models are very similar in shape to the those for the $1 M_\odot$ models, except that they cover a larger range of $\Delta\Pi_1$. The more substantial increase in $\Delta\Pi_1$ during their evolution can be explained by the greater extent of the growth of the H-exhausted core (roughly $0.2 M_\odot$ compared with $0.05 M_\odot$ for the $1 M_\odot$ runs), the importance of which was shown in Section 2.4.2.

Compared to the lower-mass case, the agreement with observations is markedly better for the $2.5 M_\odot$ sequences, with the exception of the no-overshoot model. The semiconvection and standard-overshoot models, however, still do not reach the highest $\Delta\Pi_1$ observations. In contrast, the $\Delta\Pi_1$ evolution for the mode trapping and maximal-overshoot

sequences match each other even more closely, and both exceed the highest observed values by considerably more than does the $1 M_{\odot}$ mode trapping case. The comparison between observations and models, however, is more complex than for the low-mass case. More of the increase in $\Delta\Pi_1$ is due to the growth of the H-exhausted core, and we are comparing the models to a population more diverse in mass and smaller in number. Therefore it would be imprudent to draw strong conclusions about the mixing from this sample. We note that our models do not match the observed $\Delta\nu$ (but do match the shape of the population's distribution in $\Delta\nu - \Delta\Pi_1$ space). This is not problematic because $\Delta\nu$ can easily be decreased by adjusting (in this case reducing) the MLT mixing length parameter, without affecting $\Delta\Pi_1$. Finally, we note that by the end of CHeB, the $2.5 M_{\odot}$ models are considerably more luminous than at the beginning (by around a factor of 2, apart from the shorter-lived no-overshoot model; Figure 2.19). This could introduce an observational bias for the secondary clump towards more luminous evolved stars, which have higher $\Delta\Pi_1$ (for all of the mixing schemes we have examined). Accounting for such a bias would help to resolve the excess of predicted low- $\Delta\Pi_1$ stars that is apparent in Figure 2.19(b).

In Section 2.4.4 we demonstrated how mode trapping may lead to an overestimation of $\Delta\Pi_1$. This is made possible because only a subset of mixed modes can be detected. Here we briefly consider how mode trapping affects the period spacing between the pairs of modes that are most likely to be detected, i.e. those with low inertia. For this, we compare a standard-overshoot model with mode trapping (Figure 2.14) to a maximal-overshoot model without mode trapping (Figure 2.13). Although these two models have different $\Delta\Pi_1$ (281 s and 314 s, respectively), the respective values determined from the period échelle diagram, $\Delta P_{\text{ech}} = 315$ s (Figure 2.15) and $\Delta P_{\text{ech}} = 316$ s, are nearly identical. The average ΔP between all modes with $20 \mu\text{Hz} < \nu < 40 \mu\text{Hz}$ for the standard-overshoot model is 270 s, which increases to 293 s if all of the (presumably undetectable) trapped modes are excluded, compared with 295 s for the maximal-overshoot model. When this calculation is restricted to the six pairs of modes closest to each low inertia trough (e.g., near $\nu = 24 \mu\text{Hz}$ in Figure 2.14) we find $\Delta P = 275$ s and $\Delta P = 277$ s for the standard-overshoot and maximal-overshoot models, respectively. If we restrict the count to sets of four pairs of low-inertia modes instead of six we again find that the two models have a similar average ΔP , except that it is reduced further, by 9 s in both cases. Moreover, the average frequency spacing between these troughs is the same for both models. This indicates that knowing the typical observed ΔP would not assist with the detection of mode trapping. It also supports our suggestion in Section 2.4.4 that modes that are not trapped behave as though the buoyancy cavity is smaller than its true size, i.e. it excludes the semiconvection/partially mixed region with $N^2 > 0$ that is surrounded by a

steep composition gradient that can trap modes. Because the observationally determined ΔP depends on how many modes are detected it is difficult to compare these results to the average or median ΔP found in populations of CHeB stars (e.g. Mosser et al., 2011; Stello et al., 2013).

2.4.6 The effect of the boundary of the convective core on pulsations

In Figure 2.20 we examine the pulsations resulting from a structure with a fully mixed convective core but with a smooth composition profile at its boundary. This structure (which was produced by artificially smoothing according to Equation 2.17) is interesting because of the physical implausibility of the core boundary in the maximal- and no-overshoot models (e.g. the magenta and black lines in Figure 2.3b). In these models there is a true composition discontinuity where material that is strongly convectively unstable ($\nabla_{\text{rad}} \gg \nabla_{\text{ad}}$) does not partially mix with the material directly adjacent to it.

All four models in Figure 2.20 with different composition profiles have a comparable period spacing over much of the frequency range shown. The model in black with the largest partially mixed region ($\Delta m = 0.01 M_{\odot}$), however, has several frequency ranges where the modes are more closely spaced (e.g., at around 35 and 45 μHz). This behaviour is also seen near $\nu = 38 \mu\text{Hz}$ and $\nu = 36 \mu\text{Hz}$, for the models with $\Delta m = 0.002 M_{\odot}$ and $\Delta m = 5 \times 10^{-4} M_{\odot}$, in orange and cyan, respectively.

These interruptions to the regular ΔP pattern shown in Figure 2.20(c) are more prevalent when the composition is smoother. This can be explained by the increasing buoyancy radius (see Section 2.4.2) of the mode trapping region enclosed by smoother composition gradients (detailed in Section 2.4.5). This trapping region is adjacent to the convective core, however, so it always has a small buoyancy radius and therefore has little effect on mode inertia (Figure 2.20d). This small buoyancy radius of the trapping region also explains the long periodicity (in radial order) in its effect on ΔP , because this gives a large Δn according to Equation 2.19. This contrasts with standard-overshoot and semiconvection models (e.g. Figures 2.14 and 2.16), where a similar buoyancy feature is surrounded on both sides by a g-mode cavity which triggers mode trapping at regular intervals in radial order n with smaller Δn . Finally, we note that the disruption to the regular period spacing caused by a composition gradient at the edge of the convective core appears most obvious for gravity-dominated modes, which are the most difficult to detect.

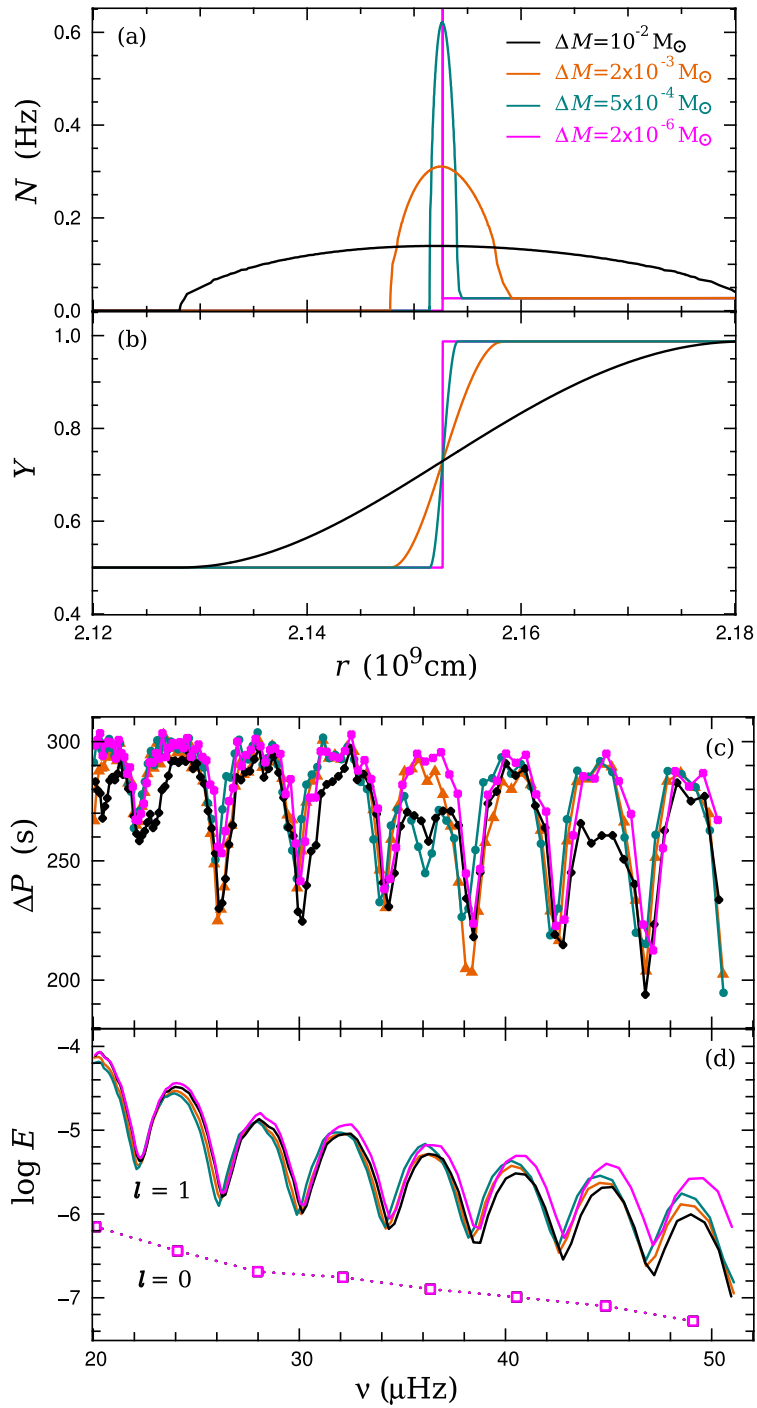


Figure 2.20: Pulsation properties of $1 M_{\odot}$ models with a small partially mixed regions outside the convective core. In all four cases the composition profile in the overshoot region has been set according to Equation 2.17 with $\Delta m/M_{\odot}$ values of 2×10^{-6} , 5×10^{-4} , 0.002, and 0.01 in magenta, cyan, orange, and black, respectively. In the same order $\Delta \Pi_1$ is 287 s, 294 s, 297 s, and 300 s. The composition between the convective core and H-burning shell has been homogenized. These models have approximately $R = 10.4 R_{\odot}$, $T_{\text{eff}} = 4770$ K, and $\nu_{\text{max}} = 29 \mu\text{Hz}$.

2.4.7 Subdwarf B models

We have also tested the effect of the core mixing scheme in sdB models. At the beginning of CHeB in these runs we homogenized the composition between the H-shell and the convective core to remove traces of core-flash burning. In each model we also set the helium mass fraction Y , at the H-exhausted core boundary according to

$$Y(m) = Y_{\text{surf}} + \frac{\Delta Y}{2} \left\{ 1 + \cos \left[\left(\frac{m - M_{\text{He}}}{\Delta m} \right)^2 \pi \right] \right\}, \quad (2.22)$$

where ΔY is the difference between the surface and interior helium abundance, M_{He} is the mass of the H-exhausted core, m is the mass coordinate, and we have chosen $\Delta m = 0.002 M_{\odot}$. We chose this smooth profile because we are only interested in the effect of the composition profile at the boundary of the convective core. We set the total mass and mass of the shell to match the mass, gravity, and effective temperature typical of the stars in the Reed et al. (2011) sample. This ad hoc approach is obviously inadequate for precision studies of particular stars (e.g., those found in Charpinet et al., 2011; Van Grootel et al., 2013a), but suits our purpose here.

The results of the pulsation calculations for the four models with different mixing schemes are presented in Figure 2.21. The appearance of the ΔP pattern for each model is broadly similar, except for a few trapped modes in the standard-overshoot model (Figure 2.21). These modes have much higher inertia than their neighbours and are more closely spaced in period. This behaviour is similar to our red clump standard-overshoot model (Figure 2.14) and the semiconvection model that includes a region with a stabilizing molecular weight gradient at the edge of the semiconvection zone (Figure 2.16).

There is a substantial difference in the mean ΔP between the four different mixing cases. ΔP spans a range of around 60s, with the no-overshoot sequence having the lowest average value, followed by the semiconvection case, then the maximal-overshoot and standard-overshoot cases (if the trapped-modes are excluded). Like its more massive counterparts, the sequence without overshooting has a lower $\Delta \Pi_1$ than is observed. In this case it is more than 10s too low to match any of the observations reported by Reed et al. (2011), which is an especially strong constraint because the model in Figure 2.21 is from the stage of CHeB when $\Delta \Pi_1$ is near its maximum. The range of ΔP between pairs of modes found for KIC 5807616 spans less than 30s (Reed et al., 2011) which is consistent with the range for our models (except near the high-inertia modes in the standard-overshoot case).

Recently, Østensen et al. (2014) found evidence for mode trapping in KIC 10553698A, an sdB star in the *Kepler* field, by classifying $\ell = 1$ and $\ell = 2$ modes. They identified both the C-O/He and He/H transition zones as possible origins of the mode trapping

and highlighted the resemblance of the period spacing pattern to existing theoretical calculations, e.g. Figure 3 in Charpinet et al. (2002). Due to the use of $q = \log [1 - m/M]$ for the horizontal axis of that figure, the structure near the core is difficult to discern, but it appears that in their ‘evolutionary model’ there is a relatively smooth buoyancy peak near where partial mixing can occur in our models. In our standard-overshoot model the mode trapping is certainly a result of the sharp composition gradient at the edge of the partially mixed zone outside the convective core. Moreover, that model’s pulsations bear perhaps an even more remarkable similarity to the observations shown in grey in Figure 2.21 (keeping in mind we made no attempt to match the frequencies). The trapped modes in our model, however, reside deep within the core, so their observability is uncertain. Finally, the theoretical ΔP for our non-trapped modes is nearly an exact match for the ΔP between most observed modes in KIC 10553698A, which suggests that the size of the convective core in the standard-overshoot model is reasonable.

We have also examined the effect of core-flash phase burning on the pulsations in our sdB models. In Figure 2.22 we demonstrate that this effect is strongly dependent on the smoothness of the remaining composition profile. The four models that we use to test this include a model without the discontinuity from the core flash (constant composition), and others with sine wave composition profiles (Equation 2.17), with Δm set as $0.01 M_{\odot}$, $0.001 M_{\odot}$, and $10^{-6} M_{\odot}$. The consequences for the computed frequencies are increasingly apparent for models with sharper composition profiles. The mode period spacing and inertia for the model with the smoothest composition profile (spread over $0.01 M_{\odot}$) is nearly identical to the model with a constant composition. By comparison, the model with the chemical profile spread over $0.001 M_{\odot}$ shows up to four times the period spacing variation for high frequency modes ($P < 1.3 \times 10^4$ s) and mode to mode variation of almost 100 s at lower frequency (where the two smoother models show almost constant ΔP). The model with the sharpest composition profile shows a pattern similar to the $\Delta m = 0.001 M_{\odot}$ case, except with more extreme variation in ΔP . In both cases the amplitude of this variation oscillates, with a period of around 1.8×10^4 s. We also note the similarity between the period spacing pattern of these two models and the model by Charpinet et al. (2014).

Overall, these results suggest that the possibility of using pulsations to determine whether a low-mass CHeB star has experienced the core flash depends principally on how discontinuous is the composition profile it has left behind.

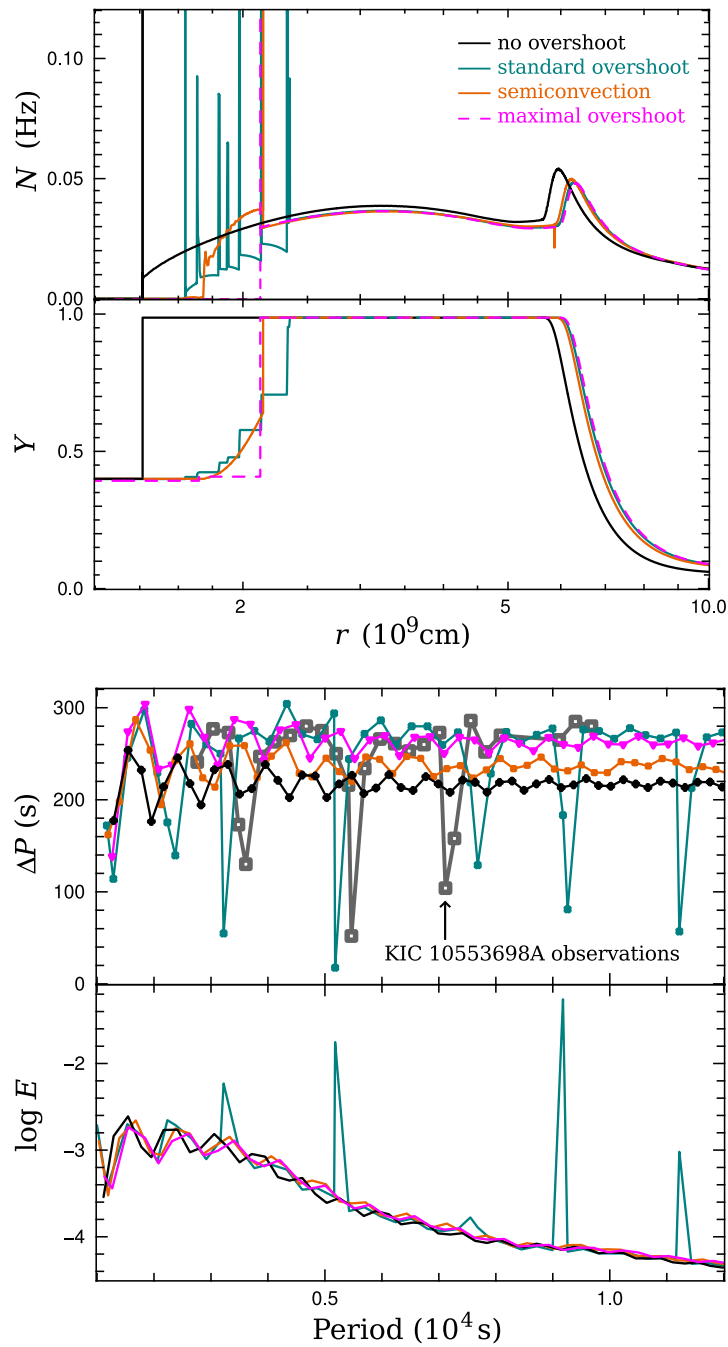


Figure 2.21: Seismic properties of synthetic sdB models and an observed pulsator in the *Kepler* field. Upper panels: Brunt-Väisälä frequency N and helium mass fraction Y for models with different mixing prescriptions. Lower panels: $\ell = 1$ mode spacing ΔP and inertia. The observations are of $\ell = 1$ modes classified by Østensen et al. (2014) for KIC 10553698A (thick grey lines and squares). The models were generated according to the method outlined in Section 2.4.7. They have $M = 0.475 M_{\odot}$, solar metallicity, and $Y_{\text{cent}} = 0.4$. The models have no overshoot (black), standard overshoot (cyan), semiconvection (orange), and maximal overshoot (magenta). These models have $\Delta\Pi_1$ of 222 s, 245 s, 238 s, and 269 s, respectively, and approximately $R = 0.20 R_{\odot}$ and $T_{\text{eff}} = 27000$ K.

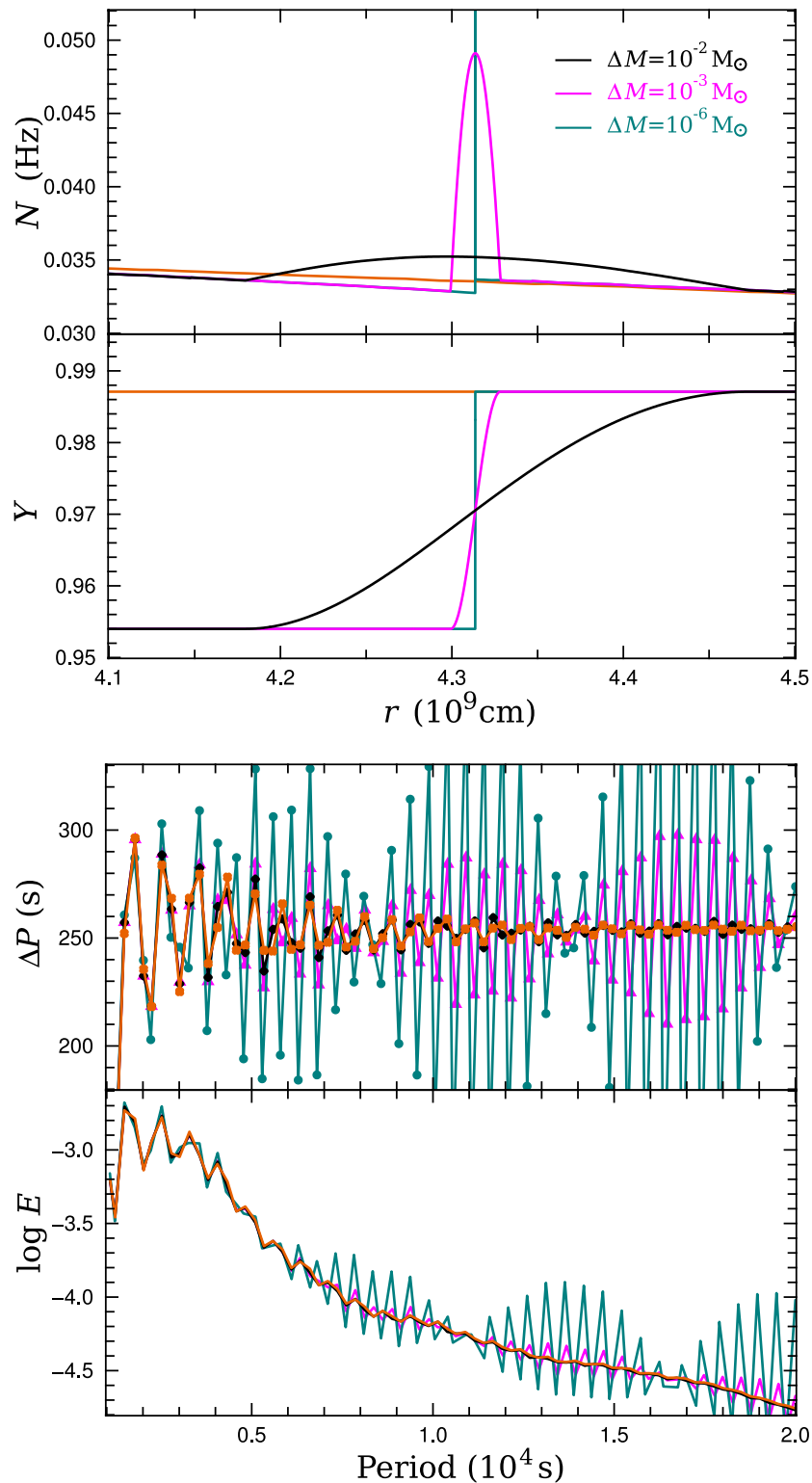


Figure 2.22: Comparison of the pulsation properties of sdB models with different composition discontinuities left behind by the core flash. One model (orange) has a constant composition between the convective core and the H-burning shell. The models in black, magenta, and cyan have chemical gradients over $0.01 M_{\odot}$, $0.001 M_{\odot}$, and $10^{-6} M_{\odot}$, respectively. Each composition profile is set according to Equation 2.17. These models have $R = 0.20 R_{\odot}$ and $T_{\text{eff}} = 27400$ K.

Table 2.1: Properties of the evolution sequences. The models have standard overshoot (SO), no overshoot (NO), semiconvection (SC), and maximal overshoot (MO). The triple- α and $^{12}\text{C}(\alpha, \gamma)^{16}\text{O}$ reaction rates are denoted by $r_{\text{C}\alpha}$ and $r_{3\alpha}$, respectively. $\Delta\Pi_{1,\text{mean}}$ is the average $\Delta\Pi_1$ value in the CHeB phase which has duration τ_{CHeB} . The initial and final H-exhausted core masses for the CHeB phase are denoted by $M_{\text{He},i}$ and $M_{\text{He},f}$ respectively.

Model notes	M (M_{\odot})	Mixing	$\Delta\Pi_{1,\text{mean}}$ (s)	τ_{CHeB} (Myr)	$M_{\text{He},i}$ (M_{\odot})	$M_{\text{He},f}$ (M_{\odot})
. . .	1	SO	267	135.0	0.466	0.503
. . .	1	SC	258	129.6	0.467	0.503
. . .	1	NO	204	79.5	0.467	0.499
. . .	1	MO	293	119.7	0.467	0.499
. . .	2.5	SO	232	221.1	0.331	0.509
. . .	2.5	SC	225	227.5	0.331	0.514
. . .	2.5	NO	182	170.0	0.331	0.475
. . .	2.5	MO	251	216.8	0.331	0.502
$\Delta M_{\text{He}} = 0.025 M_{\odot}$	1	SO	285	99.8	0.493	0.520
$\Delta M_{\text{He}} = 0.025 M_{\odot}$	1	MO	304	100.4	0.493	0.519
$r_{\text{C}\alpha}, r_{3\alpha} \times 2$	1	SO	276	137.5	0.462	0.494
$r_{\text{C}\alpha} \times 2$	1	SO	275	132.8	0.466	0.503
$r_{3\alpha} \times 2$	1	SO	270	119.9	0.462	0.491
$Y + 0.1$	1	SO	272	112.0	0.448	0.548
$[\text{Fe}/\text{H}] - 1.0$	1	SO	285	112.4	0.467	0.523

2.4.8 Dependence on input physics

In Section 2.4.2 we showed that $1 M_{\odot}$ standard-overshoot models need an increase in the H-exhausted core mass at the flash of more than $\Delta M_{\text{He}} > 0.025 M_{\odot}$ to match the range of $\Delta \Pi_1$ reported for low-mass CHeB stars by Mosser et al. (2014). The effect of uncertainties in the input physics on M_{He} at the core flash has been examined in detail previously (e.g. Catelan et al., 1996). Some of these uncertainties are not important to subsequent CHeB evolution. For instance, the expansion of the core during the flash phase decreases both its rotation rate and neutrino emission so these effects need only be considered in light of how they affect the core mass at the flash. In contrast, helium burning reaction rates and initial composition also affect the later evolution, including $\Delta \Pi_1$ (Table 2.1).

Doubling the $^{12}\text{C}(\alpha, \gamma)^{16}\text{O}$ reaction rate increases the average $\Delta \Pi_1$ during CHeB by 8 s. Once there is enough carbon in the core ($X_{\text{C}} \gtrsim 0.1$) the $^{12}\text{C}(\alpha, \gamma)^{16}\text{O}$ reaction proceeds more efficiently, slowing the rate of increase of the central temperature and density (and therefore also the triple- α rate). This increases the convective core radius and consequently $\Delta \Pi_1$, but does not significantly affect the CHeB lifetime. In contrast, increasing the triple- α rate reduces the core temperature and density from the beginning of CHeB. Although this tends to increase $\Delta \Pi_1$, it is offset by the lower M_{He} , which starts smaller and grows more slowly due to the consequently reduced hydrogen-burning luminosity. This results in only a 3 s increase in the average $\Delta \Pi_1$ during the CHeB phase. In the relevant conditions the uncertainty in the triple- α rate is less than 15 per cent while for $^{12}\text{C}(\alpha, \gamma)^{16}\text{O}$ rate it is around 40 per cent (Angulo et al., 1999), and more recent data favour the lower limit (Xu et al., 2013). Taking both of these uncertainties into account, they could together only account for around a 5 s change in $\Delta \Pi_1$, considerably less than the size of the disparity between standard models and observations (of around 30 s).

We have also tested the consequences of varying the initial composition. Increasing helium raises the average $\Delta \Pi_1$, but the dependence is weak: a large increase of $\Delta Y = 0.1$ only increases the average $\Delta \Pi_1$ by 5 s. This may be attributed to the more rapid growth of the H-exhausted core during CHeB compared to the standard case, making it $0.04 M_{\odot}$ larger at core helium exhaustion. This is partly offset, however, by the lower H-exhausted core mass at helium ignition, limiting the increase in average $\Delta \Pi_1$. Reducing the metallicity by a factor of 10 increases the average $\Delta \Pi_1$ during the CHeB phase by 18 s. This is due to a reduction in the heavy element opacity (which we confirmed by evolving an $[\text{Fe}/\text{H}] = -1$ model but with solar heavy element opacity; which had a negligible effect on $\Delta \Pi_1$). This initially increases the helium burning rate and consequently $\Delta \Pi_1$. The hydrogen burning rate increases even more substantially, which further increases $\Delta \Pi_1$ by accelerating the growth of the H-exhausted core. Composition, however, is not likely to be

the cause of the $\Delta\Pi_1$ discrepancy because the stars in the Mosser et al. (2014) sample are typically around solar metallicity (Pinsonneault et al., 2014), consistent with the models in Section 2.4.5. Indeed, none of these factors, nor any reasonable combination of them, can explain why the $1 M_\odot$ standard-overshoot run fails to match the observations.

2.4.9 Late-CHeB and early-AGB models

A number of authors have identified possible late-CHeB and AGB stars in the *Kepler* field through seismology. Mosser et al. (2012) found five stars with the same $\Delta\nu$ as the low-mass CHeB group but with lower $\Delta\Pi_1$ (around 250 s) and posited that these stars have exhausted helium in their cores. Corsaro et al. (2012) identified several members of the open clusters in the *Kepler* field (NGC 6811, NGC 6819 and NGC 6791) that are likely to be evolved red clump stars because they have similar $\ell = 1$ ΔP to the majority of clump stars, but have lower $\Delta\nu$. In their examination of field stars, Kallinger et al. (2012) suggested that lower- $\Delta\nu$ stars belong to the early-AGB. These stars also have a distinct central radial ($\ell = 0$) mode phase shift, which can be attributed to a difference in the structure of the convective envelope (Christensen-Dalsgaard et al., 2014). Although it is not examined in this paper, it would be interesting to determine if and how this phase shift depends on the CHeB mixing scheme.

Our models disagree with the earlier suggestion by Mosser et al. (2012) that red clump stars with a low $\Delta\Pi_1$ but typical $\Delta\nu$ can be explained as being post-CHeB (they are now classified with the other red clump stars in Mosser et al. 2014). These are unlikely to be post-CHeB because every one of our low-mass models – irrespective of mixing scheme – shows a decrease in $\Delta\nu$ when $\Delta\Pi_1$ begins to decrease, which occurs prior to central helium exhaustion (Figure 2.8). This causes them to move away from the location of the suspected post-CHeB stars in $\Delta\nu - \Delta\Pi_1$ space (Figure 2.18a), which is in agreement with the MESA models without overshoot shown in Figure 4b in Stello et al. (2013).

In Figure 2.23 we show a standard-overshoot model before and after core helium exhaustion, separated by 160 kyr. During this period there is a rapid increase in luminosity ($\log L/L_\odot$ increases from 2.029 to 2.117), a decrease in $\Delta\nu$ (from $1.80 \mu\text{Hz}$ to $1.47 \mu\text{Hz}$), and a decrease in $\Delta\Pi_1$ (from 153 s to 99 s; it then drops to 65 s after a further 1 Myr). This sudden decrease in period spacing has also been shown for models computed with MESA (Stello et al., 2013). If the region enclosed by the outer edge of the partially mixed zone (dashed lines in Figure 2.23) is excluded from the calculation of $\Delta\Pi_1$ (to emulate the effect of mode trapping) the drop in period spacing is less severe (from 251 s to 234 s). This, however, still suggests that the high ΔP (~ 250 s) stars, identified as possible members of the AGB by Kallinger et al. (2012), are in fact still CHeB stars. Similarly, the relatively

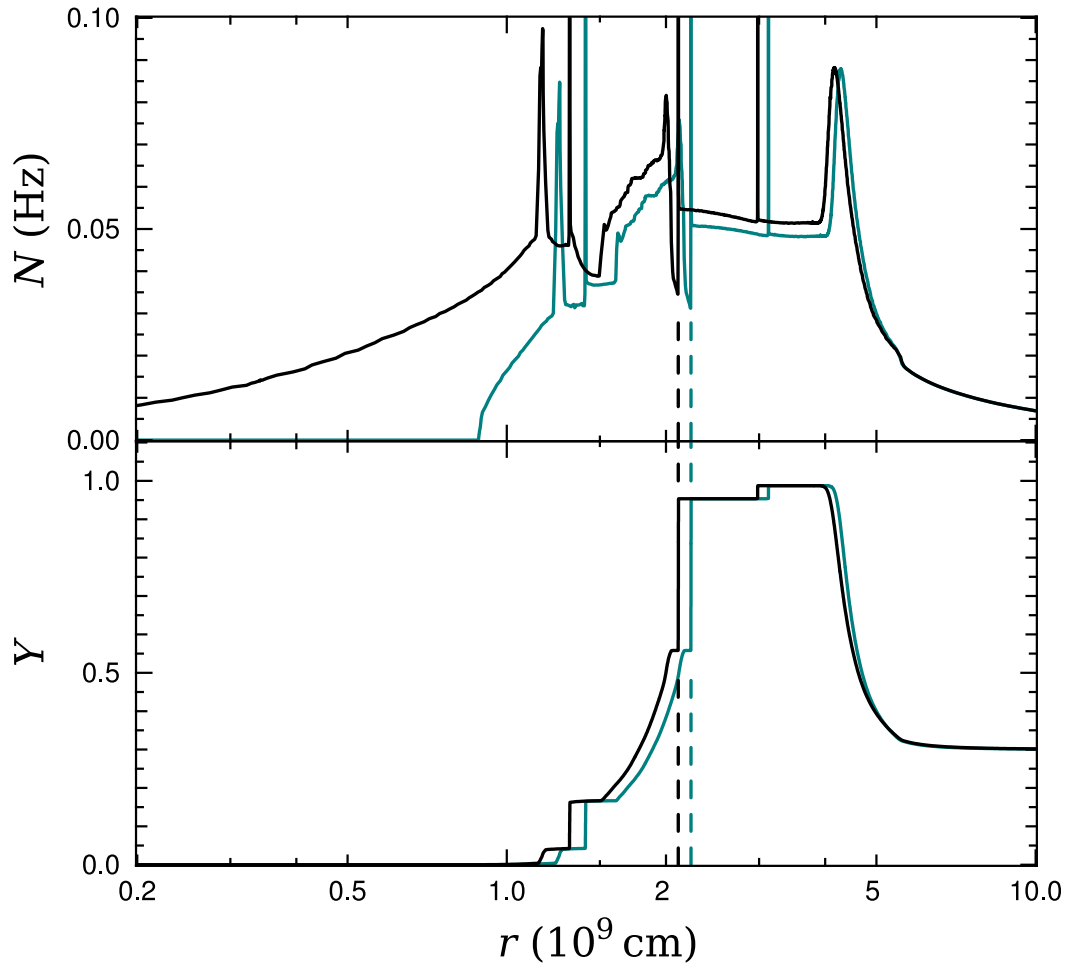


Figure 2.23: The Brunt–Väisälä frequency N (upper panel) and helium abundance Y (lower panel) for a $1 M_{\odot}$ solar-metallicity run with standard overshoot before (black) and after (cyan) core helium exhaustion. The first model has central helium abundance $Y_{\text{cent}} = 4 \times 10^{-4}$. Between the two models 160 kyr elapses. In this time $\Delta\Pi_1$ decreases from 153 s to 99 s, $\Delta\nu$ decreases from $1.80 \mu\text{Hz}$ to $1.47 \mu\text{Hz}$, radius increases from $18.9 R_{\odot}$ to $21.0 R_{\odot}$, T_{eff} decreases from 4300 K to 4250 K, and ν_{max} decreases from $9 \mu\text{Hz}$, to $7 \mu\text{Hz}$.

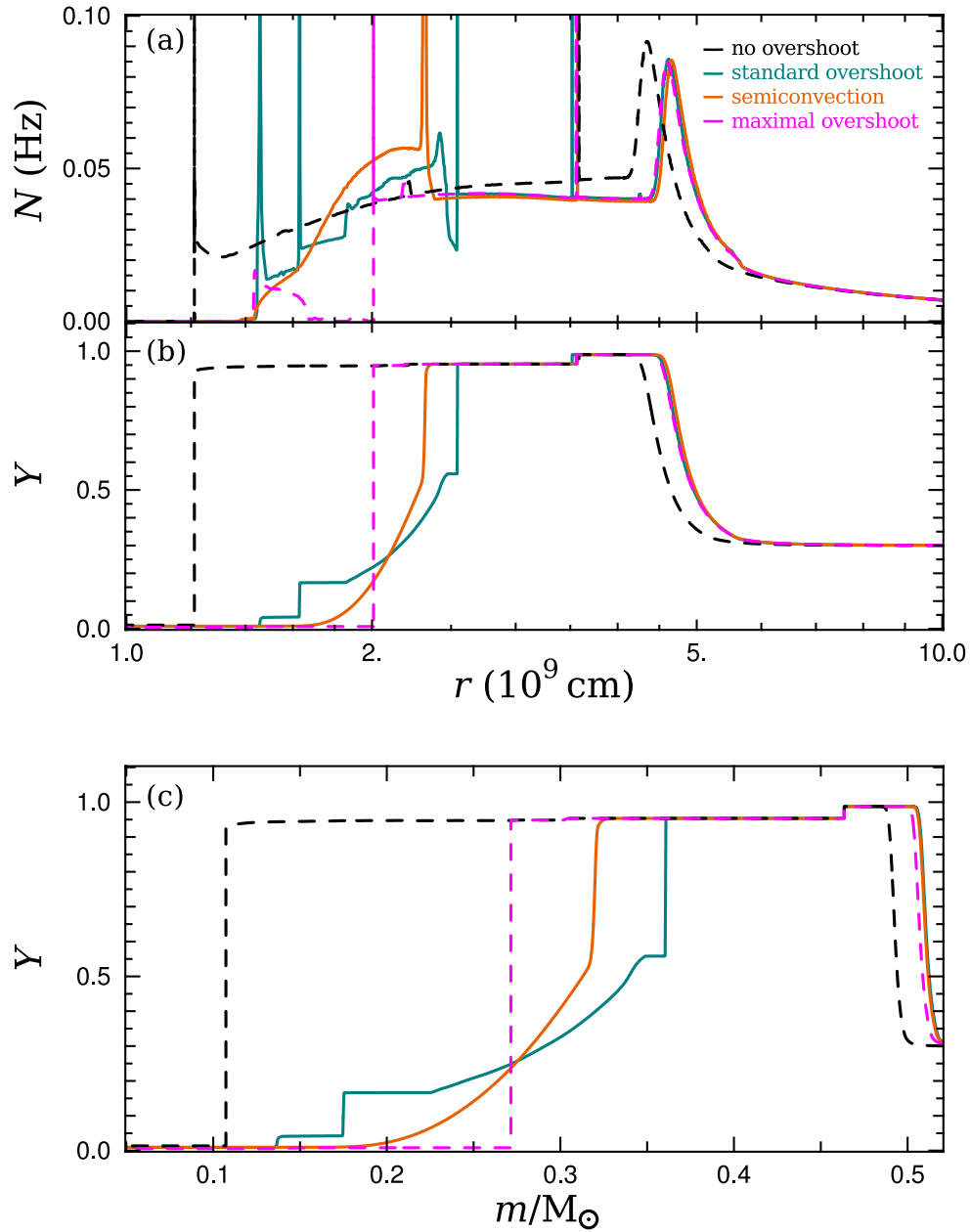


Figure 2.24: Comparison of the structure of four late-CHeB models with different treatments of convective boundaries, each with $Y_{\text{cent}} \approx 0.01$. The mass range in the lower panel approximately corresponds to the radius range in the upper two panels. The colours are the same as in Figure 2.3. The standard-overshoot, semiconvection, no-overshoot, and maximal-overshoot models have $\Delta\Pi_1$ of 208 s, 298 s, 195 s, and 247 s, respectively. These models have approximately $R = 15 R_\odot$, $T_{\text{eff}} = 4440$ K, and $\nu_{\text{max}} = 14 \mu\text{Hz}$.

low $\Delta\nu$ open cluster stars identified as evolved red clump stars in Corsaro et al. (2012) appear to be correctly classified, while the one suggested early-AGB star in NGC 6811 is probably also in the late-CHeB phase. Lastly, the position in $\Delta\nu - \Delta\Pi_1$ space of our late-CHeB models, and those from Stello et al. (2013), is generally consistent with the observed group marked by ‘A’ in Figure 1 in Mosser et al. (2014). We suggest that care should be taken when describing these stars, because ‘red clump’ and ‘core helium burning’ are not interchangeable terms. According to models, stars leave the red clump when they are still burning helium in the core.

Determinations of $\Delta\Pi_1$ from observations of stars near core helium exhaustion could be very uncertain if there is mode trapping in the partially mixed region. This is because late in CHeB the buoyancy radius of the partially mixed region, where the modes are trapped, becomes large compared to the total buoyancy radius. In the pre- and post-core helium exhaustion models in Figure 2.23 the partially mixed regions account for 41 per cent and 68 per cent of the total buoyancy radius respectively. There are thus few modes of consecutive radial order that are both not trapped, unlike the model in Figure 2.15 for instance. The extensive mode trapping in these models would make it difficult to accurately determine $\Delta\Pi_1$ from observations, but also make it unlikely they could be interpreted as having an erroneously high $\Delta\Pi_1$ from the period échelle diagram.

Core breathing pulses (CBP) only occur in the standard-overshoot model (note the rapid increases in central helium abundance that begin after 98 Myr in Figure 2.8). CBP do, however, occur in each of the remaining models if the mixing scheme is changed to standard overshoot late in CHeB (when the central helium abundance is $Y = 0.1$). This demonstrates that CBP are prevented by the mechanics of each mixing prescription rather than by the very different late-CHeB structures they eventually produce. An example of the divergence of the internal composition is shown in Figure 2.24(c) and is discussed below. Although these structural differences do not prevent CBP, they do affect the magnitude of them: a larger convective core, or the existence of a partially mixed region outside it, reduces the amount of helium transported into the core by the breathing pulses.

Finally, in Figure 2.24 we show four examples of late-CHeB models that were evolved with different mixing schemes until they have central helium abundance of around $Y = 0.01$. The contraction of the fully convective core is evident in all but the no-overshoot model (note the convectively stable region near $r = 1.6 \times 10^9$ cm in the maximal-overshoot model in magenta). By this stage the partially mixed regions in the semiconvection and standard-overshoot models extend well beyond the edge of the maximal-overshoot core, whereas earlier in the evolution their sizes are comparable (e.g. Figure 2.3a). It is also clear that by the end of CHeB those models have burned more helium than the maximal-

overshoot case. By the end of CHeB the internal structures have diverged significantly enough to suggest that (i) the mixing scheme could affect the early-AGB evolution, perhaps to an extent that is detectable in a large enough homogeneous population (e.g. globular clusters; which will be explored in a forthcoming paper) and (ii) asteroseismic studies of the population of late-CHeB (such as that found in Mosser et al. 2014) and early-AGB stars may provide vital clues about CHeB evolution.

2.5 Summary and conclusions

The asteroseismic detection of mixed modes in core helium burning stars in the *Kepler* field offers an unprecedented insight into the internal structure of these stars. With the aim of better constraining the models, we have investigated two discrepancies between the predicted asymptotic g-mode $\ell = 1$ period spacing $\Delta\Pi_1$ from standard low-mass ($1 M_\odot$) stellar models and those reported for the *Kepler* field stars (Mosser et al., 2012, 2014):

- The average value of $\Delta\Pi_1$ predicted by the models is significantly below the average inferred from observations (by more than 25s) and the models never reach the highest observed values of $\Delta\Pi_1$.
- The models spend more time with low values of $\Delta\Pi_1$ during core helium burning than is implied by the observed population (Figure 2.1).

One possible source of these discrepancies could be that there are systematic problems with the internal stellar structure of standard models. Indeed, it is well known, yet often ignored, that the models of this phase are uncertain (e.g. Figure 2.2). To explore these uncertainties in the light of the new asteroseismic observations we computed non-radial adiabatic pulsations and $\Delta\Pi_1$ for a suite of core helium burning models with varying physical inputs and mixing algorithms. The stellar models were calculated with the following.

- (i) Four different mixing schemes (Section 3.4.2).
- (ii) Three different initial chemical compositions (Section 2.4.8).
- (iii) Altered He-burning reaction rates (Table 2.1).

We found that varying the stellar composition or altering the He-burning reaction rates cannot reconcile the models and observations (Section 2.4.8; Table 2.1). Three of the four mixing schemes also failed to increase $\Delta\Pi_1$ by the magnitude required. The only

models that can match the average observed $\Delta\Pi_1$ values reported are those with large convective cores, such as those calculated with our newly proposed ‘maximal-overshoot’ scheme (Section 2.3.3). In this scheme the extent of convective overshoot is adjusted so that it produces the most massive convective core possible. This treatment was implemented, however, only as a demonstration of the effect of a large convective core: we have not proposed any physical basis for it. In the case of more massive stars ($M > 2 M_\odot$), the smaller number of observations, and the fact that their H-exhausted cores grow substantially during the core helium burning phase, allowed us to only rule out the no-overshoot model (Figure 2.19).

Another possible source of the $\Delta\Pi_1$ discrepancies is that the observations may be biased in some way. By comparing our non-radial adiabatic pulsation calculations against $\Delta\Pi_1$ across the suite of models, we identified a potential difficulty in inferring $\Delta\Pi_1$ from observations: any mode trapping that results from a convective region between two radiative zones (e.g. Section 2.4.2; Figure 2.7), or a steep composition gradient at the outer boundary of a semiconvection or partially mixed region (e.g. Section 2.4.4; Figure 2.15), increases the period spacing between most pairs of modes of consecutive radial order, and therefore the observationally inferred value of $\Delta\Pi_1$. The difference between these values could explain much of the disagreement between standard models and observations (dotted curve in Figure 2.18).

However, even after accounting for these two proposed resolutions to the discrepancy in average $\Delta\Pi_1$ values, the models still predict more core helium burning stars with low $\Delta\Pi_1$ (< 270 s) than observed. We suggested two possible remedies for this problem: (i) there may be a difficulty in observationally determining $\Delta\Pi_1$ for early core helium burning stars (when $\Delta\Pi_1$ is lowest) because the sharp composition profile at the hydrogen burning shell causes the period spacing pattern to be highly irregular compared to more evolved models (Section 2.4.3), or (ii) the mass of the helium core at the flash may be higher than predicted by standard models, thereby raising the initial $\Delta\Pi_1$ (Figure 2.18). Further information about the selection effects in asteroseismic population studies, which are alluded to by Mosser et al. (2014), would help to establish the validity of the first point. At present, the possibility of unknown systematic biases in the observations limits our ability to use them to make firm conclusions about stellar evolution theory.

We also investigated the dependence of $\Delta\Pi_1$ on the radius of the convective core, as shown by Montalbán et al. (2013). We found that the relationship to the observed period spacing is more complicated than a simple linear relationship in a number of respects (Section 2.4.2). Furthermore, $\Delta\Pi_1$ is also dependent on the steepness of any chemical profiles outside the convective core, such as those found in the semiconvection

zone (Section 2.4.5).

The structure of low-mass CHeB stars is further complicated by the stabilizing chemical gradient left behind by helium burning during the core-flash phase. This can have a significant effect on the period spacing pattern, depending on the steepness of the gradient (Figure 2.12). In fact, in models taken directly from our evolution code the mode trapping from the main discontinuity produced in the core-flash phase is the most important feature in the period spacing (e.g. Figure 2.13). This contrasts to composition gradients that may be created by overshooting (a small distance) from the convective core which have a more subtle effect on the period spacing (Figure 2.20).

We also tested low-mass models that imitate sdB stars (Section 2.4.7). In these models we find the same dependence of $\Delta\Pi_1$ and ΔP from pulsation calculations on mixing scheme as for our solar-mass models. We also found that it may be difficult to use asteroseismology to constrain sdB formation channels. This is because the effect of the composition discontinuity resulting from core-flash burning is smallest for the low radial-order modes (Figure 2.22) that are typically detected. We noted, however, that there may be other evidence from asteroseismology such as differences in the H–He transition region (Hu et al., 2008).

In Section 2.4.9 we showed that our models of core helium exhaustion suggest that early-AGB stars will not be found near the bulk of core helium burning stars in the $\Delta\nu$ - $\Delta\Pi_1$ diagram, independent of mixing scheme. This is because both $\Delta\Pi_1$ and $\Delta\nu$ have decreased by the time core helium burning ceases. This expands on the earlier finding by Stello et al. (2013) for models without convective overshoot.

Finally, although we have highlighted some possible explanations for the discrepancies in $\Delta\Pi_1$, further work is needed to pinpoint the cause(s). In order to better gauge the extent of the problem, and therefore the merit of our proposed solutions, it is necessary to account for any selection bias in the observations. Our possible solution involving the mode trapping phenomenon affecting the observationally inferred $\Delta\Pi_1$ values (e.g. Section 2.4.4) could be investigated by comparing models to specific frequency patterns observed. Constraints on the core mass at the helium flash and the mixing during the CHeB phase could be investigated by using the latest photometry of globular clusters – this is the subject of the next paper in this series.

Acknowledgements

This research was supported under Australian Research Councils Discovery Projects funding scheme (project numbers DP1095368 and DP120101815). Funding for the Stellar

Astrophysics Centre is provided by The Danish National Research Foundation (Grant D NRF106). The research is supported by the ASTERISK project (ASTERoseismic Investigations with SONG and Kepler) funded by the European Research Council (Grant agreement no.: 267864). This work was supported in part by computational resources provided by the Australian Government through the National Computational Infrastructure under the National Computational Merit Allocation Scheme (projects g61 and ew6).

Monash University

Declaration for Thesis Chapter 3

Declaration by candidate


In the case of Chapter 3, the nature and extent of my contribution to the work was the following:

Nature of contribution	Extent of contribution (%)
First author; code development, calculations, analysis of results, figure preparation, writing, manuscript preparation.	80

The following co-authors contributed to the work. If co-authors are students at Monash University, the extent of their contribution in percentage terms must be stated:

Name	Nature of contribution	Extent of contribution (%) for student co-authors only
Simon Campbell	Project development, analysis of results, manuscript editing.	
John Lattanzio	Project development, analysis of results.	
Adam van Duijneveldt	Preliminary work on methodology.	5

The undersigned hereby certify that the above declaration correctly reflects the nature and extent of the candidate's and co-authors' contributions to this work*.

Candidate's Signature		Date 2-9-15
------------------------------	---	-----------------------

Main Supervisor's Signature		Date 2-9-15
------------------------------------	---	-----------------------

*Note: Where the responsible author is not the candidate's main supervisor, the main supervisor should consult with the responsible author to agree on the respective contributions of the authors.

The treatment of mixing in core helium burning models – II. Cluster star counts

Thomas Constantino¹, Simon W. Campbell^{2,1}, John C. Lattanzio¹,
and Adam van Duijneveldt¹

¹Monash Centre for Astrophysics (MoCA), School of Physics and Astronomy, Monash
University, Victoria, 3800, Australia

²Max-Planck-Institut für Astrophysik, Karl-Schwarzschild-Straße 1, 85748 Garching bei
München, Germany

Submitted to *MNRAS*, July 2015.

3.1 Abstract

The treatment of convective boundaries during the core helium burning phase is a fundamental problem in stellar evolution calculations. In Chapter 2 we showed that new asteroseismic observations can only be matched by models with a very large convective core, or a semiconvection/partially mixed zone that can trap g-modes. In this paper we utilise new data to re-examine R_2 , the ratio of AGB to HB stars observed in globular clusters. This corresponds to the ratio of the lifetimes of the horizontal branch (HB) and asymptotic giant branch (AGB) phases of evolution, which is strongly affected by the treatment of mixing in stellar models. We have performed star counts for 48 Galactic globular clusters for which there is suitable HST photometry. The cluster to cluster scatter in R_2 is smaller than it is for previous determinations of R_2 . Because of the large sample size, our determination of $R_2 = 0.117 \pm 0.005$ is the most statistically robust now available. We have also constrained the luminosity difference between the HB and the AGB clump to $\Delta \log L_{\text{HB}}^{\text{AGB}} = 0.455 \pm 0.012$. Our results accord with earlier findings that standard models predict fewer AGB stars than are observed. By quantifying the effect of physical uncertainties, other than the treatment of mixing, we demonstrate that they cannot account for the problems with standard models. We have derived observational luminosity probability density functions that feature a sharp peak near the AGB clump. This constitutes a new and strong argument against core breathing pulses, which tend to broaden the predicted width of this peak. We conclude that both of the mixing schemes that can match the asteroseismology are also capable of matching the constraints from globular clusters, provided (i) there are no strong core breathing pulses in the models with a semiconvection/partially mixed zone, and (ii) the models with large convective cores have overshooting beneath subsequent early-AGB ‘gravonuclear’ convection zones. Further work is needed to break the degeneracy between these different scenarios.

3.2 Introduction

In stellar evolution calculations the core helium burning (CHeB) phase is subject to considerable uncertainty. The fundamental reason for this is that the amount of helium fuel that is brought into the convective core where it can burn, and hence the phase lifetime, is critically dependent on the treatment of convective boundaries. Historically, star counts in Galactic globular clusters have been the most important empirical test for the efficiency of mixing in CHeB stars. More recently, asteroseismology has provided complementary constraints on the structure and evolution of CHeB stars. In this study we test insights gleaned from recent asteroseismology studies, particularly those in Constantino et al.

(2015, hereinafter Chapter 2), against the wealth of high-quality photometry of globular clusters now available.

3.2.1 CHeB models: Key properties and uncertainties

In low-mass CHeB models with convective overshoot, the position of the boundary of the convective core is volatile. This is because carbon and oxygen, the products of helium burning, are more opaque than helium, so if any of the material is mixed across the formal convective boundary it tends to increase the opacity enough in the adjacent zone to make it unstable to convection according to the Schwarzschild criterion. In such models, the feedback from this process generally precipitates the development of a large region with slow mixing that is approximately neutrally stable according to the Schwarzschild criterion. This tends to happen regardless of whether there is a specific implementation for semiconvection (see e.g. Lattanzio, 1986; Caloi and Mazzitelli, 1990). The feedback from overshoot also causes the evolution of models with different treatments of convective boundaries to diverge significantly. The prescription for overshoot can cause the total mass of helium consumed during CHeB, and therefore the duration of this phase, to vary by more than a factor of two (see e.g., Castellani et al., 1971a; Bressan et al., 1986; Paxton et al., 2013; Constantino et al., 2015).

The uncertainty in the evolution worsens as CHeB progresses. Depending on the mixing scheme, the phenomenon of ‘core breathing pulses’ (CBP) may occur near the end of CHeB (Sweigart and Demarque, 1973; Castellani et al., 1985). CBP are characterized by a rapid growth in the mass of the convective core when the central helium abundance is very low. This process relies on feedback from the energy released by the $^{12}\text{C}(\alpha, \gamma)^{16}\text{O}$ reaction, which dominates when the helium abundance is low.

Despite the considerable difference in the core structure produced by different treatments of mixing in models, there is little immediate effect on the conditions at the surface, e.g. luminosity, temperature, and composition. Consequently, it is difficult to use observations to constrain the mixing treatment for stellar evolution calculations. The most common method found in the literature makes use of star counts from globular clusters to infer the relative lifetimes of the CHeB and (shell helium burning) asymptotic giant branch (AGB) phases, because these strongly depend on the mixing prescription in models. Recently, asteroseismology of white dwarfs (e.g. Metcalfe et al., 2002), red giants (e.g. Bedding et al., 2011; Mosser et al., 2012, 2014) and sdB stars (e.g. Reed et al., 2011) has opened a new and much needed avenue for further constraining stellar models of the CHeB phase (see also Chapter 2).

3.2.2 Insights from asteroseismology

Early attempts to constrain CHeB evolution from asteroseismology were indirect. Metcalfe et al. (2002) deduced that a higher $^{12}\text{C}(\alpha, \gamma)^{16}\text{O}$ reaction rate was needed to match the central C/O determination for a pulsating white dwarf. Straniero et al. (2003) then extended the study to the efficiency of mixing from overshoot. While the former argued an increase in the $^{12}\text{C}(\alpha, \gamma)^{16}\text{O}$ rate was required to match the high central oxygen abundance, the latter found that the observations were consistent with the standard rate after accounting for semiconvection. This highlights how inferences from asteroseismology can still suffer from some degeneracy caused by other uncertainties in stellar models, such as nuclear reaction rates.

Following the detection of modes of mixed g- and p-character in the oscillations of red giants in the *Kepler* field (Bedding et al., 2011), Mosser et al. (2012, 2014) inferred the asymptotic g-mode period spacing $\Delta\Pi_1$ for hundreds of subgiant, red giant branch (RGB), and CHeB stars in the *Kepler* field. This is a particularly powerful probe because it is sensitive to the conditions deep in the core where g-modes propagate. The high values of $\Delta\Pi_1$ typically inferred strongly contradict calculations from models with small convective cores (see e.g. Montalbán et al., 2013; Constantino et al., 2014b, 2015). In Chapter 2 we also demonstrated that they are inconsistent with models with a semiconvection or partially mixed zone. To match the range of $\Delta\Pi_1$ reported, we required models with our newly developed ‘maximal overshoot’ scheme, which produces the largest possible convective core. We also showed, however, that some modes can be strongly trapped at the boundary of the semiconvection or a partially mixed zone, raising the apparent $\Delta\Pi_1$ so that it is consistent with the determinations by Mosser et al. (2012, 2014).

3.2.3 Globular cluster star counts and the AGB clump

In Galactic globular clusters, which are composed of old, approximately coeval stars, the lifetime of each late phase of evolution is proportional to the number of stars observed in that phase. This property is important in the current context because the mixing scheme strongly governs the amount of helium burned during CHeB. It therefore also controls the respective longevity of the CHeB and early-AGB (subsequent helium-shell burning) phases.

By considering the then available determinations of $R = n_{\text{HB}}/n_{\text{RGB}}$ and $R_1 = n_{\text{AGB}}/n_{\text{RGB}}$ for three clusters (M15, M93, and NGC 5466), Caputo et al. (1978) concluded that the models with semiconvection by Castellani et al. (1971a), that spend longer on the HB and more rapidly ascend the AGB, were a better match to the observations compared with

the models without semiconvection from Iben and Rood (1970) and Rood (1972). This finding was then further supported by R and R_1 determinations for 15 clusters (Buzzoni et al., 1983). Although models with semiconvection were used for this comparison, the key finding is that CHeB models require a mechanism to transport additional helium into the convective core, prolonging the HB lifetime and speeding up the early-AGB evolution.

The ratio $R_2 = n_{\text{AGB}}/n_{\text{HB}}$ is the most direct probe of the efficiency of mixing in CHeB globular cluster stars. This was used by Caputo et al. (1989), who found that models with semiconvection, but without CBP (which decrease R_2), were consistent with observations of M5 from Buonanno et al. (1981), for which it was found that $R_2 = 0.18 \pm 0.04$. Interestingly, this and the more precise value of $R_2 = 0.176 \pm 0.018$ determined from later observations by Sandquist and Bolte (2004), are both higher than predicted from the models without CBP favoured by Caputo et al. (1989), which had $R_2 = 0.14$ and $R_2 = 0.15$, depending on the mass fraction of carbon in the core in the zero-age horizontal branch (ZAHB) models. In contrast, Bressan et al. (1986) calculated relevant models with $R_2 = 0.16$ and $R_2 = 0.21$, depending on the overshoot parameter in their non-local overshoot treatment that produces large, fully mixed cores. These examples demonstrate that R_2 has been used to both show the need for some kind of overshooting/semiconvection and also constrain the details of proposed mechanisms.

An inspection of the literature demonstrates why conclusions based on observations of R_2 ought to be revisited. Studies that include star counts for several different clusters show a significant scatter in R_2 . In other studies, only a single cluster is used. The nine clusters with more than 100 HB stars included in Buzzoni et al. (1983), for example, span a range of $0.109 \leq R_2 \leq 0.215$. Determinations of R_2 , even for the same cluster, can vary considerably. In the cluster NGC 6809 (M55), for example, Buzzoni et al. (1983), Sandquist (2000), and Vargas Álvarez and Sandquist (2007) determined $R_2 = 0.215$, 0.182, and 0.156, respectively, each with samples of more than 200 stars. The disagreement can be even worse when fewer stars are observed: Buzzoni et al. (1983) found $R_2 = 0.133$ from 51 stars in NGC 6171 whereas Sandquist (2000) report $R_2 = 0.248$ from 146 stars. The sizes of these differences suggest that inferences about stellar physics from R_2 may be bolstered by exploiting the more recent and numerous globular cluster photometry from HST.

Another related diagnostic is the magnitude (or luminosity) of the AGB clump, which is the observed clustering of early-AGB stars in the colour-magnitude diagram (CMD). Lee (1977) first noted that such a clump was visible 1.5 mag above the HB level in globular clusters with clear AGB sequences. In evolution calculations this coincides with core helium exhaustion and the subsequent slow luminosity change at the beginning of shell

helium burning. Importantly, the surface luminosity during this event is dependent on the mixing during the earlier CHeB phase. Cassisi et al. (2001) showed, for example, that artificially suppressing CBP increases the luminosity of the AGB clump. This suppression also shortens the HB lifetime and increases the AGB lifetime, better matching the observed ratio R_2 in M5.

3.2.4 Other uncertainties

Despite Nature having provided us with a large sample of nearby globular clusters, the interpretation of the observations presents a number of challenges. In order to identify the current stage of evolution of a star from photometry we require the AGB and the RGB stars to form distinct sequences. To correctly infer lifetimes the photometry must be nearly complete, or not have a bias against one of the populations, e.g. by excluding hot HB stars. Cluster membership should also be verified to avoid contamination.

The ability to use star counts to explain specific physical phenomena is also dependent on our wider understanding of stellar evolution. The determination of initial helium content from the ratio $R = n_{\text{HB}}/n_{\text{RGB}}$, for example, is sensitive to the $^{12}\text{C}(\alpha, \gamma)^{16}\text{O}$ reaction rate (Brocato et al., 1998) and binary interaction which could affect that ratio by truncating the evolution before the HB. Fortunately, binary interaction is unlikely to be problematic for inferring lifetimes from R_2 because those stars have already survived the RGB. Instead, we must consider the possibility that R_2 is reduced because some HB stars, whose envelope is too small for there to be a second ascent of the giant branch, become ‘AGB-manque’ stars (see e.g., Sweigart et al., 1974; Gingold, 1976; Caloi, 1989; Greggio and Renzini, 1990; Dorman et al., 1993). Recent spectroscopic evidence suggests this evolution may be more common than predicted from models (Campbell et al., 2013), which is an additional hazard for the interpretation of R_2 .

3.2.5 Revisiting the R-method

The mixing in the cores of CHeB models is a fundamental uncertainty that has existed since it was first shown that a slowly mixing semiconvection zone could develop outside the convective core. Efforts to understand this structure have been hampered by the absence of any immediately observable effects. Lately however, asteroseismology of red giants, sdB stars, and white dwarfs has offered new insights into this phase of evolution. In light of this recent progress, and with the aid of photometry superior in quality and quantity, we revisit the R-method for inferring the properties of CHeB evolution from observations of globular clusters. Specifically, we compare the HB and AGB luminosity

evolution implied from the populations in globular clusters with a suite of stellar models computed using different mixing schemes, composition, and input physics.

3.3 Observational data

3.3.1 Photometry

In this study we use HST photometry of 74 Galactic globular clusters from the Wide Field Planetary Camera 2 (WFPC2) in the $F439W$ and $F555W$ filters (Piotto et al., 2002) and 65 clusters from the ACS Wide Field Channel (WFC) in the $F606W$ and $F814W$ filters (Sarajedini et al., 2007). Together, these samples contain photometry of 104 unique clusters. These data are advantageous for two reasons: they comprise two large homogeneous samples, and the photometry is reasonably complete at the magnitudes relevant for this study. The two filter sets do not exactly match any other systems. Sirianni et al. (2005) describes $F439W$ and $F555W$ bands as Johnson B and Johnson V, and the $F606W$ and $F814W$ bands as broad V and broad I, respectively.

In the ACS Globular Cluster Survey (Sarajedini et al., 2007), the flux of each unsaturated star was determined by fitting a point spread function constructed for each exposure. The technique from Gilliland (2004) was used to find the flux for stars with saturated pixels. The reliability of the method for determining flux from saturated pixels was confirmed by comparing against unsaturated shorter exposures.

Crowding is only problematic for stars in the centre of clusters with compact cores, such as NGC 2808. In that case, the artificial star tests by Anderson et al. (2008) predict a completeness of 60 per cent in the cluster centre for stars with the magnitude of the extreme HB (the faintest stars we are interested in). The completeness then rapidly improves with increasing distance from the centre. Fortunately, most clusters in the photometry sample are close to 100 per cent complete above the subgiant branch level (Anderson et al., 2008). The artificial star experiments performed by Piotto et al. (2002) for NGC 104 and NGC 6723 (clusters with high and low central density, respectively) showed that the photometry has high completeness to more than 2 magnitudes fainter than the faintest HB stars. Therefore, except for clusters with extreme HBs, we do not expect incompleteness to influence any of our findings.

We correct for reddening in the Piotto et al. (2002) data by using the corrections provided, which are originally from the Harris (1996) catalogue. We also use the Harris (1996) catalogue (2010 edition) to correct for reddening in the Sarajedini et al. (2007) photometry. In that case we use the $E(B - V)$ correction because, according to the extinction law from Cardelli et al. (1989), it corresponds almost exactly to the $E(F606W -$

$F814W$) correction required.

3.3.2 Sample selection

We limit our analysis to clusters that have clearly defined HB and AGB sequences, which excludes photometry with obvious large photometric errors. We note that this procedure could introduce a selection bias but that we have still found 48 clusters out of 104 that meet our requirements, representing a sizeable fraction of the 157 known globular clusters in the Galaxy (Harris, 2010). We do not expect this to impact on our conclusions because most of the reasons that photometry does not meet our requirements are not related to stellar evolution during or after the CHeB phase. Additionally, we have rejected clusters with only a very small number of (identifiable) AGB stars. Selecting against clusters with few AGB stars could possibly introduce a bias because they could be a true reflection of the lower tail of real scatter in R_2 .

3.3.3 Comparison of R_2 between different data sets

In Table 3.1 we present the results of our star counts for 48 Galactic globular clusters using data from Piotto et al. (2002) and Sarajedini et al. (2007). We also include, for comparison, counts from Sandquist (2000). In these star counts we include all AGB stars that could be identified, but we later restrict the AGB count to stars no more than 10 times as luminous as the HB level. Interestingly, there is significant variation in R_2 , both between and within each data set. Including only the 15 clusters common to all three data sets, we find that R_2 has a standard deviation of 0.05, 0.03, and 0.05 for the respective Piotto et al. (2002), Sarajedini et al. (2007) and Sandquist (2000) samples. The Piotto et al. (2002) and Sarajedini et al. (2007) data sets are the most concordant pair, with an average size of the discrepancy in R_2 between the two sources of 0.03. Despite the differences between R_2 determinations for individual clusters, the overall average R_2 is consistent between those two data sets, at 0.131 for the Piotto et al. (2002) and 0.134 for the Sarajedini et al. (2007) photometry, compared with 0.166 for the Sandquist (2000) sample. When this analysis is further restricted to the seven clusters that have more than 150 (total AGB and HB) stars in each data set, we find similar results except the average R_2 from the Sandquist (2000) data reduces to 0.141, improving the agreement with the other data.

In Figure 3.1 we plot R_2 for the 31 clusters with multiple sources of photometry. The dotted grey line shows the largest difference between R_2 determinations for each cluster. Several clusters have R_2 determinations that differ by more than 0.1, which is almost as

large as the average R_2 . There is no obvious dependence of R_2 , or its consistency between data sets, on metallicity. We further discuss the statistics of this data in Section 3.3.6 and the effect of the metallicity and HB morphology in Section 3.3.7.

We have investigated the causes of some of the significant discrepancies between R_2 determinations from different photometry. To this end, we have chosen three clusters with three independent counts: NGC 6093, NGC 6652, and NGC 7078. There is a total of more than 190 HB and AGB stars in each of the three CMDs of NGC 6093. Despite the large sample sizes, R_2 is not consistent: we find $R_2 = 0.229$, 0.191, and 0.150, from Sandquist (2000), Piotto et al. (2002), and Sarajedini et al. (2007), respectively. When examining the photometry from Alcaïno et al. (1998), which was used for the Sandquist (2000) count, the reason for the disagreement is obvious – most of the blue HB, which is clear in the deeper Sarajedini et al. (2007) photometry, is missing. Excluding these (~ 100) stars from the Sarajedini et al. (2007) count increases R_2 to about 0.22, consistent with the Sandquist (2000) result. The disagreement for this cluster is also worsened to a lesser extent by the availability of U -band photometry in the Alcaïno et al. (1998) photometry. This better separates the luminous-AGB from RGB, allowing more AGB stars to be identified, therefore increasing R_2 .

The most metal-poor cluster in our collection, NGC 7078 (M15), also has a blue HB and a similarly large number of stars in each CMD, but it appears that in this instance the difference in R_2 , which ranges from 0.106 to 0.150, is due to the difficulty of distinguishing AGB from RGB stars. A gap is apparent between the blue and red parts of the HB in both the Piotto et al. (2002) and Sarajedini et al. (2007) photometry. The fraction of HB stars that are on the blue side is around 0.41, with agreement between the two sets to about one per cent, suggesting incompleteness is not a problem. Unlike the previous example, the blue HB also is well populated in the older photometry from Buonanno et al. (1983) used in Sandquist (2000). A similar issue seems to be at play for NGC 6752. We find $R_2 = 0.116$ from the Sarajedini et al. (2007) photometry, which is exactly double the result in Sandquist (2000). Again, this difference appears to be due to the difficulty of distinguishing between AGB and RGB stars in the older BV photometry from Buonanno et al. (1986), rather than missing blue HB stars. Our result is also consistent with UBV photometry from Y. Momany (private communication) that has a very clear AGB sequence, from which we find $R_2 = 0.104$.

There is a considerable spread in R_2 determinations for NGC 6652. We find $R_2 = 0.082$ and $R_2 = 0.108$ from the Piotto et al. (2002) and Sarajedini et al. (2007) photometry, respectively, while Sandquist (2000) reports $R_2 = 0.267$. We attribute this variation to the small number of HB and AGB stars (there are fewer than a total of 100 in each CMD),

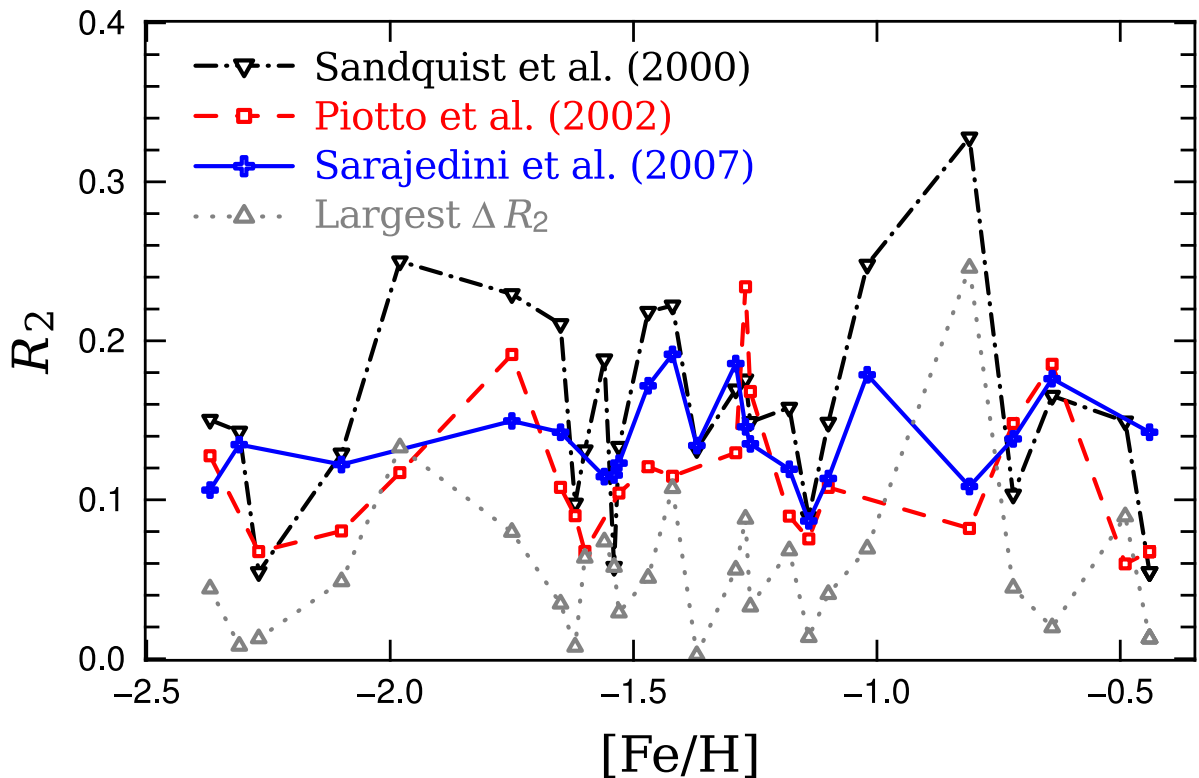


Figure 3.1: Comparison of R_2 for clusters shown in Table 3.1, limited to those with at least two different sources of photometry. The R_2 determined from the Sandquist (2000), Piotto et al. (2002), and Sarajedini et al. (2007) data are shown in black dash-dots, red dashes, and a blue solid line, respectively. The dotted grey line shows the maximum difference between R_2 determinations from different photometry.

and the difficulty in positively identifying AGB stars, especially for the photometry from Ortolani et al. (1994) used by Sandquist (2000).

3.3.4 Colour transformations and bolometric corrections

In order to compare observations with theoretical models we must relate the observed magnitude to luminosity. Throughout this study we do this by converting from the magnitude observed to luminosity. This conveniently minimizes the importance of colour-temperature transformations and the MLT mixing length calibration (in Section 3.4.6 we show that this has a negligible influence on luminosity evolution). To convert magnitude to luminosity we use the colour-temperature relations from Origlia and Leitherer (2000) and the bolometric corrections from Girardi et al. (2008) for the Piotto et al. (2002) photometry. We also use bolometric corrections from Girardi et al. (2008) for the Sarajedini et al. (2007) photometry, but in that case also use them to derive a colour-temperature relation. Both of these bolometric corrections (as a function of the respective colours) are

shown in Figure 3.2. We do not attempt to find the absolute luminosity of the observed stars, which would be subject to the uncertainties in the distance of each cluster. We instead rescale the luminosity so that it is expressed relative to that of the HB, i.e. we use

$$\Delta \log L = \log L - \log L_{\text{HB}}, \quad (3.1)$$

where L is the derived luminosity and $\log L_{\text{HB}}$ is the mode of the $\log L$ distribution for a cluster, i.e. the typical luminosity for HB stars.

In our analysis of some clusters in the Piotto et al. (2002) sample, the bluest HB stars appear to be more luminous than the red HB after the bolometric correction is applied. At this colour, near the ‘knee’ at $F439W - F555W = 0$ in the bolometric correction-colour relation shown in red in Figure 3.2, the luminosity is extremely sensitive to the colour, magnifying the effect of small inaccuracies in the colour-temperature relation. Consequently, we do not include stars bluer than $F439W - F555W = 0$ in our determination of $\Delta \log L_{\text{HB}}^{\text{AGB}}$ (defined in Section 3.3.5). This uncertainty does not affect the calculation of R_2 because those stars undoubtedly belong to the HB. In contrast to the Piotto et al. (2002) photometry, the bolometric correction adopted for the Sarajedini et al. (2007) sample is smoother and thus we did not need to use this procedure.

3.3.5 Luminosity probability density functions

We calculate R_2 and $\Delta \log L_{\text{HB}}^{\text{AGB}}$ (defined below) from the luminosity probability density function (PDF) determined from the observations. Each luminosity PDF $P(\Delta \log L)$ is constructed from a sample of N stars by the addition of Gaussian functions so that

$$P(\Delta \log L) = \frac{1}{N} \sum_{i=1}^N \frac{1}{\sigma \sqrt{2\pi}} \exp \left[-\frac{(\Delta \log L - \Delta \log L_i)^2}{2\sigma^2} \right], \quad (3.2)$$

where i represents each star, $\Delta \log L_i = \log L_i - \log L_{\text{HB}}$, L_i is the luminosity of each star, L_{HB} is the mode of the $\log L$ distribution, and σ is the standard deviation which determines the smoothness of the resulting function. The value of σ chosen for each cluster depends on the number of stars but it is generally around $\sigma = 0.04$. This is typically large enough for there to be a well defined peak from the AGB clump in the luminosity PDF.

The luminosity difference between the AGB clump and the HB is defined as

$$\Delta \log L_{\text{HB}}^{\text{AGB}} = \log L_{\text{AGB}} - \log L_{\text{HB}}. \quad (3.3)$$

This is just the difference in $\Delta \log L$ between the two peaks in the luminosity PDF. We can also calculate R_2 from the luminosity PDF. We define the boundary between the HB

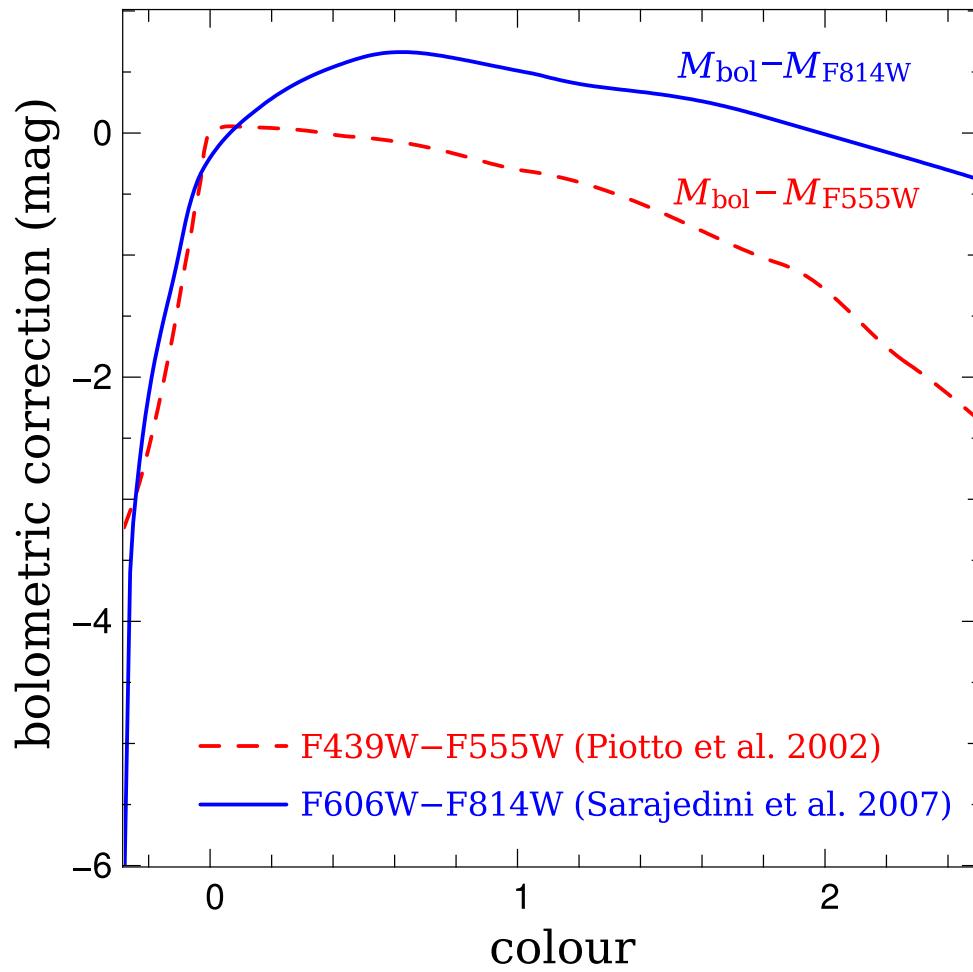


Figure 3.2: Bolometric corrections as a function of colour derived from colour-temperature relations and bolometric corrections from Origlia and Leitherer (2000) for the Piotto et al. (2002) photometry (red dashes) and from colour-temperature relations derived from Girardi et al. (2008) and bolometric corrections from Origlia and Leitherer (2000) for the Sarajedini et al. (2007) photometry (solid blue line).

and AGB to be the location of the minimum in the luminosity PDF between the HB and AGB clump peaks, $\Delta \log L_{\min}$. R_2 is thus the ratio of the integral of the luminosity PDF above and below this peak:

$$R_2 = \frac{\int_{\Lambda_{\min}}^{\Lambda_{\lim}} P(\Lambda) d\Lambda}{\int_{-\infty}^{\Lambda_{\min}} P(\Lambda) d\Lambda} \simeq \frac{n_{\text{AGB}}}{n_{\text{HB}}}, \quad (3.4)$$

where for convenience we have defined Λ as $\Delta \log L$, and Λ_{\lim} is the luminosity cut-off for the AGB that we introduce in Section 3.3.7.

3.3.6 Statistical errors

We account for statistical errors in a manner similar to previous studies (e.g., Iben, 1971; Buzzoni et al., 1983; Sandquist and Bolte, 2004), i.e. by assuming that the ratio of AGB to HB stars follows a Poisson distribution. This gives a variance

$$\sigma^2(n_{\text{AGB}}) = n_{\text{HB}} R_2, \quad (3.5)$$

and therefore standard error

$$\sigma(R_2) = \frac{\sigma(n_{\text{AGB}})}{n_{\text{HB}}} = \sqrt{\frac{R_2}{n_{\text{HB}}}}. \quad (3.6)$$

This is strictly true only if the observed ratio $R_2 = n_{\text{AGB}}/n_{\text{HB}}$ is the ratio expected from an infinitely large sample. It is also larger, by a very small factor of $\sqrt{1 + R_2}$, than the result found by assuming that there is a binomial distribution of HB and AGB stars. It is important to note that this error analysis is not exhaustive. There are other sources of error that were raised in Section 3.2, but which are not easily quantifiable.

We have determined the statistical uncertainty in R_2 and $\Delta \log L_{\text{HB}}^{\text{AGB}}$ in our aggregate data sets (e.g. those in Section 3.3.8) from Monte Carlo simulations. In this method we use the observed luminosity probability density functions to randomly populate hundreds of artificial data sets from which we calculate R_2 and $\Delta \log L_{\text{HB}}^{\text{AGB}}$ using the same method as for observations.

The error bars for $\Delta \log L_{\text{HB}}^{\text{AGB}}$ in Figure 3.3 and Figure 3.4 are $1\text{-}\sigma$ and generated by determining $\Delta \log L_{\text{HB}}^{\text{AGB}}$ from Monte Carlo simulations using different sample sizes and the luminosity PDF of the data set comprising every cluster without a blue HB. This also revealed a bias towards higher $\Delta \log L_{\text{HB}}^{\text{AGB}}$ for smaller data sets. For example, we calculated the average $\Delta \log L_{\text{HB}}^{\text{AGB}}$ for samples of 100 and 200 stars to be 0.496 and 0.474, respectively, compared with the true value of 0.455. This discrepancy, however, is well

within the respective 1- σ uncertainties (0.096 and 0.065). We have not corrected for this source of error in Figure 3.3 and Figure 3.4.

We have also tested the effect of random photometric errors σ_{phot} by allowing for them when populating the luminosity PDF in the Monte Carlo simulations. With sample sizes of $N = 100$ and $N = 200$ the error in R_2 and $\Delta \log L_{\text{HB}}^{\text{AGB}}$ is unaffected if $\sigma_{\text{phot}}(\log L) \lesssim 0.05$ and $\sigma_{\text{phot}}(\log L) \lesssim 0.065$, respectively. This increases to $\sigma_{\text{phot}}(\log L) \lesssim 0.10$ for the combined data set 6366 stars from all clusters without a blue HB. This allowance can accommodate the size of the estimated errors provided with the photometry, with the possible exception of blue HB stars. The uncertainty for these stars does not, however, affect the determination of R_2 and $\Delta \log L_{\text{HB}}^{\text{AGB}}$.

It is still possible that photometric errors affect our results by causing the misidentification of stars, e.g. blending of the RGB and AGB sequences, or the blue HB and the main sequence. The former is possible because the two are so close in the CMD while the latter is possible because the error is larger for fainter stars. However, if it is assumed that the HB and AGB stars are properly identified then the photometric errors do not add to the uncertainty of either R_2 or $\Delta \log L_{\text{HB}}^{\text{AGB}}$.

We have tested whether, after accounting for the known statistical uncertainty, the values of R_2 are consistent with the overall weighted mean $R_2 = 0.113 \pm 0.002$. In Figure 3.6 we show the distribution of the difference between R_2 for each cluster and the overall mean, expressed as a fraction of the 1- σ standard error. In both the Piotto et al. (2002) and Sarajedini et al. (2007) cases, the distribution is wider than expected from the above hypothesis. The standard deviations for the respective samples are 1.81 and 1.40 compared with an expected value of 1.0. This suggests that (i) we have underestimated the errors and/or (ii) R_2 is cluster dependent. We already know that the first possibility is true, since we have only accounted for one of the possible sources of error (which were discussed in Section 3.3). In Section 3.3.7 we investigate the second possibility by analysing the observations and in Section 3.4.6 we quantify how various factors, such as composition and stellar mass, affect theoretical predictions of R_2 .

3.3.7 Cluster metallicity and HB morphology

In Figure 3.3 we present R_2 and $\Delta \log L_{\text{HB}}^{\text{AGB}}$ for the 48 clusters in this study. In this calculation of R_2 , we limit the AGB count to $\log L < \log L_{\text{HB}} + 1.0$, which is different from the method used for Figure 3.1 where all (identified) AGB stars are included. We use this luminosity limit for the remainder of the paper because it enables a consistent comparison of R_2 between different clusters and between observations and predictions from models. Figure 3.1 shows that we do not detect any significant trend in either R_2

or $\Delta \log L_{\text{HB}}^{\text{AGB}}$ with metallicity. The lines of best fit (and those in subsequent figures) are constructed by weighting the data points according to the reciprocal of the $1\text{-}\sigma$ error. The weighted average $\Delta \log L_{\text{HB}}^{\text{AGB}} \approx 0.5$ is the same for both data sets (note that this is higher than $\Delta \log L_{\text{HB}}^{\text{AGB}}$ calculated in Section 3.3.8 from combined data sets). When accounting for the uncertainties there is also agreement in the average R_2 : we find $R_2 = 0.111 \pm 0.007$ from the Piotto et al. (2002) data and $R_2 = 0.127 \pm 0.009$ from the Sarajedini et al. (2007) data.

Figure 3.4 is the same as Figure 3.3 except that R_2 and $\Delta \log L_{\text{HB}}^{\text{AGB}}$ are plotted against $L1 + L2/2$, the colour ($F606W - F814W$) difference between the middle of the HB and the RGB determined by Milone et al. (2014), i.e. a measure of the ‘blueness’ of the HB. The 14 clusters without $L1$ and $L2$ determinations (i.e. those with only Piotto et al. 2002 photometry) are not shown in this figure. The clusters from both sets of data divide into three groups with distinct $L1 + L2/2$. In the middle group of clusters, with $L1 + L2/2 \approx 0.5$, there appears to be a strong negative correlation between R_2 and $L1 + L2/2$, but this trend is not preserved when the more red and the more blue HB groups are included. When all of the clusters are considered, there appears to be at most a weak correlation between R_2 and $L1 + L2/2$, i.e. R_2 does not strongly depend on the stellar factors that control HB morphology, principally mass, metallicity, and helium content.

We did not detect any dependence of $\Delta \log L_{\text{HB}}^{\text{AGB}}$ on $L1 + L2/2$ for the Piotto et al. (2002) observations shown in Figure 3.4. Although the trend line for the Sarajedini et al. (2007) sample shows a positive correlation between $\Delta \log L_{\text{HB}}^{\text{AGB}}$ and $L1 + L2/2$ (with a gradient of 0.18) that is concordant with the example models, the trend in the observations is due entirely to the six clusters with the bluest HBs, and these have a large scatter. We further discuss the dependence of $\Delta \log L_{\text{HB}}^{\text{AGB}}$ on HB morphology with reference to the stellar models in Section 3.4.4.

It has been proposed that the lack of CN-strong (Norris et al., 1981; Ivans et al., 1999; Campbell et al., 2010, 2012) and sodium-rich (Campbell et al., 2013; Charbonnel et al., 2013; Cassisi et al., 2014; Johnson et al., 2015) AGB stars in globular clusters could be due to a sizeable fraction of the (low mass) blue HB stars not evolving to the AGB. Our analysis of the observations reveals there is no dependence of R_2 on the colour of the midpoint of the HB (Figure 3.4), which would appear to contradict assertions that some blue HB stars do not reach the AGB. The picture is changed, however, when the colour of the bluest extent, rather than the midpoint, of the HB is considered. In Figure 3.5 we show R_2 and $\Delta \log L_{\text{HB}}^{\text{AGB}}$ for the clusters with a blue HB plotted against the colour difference between the blue end (fourth percentile) of the HB and the RGB ($L1 + L2$). It

is clear from both the Piotto et al. (2002) and Sarajedini et al. (2007) data sets that R_2 is lower in clusters with a bluer HB tail.

It is conceivable that the dependence of R_2 on the extent of the blue HB results from the lower luminosity of blue HB stars: this would reduce the luminosity cut-off for the AGB and reduce the number of AGB stars included in the count, and therefore R_2 . There are two arguments against this though: (i) there is only a weak dependence of $\Delta \log L_{\text{HB}}^{\text{AGB}}$ on $L1+L2$ (i.e. we are still including the same luminosity range of AGB stars, independent of the extent of the blue HB), and (ii) R_2 is not substantially lower for clusters in which the middle of the HB is blue (i.e. those with the highest $L1 + L2/2$), which would be the case if more AGB stars were excluded from our counts in clusters with a blue HB. It thus appears from this sample that a considerable fraction of blue HB stars do not evolve to the AGB phase.

3.3.8 General observed properties of red-HB clusters

In Figure 3.7 we present the luminosity PDFs from all of the HB and AGB stars in the 14 clusters in the Piotto et al. (2002) or Sarajedini et al. (2007) data sets that do not have a blue extension to the HB. Restricting the analysis to these clusters is beneficial for several reasons:

1. The total luminosity (and magnitude) range of the HB and the AGB is smaller, reducing the importance of any potential magnitude-dependent completeness function (such as that for the centrally dense cluster NGC 2808; Anderson et al. 2008).
2. The colour range is smaller, reducing the effect of imperfect bolometric corrections.
3. The luminosity of the HB is unambiguous and therefore so is the cut-off for the AGB luminosity. This also makes estimates of $\Delta \log L_{\text{HB}}^{\text{AGB}}$ more certain.
4. We expect all of the HB stars to be massive enough to ascend the AGB.

The clusters NGC 104, NGC 362, NGC 1261, NGC 1851, NGC 6624, NGC 6637, and NGC 6652 are common to both samples while NGC 5927, NGC 6304, NGC 6356, NGC 6441, NGC 6539, and NGC 6569 are only in the Piotto et al. (2002) set and NGC 6171 is only in the Sarajedini et al. (2007) set. In the luminosity PDFs shown in Figure 3.7, each cluster is weighted according to the total number of stars. The agreement between the two consolidated data sets is remarkable. The consistency between both R_2 and $\Delta \log L_{\text{HB}}^{\text{AGB}}$ provides a strong constraint for models. The Piotto et al. (2002) sample gives $R_2 = 0.114 \pm 0.007$ and $\Delta \log L_{\text{HB}}^{\text{AGB}} = 0.436 \pm 0.017$ compared with $R_2 = 0.127 \pm 0.009$ and

$\Delta \log L_{\text{HB}}^{\text{AGB}} = 0.460 \pm 0.010$ for the Sarajedini et al. (2007) sample, where the $1\text{-}\sigma$ uncertainty is determined from the Monte Carlo method described in Section 3.3.6. When the two data sets are combined, we find $R_2 = 0.117 \pm 0.005$ and $\Delta \log L_{\text{HB}}^{\text{AGB}} = 0.455 \pm 0.012$. We use these observational constraints – the tightest yet – in the following sections.

3.4 Stellar models

3.4.1 Description of models

We have constructed a grid of stellar models that contains a range of values for the three important parameters for the evolution of HB stars: stellar mass, helium abundance, and metallicity (and hence also stellar age). We have chosen not to make stellar models to specifically match each of the 48 clusters in our sample. This would require at the very least running models with a suitable initial mass, metallicity, MLT mixing length parameter α_{MLT} , and RGB mass loss rate (and then additional models with different initial mass and helium abundance to account for multiple populations) for each cluster.

The stellar models were computed with the Monash University stellar evolution code MONSTAR (which has been described previously, e.g. Campbell and Lattanzio, 2008). The models initially have a metal abundance in the solar ratio according to Asplund et al. (2009), except with oxygen enhancement of $[\text{O}/\text{Fe}] = +0.4$ to mimic the α -element enhancement observed in globular cluster stars (see e.g. Gratton et al., 2012a). During the RGB evolution the models have the mass loss rate from Reimers (1975) with $\eta = 0.4$.

The grid includes a total of 24 models with each of the four mixing schemes described in Section 3.4.2 and every combination of $[\text{Fe}/\text{H}] = -2, -1, -0.5$, and $Y = 0.245$ and 0.284 . The initial mass of each model was set so that the HB age is close to 13 Gyr, consistent with that of the oldest Galactic globular clusters (e.g. VandenBerg et al., 2013). Note that obtaining the correct ZAHB age and RGB mass loss rate is not important because the stellar structure is so well described by the aforementioned properties. The difference in helium chosen, $\Delta Y = +0.039$, has an equivalent effect on lifetime as a $0.05 M_{\odot}$ decrease in initial mass for the $[\text{Fe}/\text{H}] = -1$ case, and is comparable to the modest limit on the spread of helium inferred for the majority of clusters (see Section 3.4.6 for references).

In the following sections we quantify how the CHeB mixing scheme, initial stellar mass, initial composition, and physical uncertainties affect the predictions for the observed quantities R_2 and $\Delta \log L_{\text{HB}}^{\text{AGB}}$. When testing variables other than the mixing scheme we predominantly make use of models with the semiconvection and maximal-overshoot prescriptions because, unlike the standard-overshoot sequences, their evolution is not strongly affected by the numerical treatment (see Section 3.4.7). Unless stated otherwise,

Table 3.1: Comparison of horizontal branch (HB) and asymptotic giant branch (AGB) star counts from three different sources. The photometry from Piotto et al. (2002) and Sarajedini et al. (2007) for each cluster are included according to the criteria in Section 3.3.2. The counts by Sandquist (2000) were performed on photometry available from various sources in the literature. Metallicity [Fe/H] is from the Harris (1996) catalogue (2010 edition) and the HB morphology parameters $L1$ and $L2$ are from Milone et al. (2014).

NGC	[Fe/H]	$L1$	$L2$	Piotto et al. (2002)			Sarajedini et al. (2007)			Sandquist (2000)		
				n_{HB}	n_{AGB}	R_2	n_{HB}	n_{AGB}	R_2	n_{HB}	n_{AGB}	R_2
104	-0.72	0.078	0.068	358	53	0.148	591	82	0.139	368	38	0.103
362	-1.26	0.086	0.608	238	40	0.168	318	43	0.135	94	14	0.149
1261	-1.27	0.088	0.644	94	22	0.234	233	34	0.146	148	26	0.176
1851	-1.18	0.098	0.679	272	37	0.136	411	49	0.119	209	24	0.115
1904	-1.60	163	11	0.067	122	16	0.131
2419	-2.15	0.192	0.852	225	22	0.098
2808	-1.14	0.094	0.904	809	61	0.075	1200	104	0.087	247	22	0.089
4833	-1.85	0.287	0.538	94	10	0.106
5024	-2.10	0.158	0.602	224	18	0.080	360	44	0.122	302	39	0.129
5272	-1.50	0.150	0.613	323	40	0.124	562	65	0.116
5634	-1.88	130	15	0.115
5694	-1.98	222	26	0.117	56	14	0.250
5824	-1.91	463	63	0.136
5904	-1.29	0.150	0.681	162	21	0.130	280	52	0.186	555	94	0.169
5927	-0.49	0.043	0.062	201	12	0.060	134	20	0.149
6093	-1.75	0.464	0.447	162	31	0.191	341	51	0.150	170	39	0.229
6139	-1.65	282	35	0.124	114	24	0.211
6171	-1.02	0.100	0.513	56	10	0.179	117	29	0.248
6205	-1.53	0.527	0.441	192	20	0.104	390	48	0.123	90	12	0.133
6218	-1.47	0.561	0.299	82	11	0.134	91	12	0.132
6229	-1.18	278	34	0.122	92	19	0.207
6254	-1.26	0.588	0.260	157	18	0.115	69	13	0.188
6266	-1.18	446	40	0.090	114	18	0.158
6284	-1.26	127	16	0.126
6304	-0.45	0.062	0.060	99	8	0.081
6341	-2.31	0.261	0.542	245	33	0.135	140	20	0.143
6356	-0.40	362	25	0.069
6362	-0.59	0.122	0.621	38	6	0.158
6388	-0.55	0.057	0.836	1347	176	0.131
6402	-1.28	349	29	0.083
6441	-0.46	0.048	0.904	1380	154	0.112
6539	-0.63	114	15	0.132
6541	-1.81	0.563	0.347	248	41	0.165
6569	-0.76	166	30	0.181
6584	-1.50	0.102	0.558	55	8	0.145
6624	-0.44	0.077	0.085	121	9	0.074	188	20	0.106	126	30	0.238
6637	-0.64	0.078	0.065	135	25	0.185	244	43	0.176	127	21	0.165
6638	-0.95	101	28	0.277
6652	-0.81	0.073	0.080	61	5	0.082	83	9	0.108	75	20	0.267
6681	-1.62	0.558	0.334	100	9	0.090	82	8	0.098
6723	-1.10	0.127	0.704	102	11	0.108	194	22	0.113	101	15	0.149
6752	-1.54	0.378	0.578	173	20	0.116	225	13	0.058
6864	-1.29	363	69	0.190	55	12	0.218
6934	-1.47	0.097	0.678	149	18	0.121	99	17	0.172
6981	-1.42	0.142	0.570	61	7	0.115	188	36	0.191	45	10	0.222
7078	-2.37	0.174	0.713	376	48	0.128	537	57	0.106	153	23	0.150
7089	-1.65	0.150	0.790	167	18	0.108	702	100	0.142
7099	-2.27	0.462	0.261	89	6	0.067	202	11	0.054

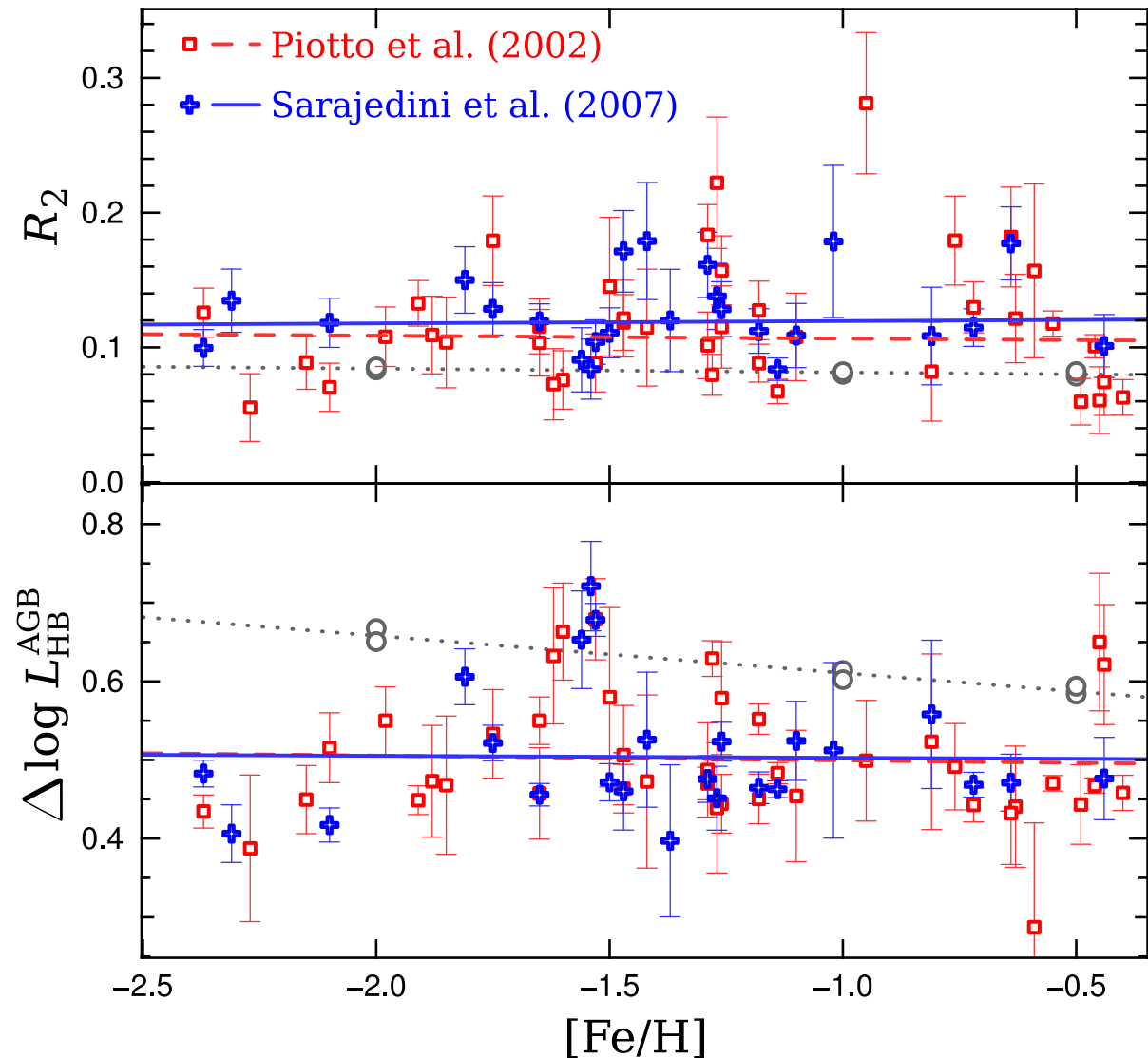


Figure 3.3: **Upper panel:** R_2 as a function of cluster metallicity (from the Harris 1996 catalogue; 2010 edition) for selected clusters from Piotto et al. (2002) photometry (red squares) and Sarajedini et al. (2007) photometry (blue crosses). Error bars are $1\text{-}\sigma$ according to Equation 3.6. **Lower panel:** luminosity difference between the HB (defined as the peak of the luminosity probability density function) and the AGB clump (similarly defined) for the same clusters. Error bars are $1\text{-}\sigma$ according to the method in Section 3.3.6. The lines of best fit (dashed red and solid blue lines for the Piotto et al. 2002 and Sarajedini et al. 2007 photometry, respectively) were constructed by weighting the clusters according to the reciprocal of the $1\text{-}\sigma$ error. Example results of theoretical evolution calculations with the semiconvection mixing scheme are denoted by grey circles and a grey dotted trend line (see Section 3.4.4).

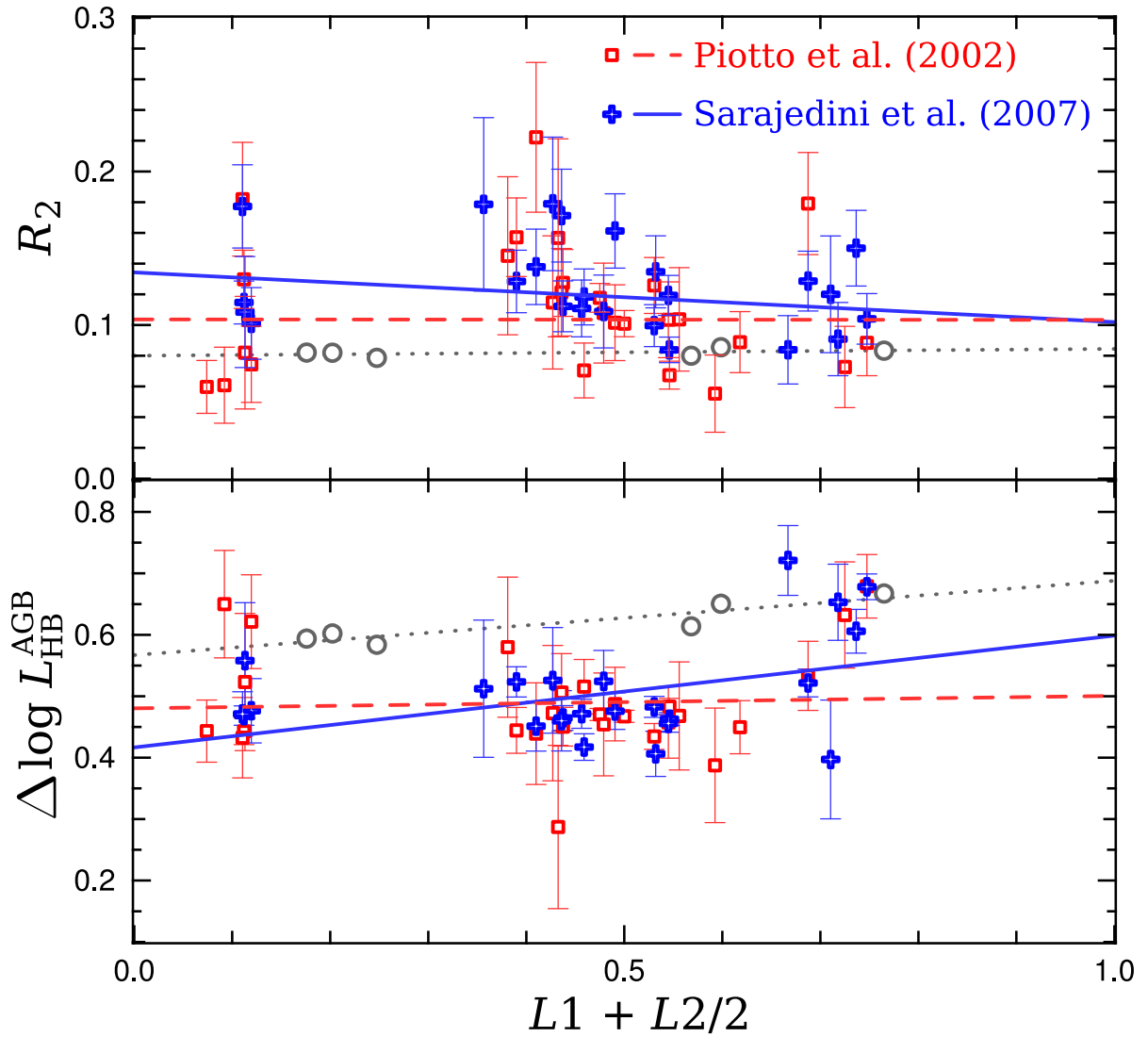


Figure 3.4: Same as Figure 3.3 except R_2 and $\Delta \log L_{\text{HB}}^{\text{AGB}}$ are plotted against $L1 + L2/2$, which is the colour ($F606W - F814W$) difference between the RGB and the middle of the HB determined by Milone et al. (2014). Note that this sample is restricted to those clusters in Figure 3.3 that have $L1$ and $L2$ determinations.

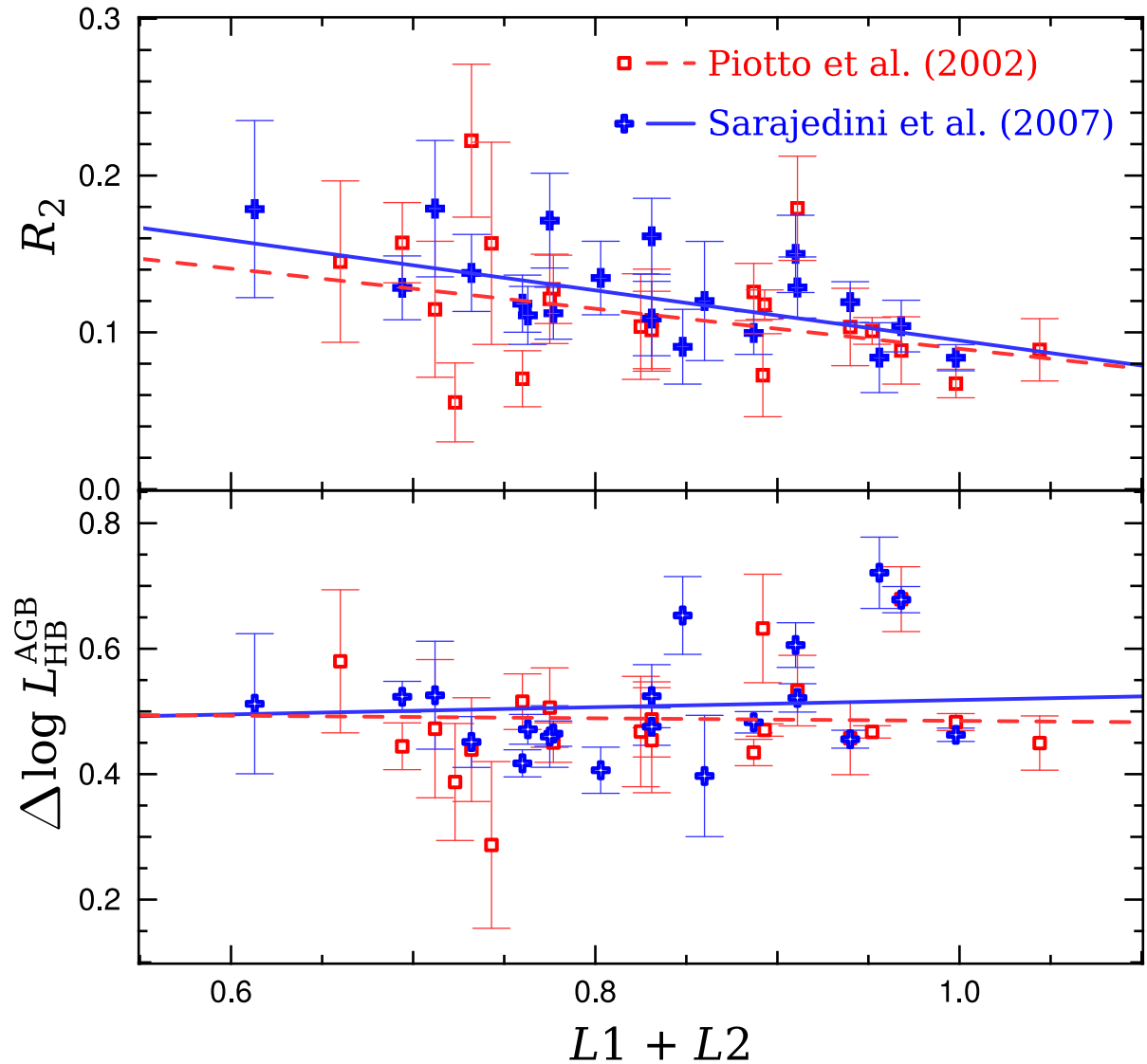


Figure 3.5: Same as Figure 3.3 except R_2 and $\Delta \log L_{\text{HB}}^{\text{AGB}}$ are plotted against $L1 + L2$, which is the colour ($F606W - F814W$) difference between the RGB and the fourth percentile of the HB population, determined by Milone et al. (2014). Note that this sample is restricted to those clusters in Figure 3.3 that have $L1$ and $L2$ determinations and a blue extension to the HB.

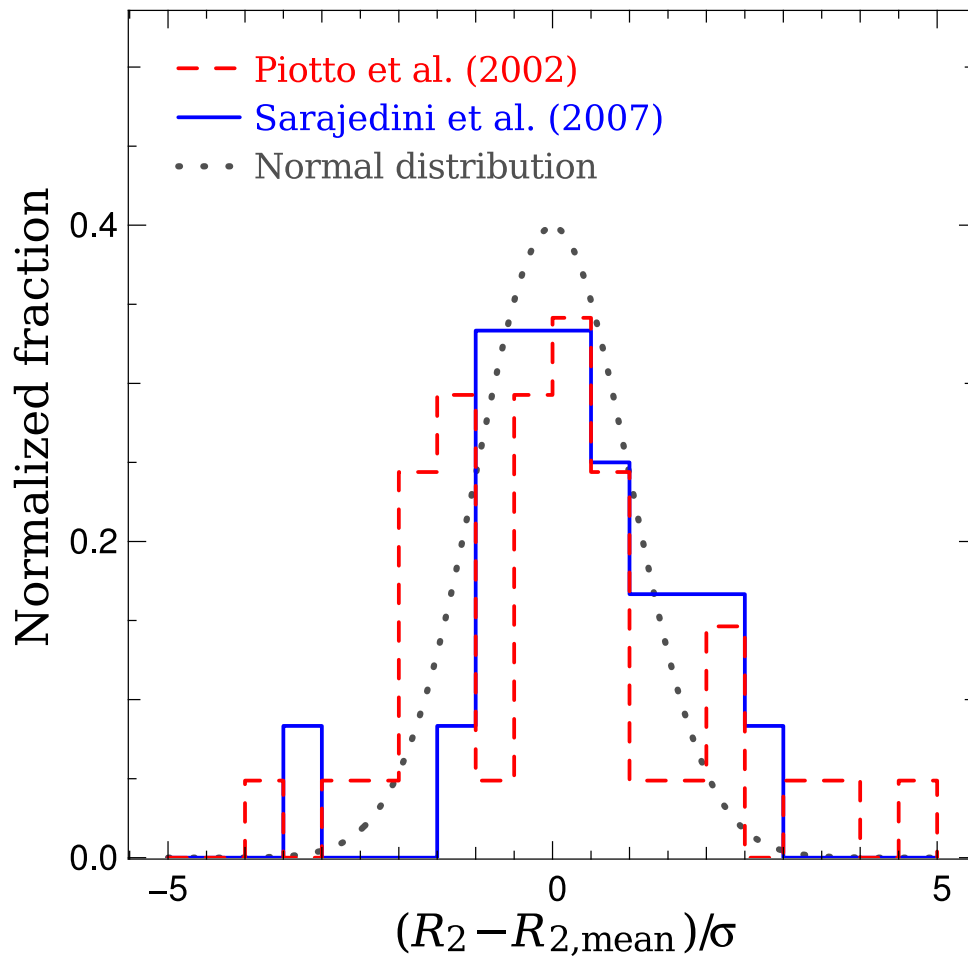


Figure 3.6: Histogram of the difference, as a fraction of the standard error (calculated from Equation 3.6), between R_2 for each cluster shown in Figure 3.3 and the overall mean value of $R_2 = 0.113$ for the Piotto et al. (2002) photometry (dashed red line) and Sarajedini et al. (2007) photometry (solid blue line). The dotted grey curve is the standard normal distribution, i.e. with standard deviation $\sigma = 1$.

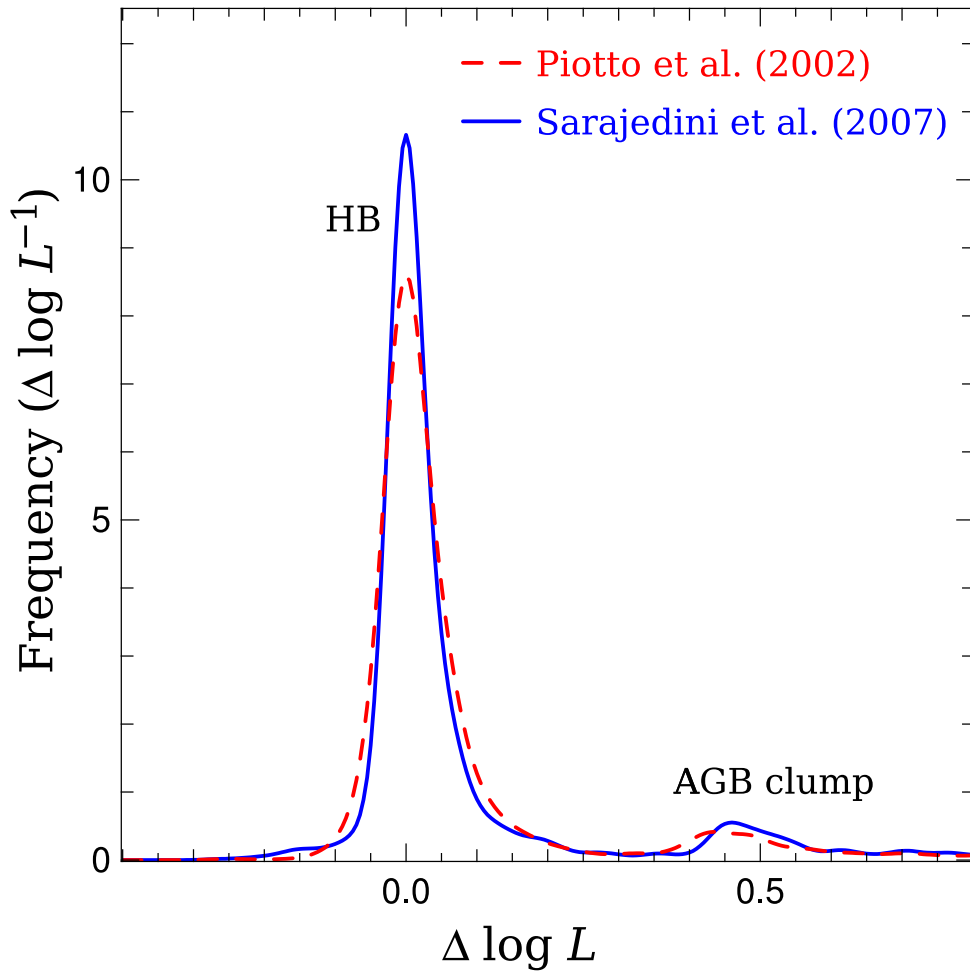


Figure 3.7: Observed probability density function of the luminosity of all HB and AGB stars in clusters without a blue extension of the HB (listed in Section 3.3.3). The luminosity of the HB for each cluster (defined here as the peak of the distribution) has been rescaled so that $\log L_{\text{HB}} = 0$. The sample has been truncated at $\Delta \log L = 1.0$. The PDF for each cluster was constructed by adding a Gaussian function with $\sigma = 0.04$ for each star (see Section 3.3.5). These were then combined by weighting each cluster according to the number of stars counted. Transformations from magnitude to luminosity are in accordance with the method in Section 3.3.4.

tests were carried out with models that have an initial mass $M_1 = 0.83 M_\odot$, initial helium $Y = 0.245$, and metallicity $[\text{Fe}/\text{H}] = -1$.

3.4.2 Mixing schemes

In the CHeB phase we use the four different mixing schemes from Chapter 2: (i) no overshoot, (ii) standard overshoot, (iii) semiconvection, and (iv) maximal overshoot. In this paper we include only a brief summary of the mechanics and outcomes of these four mixing schemes: they are shown in more detail in Chapter 2. We also test the effects of uncertainties in the input physics, which are described in the relevant sections.

The **no-overshoot** models have the Schwarzschild criterion strictly applied. That is, the location of the convective boundary is not found each time step by extrapolating $\nabla_{\text{rad}} - \nabla_{\text{ad}}$ across the prior position of the boundary to find the point of neutrality. A zone may only become convective if the conditions (T , p , ρ , or composition) change so that it becomes convectively unstable. This cannot happen as a result of a change in composition due to mixing or numerical diffusion, however, because that is not allowed.

In the **semiconvection** scheme, slow mixing is allowed in regions that are formally stable according to the Schwarzschild criterion. In this scheme, mixing is modelled as a diffusive process where the diffusion coefficient depends exponentially on how far $\nabla_{\text{rad}}/\nabla_{\text{ad}}$ is from unity. The particular formulation and parameters used for this study are given in Chapter 2.

The **standard overshoot** runs have overshooting at every convective boundary according to the scheme proposed by Herwig et al. (1997) where there is an exponential decay of the diffusion coefficient that depends on the parameter f_{OS} (see Section 3.4.7). Unless specified otherwise, we use $f_{\text{OS}} = 0.001$ in this study.

In the **maximal overshoot** scheme, convective overshoot is applied at the boundary of the convective core, and the core then allowed to grow, only if $\nabla_{\text{rad}}/\nabla_{\text{ad}} > 1 + \delta$ everywhere in the convection zone, where δ is a (small) parameter. This ensures that mixing from overshoot does not reduce $\nabla_{\text{rad}}/\nabla_{\text{ad}}$ enough for part of the convection zone to become convectively stable (see Chapter 2 for details). This scheme produces the largest convective core possible, i.e, there is a point in the convection zone (not necessarily at the boundary) that is close to convective neutrality, and would become stable if any more helium were mixed into the convection zone (Figure 2.3 in Chapter 2).

The four mixing schemes in this study produce very different internal structures. The models without overshoot have the smallest possible convective core, i.e. the material adjacent to the boundary is close to convective neutrality according to the Schwarzschild criterion. Because this boundary does not move during the evolution, the conversion of

helium to carbon and oxygen causes a large composition discontinuity to develop. This is the only one of the four mixing schemes in which no helium is transported into the convective core, and consequently it has the shortest CHeB lifetime. In calculations with standard overshoot, a large partially mixed region with a stepped composition profile develops around the convective core (Figure 2.2 in Chapter 2). This growth occurs via discrete mixing episodes and is driven by the higher opacity of the products of helium burning. By the end of core helium burning, the mass of the partially mixed region can be comparable to that of the convective core beneath it. The same effect is apparent in the semiconvection models except there is continuous, slow mixing, which results in a smooth composition gradient outside the convective core. The maximal-overshoot sequences develop a structure that is similar to the models without overshoot, i.e. a large composition discontinuity at the core boundary, except that the mass enclosed by the convective core is much larger, and comparable to the total mass of the convective core plus the partially mixed region in the standard overshoot models.

3.4.3 Diagnostics for models

We use the evolution sequences to produce theoretical $\log L$ PDFs $P(\Delta \log L)$ which can then be compared with that derived from the observations using Equation 3.2. These are constructed from models by iterating over the (post-core flash) evolution sequences and adding Gaussian functions so that

$$P(\Delta \log L) = \frac{1}{\tau} \sum_{i=1}^n \frac{\Delta t_i}{\sigma \sqrt{2\pi}} \exp \left[-\frac{(\Delta \log L - \Delta \log L_i)^2}{2\sigma^2} \right], \quad (3.7)$$

where i represents each model in the sequence of n models (where typically $n \approx 10^4$), Δt_i is each time step, $\Delta \log L_i = \log L_i - \log L_{\text{HB}}$, L_i is the luminosity of model i , L_{HB} is the HB luminosity determined from the mode of the $\log L$ distribution, τ is the total time the model spends within the luminosity limits ($\log L < \log L_{\text{HB}} + 1.0$), and we have chosen $\sigma = 0.02$, which is sufficient to ensure that the theoretical luminosity PDFs are smooth.

3.4.4 Overall comparison between models and observations

Along with the observations, Figure 3.3 and Figure 3.4 also include comparisons to models with the semiconvection mixing scheme. This particular scheme was just chosen as an example; the effects of different mixing schemes are explored in the following sections. The trend line (grey dots) is constructed from six models with combinations of $[\text{Fe}/\text{H}] = -2$, -1 , and -0.5 , and initial helium $Y = 0.245$ and $Y = 0.284$.

The predictions for R_2 from the semiconvection scheme sit around 3σ below the observed average. Although previous studies have shown examples of standard models with semiconvection zones predicting R_2 lower than that observed (e.g. Caputo et al., 1989; Cassisi et al., 2001, 2003; Vargas Álvarez and Sandquist, 2007), our tighter constraint on R_2 from two sets of homogeneous observations of 48 clusters provides much stronger evidence that a discrepancy truly exists between the observations and standard models. Importantly, however, the trend lines for R_2 in Figure 3.3 demonstrate that models and observations have the same insensitivity to stellar composition. This implies that our conclusions about the validity of different mixing schemes are not weakened by uncertainty in the composition of the multiple populations of globular cluster stars.

The predicted $\Delta \log L_{\text{HB}}^{\text{AGB}}$ from the models with semiconvection is higher than the observed average. This strongly suggests that in these models the mass enclosed by the partially mixed region at the end of CHeB is too large. We also compare the observations of $\Delta \log L_{\text{HB}}^{\text{AGB}}$ with predictions from the different mixing schemes in Section 3.4.5, and specifically from standard-overshoot models in Section 3.4.7 and 3.4.8, and from maximal-overshoot models in Section 3.4.9.

The comparison between models and observations in Figure 3.4 using the ‘blueness’ of the HB ($L1 + L2/2$) shows the same offsets evident in Figure 3.3. In contrast to the models and the Piotto et al. (2002) data, the Sarajedini et al. (2007) observations show a slight decrease of R_2 with an increase in $L1 + L2/2$. These observations also show a dependence of $\Delta \log L_{\text{HB}}^{\text{AGB}}$ on $L1 + L2/2$ that is consistent with the example models (apart from the offset), especially given their large scatter (Figure 3.4). In models, this slope is mostly due to the lower luminosity of bluer HB stars (luminosity is a strong function of envelope mass), rather than any affect on the luminosity of the AGB clump. Our analysis of the Sarajedini et al. (2007) data is subject to less uncertainty from the bolometric correction so it is not surprising that it better matches the models.

3.4.5 Effect of the mixing prescription

In Figure 3.8 we show the evolution of four models with different mixing schemes. The resulting predictions of R_2 and $\Delta \log L_{\text{HB}}^{\text{AGB}}$ for these models are summarized in Table 3.2. It is evident from panel (a) in Figure 3.8 that each model follows the same path in the HR diagram. The luminosity evolution of each sequence is nearly identical until they are close to exhausting helium in the core (Figure 3.8b). The no-overshoot model is an obvious outlier because the lack of growth in the mass of the convective core restricts the fuel available and shortens the CHeB lifetime to less than half that of the others. This increases the early-AGB lifetime and decreases $\Delta \log L_{\text{HB}}^{\text{AGB}}$ compared with the ob-

Table 3.2: Summary of observations and model predictions. The models have initial mass $M_i = 0.83 M_\odot$, metallicity $[\text{Fe}/\text{H}] = -1$, and initial helium $Y = 0.245$. The observed values are derived from the 14 clusters without blue HBs (see Section 3.3.8). The uncertainty for the standard-overshoot models is the standard deviation from the results of the calculations using different f_{OS} that are discussed in Section 3.4.7.

	R_2	$\Delta \log L_{\text{HB}}^{\text{AGB}}$
Observations	0.117 ± 0.005	0.455 ± 0.012
No overshoot	0.783	0.22
Semiconvection	0.068	0.53
Standard overshoot	0.075 ± 0.025	0.46 ± 0.15
Maximal overshoot	0.082	0.60

servations, producing a luminosity PDF (Figure 3.8c) that is starkly at odds with the observations shown in Figure 3.7. This result has been found previously (e.g. Buzzoni et al., 1983; Buonanno et al., 1985; Bressan et al., 1986; Chiosi et al., 1987; Renzini and Fusi Pecci, 1988; Caputo et al., 1989; Cassisi et al., 2001) and is consistent with the finding from asteroseismology that larger convective cores are preferred (Montalbán et al., 2013, ; Chapter 2). It also has a strong theoretical basis because of the physical instability of the convective boundary. We do not discuss these models further.

Among the other three models, the CHeB lifetime differs by less than 9 Myr, which is only around 8 per cent. The maximal-overshoot sequence has a larger R_2 and $\Delta \log L_{\text{HB}}^{\text{AGB}}$ than the semiconvection sequence; this is also true throughout this study, regardless of initial composition or input physics. Of the three sequences in Figure 3.8, the one with standard overshoot has the lowest $\Delta \log L_{\text{HB}}^{\text{AGB}}$. However, $\Delta \log L_{\text{HB}}^{\text{AGB}}$ and CHeB lifetime for the standard-overshoot sequences strongly depend on the time step constraints and the overshooting parameter f_{OS} . These dependences are explored in Section 3.4.7. Each of these three mixing schemes fails to match the average R_2 observed: the standard-overshoot, semiconvection, and maximal-overshoot sequences have $R_2 = 0.096$, 0.068, and 0.082, respectively, compared with the observed average $R_2 = 0.117 \pm 0.005$.

In addition to the R_2 discrepancy, none of the models in Figure 3.8 can match $\Delta \log L_{\text{HB}}^{\text{AGB}} = 0.455 \pm 0.012$ from observations. The standard-overshoot, semiconvection, and maximal-overshoot sequences have $\Delta \log L_{\text{HB}}^{\text{AGB}} = 0.38$, 0.53, and 0.60, respectively. Contrary to the case for R_2 , the observed $\Delta \log L_{\text{HB}}^{\text{AGB}}$ at least sits within the spread resulting from the three mixing schemes. Figure 3.8(b) shows that the luminosity during CHeB is independent of the mixing scheme. The broad range in $\Delta \log L_{\text{HB}}^{\text{AGB}}$ is due to the disparity in the masses of the helium-exhausted cores at the onset of shell helium burning. In these sequences, shell helium burning begins with carbon-oxygen core masses of

approximately $0.05 M_{\odot}$, $0.10 M_{\odot}$, and $0.14 M_{\odot}$, respectively. The dependence of the AGB clump luminosity on the mass enclosed by the early-AGB helium-burning shell strongly suggests that the CHeB partially mixed region extends too far in the semiconvection and maximal-overshoot models.

After CHeB, when helium burning moves to a shell, the no-overshoot and maximal-overshoot models both have chemical discontinuities at the convective core boundary. This leads to ‘gravonuclear loops’ (see e.g. Bono et al., 1997a,b; Sweigart et al., 2000; Bressan et al., 2015), which cause an oscillation in surface luminosity that lasts for a few million years (near 55 Myr and 110 Myr for the respective sequences in Figure 3.8b). These convection and burning episodes eventually end once a smooth helium composition profile has been established. We discuss their effect on R_2 and $\Delta \log L_{\text{HB}}^{\text{AGB}}$ in the maximal-overshoot case in Section 3.4.9. In addition, we show that convective overshoot during the early-AGB phase in these models can reduce the disagreement with observations.

3.4.6 Effects of composition and other input physics

MLT mixing length

In Figure 3.9 we show the evolution of models with three different mixing schemes using three different values for the MLT mixing length parameter α_{MLT} . The models were evolved with the same solar-calibrated value of $\alpha_{\text{MLT}} = 1.53$ before the core flash but then with the solar-calibrated value, and increases of $\Delta\alpha_{\text{MLT}} = +0.2$ and $\Delta\alpha_{\text{MLT}} = +1.0$. It is clear from panel (a) that each group of runs with a different α_{MLT} forms a distinct evolutionary track in the HR diagram (the effective temperature T_{eff} increases with higher α_{MLT}). Models with the same mixing scheme, but different α_{MLT} , have exactly the same luminosity evolution, which is why each group of three sequences appears to form a single curve in Figure 3.9(a). The luminosity PDFs are similarly unaffected by changes to α_{MLT} (Figure 3.9c), so we may safely proceed with our luminosity comparisons between models and observations without finding a suitable α_{MLT} to match the theoretical and observed T_{eff} for each case.

Effects of initial helium abundance

It has been suggested that some globular clusters host helium-rich subpopulations. Evidence for this includes the detection of multiple main sequences (e.g. Bedin et al., 2004; Norris, 2004; Piotto et al., 2005, 2007; Milone et al., 2013; Milone, 2015), HB morphology (e.g. D’Antona et al., 2002; Lee et al., 2005; Caloi and D’Antona, 2005, 2007), spectroscopy of hot HB stars (Villanova et al., 2009, 2012; Marino et al., 2014), and abundance patterns

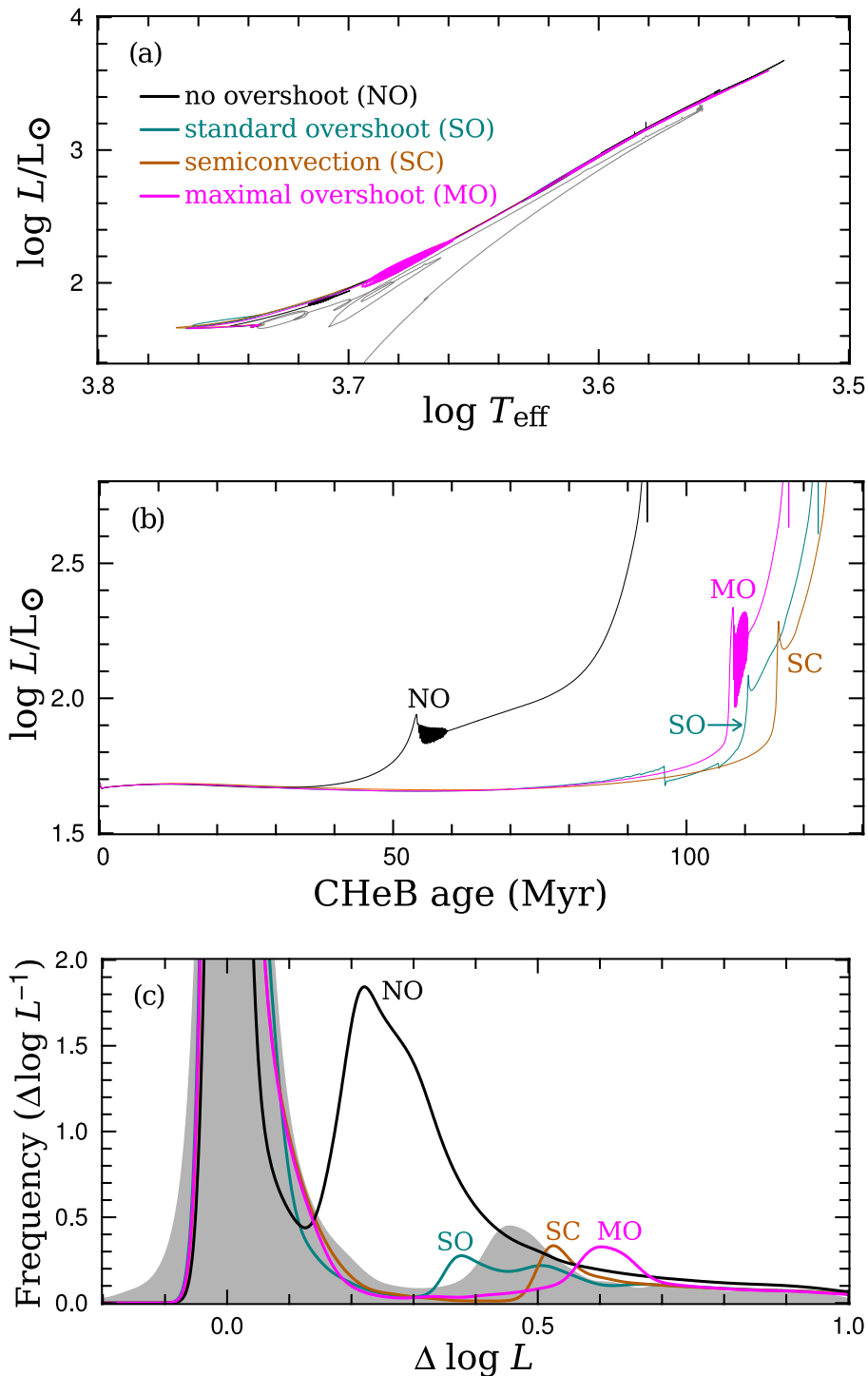


Figure 3.8: Comparison of models with different CHEB mixing schemes: standard overshoot, semiconvection, no overshoot, and maximal overshoot in cyan, orange, black, and magenta, respectively. The models have initial mass $M_i = 0.83 M_{\odot}$, metallicity $[\text{Fe}/\text{H}] = -1$, and initial helium $Y = 0.245$. **Upper panel:** evolution tracks in the HR diagram. **Middle panel:** surface luminosity evolution. **Lower panel:** post-RGB luminosity probability density functions (PDF). The shaded area is the observed PDF for all clusters without a blue HB, i.e. the combination of the two curves in Figure 3.7.

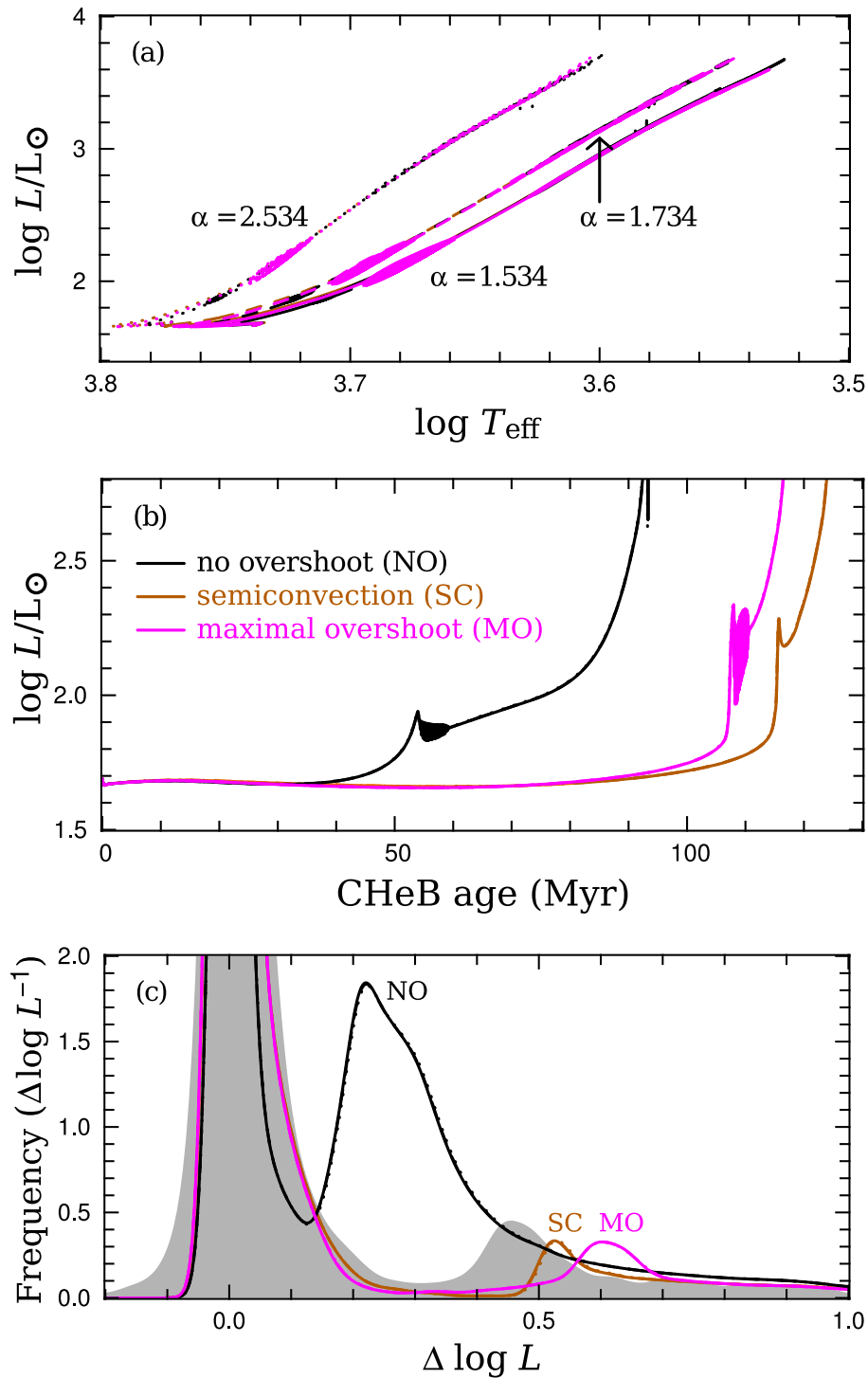


Figure 3.9: Comparison of CHeB and early-AGB models with semiconvection, no overshoot, and maximal overshoot (in orange, black, and magenta) with three different values for the MLT mixing length parameter α_{MLT} (1.534, 1.734, and 2.534, shown by solid, dashed, and dotted lines, respectively). The panels are the same as Figure 3.8. Note that the luminosity dependence on α_{MLT} is so weak that the different curves cannot be distinguished from one another.

that point towards various scenarios of self-enrichment in the products of hydrogen burning (e.g. Ventura et al., 2002; Decressin et al., 2007; de Mink et al., 2009; Denissenkov and Hartwick, 2014). The consequences of changing the initial helium abundance in models must therefore be considered.

The effect of increasing the initial helium abundance Y by $\Delta Y = 0.039$ is shown by the evolution sequences in Figure 3.10. Increasing the helium mass fraction, while decreasing the initial mass so that the age is unchanged, tends to decrease R_2 . In the metallicity range tested ($-2 \leq [\text{Fe}/\text{H}] \leq -0.5$), however, the effect is small. We find for the semiconvection and maximal-overshoot models that

$$\frac{\partial R_2}{\partial Y} \approx -0.05. \quad (3.8)$$

The important factors contributing to this trend are the decrease, with increasing helium, of the mass of both the envelope and the H-exhausted core. The envelope mass is reduced because increasing the initial helium abundance, while keeping the age constant, reduces the initial stellar mass. Both of the factors mentioned slow helium burning throughout CHeB. This lengthens the CHeB phase and lowers the absolute luminosity of the AGB cut-off (see Section 3.3.7), which both decrease R_2 . The effects of changing only the H-exhausted core mass and only the initial mass are examined in Section 3.4.6.

The reduction in R_2 resulting from increasing the initial helium becomes more substantial when the metallicity is higher, whereas the effect on $\Delta \log L_{\text{HB}}^{\text{AGB}}$ becomes smaller with increasing metallicity. There is also a significant difference between the effect on semiconvection and maximal-overshoot models. Models with the former mixing scheme show a greater increase in $\Delta \log L_{\text{HB}}^{\text{AGB}}$ with increasing initial helium. This difference appears to be due to the effect on the luminosity of the AGB clump. Increasing helium by $\Delta Y = 0.039$ decreases the HB luminosity by $\Delta \log L_{\text{HB}} = -0.015$ for both mixing schemes. In contrast, it increases the luminosity of the AGB clump by nearly $\Delta \log L_{\text{HB}} = 0.03$ for the semiconvection run while having no effect on the maximal-overshoot sequence. At its largest (for the $[\text{Fe}/\text{H}] = -2$ semiconvection model) we find that

$$\frac{\partial \Delta \log L_{\text{HB}}^{\text{AGB}}}{\partial Y} \approx 1.25. \quad (3.9)$$

It therefore appears that accounting for the small variation in initial helium allowed for most globular clusters could have a modest effect on $\Delta \log L_{\text{HB}}^{\text{AGB}}$ and a negligible effect on R_2 .

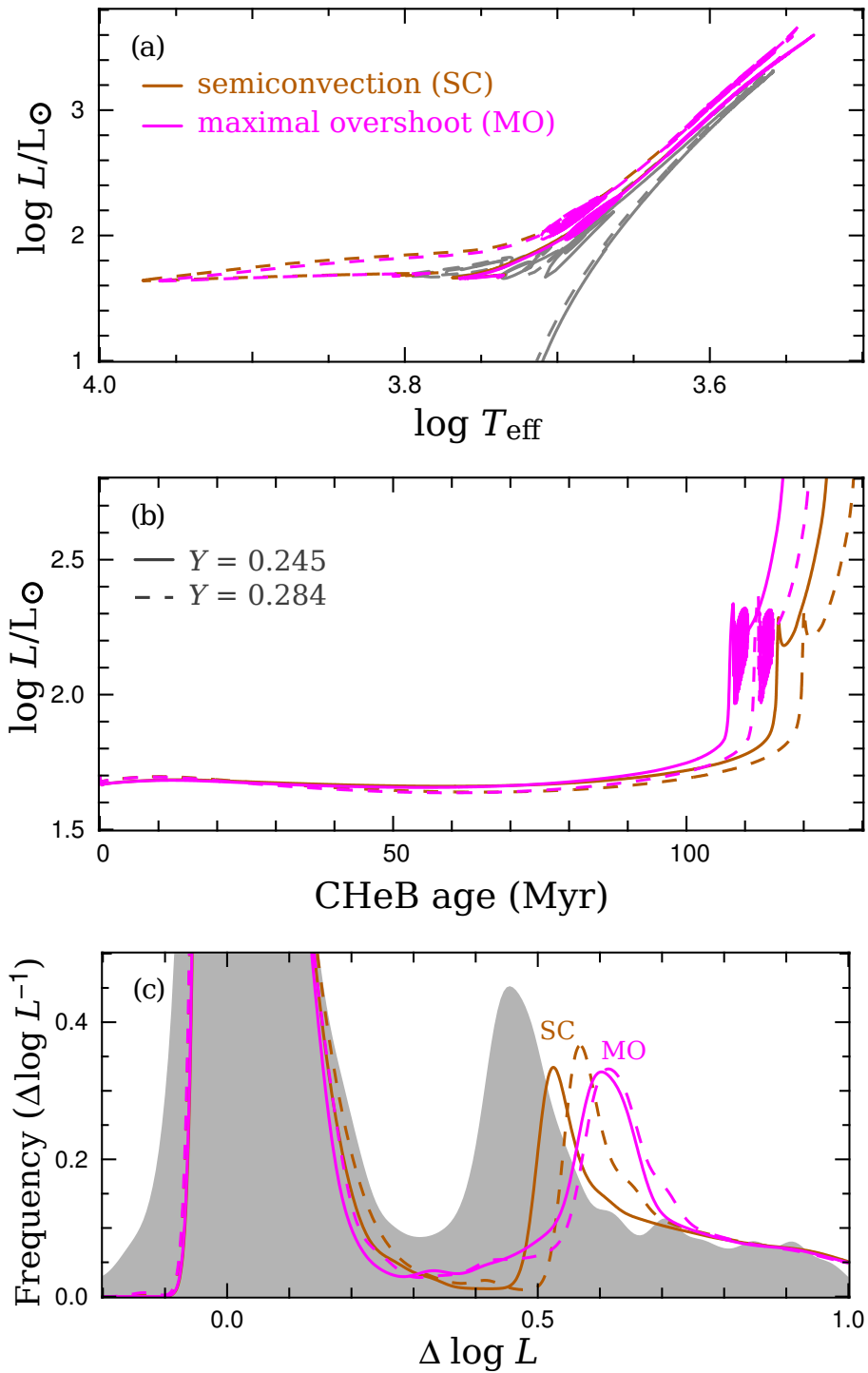


Figure 3.10: Comparison of semiconvection (orange) and maximal overshoot (magenta) models with different initial helium abundance: $Y = 0.245$ (solid lines) and $Y = 0.284$ (dashed lines). The models have metallicity $[\text{Fe}/\text{H}] = -1$ and initial mass $M/M_{\odot} = 0.83$ and $M/M_{\odot} = 0.78$, respectively, so that they have the same age. The panels are the same as Figure 3.8.

Metallicity

In Figure 3.11 we present models with three different metallicities: $[\text{Fe}/\text{H}] = -2, -1,$ and -0.5 . These span most of the metallicity range in our globular cluster sample (shown in Figure 3.3). Increasing the metallicity tends to very slightly decrease R_2 in models, where we find

$$\frac{\partial R_2}{\partial [\text{Fe}/\text{H}]} \approx -0.003. \quad (3.10)$$

Similarly, $\Delta \log L_{\text{HB}}^{\text{AGB}}$ decreases with increasing metallicity according to

$$\frac{\partial \Delta \log L_{\text{HB}}^{\text{AGB}}}{\partial [\text{Fe}/\text{H}]} \approx -0.02, \quad (3.11)$$

but this change is not consistent between models with different mixing schemes or composition. Both of these trends are small enough to be consistent with the absence of a detectable metallicity trend in the observations, for which there is also considerable scatter (Figure 3.3) and an unknown trend in helium abundance and cluster age which also affect theoretical predictions.

Effects of helium burning reaction rates

Uncertainties in helium burning reaction rates are an important complication for efforts to constrain the mixing in CHeB models. We have examined the effects of changing the triple- α and $^{12}\text{C}(\alpha, \gamma)^{16}\text{O}$ reaction rates, both separately and concurrently. We change these reaction rates by up to factors of two and four, which is larger than their respective uncertainties of 15 per cent and 40 per cent (Angulo et al., 1999). Examples of these tests are presented in Figures 3.12 and 3.13.

Increasing the triple- α rate reduces the H-exhausted core mass at the flash and therefore also the mass of the subsequent convective core (see Chapter 2). Later in CHeB the triple- α reaction is then favoured at the expense of the $^{12}\text{C}(\alpha, \gamma)^{16}\text{O}$, reducing the total energy that can be released from helium burning. Both of these consequences contribute to the shortening of the CHeB phase. In contrast, increasing the $^{12}\text{C}(\alpha, \gamma)^{16}\text{O}$ rate obviously favours that reaction, releasing more energy, which then causes an increase in the fuel supply by expanding the mass enclosed by the convective core. These effects lead to an increase in the CHeB lifetime.

Doubling the triple- α rate decreases the absolute luminosity of the HB and AGB clump equally and therefore has little effect on $\Delta \log L_{\text{HB}}^{\text{AGB}}$. Increasing the $^{12}\text{C}(\alpha, \gamma)^{16}\text{O}$ rate by the same factor has only about one fifth of the effect on the HB luminosity compared with an equal change of the triple- α rate. In the semiconvection models the early-AGB

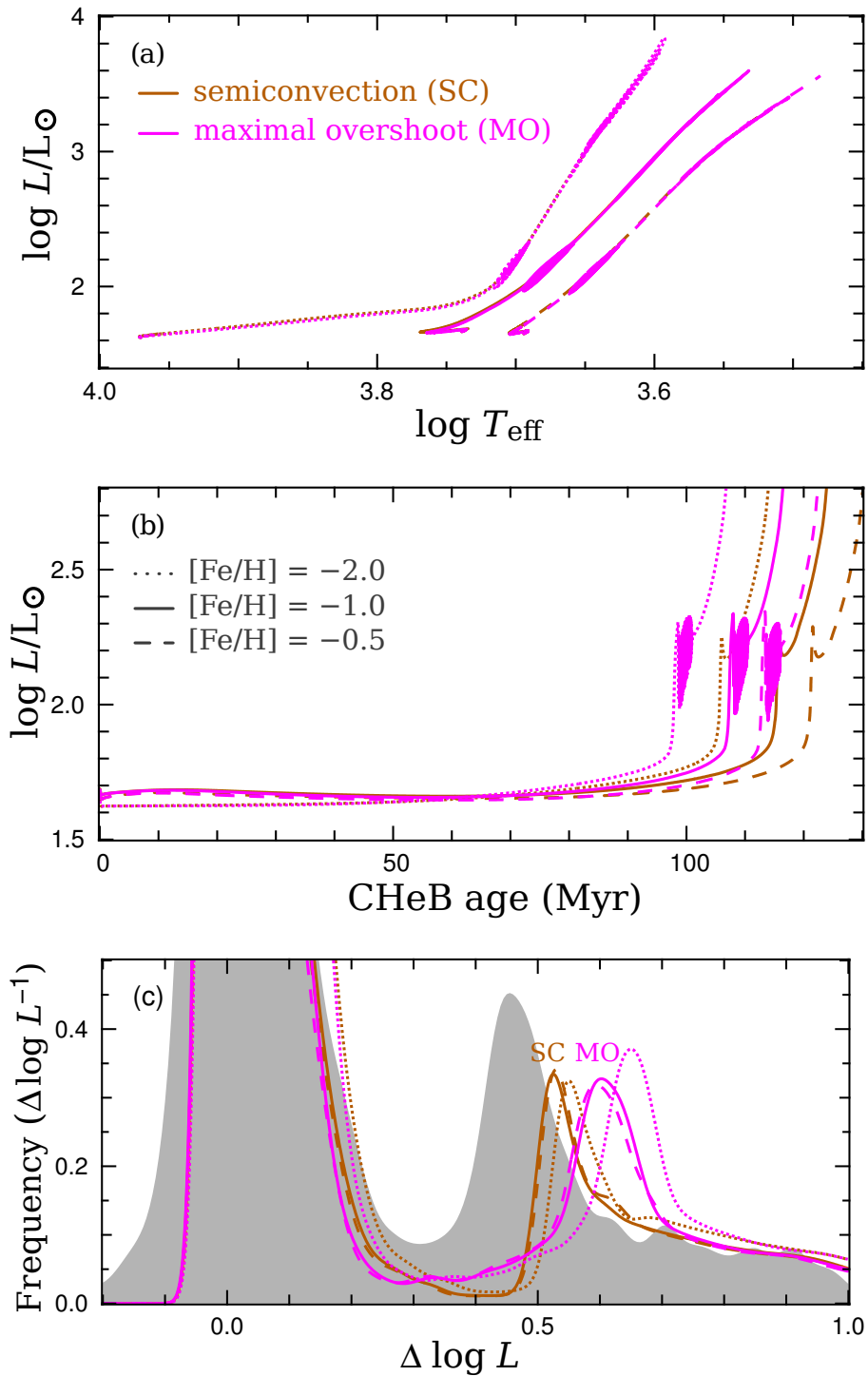


Figure 3.11: Comparison of semiconvection (orange) and maximal overshoot (magenta) models with different metallicities, $[\text{Fe}/\text{H}] = -2$, -1 , and -0.5 (shown by dotted, solid, and dashed lines, respectively), and initial masses $M_i/M_{\odot} = 0.80$, 0.83 , and 0.89 so that they are each 13 Gyr old. The panels are the same as Figure 3.8.

luminosity (and therefore also $\Delta \log L_{\text{HB}}^{\text{AGB}}$) is relatively unaffected. This contrasts with the maximal-overshoot models, where the increased $^{12}\text{C}(\alpha, \gamma)^{16}\text{O}$ rate, and consequently larger convective core at the end of CHeB, pushes the position of subsequent He-burning shell outward during the early-AGB and increases the luminosity, and thus also $\Delta \log L_{\text{HB}}^{\text{AGB}}$. In these maximal-overshoot models we find that

$$\frac{\partial \Delta \log L_{\text{HB}}^{\text{AGB}}}{\partial \log r_{\text{C}\alpha}} = 0.09. \quad (3.12)$$

In models with either semiconvection and maximal overshoot, increasing the triple- α rate increases R_2 whereas increasing the $^{12}\text{C}(\alpha, \gamma)^{16}\text{O}$ rate decreases R_2 . The strength of the effects, however, depends on the mixing scheme. In the maximal-overshoot case we find that

$$\frac{\partial R_2}{\partial \log r_{3\alpha}} = 0.025, \quad (3.13)$$

and

$$\frac{\partial R_2}{\partial \log r_{\text{C}\alpha}} = -0.04, \quad (3.14)$$

which are both around double that for the semiconvection models. We have also confirmed that these partial derivatives hold when the two reaction rates are changed simultaneously.

Effect of neutrino emission rate

The neutrino production mechanism most important to the evolution of CHeB stars is the plasma process, which is an efficient cooling mechanism for the degenerate core prior to the ignition of helium. Observations of globular cluster stars provide some of the best constraints for non-standard neutrino electromagnetic coupling (e.g. Raffelt, 1999; Viaux et al., 2013a). This is because additional cooling from plasma neutrino emission would delay the core flash and allow the core mass to grow further, thereby increasing the luminosity of the RGB-tip stars. In Chapter 2 we showed that an increased H-exhausted core mass at the flash could help resolve the discrepancy between the predicted and observationally inferred asymptotic g-mode period spacing $\Delta \Pi_1$ in *Kepler* field stars. Other exotic processes could also affect CHeB evolution, such as axion production via the Primakoff effect. This would be most significant during the CHeB phase, when the core is non-degenerate, and would shorten the HB lifetime (Raffelt, 2012).

In this section we test the results of an ad hoc increase to the neutrino emission rate by a factor of four. Because this prolongs the RGB evolution we also halt mass loss when the total mass reaches that of the standard run at the RGB-tip, ensuring that the comparisons are between models of the same total mass. We have also computed sequences in which the neutrino emission rate is returned to the standard rate after the core flash. This serves

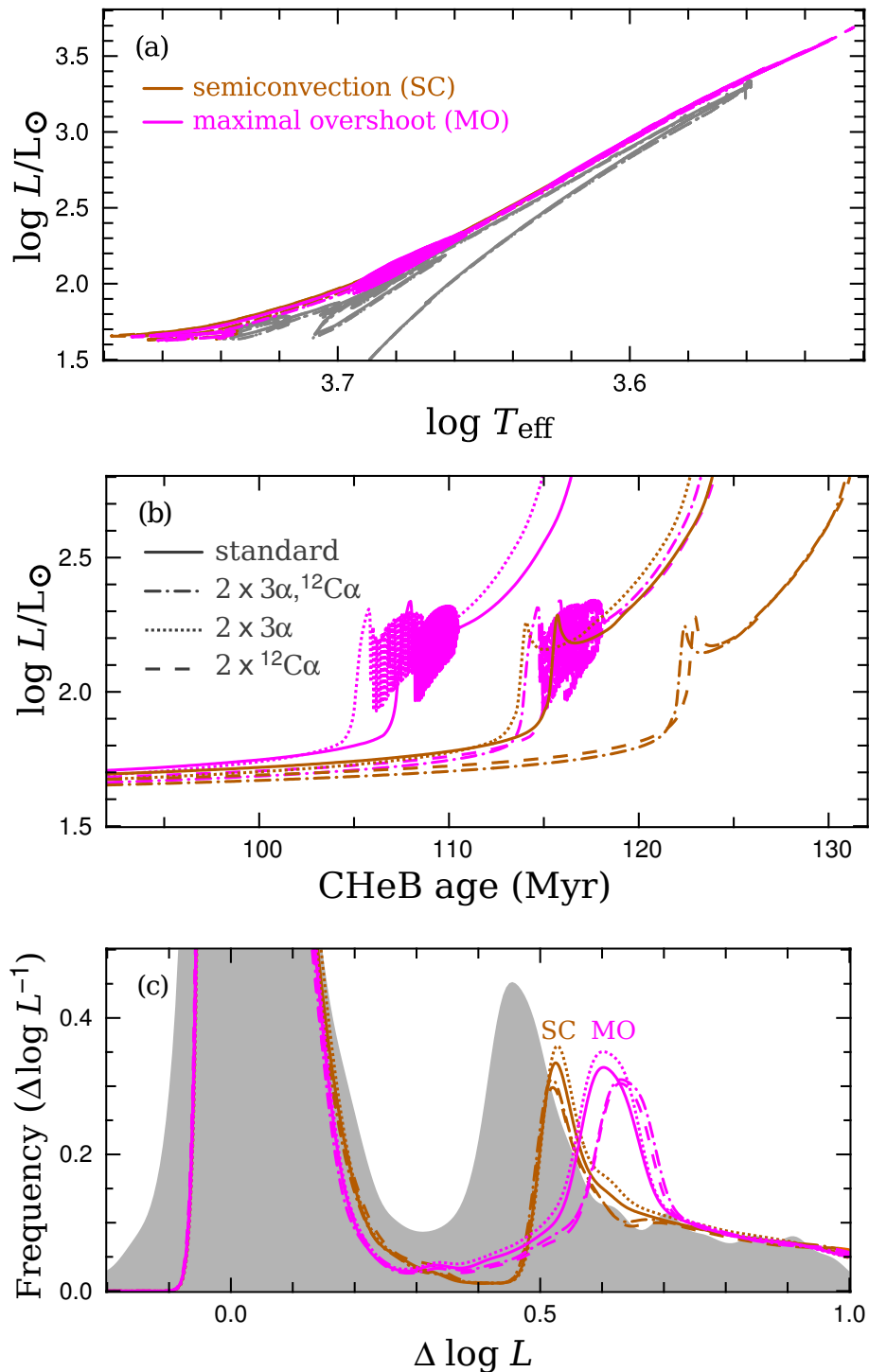


Figure 3.12: Comparison of CHeB and early-AGB evolution for models with semiconvection (orange) and maximal overshoot (magenta) and different helium-burning reaction rates. The models have standard reaction rates (solid lines), double the triple- α rate (dotted lines), double the triple- α and ${}^{12}\text{C}(\alpha, \gamma){}^{16}\text{O}$ rates (dotted dashed lines), and double the ${}^{12}\text{C}(\alpha, \gamma){}^{16}\text{O}$ rate (dashed lines). The panels are the same as Figure 3.8.

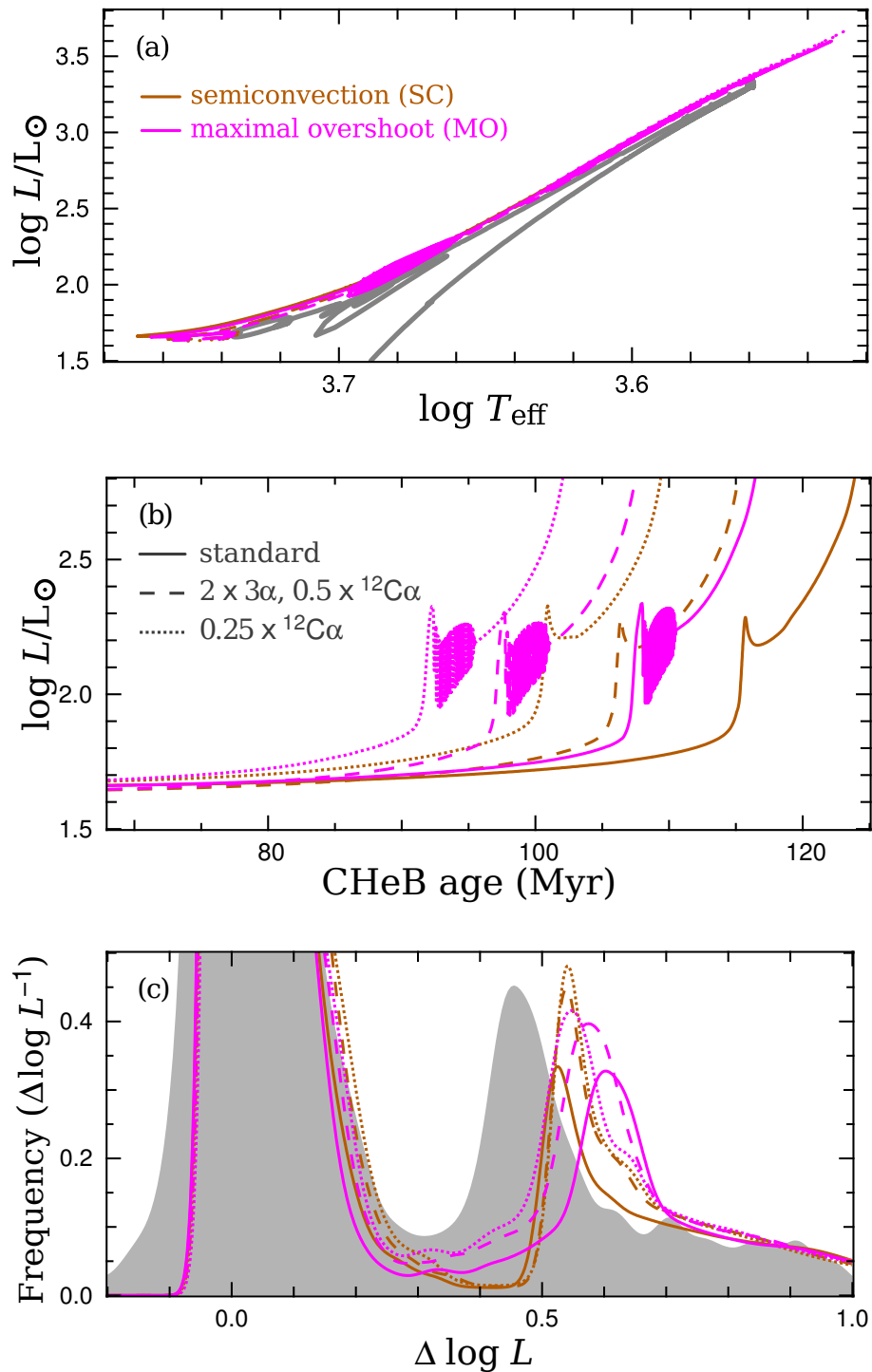


Figure 3.13: Comparison of CHeB and early-AGB evolution for models with semiconvection (orange) and maximal overshoot (magenta) and different helium-burning reaction rates. The models have standard reaction rates (solid lines), the ${}^{12}\text{C}(\alpha, \gamma){}^{16}\text{O}$ rate multiplied by a factor of a quarter (dotted lines), and double the triple- α and half the ${}^{12}\text{C}(\alpha, \gamma){}^{16}\text{O}$ rate (dashed lines). The panels are the same as Figure 3.8.

as a proxy for other physical uncertainties whose main effect is to alter the core mass at the flash.

The modification to the neutrino emission rate ϵ_ν throughout the evolution of the semiconvection and maximal-overshoot runs causes a decrease in R_2 according to

$$\frac{\partial R_2}{\partial \log \epsilon_\nu} = -0.03. \quad (3.15)$$

This dependence is due to the additional early-AGB neutrino losses rather than any effect on the preceding RGB evolution. Given that R_2 in standard models is already lower than the observed range, this appears to be another strong restriction on the magnetic dipole moments of neutrinos, which would increase the emission from plasmon decay.

If the standard neutrino emission rate is restored after the flash, the models both show

$$\left| \frac{\partial R_2}{\partial \log \epsilon_\nu} \right| < 0.008. \quad (3.16)$$

The main structural change in those models is an increase of the H-exhausted core mass at the flash. Multiplying the neutrino emission rate by a factor of four increases the H-exhausted core mass at the flash M_{He} by $0.029 M_\odot$. The dependence in Equation 3.16 can therefore be expressed as

$$\left| \frac{\partial R_2}{\partial M_{\text{He}}/M_\odot} \right| < 0.15. \quad (3.17)$$

In the maximal overshoot sequence for instance, the $0.029 M_\odot$ increase in M_{He} , which is larger than permitted by other constraints (Catelan et al., 1996), decreases R_2 by 0.001 and increases $\Delta \log L_{\text{HB}}^{\text{AGB}}$ by just 0.015. This demonstrates that reasonable uncertainty in the core mass at the flash does not significantly affect R_2 or $\Delta \log L_{\text{HB}}^{\text{AGB}}$.

The ratio R_2 could form an even tighter constraint on novel particle emission than the previously used ratio $R = n_{\text{HB}}/n_{\text{RGB}}$, because any ‘dark channel’ that is more active during the early-AGB than CHeB would further lower R_2 and worsen agreement to standard models. This should be an obligatory consideration when comparing stellar models with globular cluster observations to determine these constraints. Although this is beyond the scope of this work, we do note that unlike the earlier RGB evolution in which the core is degenerate, the burning shell that surrounds the degenerate core during the early-AGB is hot enough to support helium burning (and is hotter than CHeB), which would have implications for temperature sensitive effects, such as Primakoff conversion from axion-photon coupling which has a specific energy loss rate that goes as T^7/ρ (Friedland et al., 2013; Aoyama and Suzuki, 2015). Indeed, Domínguez et al. (1999) have already shown that this can significantly truncate the early-AGB lifetime in more massive models

($M \geq 3 M_{\odot}$).

When the altered neutrino loss rate is applied only before the core flash we find

$$\frac{\partial \Delta \log L_{\text{HB}}^{\text{AGB}}}{\partial \log \epsilon_{\nu}} \approx 0.025, \quad (3.18)$$

or equivalently, a weak dependence on H-exhausted core mass:

$$\frac{\partial \Delta \log L_{\text{HB}}^{\text{AGB}}}{\partial M_{\text{He}}/M_{\odot}} \approx 0.50. \quad (3.19)$$

Retaining the higher neutrino emission during the CHeB and early-AGB phases further increases $\Delta \log L_{\text{HB}}^{\text{AGB}}$ in models with maximal overshoot. In models with the altered neutrino emission rate for the whole evolution, we find

$$\frac{\partial \Delta \log L_{\text{HB}}^{\text{AGB}}}{\partial \log \epsilon_{\nu}} \approx 0.08, \quad (3.20)$$

which is a rate of change more than three times that for models with altered neutrino losses only during the RGB. In contrast, ϵ_{ν} has a negligible effect on $\Delta \log L_{\text{HB}}^{\text{AGB}}$ for the semiconvection models. We further discuss the early-AGB evolution of the maximal overshoot models in Section 3.4.9.

In Chapter 2 we showed that the increased M_{He} from enhanced neutrino emission during the RGB improves the agreement between CHeB models and asteroseismology. Interestingly though, models with increased neutrino emission throughout the evolution show an even worse agreement with the observed R_2 (the quadrupling of the neutrino emission rate reduces R_2 by more than 0.015 for both the mixing schemes tested). There is also no improvement compared with ordinary models when the excess neutrino losses are stopped after the core flash (emulating any process whose main effect is to increase M_{He}). Even a substantial core mass increase of $\Delta M_{\text{HB}} = 0.029 M_{\odot}$ produces only small changes to R_2 and $\Delta \log L_{\text{HB}}^{\text{AGB}}$. The insensitivity of R_2 (according to the definition in this study) to uncertainties in M_{He} increases its diagnostic power for CHeB mixing.

Stellar initial mass / age

We have tested the effect of increasing the initial stellar mass for $[\text{Fe}/\text{H}] = -0.5$ models while keeping other parameters unchanged. In this case, increasing the initial mass of the $M = 0.84 M_{\odot}$ model by $0.05 M_{\odot}$ reduces the age at the beginning of CHeB by 2.4 Gyr. In sequences with either semiconvection or maximal overshoot, increasing the initial mass decreases both R_2 and $\Delta \log L_{\text{HB}}^{\text{AGB}}$. We can quantify the changes (with respect to either

initial mass or age) by

$$\frac{\partial \Delta \log L_{\text{HB}}^{\text{AGB}}}{\partial M_i/M_\odot} \approx -0.30, \quad (3.21)$$

or

$$\frac{\partial \Delta \log L_{\text{HB}}^{\text{AGB}}}{\partial t_{\text{ZAHB}}} \approx 0.007, \quad (3.22)$$

where t_{ZAHB} is the age in Gyr. This dependence is not significant given the size of the uncertainty in globular cluster stellar mass and age. R_2 is similarly insensitive to initial mass, although in that case the effect is not consistent between the two mixing schemes.

In both cases we find that

$$-0.07 < \frac{\partial R_2}{\partial M_i/M_\odot}, \quad (3.23)$$

and

$$\frac{\partial R_2}{\partial t_{\text{ZAHB}}} < 0.0015. \quad (3.24)$$

We have also isolated the dependence of R_2 and $\Delta \log L_{\text{HB}}^{\text{AGB}}$ on the zero-age HB mass by halting mass loss before the RGB tip. We find for the $[\text{Fe}/\text{H}] = -0.5$ models that

$$\frac{\partial \Delta \log L_{\text{HB}}^{\text{AGB}}}{\partial M_{\text{ZAHB}}/M_\odot} = -0.23, \quad (3.25)$$

and

$$\frac{\partial R_2}{\partial M_{\text{ZAHB}}/M_\odot} = -0.019. \quad (3.26)$$

In contrast, there are only negligible differences for models that differ in age by 2.4 Gyr but have the same total ZAHB mass. This conclusively shows that the dissimilar CHeB evolution in models with a different initial mass stems from how it affects the zero-age HB mass. This is important because there is some degeneracy between mass loss rate and initial mass/cluster age. Moreover, the change in R_2 from increasing the initial mass but keeping helium constant is opposite to that found when helium is also adjusted so that the age is kept constant when the mass is increased (see Section 3.4.6). The weak dependence of R_2 and $\Delta \log L_{\text{HB}}^{\text{AGB}}$ on stellar age validates our assumption in Section 3.4 that it is unnecessary to make specific models to match the age of each cluster.

Summary of these effects

We have used the dependences identified in this section to estimate the overall uncertainties in predictions for R_2 and $\Delta \log L_{\text{HB}}^{\text{AGB}}$ from factors other than the mixing scheme. In order to do this we used the following approximate uncertainties in the models: $\Delta r_{3\alpha}/r_{3\alpha} = 0.15$, $\Delta r_{\text{C}\alpha}/r_{\text{C}\alpha} = 0.40$ (Angulo et al., 1999), $\Delta Y = 0.04$, $\Delta[\text{Fe}/\text{H}] = 1.0$,

$\Delta t_{\text{ZAHB}} = 2 \text{ Gyr}$, $\Delta M_{\text{He}} = 0.01 M_{\odot}$, and $\Delta M_{\text{ZAHB}} = 0.05 M_{\odot}$. By adding each of the consequential contributions to the uncertainties in R_2 and $\Delta \log L_{\text{HB}}^{\text{AGB}}$ in quadrature, we find that the $1\text{-}\sigma$ uncertainty in R_2 is 0.009 and in $\Delta \log L_{\text{HB}}^{\text{AGB}}$ it is 0.04. The dominant source of uncertainty for R_2 is the $^{12}\text{C}(\alpha, \gamma)^{16}\text{O}$ reaction rate. The most important factor for $\Delta \log L_{\text{HB}}^{\text{AGB}}$ is composition, including both helium abundance and metallicity. The uncertainty of R_2 in models is comparable to the statistical uncertainty in the observations ($\sigma_{R_2, \text{obs}} = 0.005$) but for $\Delta \log L_{\text{HB}}^{\text{AGB}}$ the uncertainty in models is many times larger than the statistical uncertainty in the observations ($\sigma_{\Delta \log L, \text{obs}} = 0.012$). Both of these uncertainties are smaller than the changes resulting from the use of different mixing schemes (see e.g. Figure 3.8c). This confirms that R_2 and $\Delta \log L_{\text{HB}}^{\text{AGB}}$ are powerful constraints for the mixing in the core.

3.4.7 Numerical effects

Dependence on the overshooting parameter

In our standard overshoot runs we apply the overshooting scheme proposed by Herwig et al. (1997) that has an exponential decay in diffusion coefficient according to

$$D_{\text{OS}}(z) = D_0 e^{-\frac{2z}{H_v}}, \quad (3.27)$$

where $D_{\text{OS}}(z)$ is the diffusion coefficient at distance z from the convective boundary and D_0 is the diffusion coefficient just inside the boundary. H_v is the ‘velocity scale height’ defined as

$$H_v = f_{\text{OS}} H_p, \quad (3.28)$$

where H_p is the pressure scale height, and we have chosen $f_{\text{OS}} = 0.001$ for this study. In Figure 3.14 we show the consequences of altering this value and an example of suppressing core breathing pulses (thick line) by stopping overshooting when the central helium abundance is low (this is analysed in Section 3.4.8).

It is clear from Figure 3.14(b) that the extent of overshoot does not significantly alter the luminosity until late in core helium burning. This is not surprising, given that the luminosity evolution during CHeB is scarcely affected by the choice of mixing prescription (Figure 3.8). Near core helium exhaustion, however, the range of variation between standard overshoot models with different values of f_{OS} is greater than it is for models with entirely different mixing schemes (compare e.g. the standard overshoot and semiconvection runs in Figures 3.8b and 3.14b). In these tests, modifying f_{OS} can change the CHeB lifetime by up to 30 Myr (more than 20 per cent of the CHeB lifetime).

This also leads to extremely large variations in R_2 and $\Delta \log L_{\text{HB}}^{\text{AGB}}$. In the five models shown in Figure 3.14 with $0.001 \leq f_{\text{OS}} \leq 0.05$ we find ranges of $0.036 \leq R_2 \leq 0.091$ and $0.38 \leq \Delta \log L_{\text{HB}}^{\text{AGB}} \leq 0.72$. During CHeB, these models have average time step $10^4 \text{ yr} < \overline{\Delta t} < 2 \times 10^4 \text{ yr}$.

Two of the five evolution sequences in Figure 3.14(a) show blueward excursions, or ‘blue loops’, in the HR diagram. In this example they belong to the two longest lived CHeB sequences. They immediately follow the ingestion of helium into the core during CBP and last for about 200 kyr (which is less than 0.2 per cent of the CHeB lifetime). If real, these would be sufficiently short-lived to make it unlikely that a star in this phase would be observed and thus provide evidence for the existence of CBP. Even if they were observed, they could also be interpreted as less massive stars because they share the same position in the HR diagram (see e.g. the lower-mass models Figure 3.10).

Each of the models in Figure 3.14(c) shows multiple peaks in AGB region of the luminosity PDF. These are not seen in models with the other mixing schemes. The first (lowest $\log L$) peak is caused by the drop and subsequent slow increase in luminosity immediately after core helium exhaustion. The subsequent peaks are caused by the helium burning shell encountering a region richer in helium when it moves through a composition discontinuity in the partially mixed region. This temporarily speeds up the rate of increase of the surface luminosity. These episodes are analogous to the RGB luminosity function bump which is caused by the advance of the hydrogen burning shell through the composition discontinuity left by first dredge-up. This explanation makes it clear why none of the other mixing schemes show this phenomenon: the no-overshoot and maximal-overshoot models do not have a partially mixed zone and the semiconvection models do not leave behind any composition discontinuities.

The clarity of the subsequent peaks in the AGB luminosity PDF depends on both the difference in composition across the discontinuities and the mass enclosed by them. If two discontinuities are close together in mass (or one is near to the earlier boundary of the convective core) then it can be hard to distinguish the two peaks. In the case where CBP are prevented, for example, the first two peaks are separated by $\Delta \log L = 0.07$ (thick line in Figure 3.14). If the partially mixed region is very large it is similarly difficult to detect the second peak because the burning front moves through the edge of the partially mixed region at higher luminosity, when the evolution is fast (there are examples of this in the range $0.6 \leq \Delta \log L \leq 0.9$ shown in Figure 3.14c). The differences in the luminosity PDFs that arise from the suite of standard overshoot sequences reflects the broad variation in the structure of their partially mixed regions by the end of CHeB.

In general, there is a stochastic dependence of R_2 and $\Delta \log L_{\text{HB}}^{\text{AGB}}$ on f_{OS} . An excep-

tion to this is when a very large f_{OS} is used. In the example run with $f_{\text{OS}} = 0.05$ the overshoot penetrates so far that the partially mixed region consists of a single zone with a homogeneous helium abundance between that of the convective core and the helium-rich shell surrounding it. This means that after core helium exhaustion there is no composition discontinuity to burn through until the front moves to the edge of the partially mixed zone, which occurs when the luminosity is much higher (when $\log L/L_{\odot} > 2.5$ in that example). That model also shows the earliest instability in the core boundary, after only about 40 Myr. There are four small CBP throughout CHeB, each separated by 16 Myr, rather than the typical large CBP late in CHeB (when $Y < 0.1$ in the core). Despite the unusual evolution during CHeB, the sequence has $R_2 = 0.086$ and $\Delta \log L_{\text{HB}}^{\text{AGB}} = 0.44$ which are both unremarkable for standard overshoot.

Time step dependence

In this section we investigate how different time step constraints affect the evolution of our standard-overshoot runs. In Figure 3.15 we show five standard-overshoot models with $f_{\text{OS}} = 0.001$ that differ only in the number of time steps taken during the CHeB phase. Among the different runs we find $0.36 \leq \Delta \log L_{\text{HB}}^{\text{AGB}} \leq 0.51$ and $0.080 \leq R_2 \leq 0.096$. Overall, the evolution of the suite of standard-overshoot models with different average time step is more consistent than it is among the group with different f_{OS} shown in the previous section. The ranges of $\Delta \log L_{\text{HB}}^{\text{AGB}}$ and R_2 are both smaller, but there is still a significant spread. The variation in the CHeB lifetime from changing the time step, of around 10 Myr (~ 9 per cent of the CHeB lifetime; Figure 3.15b), is also smaller than for the suite of models with different f_{OS} (Figure 3.14b). We do not find a correlation between the size of the time steps and the properties of the evolution, mirroring our finding for modifications to f_{OS} .

We have shown that time step constraints and the overshoot prescription can both have unpredictable and severe effects on the evolution of standard-overshoot models late in CHeB, importantly including predictions for $\Delta \log L_{\text{HB}}^{\text{AGB}}$ and R_2 . The stochasticity of the evolution is the reason we have not used standard overshoot in the earlier sections to quantify the effects of altering the input physics. Moreover, we note that the evolution of a single model produces AGB clump peaks in the luminosity PDF (e.g. Figure 3.14c and 3.15c) that are broader than both of those resulting from the addition of observed data for multiple clusters (Figure 3.7). Considering that combining data from different clusters, photometric errors, and contamination are all likely to *widen* the AGB clump peak, this disagreement provides further strong evidence against the credibility of the late CHeB evolution that arises from the use of standard overshoot (i.e. CBP). Instead, it

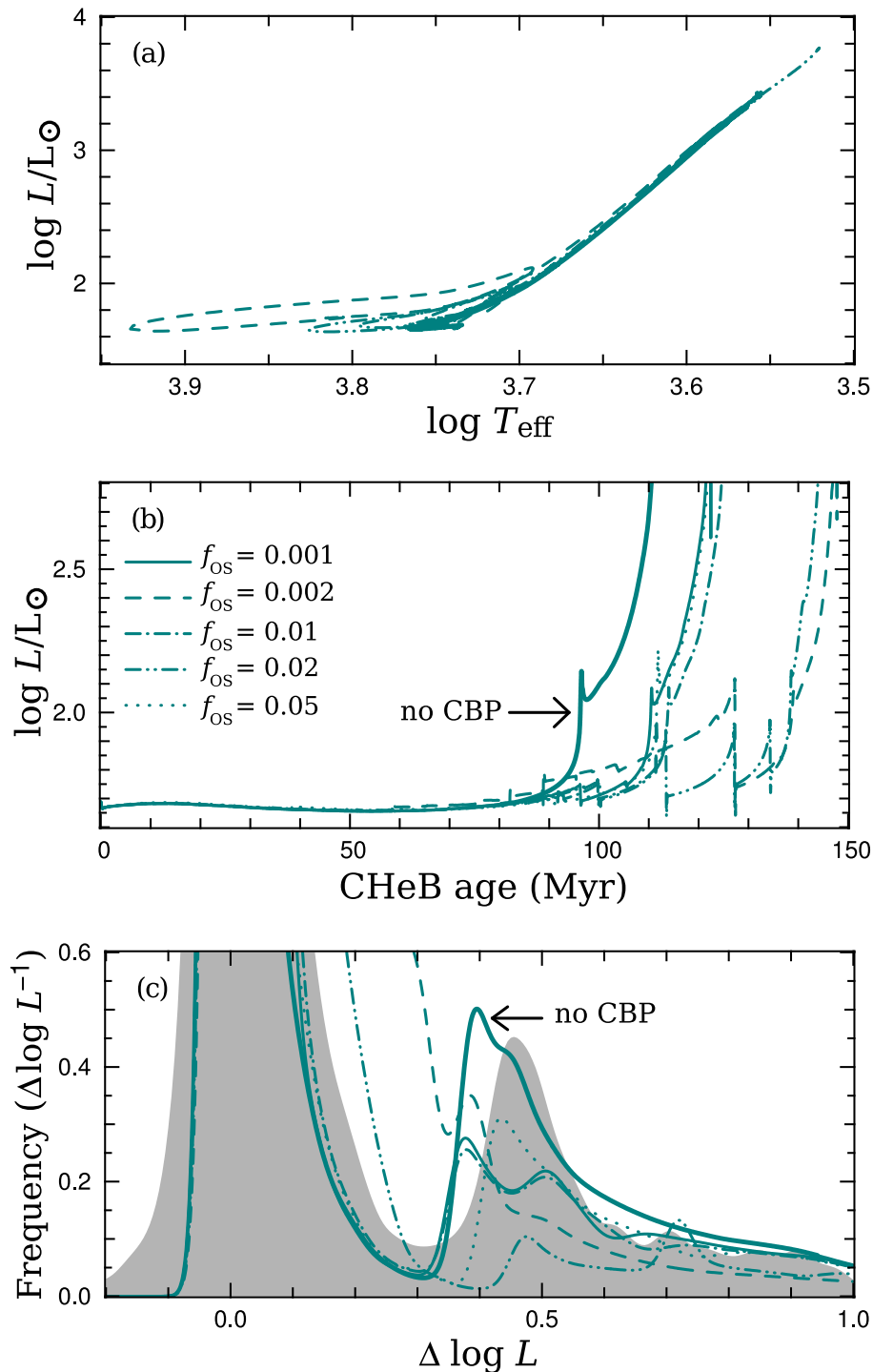


Figure 3.14: Comparison of standard overshoot evolution sequences with different overshooting parameter f_{OS} . Another model, with $f_{OS} = 0.001$ (thick lines), has overshoot only until the central helium abundance drops to 0.17, to emulate the suppression of breathing pulses from, e.g., Caputo et al. (1989). These models have average time step $10^4 \text{ yr} < \Delta t < 2 \times 10^4 \text{ yr}$. The panels are the same as Figure 3.8.

points towards the existence of a smooth or entirely flat composition profile outside the convective core.

3.4.8 Core breathing pulses and their suppression

Among the four treatments of convective boundaries, only the runs with standard overshoot exhibit CBP (e.g. near 96 Myr in Figure 3.8b). The other sequences have a monotonic decrease in central helium abundance and a stability in the size of the convective core.

We have performed an experiment to separate the immediate effects of each mixing prescription from their cumulative effect on the stellar structure. We began by selecting three late-CHeB $1 M_{\odot}$ models from Chapter 2 with no overshoot, semiconvection, and maximal overshoot – the three schemes that avoid CBP. Beginning from models with the same central helium abundance ($Y = 0.1$), we then continued the evolution using the standard-overshoot prescription. Each of the three then displayed CPB, but to different extents. The no-overshoot model showed the largest breathing pulse. This led to an increase in central helium abundance of $\Delta Y = 0.58$, compared with $\Delta Y = 0.17$ for the largest core breathing pulse in the original standard overshoot run. This demonstrates how unstable this small core is late in CHeB. The next largest core breathing pulse was seen in the maximal-overshoot model which had $\Delta Y = 0.04$. The substantial difference between this and the no-overshoot model may be attributed to the already large convective core. The smallest CBP were seen in the semiconvection model, which had $\Delta Y = 0.02$. In that case, the radiative region immediately outside the convective core was only marginally richer in helium, limiting the potential for feedback when it was mixed into the burning region by overshoot.

CBP can be prevented in models by omitting the gravitational energy term (Dorman and Rood, 1993) or by halting the enlargement of the convective core if it will lead to an increase in the central helium abundance (e.g. Caputo et al., 1989; Bono et al., 1997a; Cassisi et al., 2001). Our semiconvection scheme is unusual in that CBP are avoided without explicitly altering the physics for the end of CHeB. We have shown that in this phase the structure is such that if the Schwarzschild criterion for convection is used, any overshoot will trigger CBP. Like the models from Bressan et al. (1986) without CBP, our two methods that do have mixing beyond the Schwarzschild boundary but avoid CBP also have a non-local treatment of convection. The semiconvection method has a limit on how steeply the diffusion coefficient can change through the structure. In the maximal overshoot method, the extent of overshooting at the boundary is determined by $\nabla_{\text{rad}}/\nabla_{\text{ad}}$ further inside the convection zone.

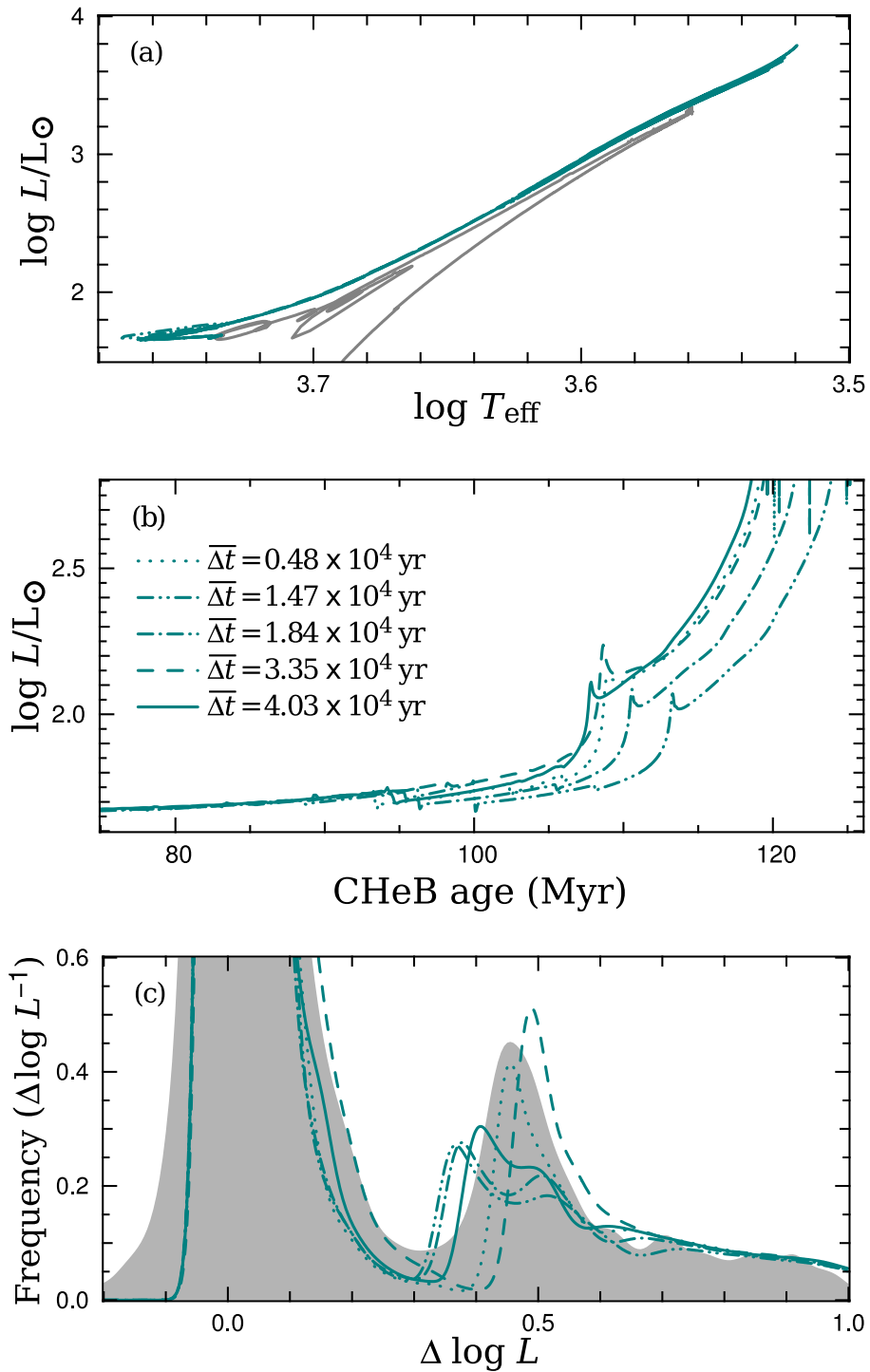


Figure 3.15: Comparison of standard overshoot runs with different time step constraints. Each run is identified by the resulting average time step $\overline{\Delta t}$ during CHeB. Each model has overshooting parameter $f_{\text{OS}} = 0.001$. The panels are the same as Figure 3.8.

The models by Bressan et al. (1986) with ‘non-local treatment’ of convective overshoot have a convectively stable, fully-mixed region extending about twice as far (in mass) as the formally convectively unstable region. This structure resembles our maximal-overshoot case. One key difference is that our maximal overshoot scheme has no free parameter. The Bressan et al. (1986) models are of particular interest because unlike ours they predict unusually high R_2 values (up to 0.22, depending on the choice of the mixing parameter) for models with HB mass $0.6 \leq M/M_\odot \leq 0.9$.

The thick line in Figure 3.14 shows the result of suppressing CBP by turning off convective overshoot before the size of the convective core becomes unstable (in this case when the central helium abundance is $Y = 0.17$). It is clear from panel (c) that this model spends relatively more time on the AGB (i.e. with $\Delta \log L > 0.3$), and therefore that this method of preventing CBP increases R_2 . This is caused by both a reduction in the CHeB lifetime and an increase in the early-AGB lifetime (Figure 3.14b). It is also clear from comparisons with the other models (which have a different overshooting parameter f_{OS}) that the luminosity of the AGB clump is not strongly affected by this method of suppressing of breathing pulses. Finally, we note how the AGB clump in the luminosity PDF in Figure 3.14(c) is more strongly peaked than most of the other models (the cause of the double peaks, unique to models with standard overshoot, is addressed in Section 3.4.7).

The drastic effect on the evolution of standard-overshoot sequences from small changes in f_{OS} and time step (Section 3.4.7) is primarily due to how these influence the development of CBP. The luminosity of the AGB clump for the model with CBP suppressed (thick solid line in Figure 3.14c) is consistent with that in models with CBP. The peak in the luminosity PDF is noticeably thinner, however, for reasons explained in Section 3.4.7, and it better matches the observations. In contrast with $\Delta \log L_{\text{HB}}^{\text{AGB}}$, R_2 is strongly affected by the prevention of CBP. In the test model, R_2 is increased to 0.143, compared with a range of $0.036 \leq R_2 \leq 0.091$ (with median $R_2 = 0.086$) for the other sequences shown. This consequence of the suppression of CBP (by different means) has been shown before (e.g. Caputo et al., 1989; Cassisi et al., 2001).

3.4.9 Post-CHeB maximal overshoot evolution

In Chapter 2 we showed that the maximal-overshoot mixing scheme is the only one of the four that can match the high asymptotic g-mode period spacing inferred from asteroseismic observations (without relying on the effects of mode trapping). The maximal-overshoot models that we have shown so far, however, predict R_2 much lower, and $\Delta \log L_{\text{HB}}^{\text{AGB}}$ much higher, than the observed values (Figure 3.8).

The no-overshoot and maximal-overshoot sequences display a phenomenon known as gravonuclear loops (see e.g. Iben et al., 1986; Bono et al., 1997b,a; Sweigart et al., 2000; Prada Moroni and Straniero, 2009). These are evident from the oscillation in surface luminosity near 55 Myr and 108 Myr for the respective sequences in Figure 3.8(b). There is also an oscillation in the effective temperature during this period, thereby giving rise to 'loops' within the AGB clump in the HR diagram. The phenomenon occurs when the He-burning shell encounters the large composition discontinuity at the former boundary of the convective core, causing discrete episodes of strong helium burning (see e.g. Sweigart et al., 2000). The energy generation is high enough to trigger convection temporarily. The gravonuclear loops finally end when the convective mixing has smoothed the composition gradient that originally induced them. The standard overshoot and semiconvection models have (relatively) smooth composition gradients at the end of CHeB, and hence avoid the gravonuclear instability.

In the maximal-overshoot sequences shown in Figures 3.8-3.13 there is no overshooting at convective boundaries after core helium burning finishes. In Figure 3.16 we show the effect of including overshooting at the boundaries of the convection zones that emerge during shell helium burning. Those three sequences show that the existence and extent of overshooting has a substantial impact on the early-AGB evolution. In the run with $f_{OS} = 0.01$, for example, the early-AGB lifetime is extended by 4 Myr, increasing R_2 from 0.082 to 0.139, i.e. to above the observed value of $R_2 = 0.117 \pm 0.005$.

Figure 3.17 shows the internal evolution for three cases: no overshooting, overshooting only at the outer convective boundaries, and overshooting at all convective boundaries. The two runs that only differ in the treatment of overshoot at the outer boundaries of convection zones are nearly identical. In contrast, overshooting beneath the helium burning convection zones has profound consequences. The inclusion of convective overshooting with $f_{OS} = 0.005$ beneath convection zones has a significant effect. The position of peak helium burning moves inward by about $0.04 M_{\odot}$. The gravonuclear loop phase is extended by about 0.5 Myr, but this only accounts for part of the almost 2 Myr increase in early-AGB lifetime. The model also finishes the gravonuclear loop phase with lower luminosity and having burnt less helium. Once the luminosity increases, the rates of change of the H-burning and He-burning luminosity are the same as for models without overshooting beneath the helium burning convection zones (only it is offset by 1.8 Myr).

If more penetrating overshoot is used, such as in the run with $f_{OS} = 0.01$, the gravonuclear loop convection zones rapidly reach the ashes of helium burning. This puts an end to the gravonuclear loop phase and quiescent shell helium burning begins. During this period, the peak of nuclear burning moves inward by $0.12 M_{\odot}$ and the surface luminosity

drops almost to the HB level (Figure 3.16b). Once the helium burning shell advances far enough to enclose the same mass as it does in the model without overshoot after the gravonuclear loop phase, the rates of change of the H-burning and He-burning luminosity are again the same as that model (this time offset by 4 Myr). The subsequent slow luminosity increase during quiescent helium burning produces a diffuse peak in the luminosity PDF (Figure 3.16c) that is at odds with observations (e.g. Figure 3.7).

Analogous with the case of hydrogen shell burning, when helium burning occurs with a less massive helium exhausted core beneath it, the burning occurs at a lower temperature. This happens at the beginning of shell helium burning as a consequence of overshoot eroding the He-exhausted core. Introducing overshoot of $f_{\text{OS}} = 0.005$ and $f_{\text{OS}} = 0.01$ reduces the shell temperature immediately after the cessation of gravonuclear loops from 128 MK to 99 MK and 90 MK, respectively. As previously mentioned, this slows the evolution, but it also favours the $^{12}\text{C}(\alpha, \gamma)^{16}\text{O}$ reaction, decreasing the final C/O ratio in the degenerate CO core.

Figure 3.16(c) shows that increasing f_{OS} decreases $\Delta \log L_{\text{HB}}^{\text{AGB}}$ and increases R_2 . Although the values of f_{OS} were arbitrary, if we take the average from the models with $f_{\text{OS}} = 0.005$ and $f_{\text{OS}} = 0.01$ we find $R_2 = 0.118$ and $\Delta \log L_{\text{HB}}^{\text{AGB}} = 0.42$ which is a reasonable match to the observations. This demonstrates that a configuration with a large convective core and a single composition discontinuity at the end of CHeB can be consistent with the observations, if convective overshoot moves the helium burning front inward (in mass) by a particular amount.

The maximal overshoot runs with subsequent convective overshoot have a core helium burning lifetime more than 10 Myr longer than the standard overshoot models without core breathing pulses. Both of these models can fit the R_2 and $\Delta \log L_{\text{HB}}^{\text{AGB}}$ constraints and neither can yet be ruled out by asteroseismology (see Chapter 2). The lifetime disparity is therefore an important uncertainty for various other constraints that are derived from counting HB stars, such as globular cluster initial helium abundance (e.g. Cassisi et al., 2003; Salaris et al., 2004) and bounds on axion-photon coupling (e.g. Ayala et al., 2014). The difference in CHeB lifetime between these two runs, and therefore predictions for the ratio $R = n_{\text{HB}}/n_{\text{RGB}}$, equates to a change in inferred initial helium abundance of $\Delta Y \approx 0.02$.

3.4.10 The AGB luminosity limit

In this section we examine how the R_2 comparison between models and observations is affected by the choice of the luminosity cut-off for the AGB that we introduced in Section 3.3.8. We tested reducing the maximum AGB luminosity from $\log L_{\text{AGB}} =$

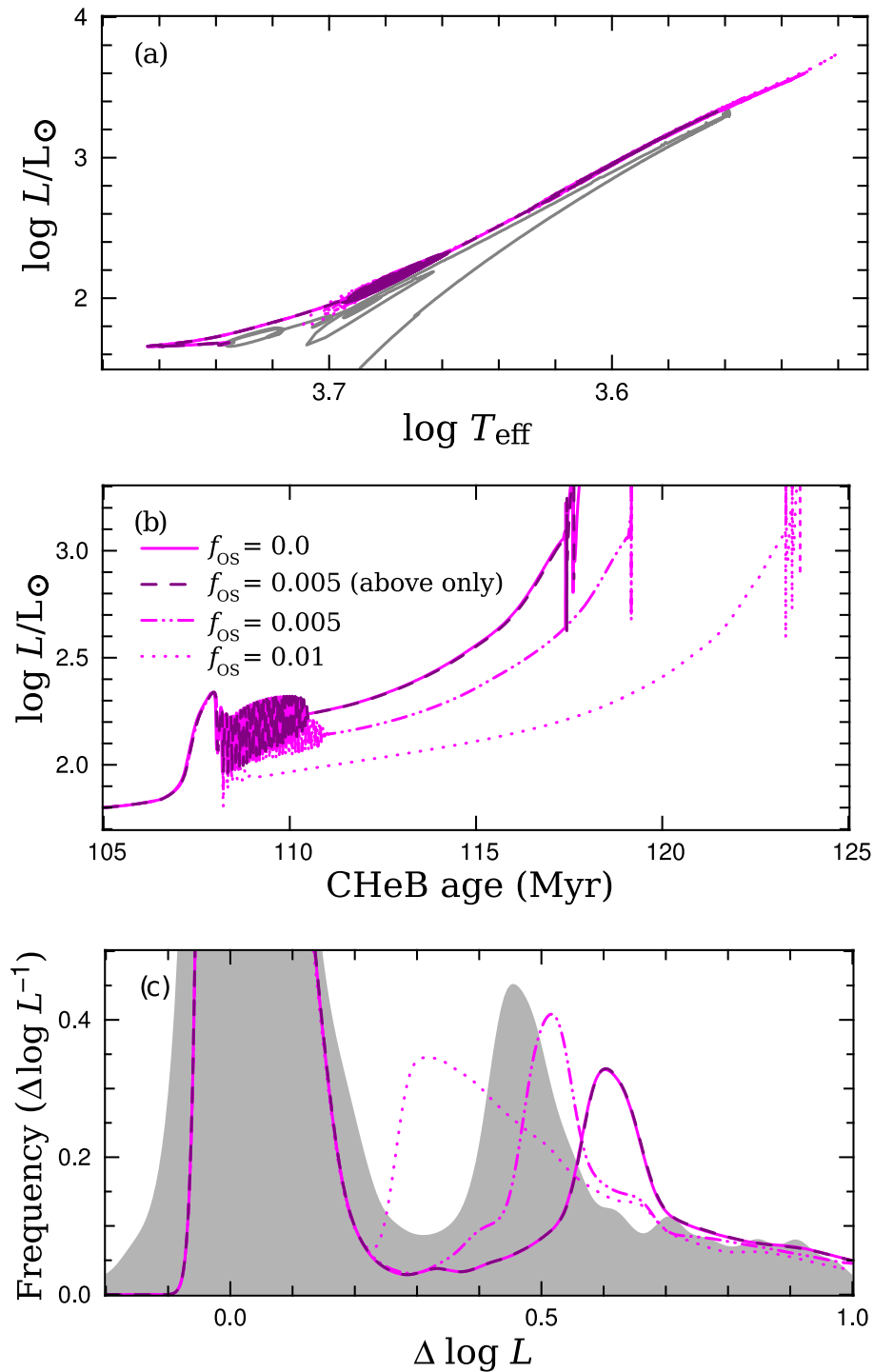


Figure 3.16: Comparison of early-AGB (post maximal-overshoot) evolution sequences with different treatments of convective overshoot. The models have no overshoot (solid magenta line), overshoot with $f_{\text{OS}} = 0.01$ (magenta dots), overshoot with $f_{\text{OS}} = 0.005$ (magenta dashed dotted line), and overshoot only at outer boundaries with $f_{\text{OS}} = 0.005$ (dark magenta dashes). The panels are the same as Figure 3.8.

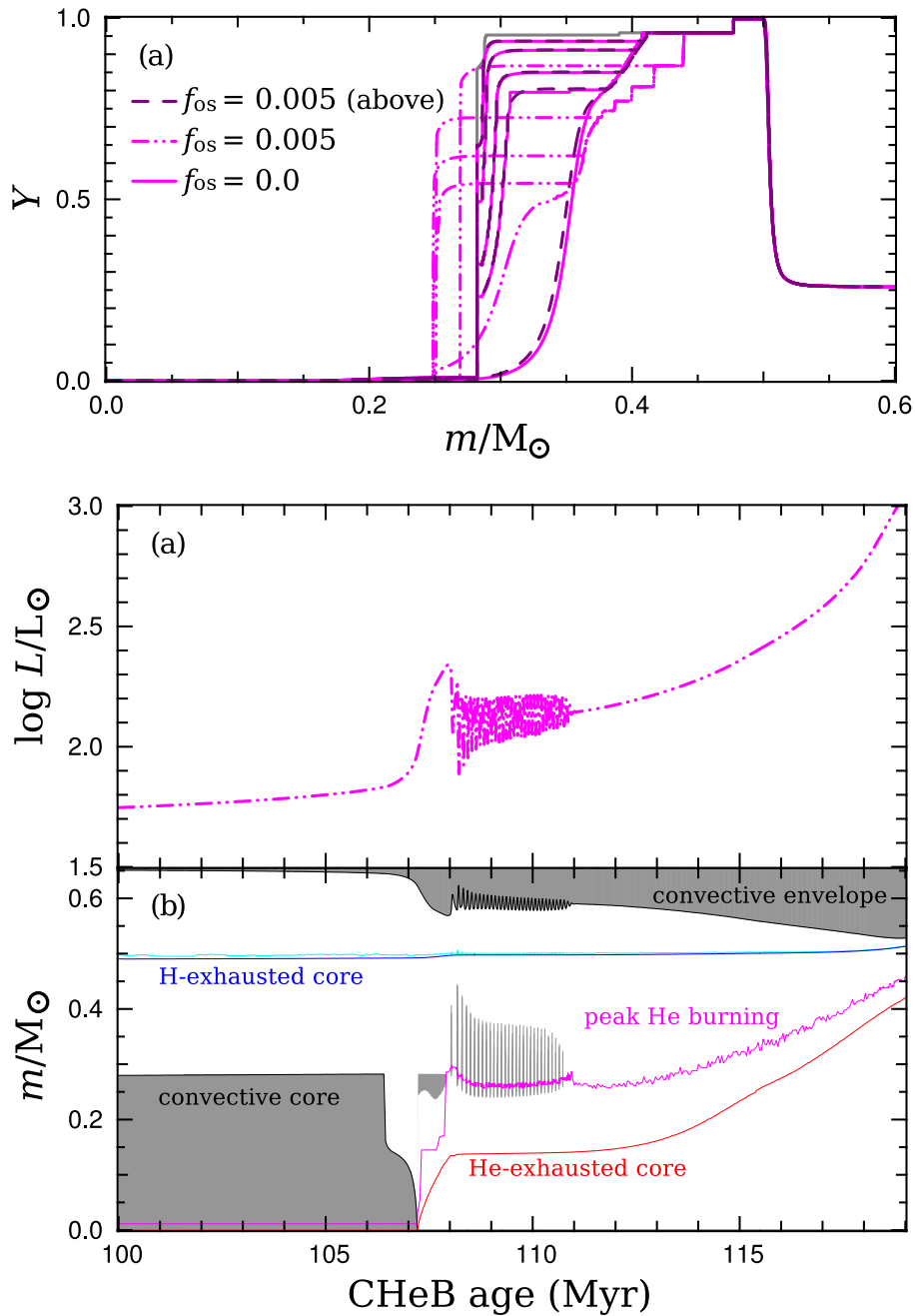


Figure 3.17: Upper panel: evolution of internal helium mass fraction Y of early-AGB (post maximal-overshoot) models with different treatments of convective overshoot. The models have no overshoot (solid magenta line), overshoot with $f_{\text{OS}} = 0.005$ (magenta dashed dotted line), and overshoot only at outer boundaries with $f_{\text{OS}} = 0.005$ (dark magenta dashes). The composition at the end of CHeB is shown in grey. **Lower panels:** evolution of surface luminosity and Kippenhahn plot of the sequence with overshoot at all boundaries that is shown in the upper panel. The positions of peak H burning, H exhaustion, peak He burning, and He exhaustion are shown by cyan, blue, magenta, and red lines, respectively.

$\log L_{\text{HB}} + 1.0$ to $\log L_{\text{AGB}} = \log L_{\text{HB}} + 0.7$, which is high enough for the AGB clump to still be included in the luminosity PDF for clusters without a blue extension to the HB (Figure 3.3) as well as (most of) the computed sequences. This change reduces the observed R_2 from 0.114 and 0.127 to 0.091 and 0.095 for the Piotto et al. (2002) and Sarajedini et al. (2007) samples, respectively, and interestingly improves their consistency.

Reducing the AGB luminosity limit has variable consequences for predictions of R_2 . Unsurprisingly, the decrease in the predicted R_2 is largest for models with a high $\Delta \log L_{\text{HB}}^{\text{AGB}}$, because this truncation excludes part of the AGB clump peak in the luminosity PDF (but almost never more than half). The luminosity PDFs for the models with different mixing schemes are generally quite similar when $\Delta \log L > 0.7$ (and especially so for $\Delta \log L > 0.8$) so reducing the cut-off has a uniform effect on R_2 for most cases (see e.g. Figure 3.8c, 3.13c, 3.15c, 3.16c). The sequences shown in Figure 3.8 are typical: by decreasing the cut-off to $\Delta \log L = 0.7$, R_2 is reduced from 0.096, 0.068, and 0.082 to 0.070, 0.043, and 0.057 for the standard-overshoot, semiconvection, and maximal overshoot cases, respectively, giving $\Delta R_2 \approx -0.025$ in all three cases, compared with $\Delta R_2 \approx -0.028$ for the observations. The equivalent standard-overshoot model with CBP suppressed (thick line in Figure 3.14) shows a larger reduction of R_2 , from 0.143 to 0.099. Reducing the luminosity cut-off for the R_2 calculation for the two maximal-overshoot sequences that include overshooting after CHeB ceases (with $f_{\text{OS}} = 0.005$ and $f_{\text{OS}} = 0.01$ respectively; described in Section 3.4.9) has an effect similar to the effect it has on the observations. Those respective models show reductions of R_2 from 0.097 and 0.139 to 0.075 and 0.119.

Overall, it appears that reducing the luminosity limit for the AGB does not significantly alter the (dis)agreement between models and observations: those which can match with $\log L_{\text{AGB}} < \log L_{\text{HB}} + 1.0$ can also match with $\log L_{\text{AGB}} < \log L_{\text{HB}} + 0.7$, and vice versa, although in some cases the disagreement is exacerbated. The insensitivity to the luminosity limit is not unexpected considering the predominance of AGB stars near the clump in both observations and theoretical predictions (e.g., near $\Delta \log L_{\text{HB}}^{\text{AGB}} \approx 0.5$ in Figure 3.8c).

3.5 Summary and conclusions

In this study we extended our investigation into the mixing in core helium burning stars in Chapter 2 by confronting models with observations of globular clusters. The particular observational probes of core helium burning we used were (i) R_2 , the ratio of AGB to HB stars, and (ii) $\Delta \log L_{\text{HB}}^{\text{AGB}}$, the luminosity difference between the AGB clump and the HB, for 48 Galactic globular clusters with suitable HST photometry (Piotto et al.,

2002; Sarajedini et al., 2007). We compared these results to a suite of stellar models that included four different mixing prescriptions, variations in the initial composition, and an exploration of their numerical dependence and physical uncertainties.

In Section 3.3.3 we showed there is a considerable spread in R_2 determinations from observations. The scatter is apparent for distinct photometry of a given cluster and for homogeneous photometry of different clusters. This casts doubt on inferences about stellar evolution from R_2 derived from the photometry of a small number of clusters, or even a single cluster, which are common in the literature. By combining data for 48 clusters from two HST surveys, we minimized the dominant statistical uncertainty. Encouragingly, the cluster to cluster variation in R_2 is also smaller for the newer HST photometry than for inhomogeneous photometry in the literature.

By combining photometry for the 15 clusters common to the three data sets, we found $R_2 = 0.121 \pm 0.006$ (Piotto et al., 2002), $R_2 = 0.125 \pm 0.005$ (Sarajedini et al., 2007), and $R_2 = 0.152 \pm 0.007$ (Sandquist, 2000), where the 1-sigma errors are calculated from Equation 3.6. The two new determinations of a lower R_2 lessen the disagreement with standard models, and bring R_2 into alignment with models in the literature where core breathing pulses have been suppressed (e.g. Cassisi et al., 2003).

We investigated the sources of the discrepancies between star counts from different photometry of the same clusters and found two main causes: (i) photometry can be incomplete, especially for blue HB stars, and (ii) it can be impossible to distinguish between the more luminous RGB and AGB stars. To minimize errors from the latter problem we restricted the counts to stars less than 10 times as luminous as HB stars. When this method was used we did not detect any dependence of R_2 on metallicity (see Section 3.3.7). Furthermore, we showed in Section 3.3.3 that the statistics of finite sampling can explain the majority of the scatter in R_2 . We also found evidence that clusters that host the bluest HB stars have abnormally low R_2 , supporting conjecture that a significant proportion of those stars do not evolve to the AGB.

In order to better compare our models with observations we further limited the star counts in Section 3.3.8 to clusters without a blue extension of the HB. This yielded a sample of 21 CMDs (of 14 unique clusters) comprising 6366 stars. Models with each of the four different mixing schemes that were tested (standard overshoot, no overshoot, semiconvection, and maximal overshoot; described in Section 3.4.2) typically cannot simultaneously match $R_2 = 0.117 \pm 0.005$ and $\Delta \log L_{\text{HB}}^{\text{AGB}} = 0.455 \pm 0.012$ from the observations.

Compared with observations, the evolution sequences without convective overshoot have $\Delta \log L_{\text{HB}}^{\text{AGB}}$ far too low and R_2 far too high. This is consistent with previous findings that models without overshoot disagree with globular cluster observations and asteroseis-

mology (e.g. Chapter 2). In contrast, our initial tests with each of the other schemes predicted R_2 well below that derived from observations. The semiconvection models have $\Delta \log L_{\text{HB}}^{\text{AGB}}$ slightly too large whereas the standard overshoot models typically have about the observed value. In Section 3.4.7 we showed that the predicted luminosity probability density functions from standard-overshoot models with core breathing pulses are not strongly peaked enough near the AGB clump (Figure 3.14c). Suppressing core breathing pulses removes this discrepancy and also increases R_2 (to even higher than the observed value in our ad hoc test). These two factors are strong arguments against the validity of standard-overshoot runs with core breathing pulses that produce multiple large composition discontinuities in the partially mixed region. Furthermore, in Section 3.4.9 we demonstrated that models with the maximal-overshoot prescription can simultaneously match the observed R_2 and $\Delta \log L_{\text{HB}}^{\text{AGB}}$, but only if there is a particular amount of convective overshoot beneath the shell helium burning ‘gravonuclear’ convection zones that appear during the early-AGB phase.

In Section 3.4.6 we quantified the effect that stellar mass and composition, and various physical uncertainties (other than mixing) have on predictions of R_2 and $\Delta \log L_{\text{HB}}^{\text{AGB}}$. By adding each effect in quadrature, we found that the respective uncertainties are $\sigma_{R_2} \approx 0.009$ and $\sigma_{\Delta \log L} \approx 0.04$. Initial composition and HB stellar mass can each account for small changes in R_2 , but not enough to resolve the difference between models and observations. The most important uncertainty for R_2 is the $^{12}\text{C}(\alpha, \gamma)^{16}\text{O}$ reaction rate, which dominates late in core helium burning. A reduction of this rate tends to decrease the HB lifetime and increase R_2 . We found that uncertainty in the H-exhausted core mass, which we showed in Chapter 2 could potentially account for some of the disagreement with asteroseismology, makes no appreciable change to either R_2 or $\Delta \log L_{\text{HB}}^{\text{AGB}}$. The treatment of mixing is the dominant source of uncertainty in the models (see Section 3.4.6). Even among models with mixing beyond the Schwarzschild boundary, uncertainties in the treatment of convective boundaries can cause a 40 Myr (roughly 30 per cent) variation in the HB lifetime, which would significantly affect any inferences from counts of HB stars.

In our asteroseismology study in Chapter 2, we found that mixing schemes that produce either a very large convective core, or a large partially mixed region that can trap modes, predict an $\ell = 1$ mixed-mode period spacing that can be consistent with the observations. This work is ongoing, but it should be pointed out that these mixing schemes are only consistent with globular cluster observations if (i) core breathing pulses do not significantly extend the core helium burning lifetime or create large composition discontinuities within the partially mixed region (see Section 3.4.7), or (ii) they develop very large convective cores (e.g. maximal overshoot) and there is a particular extent of convective

overshoot beneath the convection zones that appear in the subsequent ‘gravonuclear loop’ phase during the early-AGB (Section 3.4.9). The physics behind these different possibilities may perhaps now best be addressed with multi-D hydrodynamic simulations. Finally, we emphasise that this work could be complemented by ground-based photometry that can better differentiate the AGB and RGB sequences, e.g. with the *UBV* bands.

Monash University

Declaration for Thesis Chapter 4

Declaration by candidate


In the case of Chapter 4, the nature and extent of my contribution to the work was the following:

Nature of contribution	Extent of contribution (%)
First author; code development, calculations, analysis of results, figure preparation, writing, manuscript preparation.	80

The following co-authors contributed to the work. If co-authors are students at Monash University, the extent of their contribution in percentage terms must be stated:

Name	Nature of contribution	Extent of contribution (%) for student co-authors only
Simon Campbell	Project development, analysis of results, manuscript editing.	
Pilar Gil-Pons	Preliminary work, analysis of results.	
John Lattanzio	Project development, analysis of results.	

The undersigned hereby certify that the above declaration correctly reflects the nature and extent of the candidate's and co-authors' contributions to this work*.

Candidate's Signature		Date 2-9-15
----------------------------------	---	-----------------------

Main Supervisor's Signature		Date 2-9-15
--	---	-----------------------

*Note: Where the responsible author is not the candidate's main supervisor, the main supervisor should consult with the responsible author to agree on the respective contributions of the authors.

On the necessity of composition-dependent low-temperature opacity in metal-poor AGB models

Thomas Constantino¹, Simon W. Campbell¹, Pilar Gil-Pons², and John C. Lattanzio¹

¹Monash Centre for Astrophysics (MoCA), School of Mathematical Sciences, Monash University, Victoria, 3800, Australia

²Department of Applied Physics, Polytechnic University of Catalonia, 08860 Barcelona, Spain

Published in *The Astrophysical Journal*, 784, 56, 4 March 2014.

4.1 Abstract

The vital importance of composition-dependent low-temperature opacity in low-mass ($M \leq 3 M_{\odot}$) asymptotic giant branch (AGB) stellar models of metallicity $Z \geq 0.001$ has recently been demonstrated (e.g. Marigo, 2002; Ventura and Marigo, 2010). Its significance to more metal-poor, intermediate mass ($M \geq 2.5 M_{\odot}$) models has yet to be investigated. We show that its inclusion in lower-metallicity models ($[\text{Fe}/\text{H}] \leq -2$) is essential and that there exists no threshold metallicity below which composition-dependent molecular opacity may be neglected. We find it to be crucial in all intermediate-mass models investigated ($[\text{Fe}/\text{H}] \leq -2$ and $2.5 \leq M/M_{\odot} \leq 5$), because of the evolution of the surface chemistry, including the orders of magnitude increase in the abundance of molecule-forming species. Its effect on these models mirrors that previously reported for higher-metallicity models – increase in radius, decrease in T_{eff} , faster mass loss, shorter thermally pulsing AGB lifetime, reduced enrichment in third dredge-up products (by a factor of 3–10), and an increase in the mass limit for hot bottom burning. We show that the evolution of low-metallicity models with composition-dependent low-temperature opacity is relatively independent of initial metal abundance because its contribution to the opacity is far outweighed by changes resulting from dredge-up. Our results imply a significant reduction in the expected number of nitrogen-enhanced metal-poor stars, which may help explain their observed paucity. We note that these findings are partially a product of the macrophysics adopted in our models, in particular the Vassiliadis and Wood (1993) mass loss rate which is strongly dependent on radius.

4.2 Introduction

The asymptotic giant branch (AGB) is the final phase of nuclear burning experienced by stars with an initial mass of roughly $0.8 - 8 M_{\odot}$. These stars are composed of a large convective envelope above hydrogen- and helium-burning shells that surround a degenerate CO core. Late in this phase the envelope is ejected in a stellar wind, enriching the interstellar medium with nuclearily processed material. Thermally pulsing (TP)-AGB stars are thought to be producers of the *s*-process elements (Busso et al., 1999), which are brought to the surface, along with carbon from helium burning, during episodes of the third dredge-up. Since Scalo et al. (1975), models of higher-mass AGB stars have shown nitrogen production through the process now referred to as hot bottom burning (HBB) in which the convective envelope penetrates into regions where the CNO-cycle is operating. This finding was later supported by observations of AGB stars in the Magellanic Clouds (McSaveney et al., 2007). The resultant material has long been a prime suspect for the characteristic abundance patterns in globular cluster stars (Cottrell and Da Costa, 1981; Gratton et al., 2004). AGB material is also thought to contribute to the formation of carbon-enhanced metal-poor (CEMP) and nitrogen-enhanced metal-poor (NEMP) stars (e.g. Suda et al., 2011; Pols et al., 2012).

When the outer region of a star is cool enough ($T \lesssim 5000$ K), molecules make an important contribution to the opacity. During the AGB phase, the third dredge-up and HBB can radically change the chemistry of the surface, but stellar evolution codes have historically used low-T Rosseland mean opacity data that assume a scaled-solar abundance pattern (e.g. Alexander, 1975; Alexander and Ferguson, 1994; Ferguson et al., 2005). There have been, however, a few notable exceptions. By using a polynomial fit for the opacity from CN molecules, Scalo and Ulrich (1975) were the first to run models that accounted for the changing composition during the AGB phase. Alexander et al. (1983) then produced tables for three additional C/O ratios (0.95, 1.0, and 1.05). Lucy et al. (1986) calculated the opacity for a C/O = 2 mixture for C-rich AGB models. Bessell et al. (1989) used the Alexander et al. (1983) tables to produce a fit for the opacity as a function of carbon abundance. More recently, Marigo (2002) demonstrated the shortcomings of using scaled-solar abundance low-T opacity in synthetic AGB models, by computing the opacity for mixtures of a range of molecular species for which data were available. These effects were also apparent when composition-dependent molecular opacity was later used in full stellar models (Cristallo et al., 2007; Kitsikis and Weiss, 2008; Weiss and Ferguson, 2009). Sets of low-temperature opacity tables for enhancements in carbon and nitrogen abundance using more detailed calculations have since been made available (Lederer and Aringer, 2009), as well as the online AESOPUS tool, which can generate low-T opacity

tables for any abundance mixture with data for about 300 atomic and 500 molecular species (Marigo and Aringer, 2009).

There are a number of important consequences from following the changing molecular composition in low to intermediate-mass models. When C/O first exceeds unity, because of the third dredge-up, the opacity in the outer envelope increases, the surface cools, and the mass loss rate increases. This reduces the AGB lifetime, halts HBB in certain cases (Marigo, 2007; Ventura and Marigo, 2010), and reduces chemical yields of certain species (e.g. Marigo, 2002). The final envelope C/O ratio in such models is more consistent with observations (Marigo, 2002).

Studies into the effect of composition-dependent low-T opacity have hitherto been confined to higher metallicity stars ($Z \geq 0.001$), apart from Cristallo et al. (2007) in which a $2 M_{\odot}$, $Z = 10^{-4}$ model was examined. Given that the molecular composition (and therefore opacity) is most sensitive to element abundances when $C/O \sim 1$ (by number), very little effect has been seen unless there is enough dredge-up to reach $C/O > 1$ (Ventura and Marigo, 2010). Low-metallicity stars can more easily become carbon-rich because there is less oxygen in the envelope for the dredged-up carbon to overcome. They can also experience orders of magnitude increase in total C+N+O, which leads to an opacity increase irrespective of C/O. Despite this, it has been argued that the adoption of composition-dependent low-temperature opacity in low-metallicity models may not be as important because of the lower absolute abundance of molecules and higher temperature, which inhibits molecule formation (Marigo, 2002, 2007). The single low-mass model from Cristallo et al. (2007), however, showed a halving of the AGB lifetime by taking into account C and N enhancement. This disagreement highlights the need for the contribution of composition-dependent low-T opacity to low-metallicity models to be tested over a range of initial mass and metallicity with a suite of full stellar models. This work forms the basis of this study.

Abundance anticorrelations, such as Na-O, are ubiquitous in Galactic globular clusters (Carretta et al., 2010), and pollution from an earlier generation of higher-mass AGB stars may be responsible for them (e.g. Ventura et al., 2013). AGB stars can produce these anticorrelations via HBB where the CNO and Ne-Na cycles are active (Gratton et al., 2004). This hypothesis constrains chemical yields because there is a limited internal spread of C+N+O in clusters. For example, in M13 the total C+N+O content differs between populations by roughly a factor of two (Cohen and Meléndez, 2005), and it is constant to within observational errors in M4 (Ivans et al., 1999). Unfortunately, this evidence is often equivocal. Models of a population with a factor of three difference in C+N+O in NGC 1851 best reproduce the observed split in the subgiant branch (Ventura

et al., 2009) and Yong et al. (2009) observed a spread in C+N+O of a factor of four in four RGB stars in the same cluster. In contrast, also in NGC 1851, Villanova et al. (2010) found no evidence for a spread in 15 RGB stars and Gratton et al. (2012b) put an upper limit of $\Delta[(\text{C+N+O})/\text{Fe}] \leq 0.2$ by observing blue horizontal branch stars. In higher-metallicity low-mass models, composition-dependent low-T opacity has been shown to reduce the enrichment of the envelope in C+N+O by truncating the evolution, but so far only in masses too low for HBB (Ventura and Marigo, 2009). Whether this distinction based on initial mass holds for lower-metallicity models is important for the globular cluster self-enrichment scenario.

Various estimates put the fraction of extremely metal-poor (EMP) stars ($[\text{Fe}/\text{H}] < -2$) that are also carbon-enhanced ($[\text{C}/\text{Fe}] \geq 1$) between around 9% and greater than 20% (Frebel et al., 2006; Lucatello et al., 2006; Carollo et al., 2012). This fraction increases with decreasing metallicity (Rossi et al., 2005) and with increasing distance from the Galactic plane (Frebel et al., 2006). Observations suggest that the *s*-process rich (CEMP-*s*) stars are all binaries (Lucatello et al., 2005), supporting the hypothesis that mass transfer from an AGB companion is responsible for the carbon-enhancement in these stars (for models see e.g. Stancliffe and Glebbeek, 2008). There is a paucity of observed nitrogen-enhanced metal-poor (NEMP) stars ($[\text{N}/\text{Fe}] > 1$ and $[\text{N}/\text{C}] > 0.5$; Johnson et al. 2007), with a handful of exceptions at very low metallicity $[\text{Fe}/\text{H}] < -2.8$ (Masseron et al., 2010). In population synthesis models (e.g. Izzard et al., 2009; Pols et al., 2012; Suda et al., 2013) the CEMP/NEMP ratio is sensitive to the mass threshold above which HBB occurs. This mass limit differs considerably from code to code and at higher metallicity has been shown to be significantly increased by adopting composition-dependent low-T opacity (Marigo, 2007). If this is also true for low-metallicity models, it would reduce the predicted number of NEMP stars. Another important ingredient that determines the HBB limit, and a poorly constrained one at low metallicity, is the mass loss formulation used, which can differ by orders of magnitude and therefore affect lifetimes enough to control whether HBB converts carbon to nitrogen. Composition-dependent low-T opacity rapidly affects the radius, and later the luminosity, which can both alter the mass loss rate, depending on the formulation, making code comparisons difficult. Modeling a population of binary systems and mass transfer adds yet another layer of complexity.

In recent years, the availability of molecular opacity data has for the first time allowed stellar evolution codes to accurately account for the significant composition changes that can occur during the AGB phase. The composition changes are most extreme for low-metallicity models, but the consequences have been studied in detail only for the more metal-rich regime ($Z \geq 0.001$). Here, we extend this inquiry to low metallicity. We

quantify the effects and establish their mass and metallicity dependence. We also consider how any changes in the evolution affect CEMP and NEMP formation and the role of AGB stars in the globular cluster self-pollution scenario.

4.3 Methods

4.3.1 Stellar structure code

We use the one-dimensional Monash University stellar structure code MONSTAR, which has previously been described in detail (e.g. Frost and Lattanzio, 1996; Campbell and Lattanzio, 2008). We have since updated the code to use the OPAL (Rogers and Nayfonov, 2002), Helmholtz (Timmes and Swesty, 2000), and Timmes equations of state (Timmes and Arnett, 1999). In this study, we use Helmholtz EOS for $T > 1$ MK, OPAL EOS for $T < 2$ MK, and a linear blend of the two in the overlapping region. During the AGB phase we use instantaneous mixing of chemical species and determine convective boundaries using a “search for convective neutrality” (Lattanzio, 1986). We have no overshoot during core helium burning. This eliminates the stochastic nature of the mixing during this phase (Castellani et al., 1985), ensuring that each model of a given mass and metallicity begins the AGB with the same H-exhausted core mass (so that opacity is the only variable). The mass loss for the RGB is Reimers (1975) with $\eta_R = 0.4$ and for the AGB it is the Vassiliadis and Wood (1993) rate.

4.3.2 Updated low-T opacity treatment

For this study, we implement a custom grid of AESOPUS low-temperature opacity tables with three values for the abundance of H, 13 for C, 6 for N, 38 for C/O, and 12 for metallicity Z (Table 4.1). We also have a grid that is used for models that are initially metal-free. It has the same mass fraction C, N, and O enhancement as the $Z = 10^{-6}$ set, which we later show is reasonable because the $Z = 0$ and $[\text{Fe}/\text{H}] = -4$ models evolve to have similar C, N, and O surface abundances (Table 4.2). We account for $-1.5 \leq [\text{C}/\text{O}] \leq +2.5$ and enhancements up to $[\text{C}/\text{Fe}] = [\text{N}/\text{Fe}] = +4$. We have tables for 38 different C/O values in order to properly resolve the opacity near and just below $\text{C}/\text{O} = 1$, where because of the strength of the molecular bonds in CO and SiO it rapidly changes (see Figure 16 in Marigo and Aringer 2009). Our resolution is considerably finer than that of others in the literature (e.g. Ventura and Marigo, 2010; Fishlock et al., 2014), although we note that Marigo et al. (2013) have very recently fully integrated AESOPUS into their synthetic AGB code so that the opacity for the particular composition in the envelope

during the evolution is computed directly. The increase in the number of tables in our code (to almost 116,000) only requires additional memory. We minimize interpolation errors by using linear interpolation in C/O, [C/Fe], [N/Fe], hydrogen X , T , and $R = \rho/T_6^3$ (where T_6 is T in MK), and logarithmic interpolation in Z . An important improvement in AESOPUS compared with the earlier Lederer and Aringer (2009) tables is that it can account for an increase in envelope oxygen abundance, which can be considerable in low-metallicity models, and is obviously essential for determining whether $C/O > 1$. We hereafter refer to composition-independent low-T opacity as the old opacity and composition-dependent low-T opacity as the new opacity. Both of these use the AESOPUS tables except that in the old case only the initial abundance is used to calculate low-T opacity. The composition-independent opacity models serve as a control group.

4.3.3 Stellar models

We have computed the evolution of 11 pairs of stellar models (with and without the new opacity) from the pre-main sequence to the late AGB. The grid of models is shown in Table 4.2. We use a scaled-solar abundance from Asplund et al. (2009) with oxygen enhancement $[O/Fe] = +0.4$ to mimic the effect of an alpha-enhancement abundance pattern (in all but the $[Fe/H] = -1$ model), and an initial helium mass fraction of $Y = 0.245$. The models have metallicity $[Fe/H] \leq -1$, which is (with the exception of one model in Cristallo et al., 2007) more metal-poor than has been studied previously. Composition-dependent low-T opacity has also been recently used in other codes for low-metallicity models but its effect has not been specifically analyzed (e.g. Cristallo et al., 2009; Lugaro et al., 2012). The uptake is so far not ubiquitous; it is not yet included in MESA, for instance (Paxton et al., 2013). Our metallicity range is relevant to CEMP (and NEMP) stars and globular cluster chemical evolution. The models span a mass range from 1.25 to $5 M_\odot$ which covers models that have a mass much too low for HBB to those that experience strong HBB. This mass range was chosen so that we could investigate how the mass limit for HBB is affected, complementing work already done for higher-metallicity models (e.g. Ventura and Marigo, 2009). We examined $2.5 M_\odot$ models down to $Z = 0$ to see if there is a metallicity cut-off below which HBB is unaffected by the updated opacity treatment. We also tested the sensitivity of our results to a change in the mixing length parameter in the mixing length theory (MLT). In the interest of time, we did not attempt to restart several of the models with the old opacity after convergence problems if the effect on the evolution was already obvious. Therefore, some of these models still had varying amounts of the envelope remaining at the end of computation.

4.4 Stellar model results

We find that the adoption of composition-dependent low-T opacity alters the evolution of all of our models. This includes the strongly HBB models (4 and 5 M_{\odot}), which in their higher-metallicity incarnation have previously been shown to be unaffected (Ventura and Marigo, 2009). When the effects become evident, during the third dredge-up, the change is qualitatively what is expected: the additional opacity increases the radius, cools the surface and the base of the envelope, and the mass loss rate increases, shortening the AGB lifetime. This lifetime reduction means that each model with the new opacity ejects less helium, nitrogen and oxygen. This reduction in yield is not true for all elements because the conversion of carbon to nitrogen is suppressed in the more weakly HBB models, increasing the carbon yield. In general, we find that these effects are not metallicity dependent when $[\text{Fe}/\text{H}] \leq -2$.

The results can best be summarized by considering three categories: (i) models that have HBB, (ii) models that no longer have HBB when composition-dependent low-T opacity is used, and (iii) models that do not have HBB. In this section we also separately analyze our $Z = 0$ models. In Figure 4.1, we show the HR diagram of four representative pairs of these models. In each example, it is apparent that when the new opacity is used, the surface becomes cooler instead of hotter during the evolution, and that the maximum AGB luminosity is decreased.

4.4.1 Importance for HBB models

In HBB models ($M > 3 M_{\odot}$) with $[\text{Fe}/\text{H}] \leq -2$, composition-dependent low-T opacity causes the AGB evolution to be truncated because of faster mass loss. The accelerated mass loss reduces the number of thermal pulses by a factor of three and the AGB lifetime by a factor of two (Figure 4.2). The maximum temperature at the base of the convective envelope ($T_{\text{bce,max}}$) is slightly reduced, by about 1–3 MK, from roughly 86–96 MK (Table 4.2). The mean mass fraction of helium Y in the ejecta is reduced by around 0.1, to approximately $Y = 0.35$, which has consequences for the globular cluster abundance pattern problem (discussed in Section 4.5.3). The total enrichment in C+N+O is reduced by a factor of 2–3 (Figure 4.3). The main component in this is the nitrogen yield, which is more than halved in the $[\text{Fe}/\text{H}] \leq -2$ models (Table 4.2). In these models, dredge-up efficiency and core growth rate are unaffected by the change in surface conditions (Figure 4.2). In our 5 M_{\odot} $[\text{Fe}/\text{H}] = -1$ model the evolution difference is less extreme but still clear. This shows that compared with Ventura and Marigo (2010), HBB models using the physics in our code are sensitive to the low-T opacity treatment up to a higher metallic-

Table 4.1: Composition and parameters for the low-T opacity tables used in this study. Z refers to the total metal content before C, N, and O alteration and $\log R = \log \rho/T_6^3$ where T_6 is T in MK. The tables were generated online with AESOPUS using the Grevesse et al. (2007) solar abundance.

Z	X	[C/Fe]	[N/Fe]	C/O	$\log R$	$\log T$
0	0.50	-3.0	-3.0	0.017	-8.0	3.20
1×10^{-6}	0.65	-1.5	0.0	0.054	-7.5	3.22
3×10^{-6}	0.80	-1.0	+1.0	0.170	-7.0	3.24
1×10^{-5}	...	-0.5	+2.0	0.380	-6.5	3.26
3×10^{-5}	...	0.0	+3.0	0.537	-6.0	3.28
1×10^{-4}	...	+0.5	+4.0	0.708	-5.5	3.30
3×10^{-4}	...	+1.0	...	0.813	-5.0	3.32
0.001	...	+1.5	...	0.852	-4.5	3.34
0.0025	...	+2.0	...	0.872	-4.0	3.36
0.005	...	+2.5	...	0.882	-3.5	3.38
0.01	...	+3.0	...	0.892	-3.0	3.40
0.02	...	+3.5	...	0.902	-2.5	3.42
0.04	...	+4.0	...	0.913	-2.0	3.44
...	0.923	-1.5	3.46
...	0.934	-1.0	3.48
...	0.945	-0.5	3.50
...	0.956	0.0	3.52
...	0.967	+0.5	3.54
...	0.978	+1.0	3.56
...	0.987	...	3.58
...	0.994	...	3.60
...	0.998	...	3.62
...	1.000	...	3.64
...	1.003	...	3.66
...	1.008	...	3.68
...	1.015	...	3.70
...	1.024	...	3.75
...	1.048	...	3.80
...	1.072	...	3.85
...	1.123	...	3.90
...	1.203	...	3.95
...	1.350	...	4.00
...	1.699	...	4.05
...	2.401
...	5.374
...	16.995
...	53.743
...	169.949

Table 4.2: Summary of the properties of each model. M is the initial mass in units of M_{\odot} . The opacity treatment is denoted by κ , with κ_X being models with composition-dependent low-T opacity and κ_0 those without it. The MLT mixing length parameter is $\alpha_{\text{MLT}} = \ell_{\text{MLT}}/H_{\text{P}}$ where ℓ_{MLT} is the mixing length and H_{P} is the pressure-scale-height. The number of thermal pulses is n_{TP} and the number with dredge-up is $n_{3\text{DU}}$. The AGB lifetime is t_{AGB} in Myr. $M_{\text{core,f}}$, M_{f} , and $M_{\text{env,f}}$ are the end-of-computation hydrogen-exhausted core, total, and envelope mass in units of M_{\odot} . $T_{\text{bce,max}}$ is the maximum temperature in MK at the base of the envelope during the interpulse phase. Abundances are given as the average in the wind ejecta (assuming the remaining envelope is ejected without any composition change), where Y is mass fraction of helium (initially $Y = 0.245$) and abundances for the $Z = 0$ models are expressed as if $[\text{Fe}/\text{H}] = -4$. R_{CNO} is the ratio of total yield of C+N+O to the initial abundance. $\text{C}/\text{O}_{\text{f}}$ is the final carbon-to-oxygen ratio by number in the envelope. All models were initially scaled-solar but with $[\text{O}/\text{Fe}] = +0.4$, except for the $5 M_{\odot}$ $[\text{Fe}/\text{H}] = -1$ model which was not oxygen-enhanced.

M	$[\text{Fe}/\text{H}]$	κ	α_{MLT}	n_{TP}	$n_{3\text{DU}}$	t_{AGB}	λ_{peak}	$M_{\text{core,f}}$	M_{f}	$M_{\text{env,f}}$	$T_{\text{bce,max}}$	Y	$[\text{C}/\text{Fe}]$	$[\text{N}/\text{Fe}]$	$[\text{O}/\text{Fe}]$	R_{CNO}	$\text{C}/\text{O}_{\text{f}}$
1.25	-2	κ_0	1.6	35	1	3.05	0.18	0.766	0.839	0.073	2.67	0.269	1.41	0.62	0.45	4	3.3
1.25	-2	κ_X	1.6	31	1	2.89	0.17	0.750	0.750	0.000	2.17	0.269	1.48	0.58	0.45	4	3.2
1.75	-2	κ_0	1.6	106	92	3.10	0.62	0.843	0.954	0.111	35.7	0.369	3.25	2.93	1.15	220	39
1.75	-2	κ_X	1.6	25	12	1.90	0.26	0.726	0.726	0.000	4.01	0.278	2.23	1.04	0.61	20	13
2.5	-2	κ_0	1.6	197	195	2.42	0.91	0.877	1.977	1.100	72.6	0.411	1.97	4.04	1.36	420	1.8
2.5	-2	κ_X	1.6	19	17	0.71	0.83	0.745	1.335	0.590	12.3	0.277	2.57	1.53	0.66	42	26
2.5	-3	κ_0	1.6	240	238	2.20	0.92	0.910	2.374	1.464	78.8	0.442	2.82	5.04	2.17	4100	1.4
2.5	-3	κ_X	1.6	19	17	0.63	0.86	0.755	1.471	0.716	15.6	0.286	3.61	2.56	1.41	460	49
2.5	-4	κ_0	1.6	193	191	1.81	0.93	0.882	2.414	1.532	78.1	0.435	3.78	6.00	3.12	37000	1.4
2.5	-4	κ_X	1.6	22	20	0.57	0.89	0.775	1.340	0.565	21.1	0.300	4.65	3.64	2.39	4900	55
2.5	$-\infty$	κ_0	1.6	206	205	1.75	0.94	0.875	0.065	2.462	78.5	0.478	3.79	5.97	3.08	...	1.6
2.5	$-\infty$	κ_X	1.6	26	25	0.64	0.92	0.748	0.172	1.438	19.7	0.369	4.78	3.94	2.49	...	60
3	-2	κ_0	1.6	232	224	1.89	0.99	0.897	1.234	0.337	77.0	0.415	1.99	4.02	1.23	400	2.0
3	-2	κ_X	1.6	25	22	0.44	0.95	0.816	1.677	0.861	34.4	0.274	2.55	1.42	0.66	41	25
4	-2	κ_0	1.6	295	292	1.43	0.95	0.921	2.144	1.223	86.2	0.430	1.82	3.89	1.07	290	1.9
4	-2	κ_X	1.6	85	81	0.65	0.95	0.884	1.991	1.107	82.9	0.328	1.64	3.39	0.74	96	3.2
4	-3	κ_0	1.6	309	306	1.38	0.95	0.925	3.844	2.919	87.8	0.459	2.71	4.88	1.99	2800	1.6
4	-3	κ_X	1.6	103	100	0.77	0.95	0.882	2.174	1.292	84.3	0.344	2.68	4.49	1.69	1200	3.9
5	-1	κ_0	1.6	142	138	0.69	0.93	0.924	1.915	0.991	88.8	0.354	0.61	2.42	-0.15	21	3.0
5	-1	κ_X	1.6	97	93	0.51	0.93	0.915	2.665	1.750	88.4	0.338	0.47	2.26	-0.15	15	1.7
5	-2	κ_0	1.6	439	436	1.29	0.93	0.975	3.565	2.590	93.6	0.453	1.68	3.80	0.99	240	1.5
5	-2	κ_X	1.6	144	144	0.65	0.93	0.929	2.260	1.331	92.0	0.362	1.52	3.39	0.62	94	3.1
5	-2	κ_0	2.0	309	306	0.99	0.94	0.950	2.006	1.056	96.2	0.452	1.56	3.67	0.76	170	2.2
5	-2	κ_X	2.0	137	134	0.59	0.93	0.924	1.657	0.733	95.3	0.375	1.46	3.35	0.46	85	5.6

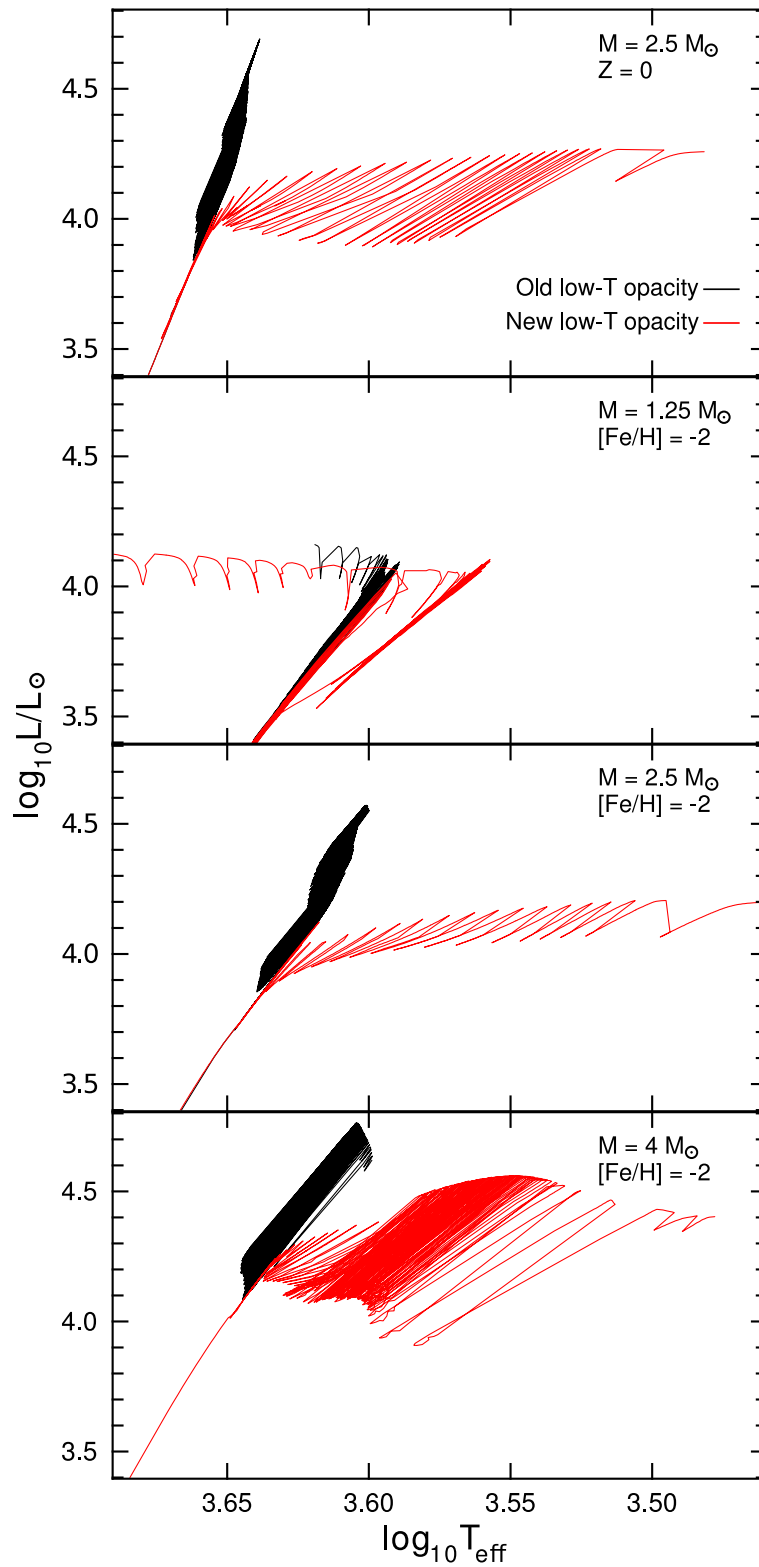


Figure 4.1: Hertzsprung-Russell (HR) diagrams for representative models. Models with composition-dependent low-T opacity are in red (grey) and those without it are in black. The top panel shows $2.5 M_{\odot}$ $Z = 0$ models, the remainder are $[\text{Fe}/\text{H}] = -2$ models with mass $1.25 M_{\odot}$, $2.5 M_{\odot}$, and $4 M_{\odot}$ (from top to bottom). This colour scheme is used throughout.

ity. The inclusion of the new opacity always makes a significant difference to the AGB evolution, so it is necessary for every one of the HBB models examined.

The evolution of our $4 M_{\odot}$ models with $[\text{Fe}/\text{H}] = -2$ and $[\text{Fe}/\text{H}] = -3$ is very similar. It is difficult to determine whether the effect of the new opacity is metallicity-dependent because the models with the old opacity still had significant envelope mass at the end of computation. The two models with the new opacity are possibly more alike than those without: the $[\text{Fe}/\text{H}] = -3$ model has 103 thermal pulses and an AGB lifetime of 0.77 Myr compared with 85 thermal pulses and 0.65 Myr for the $[\text{Fe}/\text{H}] = -2$ model, with very similar chemical yields (Table 4.2). In contrast, the envelope of the lower-metallicity model with the old opacity was more helium-rich than the higher metallicity model ($Y = 0.462$ compared with $Y = 0.442$) at the end of computation. The former model also had more envelope still remaining ($2.9 M_{\odot}$ compared with $1.2 M_{\odot}$), and would therefore become even more enriched in helium.

It is interesting that every one of our HBB models attains $\text{C}/\text{O} > 1$ during the evolution (Figure 4.4). This initially occurs quickly after carbon is dredged up, while the temperature at the base of the convective envelope (T_{bce}) is still increasing. By the time HBB becomes established the additional opacity has already had an effect – the radius of the $4 M_{\odot}$ $[\text{Fe}/\text{H}] = -2$ model with the old opacity is $60 R_{\odot}$ larger than its counterpart with the old opacity (which has radius around $350 R_{\odot}$). The envelope carbon abundance then rapidly falls (C/O reduces to below 1 in the $[\text{Fe}/\text{H}] \geq -2$ models) before C/O slowly rises again and remains above unity. By comparison, the $3.5 M_{\odot}$ $[\text{Fe}/\text{H}] \simeq -1.5$ models from Ventura and Marigo (2009) do not become carbon-rich. This difference may be attributed to a number of causes. Firstly, we use a different convection formalism, MLT instead of the full spectrum of turbulence, and have more efficient carbon dredge-up. Secondly, our models have a lower initial oxygen abundance (the $[\text{Fe}/\text{H}] = -1$ model is not oxygen-enhanced and the rest are lower metallicity). Lastly, our mass loss rate is slower. The most direct comparison we can make to Ventura and Marigo (2010) is between their $5 M_{\odot}$ $[\text{Fe}/\text{H}] \simeq -1.5$ and our $5 M_{\odot}$ $[\text{Fe}/\text{H}] = -1$ model. The core masses are comparable (within $0.04 M_{\odot}$ at most), with ours slightly smaller, giving a marginally lower temperature at the base of the convective envelope (88 MK compared with roughly 105 MK). The main difference is our larger number of thermal pulses (97 compared with their 33 and 54 when composition-dependent low-T opacity is used). This longer AGB lifetime, with more thermal pulses, allows for more third dredge-up in our models and eventually $\text{C}/\text{O} > 1$. The main reason behind this is our slower mass loss rate compared with the Bloeker (1995) and Straniero et al. (2006) rates used by Ventura and Marigo (2010). This allows for additional envelope enrichment and consequently an opacity increase when the new

opacity is used.

4.4.2 Borderline HBB models

In our lower-mass models ($1.75 \lesssim M/M_{\odot} \lesssim 3$), HBB is quenched, as it is for the higher-metallicity models in Ventura and Marigo (2010). We do not see a strong dependence of T_{bce} on metallicity (Figure 4.5), nor do we find a threshold metallicity below which HBB is no longer suppressed by the use of the new opacity (Figure 4.6). On the contrary, in our metal-poor $[\text{Fe}/\text{H}] = -2$ models we find HBB suppression between about $1.75 M_{\odot}$ and $3 M_{\odot}$. At this metallicity, the $1.75 M_{\odot}$ composition-independent low-T opacity and the $3 M_{\odot}$ composition-dependent low-T opacity models both reach the same maximum T_{bce} of about 35 MK (Table 4.2). We can therefore accurately quantify the increase in the HBB threshold to be $\Delta M_{\text{HBB}} = 1.25 M_{\odot}$. This appears to be a wider mass range compared with Ventura and Marigo (2010), both for the models with the Straniero et al. (2006) mass loss rate and (certainly) for the models with the Bloeker (1995) rate. It therefore appears that our slower mass loss rate (particularly earlier on the AGB when the pulsation period is shorter), which terminates the AGB earlier, can account for some of the difference between these models.

The evolution is so divergent in this mass range because of a feedback process. The additional opacity stops HBB, which allows the carbon abundance to increase, causing a further increase in opacity, then expansion, cooling, and mass loss. The shortened lifetime resulting from the faster mass loss then prevents the H-exhausted core from growing (and the consequential increase in T_{bce}). Compared with the models without the new opacity, the AGB lifetime is reduced by a factor of 3–4, causing the largest reduction in final core mass (Figure 4.3), which is greater than $0.1 M_{\odot}$ in all of these models. The number of thermal pulses and the total yield of C+N+O are reduced by a factor of 10 compared with equivalent composition-independent opacity models. The carbon yield is increased by up to a factor of 10, whereas the nitrogen and oxygen yields are reduced by around 99.7% and 80%, respectively. This major change in composition over such a broad mass range may have important implications for the predicted CEMP and NEMP frequency (discussed in Section 4.5.2). These models also have the largest reduction in helium production, with a mass fraction difference of up to 0.16 (Figure 4.7).

4.4.3 Low-mass models

In the mass range below which HBB can occur, the results are critically dependent on the extent of third dredge-up. Both of our $1.25 M_{\odot}$ models have only one small third

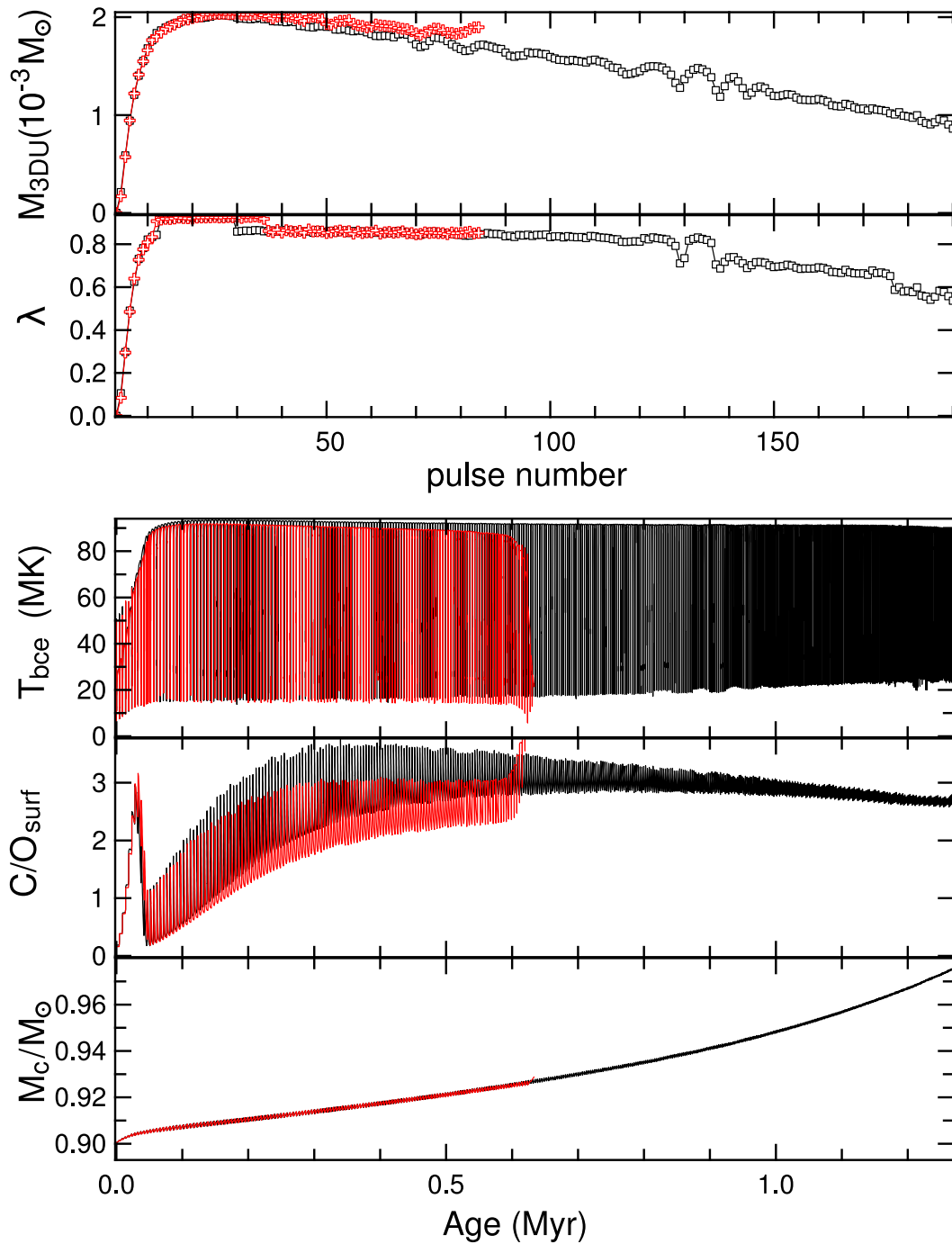


Figure 4.2: AGB evolution of $5 M_{\odot}$ $[\text{Fe}/\text{H}] = -2$ models. From top to bottom the panels show the mass dredged up after each thermal pulse, the dredge-up efficiency λ , the temperature at the base of the convective envelope, surface C/O number ratio, and hydrogen-exhausted core mass. The age has been set to zero at the beginning of the TP-AGB phase. The colours are the same as in Figure 4.1.

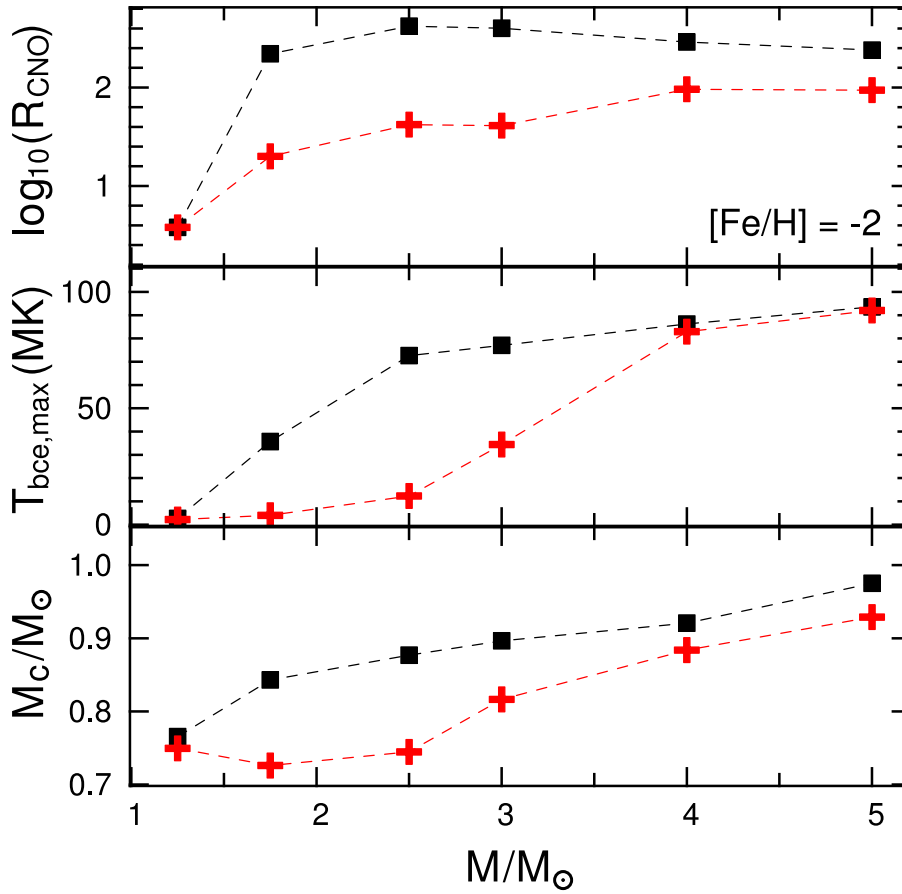


Figure 4.3: Comparison of the $[\text{Fe}/\text{H}] = -2$ models. Upper panel: ratio of the total yield of C+N+O to the initial abundance (R_{CNO}). It is assumed that the remaining envelope is ejected with the same composition as at the end of computation. Middle panel: maximum temperature at the base of the convective envelope during the interpulse period for the same models. Lower panel: end of computation hydrogen-exhausted core mass (M_c). The colours are the same as in Figure 4.1.

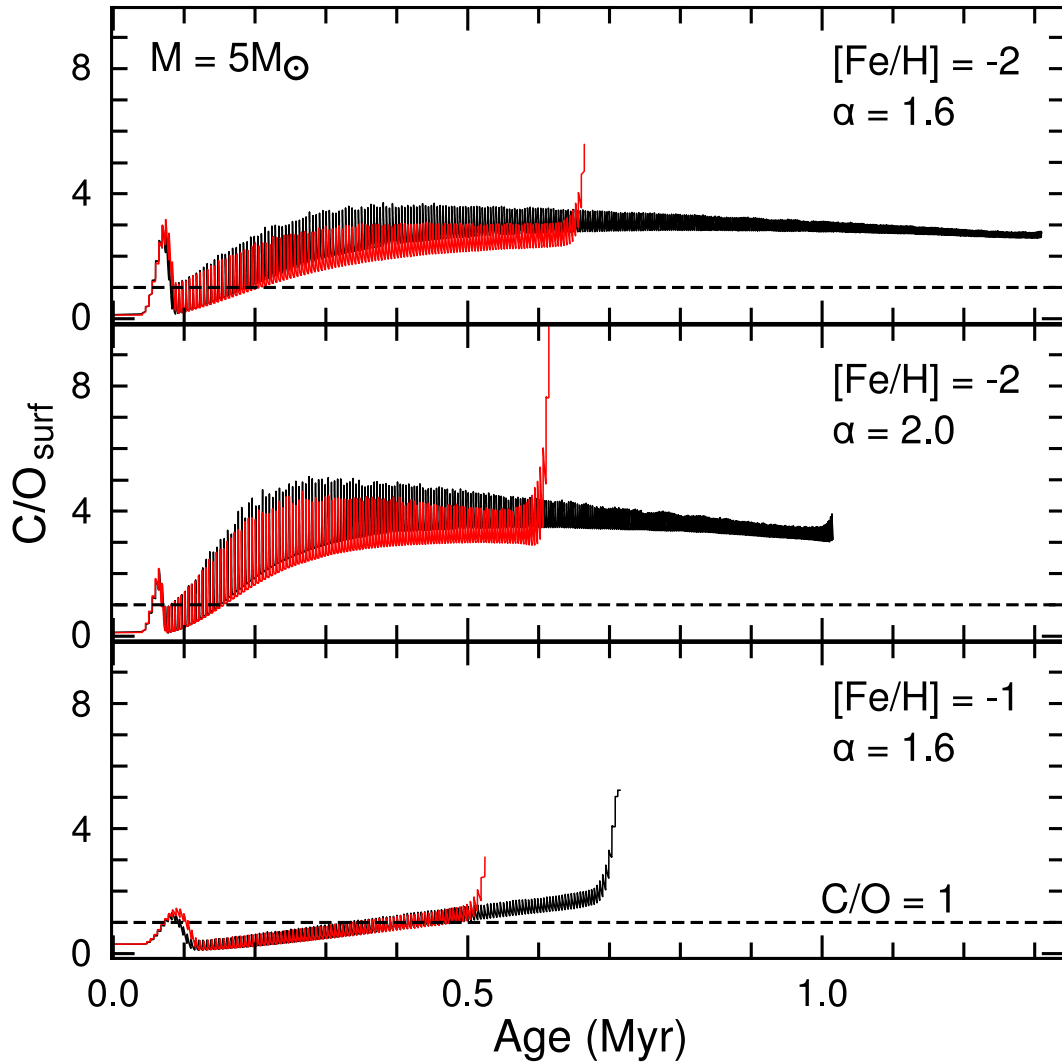


Figure 4.4: Surface C/O ratio (by number) for each of the $5 M_{\odot}$ models. The models in the top two panels have metallicity $[\text{Fe}/\text{H}] = -2$, while the model in the bottom panel has $[\text{Fe}/\text{H}] = -1$. The model in the middle panel has MLT mixing length parameter $\alpha_{\text{MLT}} = 2$ instead of 1.6. The colours are the same as in Figure 4.1.

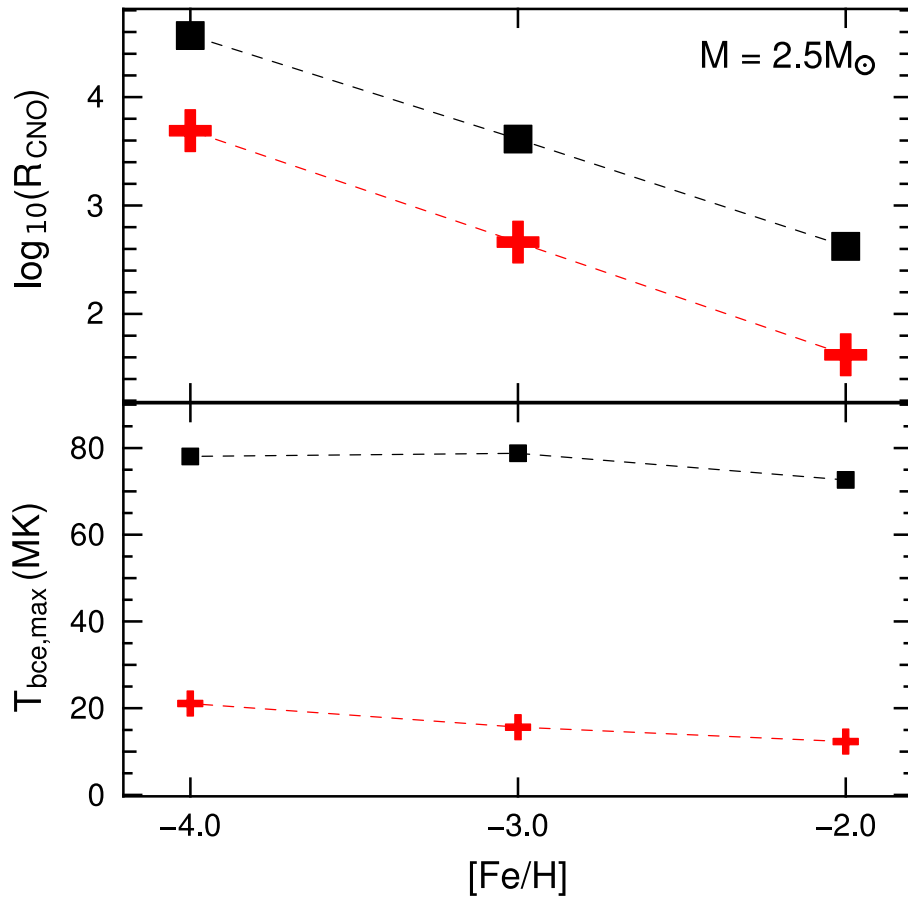


Figure 4.5: Upper panel: ratio of the total yield of C+N+O to the initial abundance (R_{CNO}) for each of the $2.5M_{\odot}$ models. It is assumed that the remaining envelope is ejected with the same composition as at the end of computation. Lower panel: maximum temperature at the base of the convective envelope during the interpulse period. The colours are the same as in Figure 4.1.

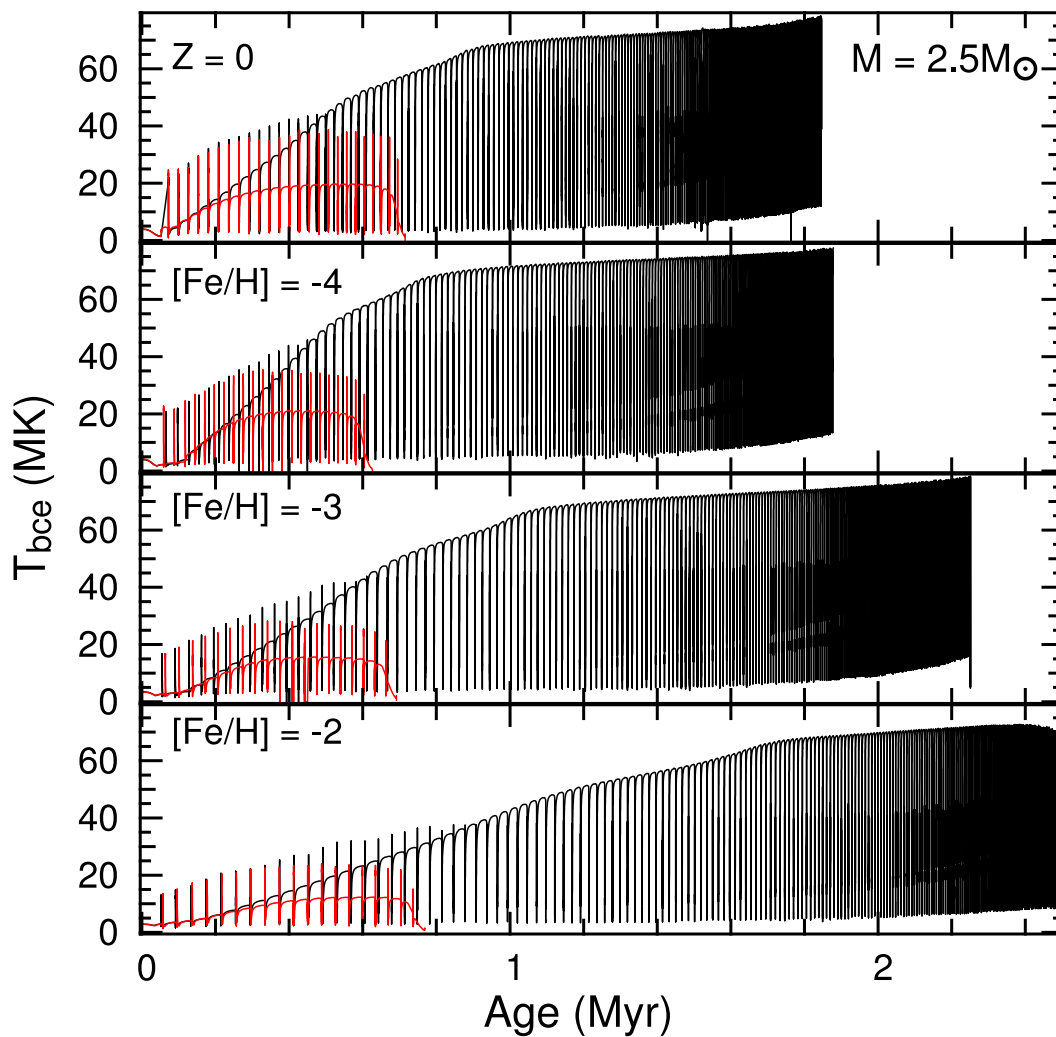


Figure 4.6: Temperature at the base of the convective envelope for each of the $2.5 M_{\odot}$ models. They have metallicity $Z = 0$, $[\text{Fe}/\text{H}] = -4$, $[\text{Fe}/\text{H}] = -3$, and $[\text{Fe}/\text{H}] = -2$, from top to bottom. The colours are the same as in Figure 4.1.

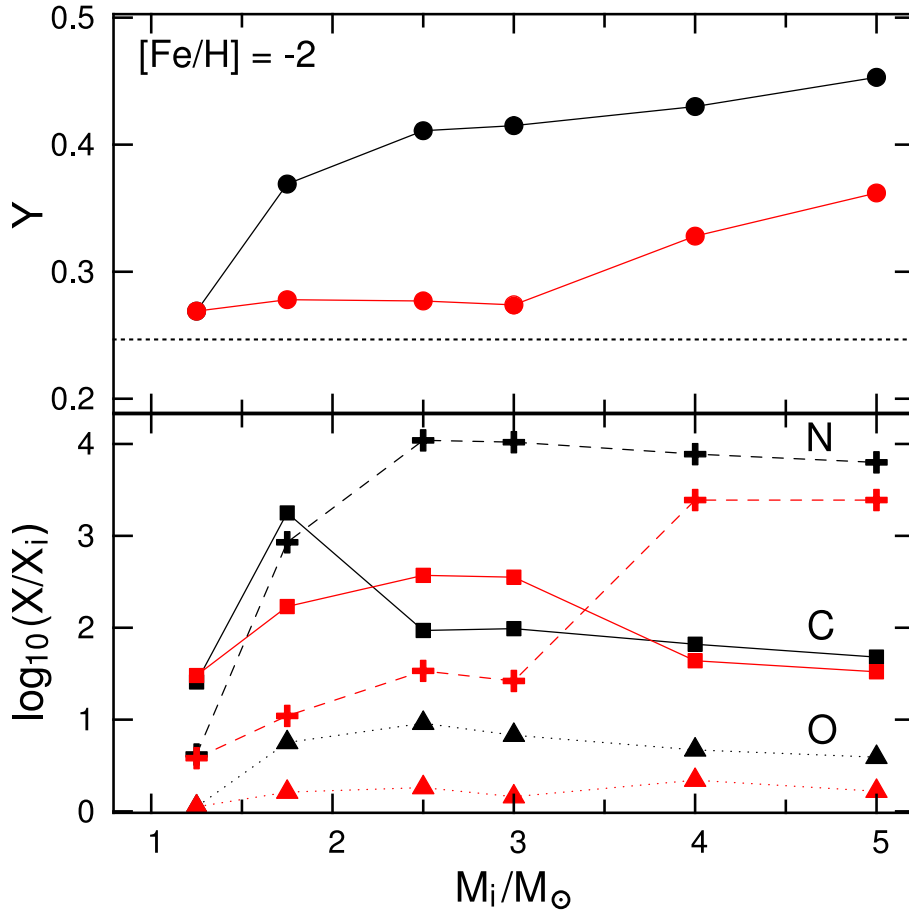


Figure 4.7: Integrated yields for each $[\text{Fe}/\text{H}] = -2$ model. Upper panel: average mass fraction of helium in ejecta. The dashed line is initial helium abundance $Y = 0.245$. Lower panel: carbon (square), nitrogen (cross), and oxygen (triangle) yields expressed as a log fraction of initial abundance. It is assumed that any remaining envelope is ejected with the end-of-computation abundance. The colours are the same as in Figure 4.1.

dredge-up episode, achieving $C/O \approx 3$ and almost identical final yields. The relatively modest change in surface composition that results, and the already fast mass loss, mean that the structure and lifetime of the new and old opacity cases are more alike than for the other models studied. Despite this, the change in structure after the dredge-up is still obvious: in the model with the new opacity, the radius increases substantially and there is a slower increase in T_{bce} (Figure 4.8). Even though this model initially had $[O/Fe] = +0.4$ and only experiences a single, low-efficiency third dredge-up episode ($\lambda = 0.17$), it easily reaches $C/O > 1$. This suggests that *any* low-mass, low-metallicity model with the third dredge-up requires composition-dependent low-T opacity.

It is evident that we cannot characterize low-mass composition-dependent low-T opacity models ($[Fe/H] = -2$) with substantial third dredge-up (e.g., the $M = 1.75 M_{\odot}$ model) as truncated copies of models without the new opacity. Differences in the structure are evident from the beginning of the TP-AGB. The additional opacity leads to increased mass loss and then a lower T_{bce} and third dredge-up efficiency (Figure 4.9). The reduced dredge-up and shorter lifetime give the same reduction in total C+N+O yield as for the models where the new opacity causes HBB to be averted. Qualitatively, these effects are similar to those for higher-metallicity models. The opacity treatment causes a more pronounced divergence in evolution in our $1.75 M_{\odot}$ than it does for the $2.5 M_{\odot}$ $[Fe/H] \simeq -1.5$ models in Ventura and Marigo (2009, which is an apt comparison because they are both just below the mass cut-off for HBB in the respective codes). We find a maximum T_{bce} of 36 MK and 4 MK compared with 31 MK and 18 MK in Ventura and Marigo (2009). Similarly, the differences in chemical yields, lifetime and number of thermal pulses in our models are larger. Although the use of the Bloeker (1995) mass loss certainly contributes to the contrast between the two sets of models, it also highlights that the lower the metallicity is, the more acute the need is for the new opacity.

The only comparable study for a metal-poor case that we could find in the literature is the $2 M_{\odot}$ $[Fe/H] = -2.17$ model in Cristallo et al. (2007). In their model, accounting for C and N enhancements reduced the number of thermal pulses by a factor of four. This compares to a factor of three for our $1.75 M_{\odot}$ $[Fe/H] = -2$ model. The halting of growth of the third dredge-up is also similar to our model. The main difference between the models is that ours have approximately double the number of thermal pulses (106 and 25 as opposed to 51 and 15). Their use of the Straniero et al. (2006) mass loss rate contributes to this, because it is higher from the beginning of the AGB, when the pulsation period P is shorter ($\log [P(\text{days})] < 2.5$). Our model with the new opacity reaches this pulsation period only after 48 thermal pulses and 80% of its TP-AGB lifetime.

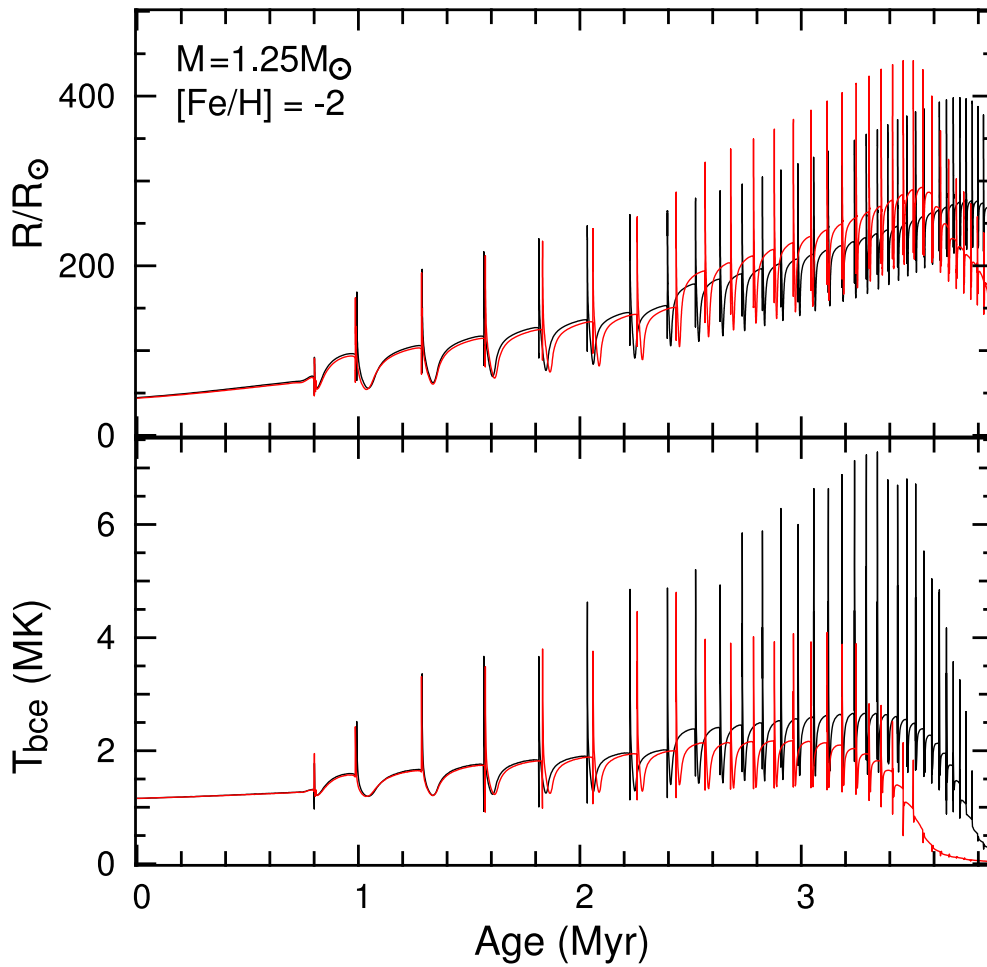


Figure 4.8: Stellar radius (upper panel) and temperature at the base of the convective envelope (lower panel) for the $1.25 M_{\odot}$ $[\text{Fe}/\text{H}] = -2$ models. The colours are the same as in Figure 4.1.

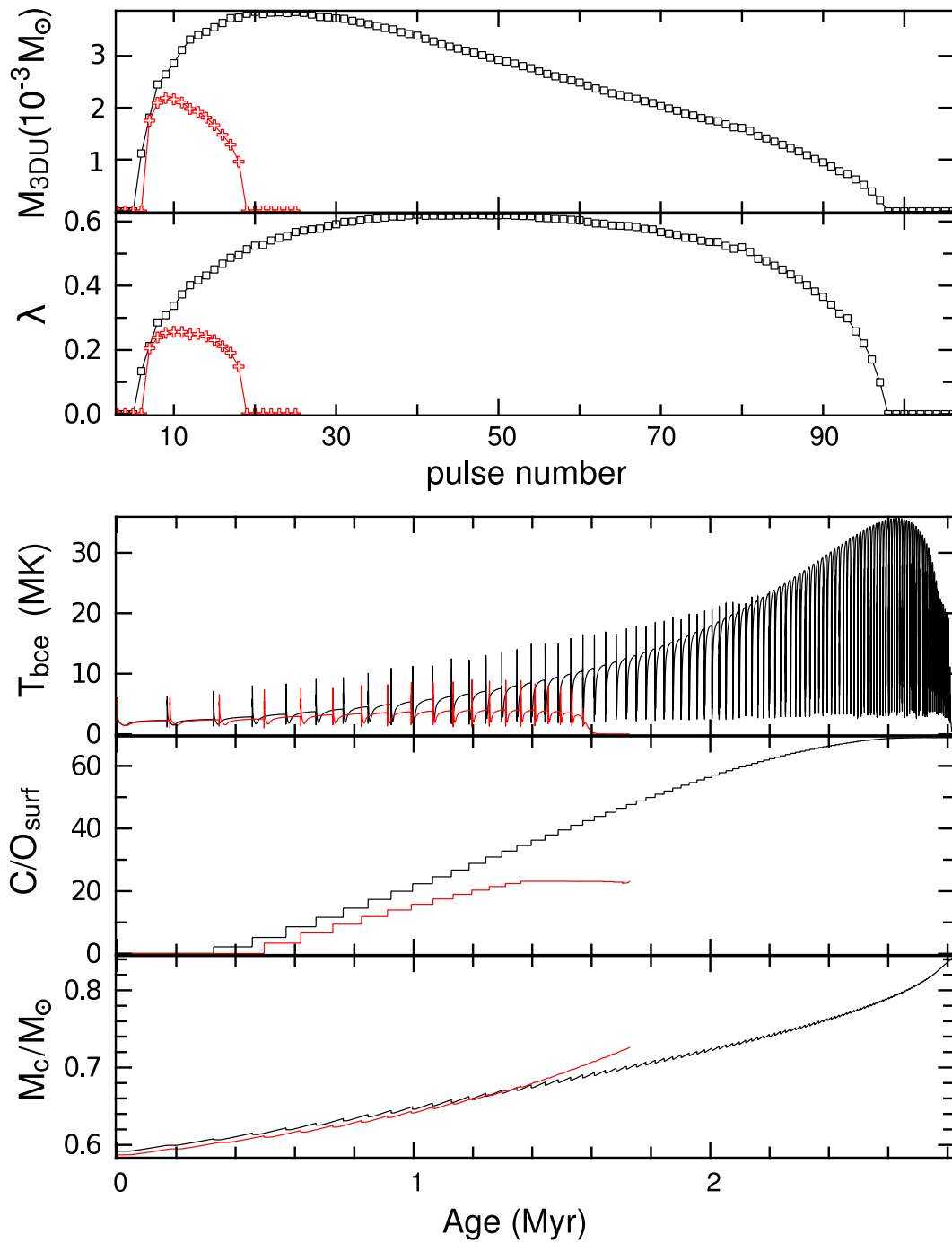


Figure 4.9: AGB evolution of $1.75 M_{\odot}$, $[\text{Fe}/\text{H}] = -2$ models. From top to bottom, the panels are the mass dredged up each thermal pulse, the dredge-up efficiency λ , the temperature at the base of the convective envelope, surface C/O number ratio, and hydrogen-exhausted core mass. The colours are the same as in Figure 4.1.

4.4.4 Lessons from zero-metallicity models

Zero-metallicity models are interesting in this study because they display the most extreme change in composition during their evolution. We examined a $2.5 M_{\odot}$ $Z = 0$ model in order to determine whether there is a metallicity limit below which the HBB quenching effect of the new opacity is no longer observed. This model presented an additional complication because it is the only one in our grid in which the intershell convection zone is able to penetrate the H-shell at the beginning of the TP-AGB, leading to an event that is variously referred as an H-flash, dual shell flash, or proton ingestion episode (Cassisi et al., 1996; Campbell and Lattanzio, 2008; Iwamoto, 2009). In one-dimensional models, this can radically alter the surface composition. Studies by Iwamoto (2009) and Suda and Fujimoto (2010), however, show that the ensuing surface enrichment decreases with increasing stellar mass. In the $Z = 0$ models from the latter, the total C+N+O fraction in the $2 M_{\odot}$ model is a factor of 20 less than the $1.5 M_{\odot}$ model. While in models with $M \geq 2 M_{\odot}$ there is some mixing to the surface from this event it is relatively minor and the envelope composition is very quickly dominated by the subsequent third dredge-up events and HBB (see e.g. the $3 M_{\odot}$ $[\text{Fe}/\text{H}] = -5.45$ model and summary schematic in Campbell and Lattanzio 2008, their Figures 2 and 4). Overall, the dual shell flash is difficult to model and the results are highly uncertain in one-dimensional codes. It is important to note that it is unlikely to be relevant to our opacity study because we expect little effect on the later evolution of a $2.5 M_{\odot}$ model. For these reasons, we began the comparison with a single TP-AGB $2.5 M_{\odot}$ $Z = 0$ model after the first thermal pulse (i.e., we did not evolve *both* the new and old opacity models from the pre-main sequence), in which we specifically prohibited the intershell convection zone from expanding into the H-shell.

With the old opacity the final AGB core mass is much larger ($\Delta M_{c,f} = 0.13 M_{\odot}$, which is consistent with the higher metallicity $2.5 M_{\odot}$ models in Table 4.2). Like the other models with the new opacity, the evolution is hastened via positive feedback: The initial cooling of the envelope prevents HBB, so dredged-up carbon is not converted to nitrogen (which contributes less to the opacity). With the new opacity, the mass limit for zero-metallicity HBB models appears to be much higher than $2.5 M_{\odot}$, compared with $2 M_{\odot}$ in Siess et al. (2002). This contrasts strongly with Campbell and Lattanzio (2008) where every one of the $Z = 0$ models ($0.8 \leq M/M_{\odot} \leq 3$) produced more nitrogen than carbon, and the 2 and $3 M_{\odot}$ models both have $\text{N}/\text{C} > 20$. This ratio is reversed for our $2.5 M_{\odot}$ model with the new opacity. Because the effect of the new opacity is evident in the most metal-poor case possible, these findings demonstrate that there is no lower metallicity limit below which the new opacity is not essential if carbon is dredged up. An examination of the AESOPUS data reveals that although the opacity is less dependent on

composition at this model’s relatively high surface temperature ($\log T \sim 3.7$), it is still much more sensitive to an increase in carbon than it is to nitrogen.

4.5 Discussion

4.5.1 Key findings

Our models do not support the suggestion by Marigo (2007) that there is a metallicity limit below which composition-dependent low-T opacity may be neglected (Figure 4.10). As metallicity decreases, there is remarkable uniformity in the differences in radius (Figure 4.11), T_{bce} (Figure 4.6), and the total yield of C+N+O relative to the initial abundance (R_{CNO} ; Figure 4.5). Moreover, the absolute mass fractions of C, N, and O in the stellar wind from models differing only in initial metallicity are almost identical. We also find the new opacity to be crucial for models massive enough to have HBB.

4.5.2 Implications for CEMP and NEMP stars

Our results go some way to explaining the paucity of NEMP stars. In the entire mass and metallicity range explored, models with composition-dependent low-T opacity produce less nitrogen than the models without it. Lifetimes are always shortened, leading to fewer dredge-up events and shorter HBB time. The higher-mass, low-metallicity models that produce the most nitrogen have their AGB lifetime reduced by around two thirds (Table 4.2). Moreover, at lower masses the cooling effect in the interior is sufficient to prevent altogether the conversion of the carbon in the envelope to nitrogen before it is shed in the stellar wind (Figure 4.12). This causes an increase in the mass threshold for HBB of $\Delta M_{\text{HBB}} = 1.25 M_{\odot}$ in our $[\text{Fe}/\text{H}] = -2$ models. With an initial mass function that favors low-mass stars (Pols et al. 2012 exclude the possibility of a top-heavy initial mass function for $-2.8 \leq [\text{Fe}/\text{H}] \leq -1.8$) we predict that such a change would give a significant reduction in the expected NEMP/CEMP ratio in a population synthesis model. There are more consequences to consider here too. Not only is the composition of the wind different, but also the evolution of radius with time, which would obviously affect Roche-lobe overflow mass transfer and common envelope evolution in binary systems. In general, the increase in maximum radius, which can result from a single third dredge-up episode (Figure 4.8), would increase the likelihood of binary interaction.

The existence of NEMP stars only below $[\text{Fe}/\text{H}] = -2.8$ is still puzzling. Although it is known that T_{bce} increases with decreasing metallicity for a given MLT mixing length (Sackmann and Boothroyd, 1991), and strengthens HBB, the difference in particular

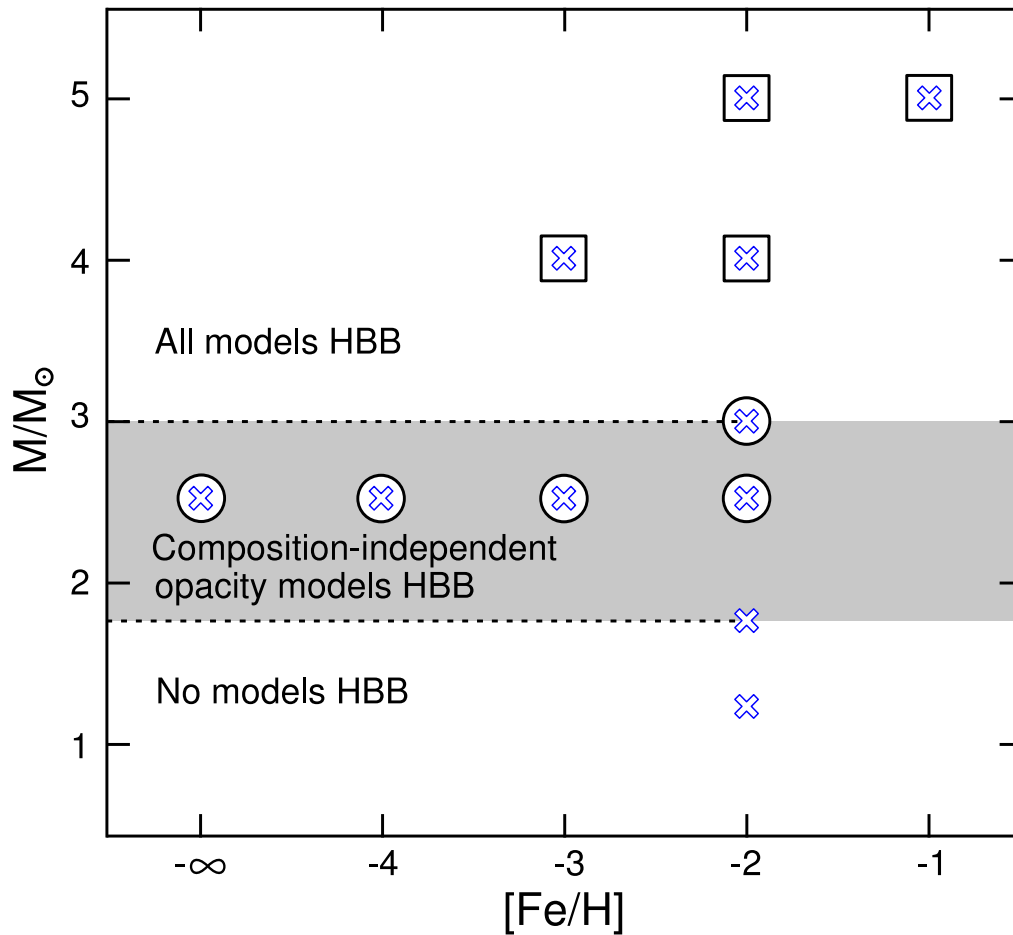


Figure 4.10: Results from the grid of stellar models. Each model pair (with and without composition-dependent opacity) is marked by a cross. Circles indicate that HBB occurs only in the model without composition-dependent opacity. Squares indicate that HBB occurs in both models. The shaded region is the approximate mass range that has HBB only when composition-independent opacity is used. The dashed lines indicate the metallicity range studied $[\text{Fe}/\text{H}] \leq -2$ and where the evolution depends little on the initial metallicity.

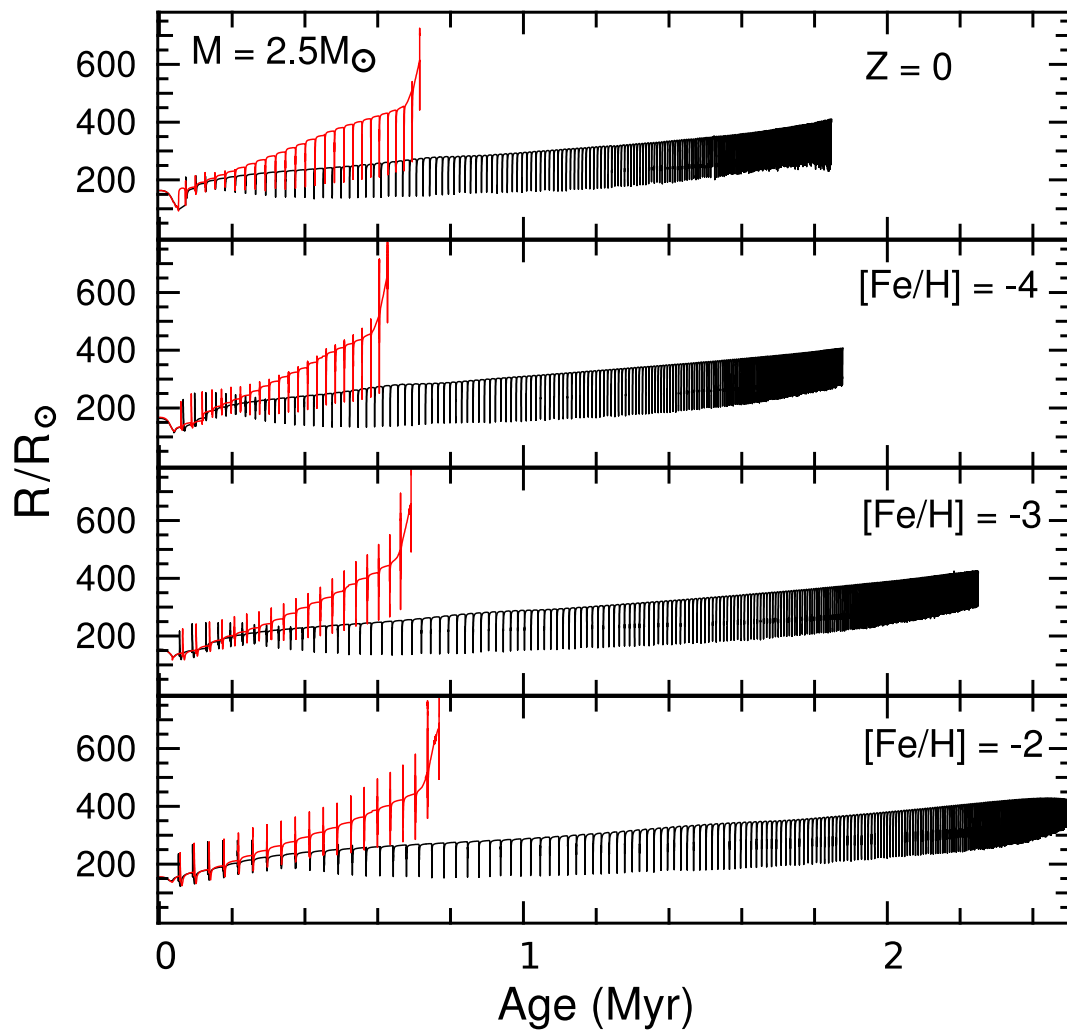


Figure 4.11: Stellar radius for each of the $2.5 M_{\odot}$ models. They have metallicity $Z = 0$, $[\text{Fe}/\text{H}] = -4$, $[\text{Fe}/\text{H}] = -3$, and $[\text{Fe}/\text{H}] = -2$, from top to bottom. The colours are the same as in Figure 4.1.

between our $[\text{Fe}/\text{H}] = -2$ and $[\text{Fe}/\text{H}] = -3$ models (Figure 4.6) cannot explain the observed $[\text{Fe}/\text{H}]$ dependence of NEMP star existence (Johnson et al., 2007). The new opacity appears not to help the situation: the magnitude of the change in T_{bce} with a change in metallicity is independent of the low-T opacity treatment. Comparing our $2.5 M_{\odot}$ $[\text{Fe}/\text{H}] = -2$ and $Z = 0$ models illustrates this point. In the new opacity case, the maximum T_{bce} increases from 12.3 to 19.7 MK with the drop in metallicity, while the composition-independent case increases from 72.6 to 78.5 MK (Table 4.2). Our new and old opacity 4 and $5 M_{\odot}$ models show almost the same drop in T_{bce} as a result of a reduction in metallicity $\Delta[\text{Fe}/\text{H}] = -1$ (to within 0.2 and 1.2 MK respectively).

Our models cannot explain the metallicity dependence of the existence of NEMP stars through binary accretion. Assuming there is a need to further reduce the HBB limit only at very low metallicity to reproduce the observed frequency of NEMP stars (i.e. the nitrogen-enhancement is not the result of another process), a metallicity or composition-dependent mass loss rate may offer an explanation, perhaps relating to dust formation (Pols et al., 2012). The Vassiliadis and Wood (1993) rate we use is only depends on stellar structure and therefore becomes relatively insensitive to $[\text{Fe}/\text{H}]$ for extremely metal-poor models. Alternatively, an initial mass function more heavily weighted to intermediate-mass stars at very low metallicity would help (Suda et al., 2013).

Our low-mass models computed with the new opacity treatment have a much shorter TP-AGB phase and reduced oxygen yield. In Figure 4 in Kennedy et al. (2011), the observed $[\text{O}/\text{Fe}]$ in 19 CEMP stars is compared with the average value for EMP stars from Spite et al. (2005). Although the error bars are large ($\gtrsim 0.5$ dex), the two groups are comparable. This suggests the reduced oxygen enhancement in models with the new opacity is reasonable. In that there is also an $[\text{O}/\text{Fe}]$ - $[\text{Fe}/\text{H}]$ relation that we replicate with our $2.5 M_{\odot}$ models using *either* opacity treatment.

In Figure 4.13, we compare the C, N, and O yields from our 1.75, 2.5, and $3 M_{\odot}$ $[\text{Fe}/\text{H}] = -2$ models to the 10 stars in Kennedy et al. (2011) for which these abundances were determined. Each of these stars has $[\text{C}/\text{N}] > 0$. This immediately rules out the $M/M_{\odot} > 1.75$ models with the old opacity from matching a donating companion because they produce far too much N from HBB. With the exception of the very O-rich star HE0017+0055, all stars can be matched reasonably (to within about 0.5 dex) by the three new opacity models. The abundance patterns in the new opacity models are very similar to three of the observed stars. A further six observed stars are closer to having $[\text{C}/\text{Fe}] = [\text{N}/\text{Fe}]$. These six observations are consistent with our models if we consider the scenario in Stancliffe et al. (2007) where thermohaline mixing of accreted material is followed by the first dredge-up, which reduces the initially high surface $[\text{C}/\text{Fe}]$. In

Stancliffe et al. (2007), the model of a $0.74 M_{\odot}$ secondary accreting $0.09 M_{\odot}$ eventually reaches $[C/Fe] - [N/Fe] < 0.5$, irrespective of initial N accretion. It is surprising that 9 out of the 10 observed abundance patterns are then better explained by the new opacity models (Figure 4.13; the very O-rich star HE0017+0055 cannot be matched by any of our models). The new opacity models are also a good fit for the observations plotted in the $[C/Fe]$ - $[O/Fe]$ plane in Figure 8 in Kennedy et al. (2011) after dilution is taken into account.

Izzard et al. (2009) suggest that more efficient dredge-up for $M < 1.25 M_{\odot}$ in binary population synthesis models is needed to fit the higher observed CEMP/EMP ratio. Although the updated low-T opacity certainly does not solve this problem (it is not even relevant unless there is dredge-up), it would be interesting to study the effect of low-T opacity in low-mass models with more efficient dredge-up.

4.5.3 AGB stars as globular cluster polluters

The $5 M_{\odot}$ $[Fe/H] = -2$ models with composition-dependent low-T opacity yield only half the oxygen and total C+N+O. Although this change is an improvement in the right direction, it is not nearly enough for these models to be consistent with the intermediate-mass AGB globular cluster self-pollution scenario. Evidence points towards a spread in the helium abundance within globular clusters, and that the extent of the spread differs immensely from cluster to cluster. Fitting stellar evolution isochrones to main sequence, subgiant and red giant branch HST photometry suggests that there is a small helium spread $\Delta Y \sim 0.03$ in NGC 6752 (Milone et al., 2013). In NGC 2808, by contrast, isochrone fits of the horizontal branch (Lee et al., 2005) and main sequence (D’Antona et al., 2005; Piotto et al., 2007) along with spectroscopic determination (Pasquini et al., 2011) show a much larger helium spread $\Delta Y \sim 0.20$. All of our $5 M_{\odot}$ models become enriched in helium (Figure 4.7), regardless of opacity treatment, because much of the increase results from the second dredge-up, which occurs before the new opacity treatment has any effect. The stellar wind in the most helium-rich model with the new opacity, however, has $Y = 0.375$ ($\Delta Y = 0.13$), which is insufficient to account for the helium-rich population in NGC 2808.

Even when the new opacity is used for the $[Fe/H] = -2$ models, we still do not find any oxygen depletion. The mean ejected $[O/Fe]$ is 0.62 and 0.46 in the standard and higher MLT mixing length cases respectively (Table 4.2). This compares to approximately scaled-solar oxygen in Na-rich stars observed in five clusters of similar metallicity $-2.5 < [Fe/H] < -1.8$ (Gratton et al., 2012b). This naturally points towards further increasing the mixing length to generate models that fit the $[O/Fe]$ constraint. A problem is that in our mixing length test (last two models in Table 4.2) R_{CNO} is barely affected

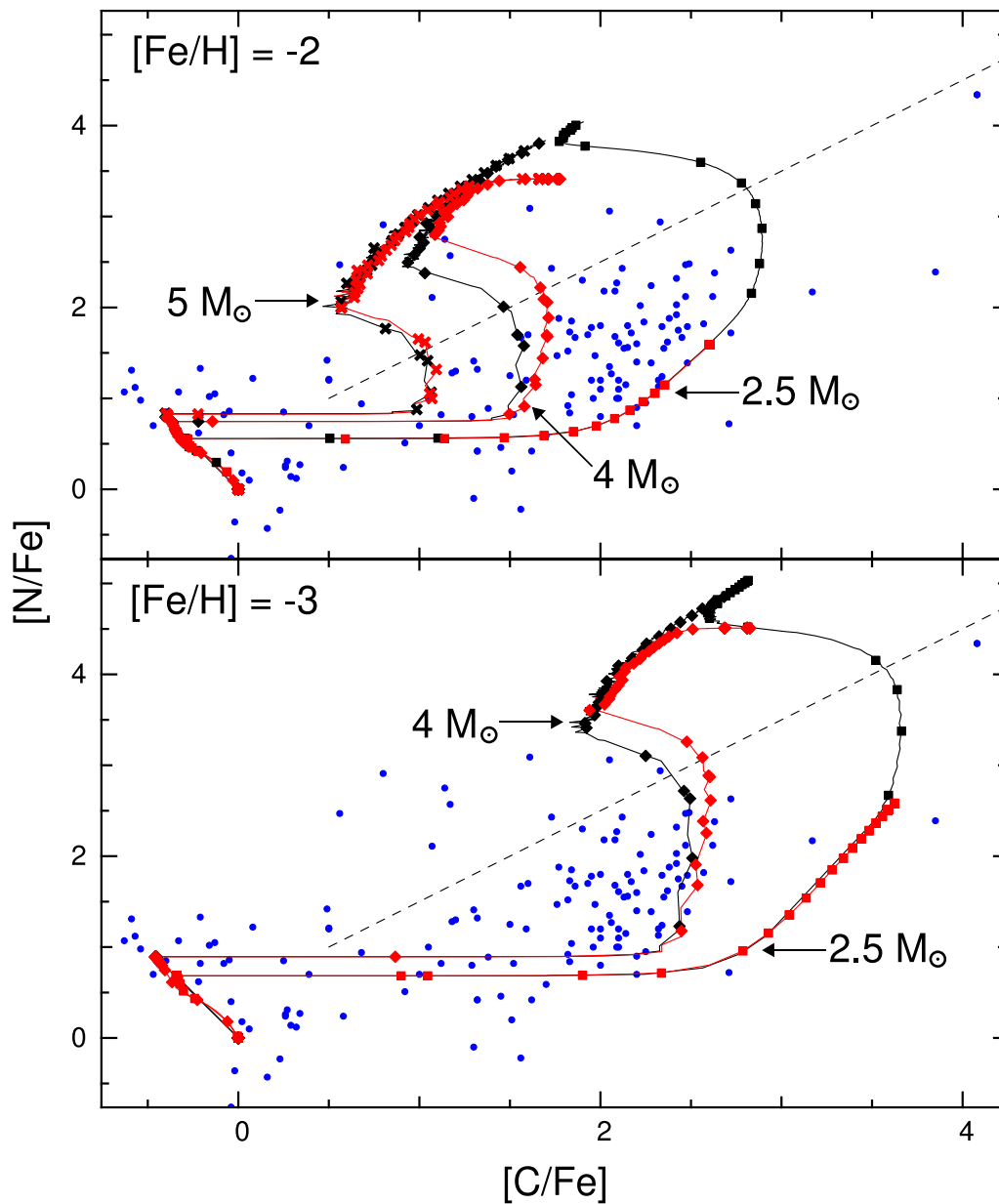


Figure 4.12: Upper panel: surface abundance of nitrogen and carbon for $2.5 M_{\odot}$, $4 M_{\odot}$, and $5 M_{\odot}$ $[\text{Fe}/\text{H}] = -2$ models (in squares, diamonds, and crosses, respectively) plotted during the evolution at intervals of $10 R_{\odot}$ (instead of time). Models with composition-dependent low-T opacity are in red (grey) and those without it are in black. Lower panel: same as upper panel except for $2.5 M_{\odot}$ and $4 M_{\odot}$ $[\text{Fe}/\text{H}] = -2$ models (in squares and diamonds, respectively). The blue circles are observations listed in Masseron et al. (2010), which have $[\text{Fe}/\text{H}] \leq -0.99$ and a mean of $[\text{Fe}/\text{H}] = -2.74$. The dashed line is $[\text{N}/\text{C}] = 0.5$ and $[\text{C}/\text{Fe}] > 0.5$, which separates CEMP and NEMP stars according to the definition in Pols et al. (2012).

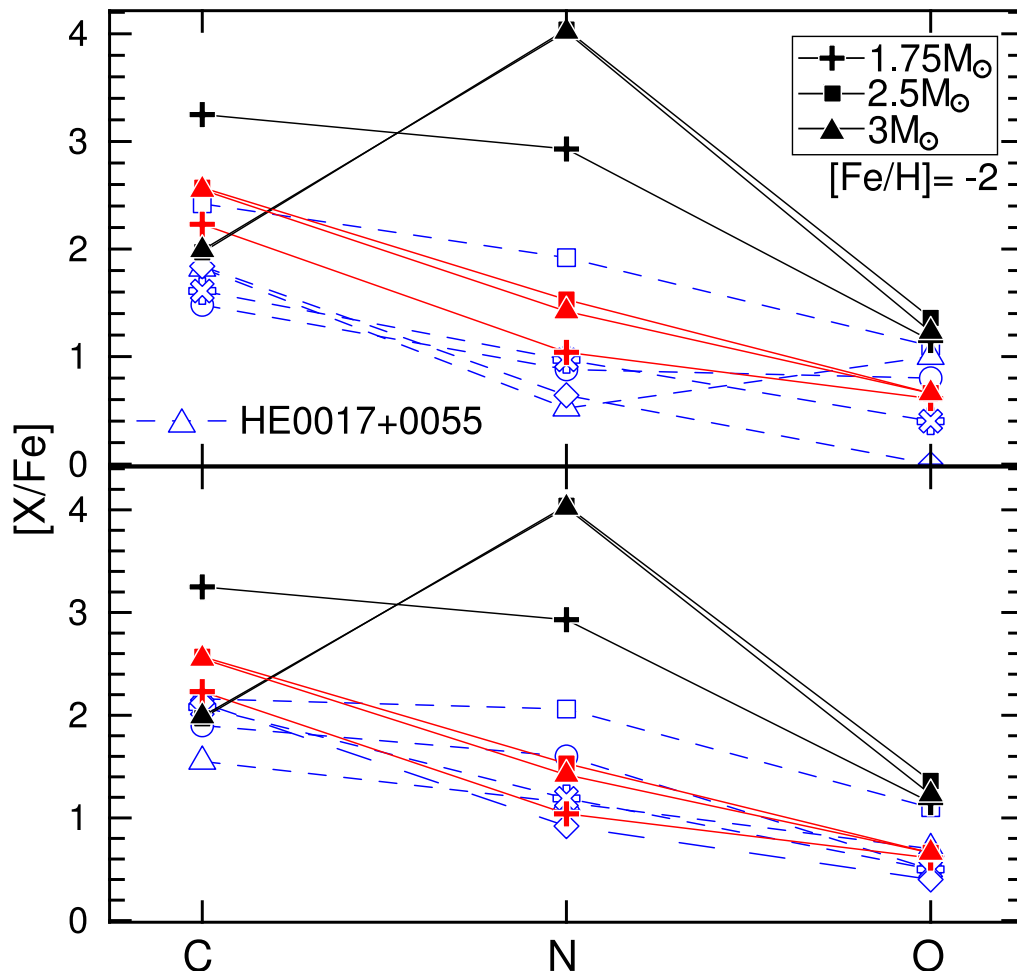


Figure 4.13: Integrated chemical yields of C, N, and O from 1.75, 2.5, and 3 M_{\odot} $[\text{Fe}/\text{H}] = -2$ models (solid symbols) compared with 10 observed CEMP stars from Figure 7 of Kennedy et al. (2011, in blue, open symbols and dashed lines). Models with composition-dependent low-T opacity are in red (grey) and those without it are in black. The observations are split between two panels, consistent with the original figure. HE0017+0055 is the only star that the models with the new opacity cannot match (see text for details).

(reducing from 94 to 85 when increasing α_{MLT} from 1.6 to 2.0 for the models with the new opacity), and is still considerably higher than the observational constraints (summarized in Section 4.2). Faster mass loss would then be required to limit the total third dredge-up mass. We note that D’Orazi et al. (2013) used a recent version of our code to reveal some additional problems with the above approach when also performing detailed nucleosynthesis calculations to replicate the abundance patterns in NGC 6121 (M4). Our higher metallicity ($[\text{Fe}/\text{H}] = -1$) $5 M_{\odot}$ models did deplete oxygen, producing ejecta with $[\text{O}/\text{Fe}] = -0.15$ (irrespective of the opacity treatment) but not enough to explain the oxygen spread observed by Gratton et al. (2012b). R_{CNO} was also too high, being 15 in the model with the new opacity and 21 in the model without it.

4.5.4 Uncertainties

The general trends we have established are dependent on the mass loss prescription, which is poorly constrained for low-metallicity AGB stars. The difference in lifetimes would be smaller, for example, if a higher mass loss rate were adopted. When the new opacity is used in our models, the mass loss rate is very heavily dependent on envelope enrichment, both compared with models without it and models with other mass loss prescriptions. Mass loss formulae principally depend on stellar mass, luminosity, and radius to different degrees. The quantity most directly affected by the new opacity is radius. Therefore, the changes are most obvious when using the mass loss formula more sensitive to radius. According to Reimers (1975) and Bloeker (1995), mass loss is proportional to radius R , compared with Nieuwenhuijzen and de Jager (1990) where it is proportional to $R^{0.81}$. This contrasts with Vassiliadis and Wood (1993) in which the mass loss rate increases exponentially with $R^{1.94}$ (before the superwind phase). This formula uses the pulsation period dependence on mass and radius originally computed for low-mass models $0.6 \lesssim M/M_{\odot} \lesssim 1.5$ (Wood, 1990), and it also does not directly account for the change in stellar structure caused by the additional low-T opacity. Even so, we believe that using the Vassiliadis and Wood (1993) rate is a reasonable choice because after the third dredge-up the Z content of the envelope and the stellar structure is comparable to the more metal-rich stars from which period-mass loss relation was empirically derived.

We investigated the effect of the MLT mixing length, which could be important because it affects the two factors that control the conditions at the surface, the temperature and chemistry. This includes its effect on the conditions at the interior boundary of the convective envelope that control dredge-up and HBB, and thus alter the surface composition. In our comparison between $5 M_{\odot}$ models with mixing length parameter $\alpha_{\text{MLT}} = \ell_{\text{MLT}}/H_{\text{p}}$ of 1.6 and 2.0 (where ℓ_{MLT} is the mixing length and H_{p} is the pressure-scale-height), we

find only a minimal difference, apart from the expected shift to slightly higher T_{eff} with increasing α_{MLT} (Table 4.2). It therefore appears that our analysis is insensitive to small changes in mixing length, at least for HBB models.

Dredge-up efficiency λ , which depends on the treatment of convection and overshoot, is another important consideration for how models are affected by the low-T opacity. This is because it leads to important changes in the structure and composition: the core growth rate is higher in models with little dredge-up, leading to increased luminosity according to the well-known relation for non-HBB models (Paczynski, 1970a), and therefore faster mass loss, while envelope enrichment will be slower. These two factors combine so that the evolution of models with a higher λ will be more affected by the new opacity than otherwise similar models with a lower λ . A comparison in Figure 4 of Marigo et al. (2013) between five full stellar structure codes (Cristallo et al., 2011; Weiss and Ferguson, 2009; Stancliffe et al., 2004; Karakas et al., 2002; Herwig, 2000) with the same initial model ($3 M_{\odot}$ $Z = 0.02$) shows how much λ and the minimum core mass for the third dredge-up can vary from code to code. The dredge-up efficiency is important in HBB models for an additional reason: C/O depends on the competition between carbon dredge-up and its destruction. Our HBB models tend to have a high λ (peaking between 0.91 and 0.99 in $M > 2.5 M_{\odot}$ models with the old opacity) which partly explains why we find the opacity to be so important where others have not (e.g. Ventura and Marigo, 2010). While the third dredge-up is crucial to determining the impact of the new opacity, the increase in computed opacity itself has little or no effect on λ (Table 4.2) except when the mass loss rate increases, terminating the AGB evolution earlier (Figure 4.4). Ventura and Marigo (2010) attribute the three-fold difference in the number of thermal pulses between their $2 M_{\odot}$ $Z = 0.001$ model and an equivalent in Weiss and Ferguson (2009) to the latter's deeper third dredge-up. This causes the envelope to become C-rich earlier and speeds up mass loss. Low-metallicity models become C-rich very easily (our $1.25 M_{\odot}$ and $1.75 M_{\odot}$ $[\text{Fe}/\text{H}] = -2$ both had $\text{C}/\text{O} > 1$ after the first third dredge-up episode) so this factor is less important in our low-mass models.

4.6 Conclusions

We find that the inclusion of composition-dependent low-T opacity influences the evolution of all of our models. Although the resulting structural effects for metal-poor models are broadly similar to those reported elsewhere for higher-metallicity models (e.g. Marigo, 2002; Ventura and Marigo, 2009), we find them to be applicable over a broader stellar mass range, at least $1.25 \leq M/M_{\odot} \leq 5$. In metal-poor models, the third dredge-up can

more easily increase the surface metal abundance relative to its initial value and transform the chemistry into the carbon-rich regime. Even during HBB there is enough dredge-up for our models to attain $C/O > 1$. This additional carbon leads to familiar effects: there is an increase in opacity which increases radius and reduces the effective temperature relative to the composition-independent low-T opacity models. These structural changes then have several consequences:

- there is a reduction in the temperature at the base of the convective envelope;
- acceleration of mass loss;
- shortening of the AGB lifetime;
- a decrease in total C+N+O yield; and
- an increase in the lower mass limit for hot bottom burning.

The inclusion of composition-dependent low-T opacity is a necessary and feasible step towards more realistic models. We note, however, that the degree of the consequences is given by a complex interplay between many factors such as mass loss, dredge-up efficiency, the treatment of convective overshooting, and convection theory. In our models, the efficient dredge-up (we find $\lambda > 0.9$ in HBB models, for example) and our use of the Vassiliadis and Wood (1993) mass loss rate both contribute to its importance.

4.6.1 Low-mass models

The effect of the low-T opacity on the evolution of low-mass models depends on the extent of the third dredge-up. It does not affect the yields of our $1.25 M_{\odot}$ models (which have only one third dredge-up episode), while we see a factor of 10 reduction in total C+N+O yield for our $1.75 M_{\odot}$ model with composition-dependent low-T opacity (which had 12 third dredge-up episodes compared with 92).

4.6.2 Borderline HBB models

HBB is avoided in our $[Fe/H] = -2$ models with composition-dependent low-T opacity in a wider mass range than the $Z = 0.001$ models in Ventura and Marigo (2010). We were able to quantify the increase in the HBB threshold to be $\Delta M_{\text{HBB}} = 1.25 M_{\odot}$, up to about $3 M_{\odot}$. Because the dredged-up carbon is prevented from being converted into nitrogen, the opacity continues to increase and the evolution of these models diverges further. The AGB lifetime is reduced by a factor of about three and the number of thermal pulses by

a factor of 10, while the final core mass is reduced by more than $0.1 M_{\odot}$. The difference in chemical yields is no less extreme: Y is decreased by up to 0.16 and $\Delta[\text{C}/\text{Fe}]$, $\Delta[\text{N}/\text{Fe}]$, and $\Delta[\text{O}/\text{Fe}]$ are around +1.0, -2.7, and -0.7 respectively, where these are defined as the yield of the models with composition-dependent low-T opacity relative to those without it. These effects are also apparent in our $2.5 M_{\odot}$ $Z = 0$ model, demonstrating that there is no metallicity limit below which composition-dependent low-T opacity may be safely neglected.

4.6.3 HBB models

In models with composition-dependent low-T opacity that are massive enough for HBB the effect on the structure is minimal. The use of composition-dependent low-T opacity causes a small decrease in T_{bce} (of about 1–3 MK) which slightly affects the surface abundances. The main difference emerges as a truncation of the AGB as a result of the faster mass loss rate. In the models with $[\text{Fe}/\text{H}] \leq -2$, there is about a factor of two reduction in lifetime and a roughly concordant decrease in C, N, O, and Y yields. Because the core growth rate is not affected by the opacity treatment, the shorter lifetime reduces the final core mass (by around $0.04 M_{\odot}$ in these models).

4.6.4 Implications for chemical evolution

Composition-dependent low-T opacity reduces the oxygen and total C+N+O yield in intermediate-mass $[\text{Fe}/\text{H}] \leq -2$ models. The degree of these two changes, however, is not strong enough to support AGB stars as being the polluters in the globular cluster self-pollution scenario because our models still do not show net oxygen depletion and the C+N+O yield is high compared with the observed internal spreads. The effects of composition-dependent low-T opacity may help to explain the observed high CEMP/EMP and CEMP/NEMP ratios because including it in models increases the stellar mass limit for HBB. In binary systems this increases the potential number of donors to make CEMP stars at the expense of NEMP stars. There are also suggestions that the prevalence of CEMP stars requires a lower stellar mass limit for the third dredge-up (Izzard et al., 2009). Composition-dependent low-T opacity would be crucial in models of such carbon-rich stars.

Conclusions

In this thesis we have improved stellar models of the two helium burning stages experienced by low-mass stars, the core helium burning and asymptotic giant branch phases, by implementing updated physics and constraining other physical uncertainties with inferences from new observations.

In Chapter 2 we confronted the uncertain stellar models of the core helium burning phase with the wealth of recent asteroseismic data. We computed the evolution and the non-radial pulsations of core helium burning models with four different mixing schemes. Standard models tend to predict an $\ell = 1$ asymptotic g-mode period spacing ($\Delta\Pi_1$) that is lower than is inferred from asteroseismology. Only models with large convective cores, such as those calculated with our newly proposed “maximal-overshoot” scheme, could match the average $\Delta\Pi_1$ reported. However, we also found another possible resolution for the $\Delta\Pi_1$ discrepancy that relates to the method used to determine $\Delta\Pi_1$: mode trapping can increase the observationally inferred $\Delta\Pi_1$ to well above its true value.

Even after accounting for the two proposed resolutions to the discrepancy in average $\Delta\Pi_1$, models still predict more low-mass ($M \lesssim 2 M_\odot$) CHeB stars with low $\Delta\Pi_1$ ($\lesssim 270$ s) than are observed. We have established two possible remedies for this. At the beginning of CHeB, when $\Delta\Pi_1$ is lowest, the composition gradient at the H-burning shell is steep (from the previous RGB phase). The resulting feature in the buoyancy profile would affect the pulsations enough to make it difficult to determine $\Delta\Pi_1$ from observations. The second possibility is that the mass of the helium core at the flash is higher than in standard models. This would increase the predictions for $\Delta\Pi_1$ at the beginning of CHeB, when it is low. The former hypothesis implies there is a population of early-CHeB stars observed with irregular period spacing from which $\Delta\Pi_1$ cannot be determined, while the latter does not. The reporting of selection effects in asteroseismic population studies would help to distinguish between the two possibilities, and therefore better allow us to safely use the observations to constrain stellar evolution theory.

In Chapter 3 we extended the work of Chapter 2 by comparing theoretical evolution sequences computed with the same four mixing schemes with HST photometry of horizontal branch (HB) and AGB stars in Galactic globular clusters. We primarily considered two probes of the internal evolution: R_2 , the observed number ratio of AGB to HB stars, and $\Delta \log L_{\text{HB}}^{\text{AGB}}$, the luminosity difference between the HB and the AGB clump.

The cluster to cluster scatter in the new determinations of R_2 is smaller than previously reported in the literature. Additionally, the large size of the combined sample means that the new finding of $R_2 = 0.117 \pm 0.005$ is the most statistically robust now available. This result accords with earlier suggestions that standard models predict fewer AGB stars than are observed. We constructed a luminosity probability density function (PDF) from the 6366 HB and AGB stars in the clusters in our sample that do not have blue HBs. Using this data set we found that $\Delta \log L_{\text{HB}}^{\text{AGB}} = 0.455 \pm 0.012$. The luminosity PDF derived from observations features a sharp peak near the AGB clump. The sharpness of this peak constitutes an additional and strong argument against core breathing pulses, which tend to broaden the predicted width of this peak. Finally, we quantified the effect of physical uncertainties, other than the treatment of mixing, and demonstrated that these cannot account for the inconsistency between standard models and cluster observations.

The combination of the seismology study in Chapter 2 and the photometry study in Chapter 3 has put further conditions on the mixing during CHeB. Both of the structures that may be consistent with the asteroseismology, i.e. those with either (i) a semiconvection or partially mixed zone or (ii) a large convective core surrounded by a composition discontinuity, are capable of matching the constraints from globular clusters. The respective conditions for that to be the case are that (i) there are no strong core breathing pulses and (ii) there is overshooting beneath the subsequent ‘gravonuclear’ convection zones.

In Chapter 4 we investigated the effect of composition-dependent low-temperature opacity on low-metallicity AGB models by implementing the latest molecular opacity data in the stellar evolution code MONSTAR. We found composition-dependent low-T opacity to be crucial in all intermediate-mass ($2.5 \leq M/M_{\odot} \leq 5$), low-metallicity ($[\text{Fe}/\text{H}] \leq -2$) models investigated. The effect mirrors that previously reported for higher-metallicity models – increased radius, decreased T_{eff} , faster mass loss, shorter thermally pulsing-AGB lifetime, reduced enrichment in third dredge-up products (by a factor of three to ten in our models), and an increased mass threshold for hot bottom burning. We concluded that the evolution of low-metallicity models with composition-dependent low-T opacity is relatively independent of the initial metal abundance. This is because the contribution to the low-T opacity from molecules containing carbon, which is brought to the surface by the third dredge-up, rapidly exceeds the contribution from the metals initially present. The increase

in the predicted minimum mass for hot bottom burning implies a significant reduction in the expected number of nitrogen-enhanced metal-poor stars, helping to explain their paucity. We note that these findings are partially a product of the macrophysics adopted in our models. This is particularly true for the Vassiliadis and Wood (1993) mass loss rate, because it strongly depends on the stellar radius, which is sensitive to the opacity treatment.

5.1 Future work

Several promising directions for future research have been identified in this thesis. In this section we briefly outline some broad topics of interest.

The results of the comparisons between models and seismic and photometric observations, shown in Chapter 2 and Chapter 3 respectively, constitute new constraints for the structure of core helium burning models. In both chapters we demonstrated that the consistency between observations and models with different mixing schemes is not significantly affected by the known uncertainties in other input physics, i.e. mixing is the principal uncertainty in the models. When combined, these studies provide overwhelming evidence that core helium burning stars have convective cores larger than in the no-overshoot models. Further work is needed, however, to break the degeneracy between the two scenarios (models with a large convective core or a semiconvection / partially mixed zone) that are capable of matching both the asteroseismology and globular cluster observations. We therefore now contemplate lines of inquiry that may accomplish this.

We focused on red clump stars in our seismology study of core helium burning stars in Chapter 2. This work could be extended to comparisons with subdwarf B (sdB) stars, where g-modes have been detected. It is expected that the same mixing phenomena occur in sdB and red clump stars because of the similarity of the conditions in their cores. Owing to the lack of a large convective envelope, however, the g-modes in sdB stars have the advantage that they can be detected directly from surface observations (rather than via mixed modes). We identified that the mass of the H-exhausted core in red clump models is an important uncertainty affecting $\Delta\Pi_1$. This uncertainty is smaller in sdB stars because the mass of the H-exhausted core closely corresponds to total stellar mass. Finally, calculations of the pulsations in sdB models with different mixing schemes would also complement previous sdB seismology where surface layers have been precisely modelled (e.g. Charpinet et al., 2011; Van Grootel et al., 2013a).

The respective conditions required for the evolution of the standard-overshoot and maximal-overshoot models to be consistent with the observations reported in Chapter 2

and Chapter 3 may be tested with multi-dimensional hydrodynamic simulations. Three particular areas of interest are (i) the stability of the core boundary in the maximal overshoot models, (ii) the extent of convective overshoot during the subsequent gravonuclear loop phase, and (iii) the resistance of the partially mixed (or semiconvection) zone to core breathing pulses late in core helium burning.

In the last two decades, multi-dimensional simulations have been employed to help study the problem of the extent of mixing beyond formal convective boundaries in stellar models. There are reasons to be sceptical about applying the findings in the literature to the scenarios in this thesis. The widely adopted prescription that has an exponential decay in the diffusion coefficient beyond the Schwarzschild boundary is derived from two-dimensional simulations of the shallow convection zones in main sequence and DA white dwarf stars (Freytag et al., 1996). Moreover, the popular choice for the free parameter in this formulation was calibrated by matching observations of main sequence stars (Schaller et al., 1992; Herwig et al., 1998). There have been multi-dimensional simulations of the core flash that initiates core helium burning (e.g. Mocák et al., 2011; Stancliffe et al., 2011) but the burning there is more vigorous than later quiescent core helium burning. The low Mach number flows in core helium burning (it is typically less than 10^{-4} in the models in this study, about a factor of 100 lower than during the core flash) poses challenges for simulations that use explicit methods.

Recently, Mirouh et al. (2012) used three-dimensional hydrodynamic simulations to characterize two distinct types of semiconvection, either layered convection or inefficient ‘oscillatory’ convection, depending on the local inverse density ratio

$$R_0^{-1} = \frac{\frac{\varphi}{\delta} \nabla_{\mu}}{(\nabla - \nabla_{\text{ad}})}, \quad (5.1)$$

which is just the ratio of the respective contributions to the buoyancy frequency from the molecular weight and temperature gradients (Equation 2.6). Their models, however, probed the ‘planetary’ regime, where the Prandtl number and the ratio of molecular to thermal diffusivity are much higher than in stars. If we were to apply their criterion, core helium burning semiconvection would fall safely in the oscillatory regime.

The semiconvection in our models is characterized by extremely slow mixing. The diffusion coefficient in the semiconvection zone is of the order of $300 \text{ cm}^2 \text{ s}^{-1}$. The chemical diffusion time scale is therefore, unsurprisingly, commensurate with the core helium burning lifetime of around 100 Myr. Semiconvection in the core helium burning case also has another complication: the feedback from the opacity changes due to chemical mixing. This puts further doubt on any extrapolation from numerical simulations under different

conditions (and where the two mixing fluids do not have different opacity).

Two of the significant consequences of the inclusion of composition-dependent low-T opacity shown in Chapter 4 were (i) an increase in stellar radius and (ii) a decrease in the temperature at the base of the convective envelope that suppresses hot bottom burning. These results both have important implications for the expected frequency of carbon- and nitrogen-enhanced metal-poor stars. The magnitude of this effect should be quantified with a binary population synthesis code. The multi-dimensional dependence of the stellar structure on envelope composition, however, poses additional difficulties for generating the synthetic stellar models required for population synthesis codes.

In low-metallicity models, comparatively little carbon from the third dredge-up is required before it outnumbers the initial oxygen in the envelope. As a result of this, essentially all low-metallicity models that have the third dredge-up, but do not have hot bottom burning, become carbon-rich. It would be interesting to test the sensitivity of the evolution of these models to the efficiency of the third dredge-up. It is conceivable that faster mass loss when $C/O > 1$ limits the total chemical yields in models with efficient dredge-up. Because the updated low-T opacity increases the dependence of the stellar structure on the surface composition, specifically whether $C/O > 1$, the efficiency of the third dredge-up is of even greater importance to models that are either (i) massive enough for hot bottom burning to destroy carbon in the envelope, or (ii) not massive enough for substantial third dredge-up. The fundamental question of the mixing at convective boundaries must be investigated further to address this.

The ‘truncation’ of the evolution of models with composition-dependent low-T opacity occurs because of the increased mass loss rate. The very low metallicity and large enhancement of carbon in the AGB models in our study raises the question of how the mass loss rate depends on the envelope composition. The composition of the envelope certainly does influence the calculation of the mass loss rate in the models via its impact on fundamental stellar properties (e.g. M , L , and R). This still neglects any effect on the pulsations and dust formation, which are often invoked to explain AGB winds (see e.g. Höfner, 2011). The period-mass loss relation from observations of Galactic stars shown in Vassiliadis and Wood (1993) does not appear to depend on the spectral type (i.e. whether the atmosphere is carbon-rich). Observations of the LMC, however, suggest that the excess carbon precipitates a superwind at lower luminosity than when the composition is oxygen-rich (Lagadec and Zijlstra, 2008). Wood (1990) argues that the relation for the pulsation period (in days),

$$\log P = -2.07 + 1.94 \log R/R_{\odot} - 0.9 \log M/M_{\odot}, \quad (5.2)$$

that is used to calculate the mass loss rate in our models, is not particularly affected by metallicity (other than through R). In addition to these factors, the mass loss rate in our models also depends indirectly on the MLT mixing length parameter. This was calibrated by matching models with observations of the Sun, a metal-rich main sequence star that is unlike those relevant to our study. The evolution sequences could be improved by better constraining the mixing length parameter and the mass loss rate for carbon-rich low-metallicity models. The problem of the mixing length parameter could be addressed with a combination of empirical calibration and accounting for the T_{eff} , $\log g$, and metallicity trends found in recent three-dimensional radiative hydrodynamic calculations of surface convection (Magic et al., 2015).

Finally, the evolution of our models ceased when convergence to a hydrostatic solution was no longer possible. This problem emerges because of (sometimes minute) opacity peaks in regions in the structure where radiation pressure dominates over gas pressure. The phenomenon is also apparent for AGB models over a wide mass and metallicity range (e.g. Wood and Faulkner, 1986; Sweigart, 1999; Lawlor and MacDonald, 2003; Miller Bertolami et al., 2006; Lau et al., 2012). In three-dimensional calculations these opacity features may excite pulsations or trigger faster mass loss. This should be addressed with a suitable hydrodynamics/pulsation code.

References

- Aizenman, M., Smeyers, P., and Weigert, A.: 1977, *A&A* **58**, 41
- Alcaino, G., Liller, W., Alvarado, F., Kravtsov, V., Ipatov, A., Samus, N., and Smirnov, O.: 1998, *AJ* **116**, 2415
- Alexander, D. R.: 1975, *ApJS* **29**, 363
- Alexander, D. R. and Ferguson, J. W.: 1994, *ApJ* **437**, 879
- Alexander, D. R., Rypma, R. L., and Johnson, H. R.: 1983, *ApJ* **272**, 773
- Anderson, J., Sarajedini, A., Bedin, L. R., King, I. R., Piotto, G., Reid, I. N., Siegel, M., Majewski, S. R., Paust, N. E. Q., Aparicio, A., Milone, A. P., Chaboyer, B., and Rosenberg, A.: 2008, *AJ* **135**, 2055
- Angulo, C., Arnould, M., Rayet, M., Descouvemont, P., Baye, D., Leclercq-Willain, C., Coc, A., Barhoumi, S., Aguer, P., Rolfs, C., Kunz, R., Hammer, J. W., Mayer, A., Paradellis, T., Kossionides, S., Chronidou, C., Spyrou, K., degl’Innocenti, S., Fiorentini, G., Ricci, B., Zavatarelli, S., Providencia, C., Wolters, H., Soares, J., Grama, C., Rahighi, J., Shotter, A., and Laméhi Rachti, M.: 1999, *Nuclear Physics A* **656**, 3
- Aoyama, S. and Suzuki, T. K.: 2015, *ArXiv e-prints*
- Asplund, M., Grevesse, N., Sauval, A. J., and Scott, P.: 2009, *ARA&A* **47**, 481
- Ayala, A., Domínguez, I., Giannotti, M., Mirizzi, A., and Straniero, O.: 2014, *Physical Review Letters* **113**(19), 191302
- Beck, P. G., Bedding, T. R., Mosser, B., Stello, D., Garcia, R. A., Kallinger, T., Hekker, S., Elsworth, Y., Frandsen, S., Carrier, F., De Ridder, J., Aerts, C., White, T. R., Huber, D., Dupret, M.-A., Montalbán, J., Miglio, A., Noels, A., Chaplin, W. J., Kjeldsen, H., Christensen-Dalsgaard, J., Gilliland, R. L., Brown, T. M., Kawaler, S. D., Mathur, S., and Jenkins, J. M.: 2011, *Science* **332**, 205
- Bedding, T. R., Huber, D., Stello, D., Elsworth, Y. P., Hekker, S., Kallinger, T., Mathur, S., Mosser, B., Preston, H. L., Ballot, J., Barban, C., Broomhall, A. M., Buzasi, D. L., Chaplin, W. J., García, R. A., Gruberbauer, M., Hale, S. J., De Ridder, J., Frandsen, S., Borucki, W. J., Brown, T., Christensen-Dalsgaard, J., Gilliland, R. L., Jenkins, J. M., Kjeldsen, H., Koch, D., Belkacem, K., Bildsten, L., Bruntt, H., Campante, T. L., Deheuvels, S., Derekas, A., Dupret, M.-A., Goupil, M.-J., Hatzes, A., Houdek, G., Ireland, M. J., Jiang, C., Karoff, C., Kiss, L. L., Lebreton, Y., Miglio, A., Montalbán, J., Noels, A., Roxburgh, I. W., Sangaralingam, V., Stevens, I. R., Suran, M. D., Tarrant, N. J., and Weiss, A.: 2010, *ApJ* **713**, L176

- Bedding, T. R., Mosser, B., Huber, D., Montalbán, J., Beck, P., Christensen-Dalsgaard, J., Elsworth, Y. P., García, R. A., Miglio, A., Stello, D., White, T. R., De Ridder, J., Hekker, S., Aerts, C., Barban, C., Belkacem, K., Broomhall, A.-M., Brown, T. M., Buzasi, D. L., Carrier, F., Chaplin, W. J., di Mauro, M. P., Dupret, M.-A., Frandsen, S., Gilliland, R. L., Goupil, M.-J., Jenkins, J. M., Kallinger, T., Kawaler, S., Kjeldsen, H., Mathur, S., Noels, A., Aguirre, S. V., and Ventura, P.: 2011, *Nature* **471**, 608
- Bedin, L. R., Piotto, G., Anderson, J., Cassisi, S., King, I. R., Momany, Y., and Carraro, G.: 2004, *ApJ* **605**, L125
- Bessell, M. S., Brett, J. M., Wood, P. R., and Scholz, M.: 1989, *A&AS* **77**, 1
- Bildsten, L., Paxton, B., Moore, K., and Macias, P. J.: 2012, *ApJ* **744**, L6
- Bloecker, T.: 1995, *A&A* **297**, 727
- Bono, G., Caputo, F., Cassisi, S., Castellani, V., and Marconi, M.: 1997a, *ApJ* **489**, 822
- Bono, G., Caputo, F., Cassisi, S., Castellani, V., and Marconi, M.: 1997b, *ApJ* **479**, 279
- Brassard, P. and Fontaine, G.: 2008, in U. Heber, C. S. Jeffery, and R. Napiwotzki (eds.), *Hot Subdwarf Stars and Related Objects*, Vol. 392 of *Astronomical Society of the Pacific Conference Series*, p. 261
- Bressan, A., Bertelli, G., and Chiosi, C.: 1986, *Mem. Soc. Astron. Italiana* **57**, 411
- Bressan, A., Girardi, L., Marigo, P., Rosenfield, P., and Tang, J.: 2015, *Astrophysics and Space Science Proceedings* **39**, 25
- Brocato, E., Castellani, V., and Villante, F. L.: 1998, *MNRAS* **298**, 557
- Brown, T. M., Bowers, C. W., Kimble, R. A., Sweigart, A. V., and Ferguson, H. C.: 2000, *ApJ* **532**, 308
- Brown, T. M., Ferguson, H. C., and Davidsen, A. F.: 1995, *ApJ* **454**, L15
- Brown, T. M., Ferguson, H. C., Davidsen, A. F., and Dorman, B.: 1997, *ApJ* **482**, 685
- Brown, T. M., Gilliland, R. L., Noyes, R. W., and Ramsey, L. W.: 1991, *ApJ* **368**, 599
- Buonanno, R., Buscema, G., Corsi, C. E., Iannicola, G., and Fusi Pecci, F.: 1983, *A&AS* **51**, 83
- Buonanno, R., Caloi, V., Castellani, V., Corsi, C., Fusi Pecci, F., and Gratton, R.: 1986, *A&AS* **66**, 79
- Buonanno, R., Corsi, C. E., and Fusi Pecci, F.: 1981, *MNRAS* **196**, 435
- Buonanno, R., Corsi, C. E., and Fusi Pecci, F.: 1985, *A&A* **145**, 97
- Busso, M., Gallino, R., and Wasserburg, G. J.: 1999, *ARA&A* **37**, 239
- Buzzoni, A., Pecci, F. F., Buonanno, R., and Corsi, C. E.: 1983, *A&A* **128**, 94

- Caloi, V.: 1989, *A&A* **221**, 27
- Caloi, V. and D'Antona, F.: 2005, *A&A* **435**, 987
- Caloi, V. and D'Antona, F.: 2007, *A&A* **463**, 949
- Caloi, V. and Mazzitelli, I.: 1990, *A&A* **240**, 305
- Campbell, S. W., D'Orazi, V., Yong, D., Constantino, T. N., Lattanzio, J. C., Stancliffe, R. J., Angelou, G. C., Wylie-de Boer, E. C., and Grundahl, F.: 2013, *Nature* **498**, 198
- Campbell, S. W. and Lattanzio, J. C.: 2008, *A&A* **490**, 769
- Campbell, S. W., Yong, D., Wylie-de Boer, E. C., Stancliffe, R. J., Lattanzio, J. C., Angelou, G. C., D'Orazi, V., Martell, S. L., Grundahl, F., and Sneden, C.: 2012, *ApJ* **761**, L2
- Campbell, S. W., Yong, D., Wylie-de Boer, E. C., Stancliffe, R. J., Lattanzio, J. C., Angelou, G. C., Grundahl, F., and Sneden, C.: 2010, *Mem. Soc. Astron. Italiana* **81**, 1004
- Caputo, F., Castellani, V., and Wood, P. R.: 1978, *MNRAS* **184**, 377
- Caputo, F., Chieffi, A., Tornambe, A., Castellani, V., and Pulone, L.: 1989, *ApJ* **340**, 241
- Cardelli, J. A., Clayton, G. C., and Mathis, J. S.: 1989, *ApJ* **345**, 245
- Carollo, D., Beers, T. C., Bovy, J., Sivarani, T., Norris, J. E., Freeman, K. C., Aoki, W., Lee, Y. S., and Kennedy, C. R.: 2012, *ApJ* **744**, 195
- Carretta, E., Bragaglia, A., Gratton, R. G., Recio-Blanco, A., Lucatello, S., D'Orazi, V., and Cassisi, S.: 2010, *A&A* **516**, A55
- Cassisi, S., Castellani, V., Degl'Innocenti, S., Piotto, G., and Salaris, M.: 2001, *A&A* **366**, 578
- Cassisi, S., Castellani, V., and Tornambe, A.: 1996, *ApJ* **459**, 298
- Cassisi, S., Salaris, M., and Irwin, A. W.: 2003, *ApJ* **588**, 862
- Cassisi, S., Salaris, M., Pietrinferni, A., Vink, J. S., and Monelli, M.: 2014, *A&A* **571**, A81
- Castellani, V., Chieffi, A., Tornambe, A., and Pulone, L.: 1985, *ApJ* **296**, 204
- Castellani, V., Giannone, P., and Renzini, A.: 1971a, *Ap&SS* **10**, 355
- Castellani, V., Giannone, P., and Renzini, A.: 1971b, *Ap&SS* **10**, 340
- Catelan, M., de Freitas Pacheco, J. A., and Horvath, J. E.: 1996, *ApJ* **461**, 231
- Charbonnel, C., Chantreau, W., Decressin, T., Meynet, G., and Schaerer, D.: 2013, *A&A* **557**, L17
- Charpinet, S., Fontaine, G., Brassard, P., and Dorman, B.: 2002, *ApJS* **139**, 487
- Charpinet, S., Green, E. M., Baglin, A., Van Grootel, V., Fontaine, G., Vauclair, G., Chaintreuil, S., Weiss, W. W., Michel, E., Auvergne, M., Catala, C., Samadi, R., and Baudin, F.: 2010, *A&A* **516**, L6

- Charpinet, S., Van Grootel, V., Brassard, P., and Fontaine, G.: 2014, in J. A. Guzik, W. J. Chaplin, G. Handler, and A. Pigulski (eds.), *IAU Symposium*, Vol. 301 of *IAU Symposium*, pp 397–398
- Charpinet, S., Van Grootel, V., Fontaine, G., Green, E. M., Brassard, P., Randall, S. K., Silvotti, R., Østensen, R. H., Kjeldsen, H., Christensen-Dalsgaard, J., Kawaler, S. D., Clarke, B. D., Li, J., and Wohler, B.: 2011, *A&A* **530**, A3
- Chiosi, C., Bertelli, G., and Bressan, A.: 1987, in S. Kwok and S. R. Pottasch (eds.), *Late Stages of Stellar Evolution*, Vol. 132 of *Astrophysics and Space Science Library*, pp 213–233
- Christensen-Dalsgaard, J.: 2008, *Ap&SS* **316**, 113
- Christensen-Dalsgaard, J., Silva Aguirre, V., Elsworth, Y., and Hekker, S.: 2014, *MNRAS* **445**, 3685
- Cohen, J. G. and Meléndez, J.: 2005, *AJ* **129**, 303
- Constantino, T., Campbell, S., Gil-Pons, P., and Lattanzio, J.: 2014a, *ApJ* **784**, 56
- Constantino, T., Campbell, S. W., Christensen-Dalsgaard, J., Lattanzio, J. C., and Stello, D.: 2015, *MNRAS* **452**, 123
- Constantino, T. N., Campbell, S. W., and Lattanzio, J. C.: 2014b, in J. A. Guzik, W. J. Chaplin, G. Handler, and A. Pigulski (eds.), *IAU Symposium*, Vol. 301 of *IAU Symposium*, pp 399–400
- Corsaro, E., Stello, D., Huber, D., Bedding, T. R., Bonanno, A., Brogaard, K., Kallinger, T., Benomar, O., White, T. R., Mosser, B., Basu, S., Chaplin, W. J., Christensen-Dalsgaard, J., Elsworth, Y. P., García, R. A., Hekker, S., Kjeldsen, H., Mathur, S., Meibom, S., Hall, J. R., Ibrahim, K. A., and Klaus, T. C.: 2012, *ApJ* **757**, 190
- Cottrell, P. L. and Da Costa, G. S.: 1981, *ApJ* **245**, L79
- Cristallo, S., Piersanti, L., Straniero, O., Gallino, R., Domínguez, I., Abia, C., Di Rico, G., Quintini, M., and Bisterzo, S.: 2011, *ApJS* **197**, 17
- Cristallo, S., Straniero, O., Gallino, R., Piersanti, L., Domínguez, I., and Lederer, M. T.: 2009, *ApJ* **696**, 797
- Cristallo, S., Straniero, O., Lederer, M. T., and Aringer, B.: 2007, *ApJ* **667**, 489
- Cunha, M. S., Stello, D., Avelino, P. P., Christensen-Dalsgaard, J., and Townsend, R. H. D.: 2015, *ApJ* **805**, 127
- D’Antona, F., Bellazzini, M., Caloi, V., Pecci, F. F., Galletti, S., and Rood, R. T.: 2005, *ApJ* **631**, 868
- D’Antona, F., Caloi, V., Montalbán, J., Ventura, P., and Gratton, R.: 2002, *A&A* **395**, 69
- de Mink, S. E., Pols, O. R., Langer, N., and Izzard, R. G.: 2009, *A&A* **507**, L1
- Decressin, T., Meynet, G., Charbonnel, C., Prantzos, N., and Ekström, S.: 2007, *A&A* **464**, 1029

- Denissenkov, P. A. and Hartwick, F. D. A.: 2014, MNRAS **437**, L21
- Doherty, C. L., Gil-Pons, P., Lau, H. H. B., Lattanzio, J. C., and Siess, L.: 2014, MNRAS **437**, 195
- Domínguez, I., Straniero, O., and Isern, J.: 1999, MNRAS **306**, L1
- D’Orazi, V., Campbell, S. W., Lugaro, M., Lattanzio, J. C., Pignatari, M., and Carretta, E.: 2013, MNRAS **433**, 366
- Dorman, B., O’Connell, R. W., and Rood, R. T.: 1995, ApJ **442**, 105
- Dorman, B. and Rood, R. T.: 1993, ApJ **409**, 387
- Dorman, B., Rood, R. T., and O’Connell, R. W.: 1993, ApJ **419**, 596
- Dziembowski, W.: 1977, Acta Astron. **27**, 95
- Endal, A. S. and Sofia, S.: 1976, ApJ **210**, 184
- Faulkner, D. J.: 1968, MNRAS **140**, 223
- Faulkner, D. J. and Cannon, R. D.: 1973, ApJ **180**, 435
- Faulkner, D. J. and Wood, P. R.: 1972, ApJ **178**, 207
- Ferguson, H. C., Davidsen, A. F., Kriss, G. A., Blair, W. P., Bowers, C. W., Dixon, W. V. D., Durrance, S. T., Feldman, P. D., Henry, R. C., Kruk, J. W., Moos, H. W., Vancura, O., Long, K. S., and Kimble, R. A.: 1991, ApJ **382**, L69
- Ferguson, J. W., Alexander, D. R., Allard, F., Barman, T., Bodnarik, J. G., Hauschildt, P. H., Heffner-Wong, A., and Tamanai, A.: 2005, ApJ **623**, 585
- Fishlock, C. K., Karakas, A. I., and Stancliffe, R. J.: 2014, MNRAS **438**, 1741
- Frebel, A., Christlieb, N., Norris, J. E., Beers, T. C., Bessell, M. S., Rhee, J., Fechner, C., Marsteller, B., Rossi, S., Thom, C., Wisotzki, L., and Reimers, D.: 2006, ApJ **652**, 1585
- Freytag, B., Ludwig, H.-G., and Steffen, M.: 1996, A&A **313**, 497
- Friedland, A., Giannotti, M., and Wise, M.: 2013, *Physical Review Letters* **110**(6), 061101
- Frost, C. A., Cannon, R. C., Lattanzio, J. C., Wood, P. R., and Forestini, M.: 1998, A&A **332**, L17
- Frost, C. A. and Lattanzio, J. C.: 1996, ApJ **473**, 383
- Fryxell, B., Olson, K., Ricker, P., Timmes, F. X., Zingale, M., Lamb, D. Q., MacNeice, P., Rosner, R., Truran, J. W., and Tufo, H.: 2000, ApJS **131**, 273
- Gabriel, M., Noels, A., Montalbán, J., and Miglio, A.: 2014, A&A **569**, A63
- Gilliland, R. L.: 2004, *ACS CCD Gains, Full Well Depths, and Linearity up to and Beyond Saturation*, Technical report

- Gingold, R. A.: 1974, ApJ **193**, 177
- Gingold, R. A.: 1976, ApJ **204**, 116
- Girardi, L.: 1999, MNRAS **308**, 818
- Girardi, L., Dalcanton, J., Williams, B., de Jong, R., Gallart, C., Monelli, M., Groenewegen, M. A. T., Holtzman, J. A., Olsen, K. A. G., Seth, A. C., Weisz, D. R., and ANGST/ANGRRR Collaboration: 2008, PASP **120**, 583
- Gratton, R., Sneden, C., and Carretta, E.: 2004, ARA&A **42**, 385
- Gratton, R. G., Carretta, E., and Bragaglia, A.: 2012a, A&A Rev. **20**, 50
- Gratton, R. G., Lucatello, S., Carretta, E., Bragaglia, A., D’Orazi, V., Al Momany, Y., Sollima, A., Salaris, M., and Cassisi, S.: 2012b, A&A **539**, A19
- Green, E. M., Fontaine, G., Hyde, E. A., For, B.-Q., and Chayer, P.: 2008, in U. Heber, C. S. Jeffery, and R. Napiwotzki (eds.), *Hot Subdwarf Stars and Related Objects*, Vol. 392 of *Astronomical Society of the Pacific Conference Series*, p. 75
- Greggio, L. and Renzini, A.: 1990, ApJ **364**, 35
- Grevesse, N., Asplund, M., and Sauval, A. J.: 2007, Space Sci. Rev. **130**, 105
- Han, Z., Podsiadlowski, P., Maxted, P. F. L., Marsh, T. R., and Ivanova, N.: 2002, MNRAS **336**, 449
- Harris, W. E.: 1996, AJ **112**, 1487
- Harris, W. E.: 2010, *ArXiv e-prints*
- Henyey, L. G., Forbes, J. E., and Gould, N. L.: 1964, ApJ **139**, 306
- Herwig, F.: 2000, A&A **360**, 952
- Herwig, F., Bloeker, T., Schoenberner, D., and El Eid, M.: 1997, A&A **324**, L81
- Herwig, F., Schoenberner, D., and Bloeker, T.: 1998, A&A **340**, L43
- Höfner, S.: 2011, in F. Kerschbaum, T. Lebzelter, and R. F. Wing (eds.), *Why Galaxies Care about AGB Stars II: Shining Examples and Common Inhabitants*, Vol. 445 of *Astronomical Society of the Pacific Conference Series*, p. 193
- Hu, H., Dupret, M.-A., Aerts, C., Nelemans, G., Kawaler, S. D., Miglio, A., Montalbán, J., and Scufflaire, R.: 2008, A&A **490**, 243
- Iben, Jr., I.: 1967, ApJ **147**, 650
- Iben, Jr., I.: 1971, PASP **83**, 697
- Iben, Jr., I., Fujimoto, M. Y., Sugimoto, D., and Miyaji, S.: 1986, ApJ **304**, 217
- Iben, Jr., I. and Rood, R. T.: 1970, ApJ **161**, 587

- Ivans, I. I., Sneden, C., Kraft, R. P., Suntzeff, N. B., Smith, V. V., Langer, G. E., and Fulbright, J. P.: 1999, *AJ* **118**, 1273
- Iwamoto, N.: 2009, *PASA* **26**, 145
- Izzard, R. G., Glebbeek, E., Stancliffe, R. J., and Pols, O. R.: 2009, *A&A* **508**, 1359
- Johnson, C. I., McDonald, I., Pilachowski, C. A., Mateo, M., Bailey, III, J. I., Cordero, M. J., Zijlstra, A. A., Crane, J. D., Olszewski, E., Shectman, S. A., and Thompson, I.: 2015, *AJ* **149**, 71
- Johnson, J. A., Herwig, F., Beers, T. C., and Christlieb, N.: 2007, *ApJ* **658**, 1203
- Kallinger, T., Hekker, S., Mosser, B., De Ridder, J., Bedding, T. R., Elsworth, Y. P., Gruberbauer, M., Guenther, D. B., Stello, D., Basu, S., García, R. A., Chaplin, W. J., Mullally, F., Still, M., and Thompson, S. E.: 2012, *A&A* **541**, A51
- Karakas, A. I., Lattanzio, J. C., and Pols, O. R.: 2002, *PASA* **19**, 515
- Kennedy, C. R., Sivarani, T., Beers, T. C., Lee, Y. S., Placco, V. M., Rossi, S., Christlieb, N., Herwig, F., and Plez, B.: 2011, *AJ* **141**, 102
- Kippenhahn, R., Meyer-Hofmeister, E., and Thomas, H. C.: 1970, *A&A* **5**, 155
- Kitsikis, A. and Weiss, A.: 2008, in A. de Koter, L. J. Smith, and L. B. F. M. Waters (eds.), *Mass Loss from Stars and the Evolution of Stellar Clusters*, Vol. 388 of *Astronomical Society of the Pacific Conference Series*, p. 183
- Lagadec, E. and Zijlstra, A. A.: 2008, *MNRAS* **390**, L59
- Langer, N.: 1991, *A&A* **252**, 669
- Langer, N., El Eid, M. F., and Fricke, K. J.: 1985, *A&A* **145**, 179
- Lattanzio, J. C.: 1986, *ApJ* **311**, 708
- Lattanzio, J. C.: 1989, *ApJ* **344**, L25
- Lattanzio, J. C.: 1992, *Proceedings of the Astronomical Society of Australia* **10**, 120
- Lau, H. H. B., Gil-Pons, P., Doherty, C., and Lattanzio, J.: 2012, *A&A* **542**, A1
- Lawlor, T. M. and MacDonald, J.: 2003, *ApJ* **583**, 913
- Lederer, M. T. and Aringer, B.: 2009, *A&A* **494**, 403
- Ledoux, P.: 1947, *ApJ* **105**, 305
- Lee, S.-W.: 1977, *A&AS* **27**, 367
- Lee, Y.-W., Joo, S.-J., Han, S.-I., Chung, C., Ree, C. H., Sohn, Y.-J., Kim, Y.-C., Yoon, S.-J., Yi, S. K., and Demarque, P.: 2005, *ApJ* **621**, L57
- Lucatello, S., Beers, T. C., Christlieb, N., Barklem, P. S., Rossi, S., Marsteller, B., Sivarani, T., and Lee, Y. S.: 2006, *ApJ* **652**, L37

- Lucatello, S., Tsangarides, S., Beers, T. C., Carretta, E., Gratton, R. G., and Ryan, S. G.: 2005, *ApJ* **625**, 825
- Lucy, L. B., Robertson, J. A., and Sharp, C. M.: 1986, *A&A* **154**, 267
- Lugaro, M., Karakas, A. I., Stancliffe, R. J., and Rijs, C.: 2012, *ApJ* **747**, 2
- Magic, Z., Weiss, A., and Asplund, M.: 2015, *A&A* **573**, A89
- Marigo, P.: 2002, *A&A* **387**, 507
- Marigo, P.: 2007, *A&A* **467**, 1139
- Marigo, P. and Aringer, B.: 2009, *A&A* **508**, 1539
- Marigo, P., Bressan, A., Nanni, A., Girardi, L., and Pumo, M. L.: 2013, *MNRAS* **434**, 488
- Marino, A. F., Milone, A. P., Przybilla, N., Bergemann, M., Lind, K., Asplund, M., Cassisi, S., Catelan, M., Casagrande, L., Valcarce, A. A. R., Bedin, L. R., Cortés, C., D’Antona, F., Jerjen, H., Piotto, G., Schlesinger, K., Zoccali, M., and Angeloni, R.: 2014, *MNRAS* **437**, 1609
- Masseron, T., Johnson, J. A., Plez, B., van Eck, S., Primas, F., Goriely, S., and Jorissen, A.: 2010, *A&A* **509**, A93
- McSaveney, J. A., Wood, P. R., Scholz, M., Lattanzio, J. C., and Hinkle, K. H.: 2007, *MNRAS* **378**, 1089
- Melbourne, J., Williams, B. F., Dalcanton, J. J., Rosenfield, P., Girardi, L., Marigo, P., Weisz, D., Dolphin, A., Boyer, M. L., Olsen, K., Skillman, E., and Seth, A. C.: 2012, *ApJ* **748**, 47
- Metcalfe, T. S., Salaris, M., and Winget, D. E.: 2002, *ApJ* **573**, 803
- Miglio, A., Montalbán, J., Noels, A., and Eggenberger, P.: 2008, *MNRAS* **386**, 1487
- Miller Bertolami, M. M., Althaus, L. G., Serenelli, A. M., and Panei, J. A.: 2006, *A&A* **449**, 313
- Milone, A. P.: 2015, *MNRAS* **446**, 1672
- Milone, A. P., Marino, A. F., Dotter, A., Norris, J. E., Jerjen, H., Piotto, G., Cassisi, S., Bedin, L. R., Recio Blanco, A., Sarajedini, A., Asplund, M., Monelli, M., and Aparicio, A.: 2014, *ApJ* **785**, 21
- Milone, A. P., Marino, A. F., Piotto, G., Bedin, L. R., Anderson, J., Aparicio, A., Bellini, A., Cassisi, S., D’Antona, F., Grundahl, F., Monelli, M., and Yong, D.: 2013, *ApJ* **767**, 120
- Mirouh, G. M., Garaud, P., Stellmach, S., Traxler, A. L., and Wood, T. S.: 2012, *ApJ* **750**, 61
- Mocák, M., Siess, L., and Müller, E.: 2011, *A&A* **533**, A53
- Montalbán, J., Miglio, A., Noels, A., Dupret, M.-A., Scuflaire, R., and Ventura, P.: 2013, *ApJ* **766**, 118

- Mosser, B., Barban, C., Montalbán, J., Beck, P. G., Miglio, A., Belkacem, K., Goupil, M. J., Hekker, S., De Ridder, J., Dupret, M. A., Elsworth, Y., Noels, A., Baudin, F., Michel, E., Samadi, R., Auvergne, M., Baglin, A., and Catala, C.: 2011, *A&A* **532**, A86
- Mosser, B., Benomar, O., Belkacem, K., Goupil, M. J., Lagarde, N., Michel, E., Lebreton, Y., Stello, D., Vrad, M., Barban, C., Bedding, T. R., Deheuvels, S., Chaplin, W. J., De Ridder, J., Elsworth, Y., Montalbán, J., Noels, A., Ouazzani, R. M., Samadi, R., White, T. R., and Kjeldsen, H.: 2014, *A&A* **572**, L5
- Mosser, B., Goupil, M. J., Belkacem, K., Michel, E., Stello, D., Marques, J. P., Elsworth, Y., Barban, C., Beck, P. G., Bedding, T. R., De Ridder, J., García, R. A., Hekker, S., Kallinger, T., Samadi, R., Stumpe, M. C., Barclay, T., and Burke, C. J.: 2012, *A&A* **540**, A143
- Nieuwenhuijzen, H. and de Jager, C.: 1990, *A&A* **231**, 134
- Norris, J., Cottrell, P. L., Freeman, K. C., and Da Costa, G. S.: 1981, *ApJ* **244**, 205
- Norris, J. E.: 2004, *ApJ* **612**, L25
- Origlia, L. and Leitherer, C.: 2000, *AJ* **119**, 2018
- Ortolani, S., Bica, E., and Barbuy, B.: 1994, *A&A* **286**, 444
- Paczyński, B.: 1970a, *Acta Astron.* **20**, 47
- Paczyński, B.: 1970b, *Acta Astron.* **20**, 195
- Paczyński, B. and Stanek, K. Z.: 1998, *ApJ* **494**, L219
- Pasquini, L., Mauas, P., Käufel, H. U., and Cacciari, C.: 2011, *A&A* **531**, A35
- Paxton, B., Cantiello, M., Arras, P., Bildsten, L., Brown, E. F., Dotter, A., Mankovich, C., Montgomery, M. H., Stello, D., Timmes, F. X., and Townsend, R.: 2013, *ApJS* **208**, 4
- Pinsonneault, M. H., Elsworth, Y., Epstein, C., Hekker, S., Mészáros, S., Chaplin, W. J., Johnson, J. A., García, R. A., Holtzman, J., Mathur, S., García Pérez, A., Silva Aguirre, V., Girardi, L., Basu, S., Shetrone, M., Stello, D., Allende Prieto, C., An, D., Beck, P., Beers, T. C., Bizyaev, D., Bloemen, S., Bovy, J., Cunha, K., De Ridder, J., Frinchaboy, P. M., García-Hernández, D. A., Gilliland, R., Harding, P., Hearty, F. R., Huber, D., Ivans, I., Kallinger, T., Majewski, S. R., Metcalfe, T. S., Miglio, A., Mosser, B., Muna, D., Nidever, D. L., Schneider, D. P., Serenelli, A., Smith, V. V., Tayar, J., Zamora, O., and Zasowski, G.: 2014, *ApJS* **215**, 19
- Piotto, G., Bedin, L. R., Anderson, J., King, I. R., Cassisi, S., Milone, A. P., Villanova, S., Pietrinferni, A., and Renzini, A.: 2007, *ApJ* **661**, L53
- Piotto, G., King, I. R., Djorgovski, S. G., Sosin, C., Zoccali, M., Saviane, I., De Angeli, F., Riello, M., Recio-Blanco, A., Rich, R. M., Meylan, G., and Renzini, A.: 2002, *A&A* **391**, 945
- Piotto, G., Villanova, S., Bedin, L. R., Gratton, R., Cassisi, S., Momany, Y., Recio-Blanco, A., Lucatello, S., Anderson, J., King, I. R., Pietrinferni, A., and Carraro, G.: 2005, *ApJ* **621**, 777

- Pols, O. R., Izzard, R. G., Stancliffe, R. J., and Glebbeek, E.: 2012, *A&A* **547**, A76
- Prada Moroni, P. G. and Straniero, O.: 2009, *A&A* **507**, 1575
- Raffelt, G.: 2012, *ArXiv e-prints*
- Raffelt, G. G.: 1999, *Annual Review of Nuclear and Particle Science* **49**, 163
- Raffelt, G. G. and Dearborn, D. S. P.: 1987, *Phys. Rev. D* **36**, 2211
- Reed, M. D., Baran, A., Quint, A. C., Kawaler, S. D., O'Toole, S. J., Telting, J., Charpinet, S., Rodríguez-López, C., Østensen, R. H., Provencal, J. L., Johnson, E. S., Thompson, S. E., Allen, C., Middour, C. K., Kjeldsen, H., and Christensen-Dalsgaard, J.: 2011, *MNRAS* **414**, 2885
- Reimers, D.: 1975, *Memoires of the Societe Royale des Sciences de Liege* **8**, 369
- Renzini, A. and Fusi Pecci, F.: 1988, *ARA&A* **26**, 199
- Robertson, J. W.: 1971, *ApJ* **170**, 353
- Robertson, J. W. and Faulkner, D. J.: 1972, *ApJ* **171**, 309
- Rogers, F. J. and Nayfonov, A.: 2002, *ApJ* **576**, 1064
- Rogers, F. J., Swenson, F. J., and Iglesias, C. A.: 1996, *ApJ* **456**, 902
- Rood, R. T.: 1972, *ApJ* **177**, 681
- Rossi, S., Beers, T. C., Sneden, C., Sevestyanenko, T., Rhee, J., and Marsteller, B.: 2005, *AJ* **130**, 2804
- Sackmann, I.-J. and Boothroyd, A. I.: 1991, *ApJ* **366**, 529
- Sackmann, I.-J., Boothroyd, A. I., and Kraemer, K. E.: 1993, *ApJ* **418**, 457
- Salaris, M. and Cassisi, S.: 2005, *Evolution of Stars and Stellar Populations*
- Salaris, M., Riello, M., Cassisi, S., and Piotto, G.: 2004, *A&A* **420**, 911
- Sandquist, E. L.: 2000, *MNRAS* **313**, 571
- Sandquist, E. L. and Bolte, M.: 2004, *ApJ* **611**, 323
- Sarajedini, A., Bedin, L. R., Chaboyer, B., Dotter, A., Siegel, M., Anderson, J., Aparicio, A., King, I., Majewski, S., Marín-Franch, A., Piotto, G., Reid, I. N., and Rosenberg, A.: 2007, *AJ* **133**, 1658
- Scalo, J. M.: 1986, *Fund. Cosmic Phys.* **11**, 1
- Scalo, J. M., Despain, K. H., and Ulrich, R. K.: 1975, *ApJ* **196**, 805
- Scalo, J. M. and Ulrich, R. K.: 1975, *ApJ* **200**, 682
- Schaller, G., Schaerer, D., Meynet, G., and Maeder, A.: 1992, *A&AS* **96**, 269

- Schwarzschild, K.: 1906, *Nachrichten von der Königlichen Gesellschaft der Wissenschaften zu Göttingen. Math.-phys. Klasse, 195*, p. 41-53 **195**, 41
- Schwarzschild, M.: 1970, *QJRAS* **11**, 12
- Schwarzschild, M. and Härm, R.: 1969, in *Bulletin of the American Astronomical Society*, Vol. 1 of *Bulletin of the American Astronomical Society*, p. 99
- Siess, L., Livio, M., and Lattanzio, J.: 2002, *ApJ* **570**, 329
- Simpson, R. W.: 1971, *Proceedings of the Astronomical Society of Australia* **2**, 27
- Sirianni, M., Jee, M. J., Benítez, N., Blakeslee, J. P., Martel, A. R., Meurer, G., Clampin, M., De Marchi, G., Ford, H. C., Gilliland, R., Hartig, G. F., Illingworth, G. D., Mack, J., and McCann, W. J.: 2005, *PASP* **117**, 1049
- Smith, V. V. and Lambert, D. L.: 1990, *ApJS* **72**, 387
- Spite, M., Cayrel, R., Plez, B., Hill, V., Spite, F., Depagne, E., François, P., Bonifacio, P., Barbuy, B., Beers, T., Andersen, J., Molaro, P., Nordström, B., and Primas, F.: 2005, *A&A* **430**, 655
- Spruit, H. C.: 2002, *A&A* **381**, 923
- Stancliffe, R. J., Dearborn, D. S. P., Lattanzio, J. C., Heap, S. A., and Campbell, S. W.: 2011, *ApJ* **742**, 121
- Stancliffe, R. J. and Glebbeek, E.: 2008, *MNRAS* **389**, 1828
- Stancliffe, R. J., Glebbeek, E., Izzard, R. G., and Pols, O. R.: 2007, *A&A* **464**, L57
- Stancliffe, R. J., Lugaro, M., Karakas, A. I., and Tout, C. A.: 2005, *Nuclear Physics A* **758**, 569
- Stancliffe, R. J., Tout, C. A., and Pols, O. R.: 2004, *MNRAS* **352**, 984
- Stello, D., Huber, D., Bedding, T. R., Benomar, O., Bildsten, L., Elsworth, Y. P., Gilliland, R. L., Mosser, B., Paxton, B., and White, T. R.: 2013, *ApJ* **765**, L41
- Straniero, O., Domínguez, I., Imbriani, G., and Piersanti, L.: 2003, *ApJ* **583**, 878
- Straniero, O., Gallino, R., and Cristallo, S.: 2006, *Nuclear Physics A* **777**, 311
- Suda, T. and Fujimoto, M. Y.: 2010, *MNRAS* **405**, 177
- Suda, T., Komiya, Y., Yamada, S., Katsuta, Y., Aoki, W., Gil-Pons, P., Doherty, C. L., Campbell, S. W., Wood, P. R., and Fujimoto, M. Y.: 2013, *MNRAS* **432**, L46
- Suda, T., Yamada, S., Katsuta, Y., Komiya, Y., Ishizuka, C., Aoki, W., and Fujimoto, M. Y.: 2011, *MNRAS* **412**, 843
- Sweigart, A. V.: 1999, in Y.-H. Chu, N. Suntzeff, J. Hesser, and D. Bohlender (eds.), *New Views of the Magellanic Clouds*, Vol. 190 of *IAU Symposium*, p. 370

- Sweigart, A. V. and Demarque, P.: 1973, in J. D. Fernie (ed.), *IAU Colloq. 21: Variable Stars in Globular Clusters and in Related Systems*, Vol. 36 of *Astrophysics and Space Science Library*, p. 221
- Sweigart, A. V. and Gross, P. G.: 1976, *ApJS* **32**, 367
- Sweigart, A. V., Lattanzio, J. C., Gray, J. P., and Tout, C. A.: 2000, in A. Noels, P. Magain, D. Caro, E. Jehin, G. Parmentier, and A. A. Thoul (eds.), *Liege International Astrophysical Colloquia*, Vol. 35 of *Liege International Astrophysical Colloquia*, p. 529
- Sweigart, A. V., Mengel, J. G., and Demarque, P.: 1974, *A&A* **30**, 13
- Tassoul, M.: 1980, *ApJS* **43**, 469
- Timmes, F. X. and Arnett, D.: 1999, *ApJS* **125**, 277
- Timmes, F. X. and Swesty, F. D.: 2000, *ApJS* **126**, 501
- Ulrich, R. K.: 1986, *ApJ* **306**, L37
- Van Grootel, V., Charpinet, S., Brassard, P., Fontaine, G., and Green, E. M.: 2013a, *A&A* **553**, A97
- Van Grootel, V., Charpinet, S., Fontaine, G., and Brassard, P.: 2010a, *Ap&SS* **329**, 217
- Van Grootel, V., Charpinet, S., Fontaine, G., Brassard, P., Green, E. M., Randall, S. K., Silvotti, R., Østensen, R. H., Kjeldsen, H., Christensen-Dalsgaard, J., Borucki, W. J., and Koch, D.: 2010b, *ApJ* **718**, L97
- Van Grootel, V., Charpinet, S., Fontaine, G., Green, E. M., and Brassard, P.: 2010c, *A&A* **524**, A63
- Van Grootel, V., Fontaine, G., Charpinet, S., Brassard, P., and Green, E. M.: 2013b, in *European Physical Journal Web of Conferences*, Vol. 43 of *European Physical Journal Web of Conferences*, p. 4007
- Vandakurov, Y. V.: 1967, *AZh* **44**, 786
- VandenBerg, D. A., Brogaard, K., Leaman, R., and Casagrande, L.: 2013, *ApJ* **775**, 134
- Vargas Álvarez, C. A. and Sandquist, E. L.: 2007, *AJ* **134**, 825
- Vassiliadis, E. and Wood, P. R.: 1993, *ApJ* **413**, 641
- Ventura, P., Caloi, V., D'Antona, F., Ferguson, J., Milone, A., and Piotto, G. P.: 2009, *MNRAS* **399**, 934
- Ventura, P., Criscienzo, M. D., D'Antona, F., Vesperini, E., Tailo, M., Dell'Agli, F., and D'Ercole, A.: 2013, *MNRAS*
- Ventura, P., D'Antona, F., and Mazzitelli, I.: 2002, *A&A* **393**, 215
- Ventura, P., D'Antona, F., and Mazzitelli, I.: 2008, *Ap&SS* **316**, 93

- Ventura, P. and Marigo, P.: 2009, MNRAS **399**, L54
- Ventura, P. and Marigo, P.: 2010, MNRAS **408**, 2476
- Viaux, N., Catelan, M., Stetson, P. B., Raffelt, G. G., Redondo, J., Valcarce, A. A. R., and Weiss, A.: 2013a, *Physical Review Letters* **111(23)**, 231301
- Viaux, N., Catelan, M., Stetson, P. B., Raffelt, G. G., Redondo, J., Valcarce, A. A. R., and Weiss, A.: 2013b, A&A **558**, A12
- Villanova, S., Geisler, D., and Piotto, G.: 2010, ApJ **722**, L18
- Villanova, S., Geisler, D., Piotto, G., and Gratton, R. G.: 2012, ApJ **748**, 62
- Villanova, S., Piotto, G., and Gratton, R. G.: 2009, A&A **499**, 755
- Weiss, A. and Ferguson, J. W.: 2009, A&A **508**, 1343
- Wood, P. R.: 1990, *From Miras to Planetary Nebulae: Which Path to Stellar Evolution? : Montpellier, France, September 4-7, 1989*, Chapt. Pulsation and Evolution of Mira Variables, IAP astrophysics meeting, Editions Frontières
- Wood, P. R.: 1990, in M. O. Mennessier and A. Omont (eds.), *From Miras to Planetary Nebulae: Which Path for Stellar Evolution?*, pp 67–84
- Wood, P. R. and Faulkner, D. J.: 1986, ApJ **307**, 659
- Wood, P. R. and Zarro, D. M.: 1981, ApJ **247**, 247
- Xu, Y., Takahashi, K., Goriely, S., Arnould, M., Ohta, M., and Utsunomiya, H.: 2013, *Nuclear Physics A* **918**, 61
- Yong, D., Grundahl, F., D’Antona, F., Karakas, A. I., Lattanzio, J. C., and Norris, J. E.: 2009, ApJ **695**, L62
- Zahn, J.-P.: 1992, A&A **265**, 115
- Østensen, R. H., Telting, J. H., Reed, M. D., Baran, A. S., Nemeth, P., and Kiaeerad, F.: 2014, A&A **569**, A15